Aerothermal characterisation of a surface heat exchanger implemented in a turbofan by-pass duct

Matteo Gelain

université
PARIS-SACLAY

Caractérisation aérothermique d'un échangeur de chaleur surfacique implémenté en veine secondaire

Aerothermal characterisation of a surface heat exchanger implemented in a turbofan by-pass duct

Thèse de doctorat de l'université Paris-Saclay

École doctorale n° 579, Sciences mécaniques et énergétiques, matériaux et géosciences (SMEMAG)
Spécialité de doctorat: Mécanique des fluides
Graduate School : Sciences de l'ingénierie et des systèmes, Référent : CentraleSupélec

Thèse préparée dans l'unité de recherche EM2C (Université Paris-Saclay, CNRS, CentraleSupélec) sous la direction d'Olivier GICQUEL, professeur, et le co-encadrement de Alexandre COUILLEAUX, Marc ERRERA, Maître de Recherche, et Ronan VICQUELIN, professeur.

Thèse soutenue à Paris-Saclay, le 26 novembre 2021, par

Matteo GELAIN

Composition du jury

Benjamin Rémy Professeur, Université de Lorraine (LEMTA)	Président
Laurent Gicquel Chercheur senior, CERFACS	Rapporteur & Examinateur
Pierre Sagaut Professeur, Université d'Aix-Marseille (M2P2)	Rapporteur
Éva Dorignac Professeure, Université de Poitiers (Institut P')	Examinatrice
Olivier Gicquel Professeur, CentraleSupélec (EM2C)	Directeur de thèse
Alexandre Couilleaux Ingénieur Expert, Safran Aircraft Engines	Coencadrant
Marc Errera Maître de Recherche, ONERA	Coencadrant
Ronan Vicquelin Professeur, CentraleSupélec (EM2C)	Coencadrant

THESE DE DOCTORAT
NNT : 2021UPAST136

université PARIS-SACLAY

ÉCOLE DOCTORALE
Sciences mécaniques et énergétiques, matériaux et géosciences (SMEMAG)

Titre: Caractérisation aérothermique d'un échangeur de chaleur surfacique implémenté en veine secondaire
Mots clés: Couplage Aérothermique, CFD, Échangeur de chaleur, Turbofan, LES, WMLES

Résumé: Les configurations innovantes de moteur d'aviation civile amèneront à d'importantes réductions de consommation de carburant. Actuellement, chez Safran Aircraft Engines, des nouveaux concepts tels que le Geared Turbofan et l'Open Rotor sont étudiés attentivement. Ces concepts sont caractérisés par des architectures de plus en plus complexes qui nécessitent d'être lubrifiés et refroidis. Par conséquent, les systèmes de gestion thermique sont un module fondamental des moteurs d'aujourd'hui. Dans cette thèse, on s'intéresse aux surface air-cooled oil coolers (SACOC). Un SACOC est généralement composé d'une sérié d'ailettes orientées dans la direction de l'écoulement. La source chaude est représentée par le lubrifiant du moteur. Le premier objectif de la thèse est de caractériser les interactions aérothermiques qui ont lieu entre le SACOC et le flux secondaire. Le deuxième but est de se doter de méthodologies prédictives, validées et accessibles qui permettent d'étudier ces interactions.

Title: Aerothermal characterisation of a surface heat exchanger implemented in a turbofan by-pass duct
Keywords: Conjugate Heat Transfer, CFD, Heat Exchanger, Turbofan, LES, WMLES

Abstract: Innovative civil aircraft engine configurations of the present and of the future are leading to important reductions of fuel consumption. At Safran Aircraft Engines, new concepts like the Geared Turbofan and the Open Rotor are currently under attentive study. These concepts are characterised by an increasingly complex architecture that demands lubrication and cooling. Thermal management systems, therefore, are a fundamental module of modern engines. In this work, we take an interest in surface air-cooled oil coolers (SACOC). Common SACOC are composed of a series of staggered fins, aligned along the direction of the by-pass duct flow. The hot source is the engine lubricant. The objective of this thesis is twofold. The first goal is to characterise the aerothermal interactions taking place between the SACOC and the by-pass airflow. The second goal, is to provide predictive, validated and accessible methodologies for investigating such interactions.

Acknowledgements

This work is the outcome of numerous collaborations between industrial, research and academic institutions. It is the occasion to thank all the people who have been a part of this.

The first acknowledgements are dedicated to the ensemble of Safran Aircraft Engines, where I have grown, both personally and professionally, since the end of my studies. I would like to thank the company for its unconditional support throughout the Ph.D., and for the important resources made available to meet the ambitions of this work. I am particularly grateful to Bastien Verdier, who tutored me during my internship and recommended me for this Ph.D., to Christian Haddad, who made all of this possible, and to Nicolas Sirvin and Alexandre Couilleaux, who have followed me throughout these three years of work. I am glad to be continuing my adventure at Safran Aircraft Engines after this Ph.D., and for many years ahead.

Further acknowledgements are addressed to my tutors. Once again, I thank Alexandre Couilleaux of Safran Aircraft Engines, but also Marc Errera (ONERA), Olivier Gicquel and Ronan Vicquelin (École CentraleSupélec). Thank you for your guide, your tutoring of the highest quality and your warm welcome at Châtillon and Gif-sur-Yvette. I hope and believe that there will be other occasions to collaborate in the future.

I thank the people of Universitat Politècnica de València (in particular A. Broatch, J. García and A. Felgueroso) and Universidad Politécnica de Madrid (in particular L. González and M. Chávez) for the excellent work we have carried out since 2019 to realise the Clean Sky 2 SACOC project.

I would also like to thank several people who, although not cited in my publications, have given a decisive contribution to this Ph.D. I thank Jean Bertucchi, of Safran Aircraft Engines, for the realisation of all the complex engine and test-bench SACOC meshes used in Part III, and Teddy Chantrait of Safran Tech, for his help in implementing the aerothermal coupling.

I address the final acknowledgements to my family. To my mother, father and sister, to whom I dedicate this work.

Abstract

Innovative civil aircraft engine configurations of the present and of the future are leading, and will lead, to important reductions of fuel consumption. At Safran Aircraft Engines, new concepts like the Geared Turbofan and the Open Rotor are currently under attentive study. These concepts will allow for a considerably higher by-pass ratio, with respect to the previous generation of turbofans. However, they are characterised by an increasingly complex architecture, which features intricate mechanical transmissions and electrical components that demand, respectively, lubrication and cooling. Thermal management systems, therefore, are a fundamental module of modern engines. The most important cold heat sink available in a turbofan is the high-velocity low-temperature by-pass duct airflow. It is the reason why heat exchangers have been implemented in the by-pass duct since the early generation of engines. In this work, we take an interest in one particular type of heat exchanger, the surface air-cooled oil cooler (SACOC). Common SACOC are composed of a series of staggered fins, aligned along the direction of the by-pass duct flow. The hot source is represented by the engine lubricant, which flows in a complex system of channels placed beneath the heat exchanger. SACOC have an impact on both the operability of the engine, due to the specified heat load to remove, and on its performance, since the pressure drop generated by the SACOC reduces the engine thrust. The objective of this thesis is twofold. The first goal is to characterise the aerothermal interactions taking place between the SACOC and the by-pass airflow. The second goal, is to provide predictive, validated and accessible methodologies for investigating such interactions. The work is organised in two sets of activities, each meeting both objectives of the thesis.

In the first set of activities, one particular phenomenological aspect of the SACOC is analysed, *i.e.*, the fact that a temperature-homogeneous flow makes contact with a heated body. So as to isolate this effect, a simplified configuration of heat exchanger is proposed. It consists of a channel flow, divided into two distinct sections. The upstream section has adiabatic walls, and the flow is turbulent, fully developed, temperature-homogeneous and, above all, at an equilibrium state. The downstream section has isothermal walls. Due to the abrupt change of wall thermal conditions, the equilibrium flow is perturbed, and the non-equilibrium development of a thermal boundary layer is observed, until, further downstream, the flow reaches a new equilibrium state characterised by a fully developed temperature profile. First, in agreement with the first objective of the thesis, the physical study of this configuration is performed by direct numerical simulation, which represents the most precise numerical tool in computational fluid dynamics. The analysis focuses on the non-equilibrium effects which are expected to be encountered in phenomenologically similar flows, while providing the theoretical bases to understand them. Then, in agreement with the

second objective of the thesis, the same configuration is investigated using a potential candidate for future industrial high-fidelity flow simulations, *i.e.*, wall-modelled large-eddy simulation (WMLES). WMLES is one of the most popular strategies to reduce the computational cost of the near-wall region of the flow. The main principle of WMLES is that the momentum and energy transport taking place in the inner layer is not directly solved, but mimicked by a wall-model. Two wall-models are implemented and tested. The former, is a classic equilibrium wall-model, with which most of the non-equilibrium effects observed with the direct numerical simulation are not captured. The latter, is a new specifically constructed wall-model, which allows for considerably better predictions of the thermal boundary layer development.

In the second set of activities, the aerothermal behaviour of realistic SACOC is investigated through conjugate heat transfer (CHT). CHT refers to all those numerical strategies which involve the simultaneous resolution of heat transfer in several media, generally governed by different sets of equations. CHT, therefore, allows for taking into account the aerothermal interactions taking place among the different bodies and flows. The SACOC, in agreement with the first goal of the thesis, is first studied in its operating environment, *i.e.*, the turbofan by-pass duct. The domain extends from the fan module, composed by a rotating blade, to the outlet guide vane, composed by a stator blade, until the by-pass duct, where a realistic heat exchanger is mounted. The study throws light on the complexity of the by-pass airflow, and on how it influences the aerodynamic and thermal performance of the SACOC. Then, in agreement with the second objective of the thesis, a simpler configuration is analysed, *i.e.*, the square wind-tunnel. The results are compared to the engine configuration, and guidelines are given about the level of representativeness required in smaller-scale test rigs to reproduce realistic engine conditions. Finally, the CHT simulations are compared to wind-tunnel experimental tests, carried out throughout the duration of this thesis, which allow us to validate our numerical methodology for future applications in the engineering offices of Safran Aircraft Engines.

Résumé

Les configurations innovantes de moteur d'aviation civile, présentes et futures, ont amené, et amèneront, à d'importantes réductions de consommation de carburant. Actuellement, chez Safran Aircraft Engines, des nouveaux concepts tels que le Geared Turbofan et l'Open Rotor sont étudiés attentivement. Ces concepts permettront d'obtenir des taux de dilutions considérablement plus élevés par rapport aux générations précédentes de turboréacteurs. Cependant, ces configurations sont caractérisées par des architectures de plus en plus complexes, avec des transmissions mécaniques compliquées et des composants électriques qui nécessitent, respectivement, d'êtres lubrifiés et refroidis. Par conséquent, les systèmes de gestion thermique sont un module fondamental des moteurs d'aujourd'hui. La source froide la plus importante d'un turboréacteur est l'écoulement à haute vitesse et faible température de la veine secondaire, où, par conséquent, les échangeurs de chaleur ont été implémentés depuis les toutes premières générations de moteurs. Dans cette thèse, on s'intéresse à un type particulier d'échangeur air-huile, le *surface air-cooled oil cooler* (SACOC). Un SACOC est généralement composé d'une sérié d'ailettes orientées dans la direction de l'écoulement. La source chaude est représentée par le lubrifiant du moteur, qui s'écoule dans un système complexe de canaux placés en dessous de l'échangeur. Le SACOC a un impact à la fois sur l'opérabilité du moteur, à cause des spécifications d'échange thermique à respecter, et sur ses performances, à cause des pertes de charge générées par l'échangeur qui réduisent la poussée du moteur. La mission de cette thèse est double. Le premier objectif est de caractériser les interactions aérothermiques qui ont lieu entre le SACOC et le flux secondaire. Le deuxième but est de se doter de méthodologies prédictives, validées et accessibles qui permettent d'étudier ces interactions. Le travail est organisé en deux volets d'activités, chacun visant à la fois les deux objectifs de la thèse.

Dans le premier volet d'activités, un aspect phénoménologique particulier du SACOC est analysé, c'est-à-dire le fait qu'un écoulement à température uniforme rentre en contact avec un corps chauffé. Afin d'isoler cet effet, une configuration d'échangeur simplifiée est proposée. Il s'agit d'un canal plan qui est divisé en deux sections distinctes. La section en amont est constituée de parois adiabatiques, et l'écoulement y est turbulent, pleinement développé, à température uniforme et, surtout, à l'équilibre. Les parois de la section en aval, en revanche, sont isothermes. Par suite de la variation abrupte des conditions thermiques à la paroi, l'écoulement est perturbé et le développement hors-équilibre d'une couche limite thermique a lieu, jusqu'à ce que, plus en aval, l'écoulement atteigne un nouvel état d'équilibre, caractérisé par un profil de température pleinement développé. D'abord, en accord avec le premier objectif de la thèse, l'étude physique de cette configuration est réalisée par simulation numérique directe, qui représente l'outil numérique le plus précis

en dynamique des fluides. L'analyse se focalise sur les effets hors-équilibre qui ont vraisemblablement lieu dans tous les écoulements phénoménologiquement similaires, en fournissant les bases théoriques pour les comprendre. Ensuite, en accord avec le second objectif de la thèse, la même configuration est étudiée en utilisant un candidat potentiel pour de futures simulations industrielles à haute-fidélité, c'est-à-dire la simulation aux grandes-échelles avec modèle de paroi (*wall-modelled large-eddy simulation*, WMLES). La WMLES est l'une des stratégies le plus populaires pour réduire le coût de calcul de la zone proche paroi de l'écoulement. Le principe fondamental de la WMLES est le fait que le transport de quantité de mouvement et d'énergie au sein de la couche limite interne n'est pas directement résolu, mais modélisé par ce que l'on appelle un modèle de paroi. Deux modèles de paroi sont implémentés et testés. Le premier, est un modèle classique à l'équilibre, avec lequel la plupart des effets hors-équilibre observés par simulation numérique directe ne sont pas capturés. Le second, est un nouveau modèle de paroi construit *ad hoc*, qui permet d'obtenir des prédictions considérablement meilleures de l'évolution de la couche limite thermique.

Dans le second volet d'activités, les performances d'un SACOC réaliste sont étudiées par transfert de chaleur conjugué (*conjugate heat transfer*, CHT). Le CHT fait référence à toutes les stratégies numériques qui prévoient la résolution simultanée du transfert de chaleur dans plusieurs milieux, qui sont généralement régis par des systèmes d'équations différents. Le CHT permet donc d'avoir accès aux interactions aérothermiques qui ont lieu entre les différents corps et écoulements. Le SACOC, en accord avec le premier objectif de la thèse, est d'abord analysé dans son environnement opérationnel, c'est-à-dire la veine secondaire d'un turboréacteur. Le domaine s'étend de la soufflante, avec une aube *fan* en rotation, à l'*outlet guide vane*, avec une aube fixe, jusqu'à la veine secondaire, où l'échangeur de chaleur est implémenté. L'étude met en évidence la complexité du flux secondaire et l'impact qu'il peut avoir sur les performances aérodynamiques et thermiques du SACOC. Ensuite, en accord avec le second objectif de la thèse, une configuration plus simple est étudiée, c'est-à-dire, une veine d'essai carrée. Les résultats sont comparés à la configuration moteur, et des indications sont fournies concernant le niveau de représentativité dont les veines d'essai doivent être dotées pour reproduire fidèlement les conditions de la veine secondaire. Finalement, les simulations couplées sont comparées à des essais expérimentaux en veine carrée, lesquels, réalisés tout au long de la thèse, permettent de valider notre méthodologie numérique pour les prochaines applications dans les bureaux d'étude de Safran Aircraft Engines.

Contents

III Conjugate heat transfer investigation of a surface air-oil heat-exchanger

Nomenclature

Acronyms

ACARE	Advisory Council for Aeronautics Research in Europe
ACOC	Air-cooled oil cooler
AOHE	Air/Oil Heat Exchanger
BPD	By-pass duct
CFD	Computational fluid dynamics
CHT	Conjugate heat transfer
CS2	Clean Sky 2
CSJU	Clean Sky Joint Undertaking
DES	Detached eddy simulation
DMS	Downstream measurement station
DNS	Direct numerical simulation
FOHE	Fuel/Oil Heat Exchanger
HMHT	High Mass-flow and High Temperature
IFS	Inner-fixed structure
IR	Infra-red
ITD	Integrated Technology Demonstrator
LDA	Laser Doppler Anemometry
LEAP	Leading Edge Aviation Propulsion
LES	Large-eddy simulation
LLM	Logarithmic-layer mismatch
MEA	More electric aircraft
MPI	Message passing interface
ODE	Ordinary differential equation

OFS	Outer-fixed structure
OGV	Outlet guide vane
PIV	Particle Image Velocimetry
r.m.s.	Root mean square
RANS	Reynolds-averaged Navier-Stokes
SACOC	Surface air-cooled oil cooler
SFC	Specific Fuel Consumption
SGS	Subgrid-scale
SST	Shear-Stress Transport
TBC	Thermal barrier coating
TBLE	Thin boundary layer equations
TKI	Turbulent kinetic intensity
TMS	Thermal management system
UHBR	Ultra High By-pass Ratio
UHPE	Ultra High Propulsive Efficiency
UMS	Upstream measurement station
UPM	Universidad Politécnica de Madrid
UPV	Universitat Politècnica de València
WALE	Wall-adaptive local eddy viscosity
WMLES	Wall-modelled large-eddy simulation
WP	Working package

Non-dimensional numbers

$\mathrm{Bi}_\nu = \frac{K_f}{K_s}\frac{2}{1+\sqrt{1+\mathrm{D}_f}}$	Numerical Biot number
$\mathrm{B}_q = \frac{q_w}{\rho_w c_{p_w} u_\tau T_w}$	Heat flux parameter
$\mathrm{C}_D = \frac{\mathcal{T}_w}{\frac{1}{2}\rho u^2}$	Drag coefficient
$\mathrm{C}_f = \frac{\tau_w}{\frac{1}{2}\rho u^2}$	Friction coefficient
$\mathrm{D}_f = \frac{a_f \Delta t}{\Delta x^2}$	Mesh Fourier number
$\mathrm{Fo} = \frac{a\mathcal{T}}{L^2}$	Fourier number
$\mathrm{M} = \frac{u}{c}$	Mach number
$\mathrm{Nu} = L\frac{q_w}{\lambda \Delta T}$	Nusselt number

$\mathrm{Pr_t} = \frac{\mu_t c_p}{\lambda_t}$	Turbulent Prandtl number
$\mathrm{Pr} = \frac{\mu c_p}{\lambda}$	Prandtl number
$\mathrm{Re} = \frac{uL}{\nu}$	Reynolds number
$\mathrm{Re}_\tau = \frac{u_\tau \delta}{\nu}$	Friction Reynolds number
$y^* = \frac{y\sqrt{\tau_w/\rho}}{\nu}$	Semi-local scaling
$y^+ = \frac{y\sqrt{\tau_w/\rho_w}}{\nu_w}$	Wall scaling

Physical properties

$(\cdot)_b$	Bulk quantity
$(\cdot)_c$	Quantity at the centre
$(\cdot)_w$	Quantity at the wall
Δt	Time step, s
Δx	Mesh size, m
δ	Boundary layer's thickness, m
λ	Thermal conductivity, $\mathrm{W/(m\,K)}$
λ_t	Turbulent conductivity, $\mathrm{W/(m\,K)}$
$\mathcal{T}$	Characteristic time, s
$\mathcal{T}_w$	Shear force, N
μ	Dynamic viscosity, $\mathrm{Pa\,s}$
μ_t	Turbulent viscosity, $\mathrm{Pa\,s}$
ν	Kinematic viscosity, $\mathrm{m^2/s}$
ρ	Mass density, $\mathrm{kg/m^3}$
τ	Shear stress, Pa
a_f	Fluid diffusivity, $\mathrm{m^2/s}$
c	Velocity of sound, m/s
c_p	Thermal capacity at constant pressure, $\mathrm{J/(kg\,K)}$
$K_{f/s}$	Fluid/Solid conductance, $\mathrm{W/(m^2\,K)}$
L	Characteristic length, m
q	Heat flux, $\mathrm{W/m^2}$
T	Temperature, K
u	Streamwise velocity, m/s

u_τ	Friction velocity, m/s
v	Wal-normal velocity, m/s
w	Spanwise velocity, m/s
x	Streamwise coordinate, m
y	Wal-normal coordinate, m
z	Spanwise coordinate, m

Introduction

In the race for better performances, the architecture of civil aircraft engines is becoming increasingly complex from generation to generation of engines. In fact, the ambitious objectives set by the Advisory Council for Aviation Research and Innovation in Europe (ACARE), *i.e.*, reducing CO_2 emissions by 75% and NO_X emissions by 90% (with respect to the average aircraft in 2000) before 2050, can only be attained by drastically improving the design of aircraft engines. Therefore, engine manufacturers like Safran Aircraft Engines (Safran AE), have been intensively exploring innovative architectures which have led, and will lead, to decisive abatements of specific fuel consumption (SFC).

The new engines of the Leading Edge Aviation Propulsion (LEAP) generation developed by CFM International (see Fig. 1), for instance, are characterised by a 16% and 50% drop of CO_2 and NO_X, respectively, with respect to the previous CFM56. New Ultra High By-pass Ratio (UHBR) concepts like the Geared Turbofan and the Open Rotor, will bring further important improvements. All these architectures feature complex mechanical transmissions which, combined with the higher turbine entry temperatures, multiplying electrical components (More Electric Aircraft, MEA) and broadening use of low-conductive composite materials, make of Thermal Management Systems (TMS) a fundamental module of modern engines.

Lubricant-cooling, in particular, poses severe technological challenges, as the demand of heat removal capacity continues to grow (see Jafari and Nikolaidis, 2018). Besides, in such a high-temperature operating environment, it is evident that cold heat sinks are an extremely scarce resource, and the problem has been acknowledged since the very early years of the aircraft industry (see, for instance, Worth, 1937). The first patents openly published (Marshall, 1958; Cummings and Lance, 1963), presented complete TMS based on Fuel/Oil Heat Exchangers (FOHE) which, as the name suggests, utilise the engine's fuel to cool the lubrication circuit. This strategy is still today very popular and commonly implemented. Indeed, the high density and thermal conductivity of the fuel, allow for very compact heat exchangers. However, due to the limited fuel's maximal temperature and mass flow (especially in today's better performing engines), FOHE alone are incapable of meeting the thermal management requirements (Streifinger, 1999).

As a matter of fact, even the early patents cited above envisaged the combination of FOHE and Air/Oil Heat Exchangers (AOHE), which can benefit, in particular, from a vast heat sink, *i.e.*, the high-velocity air flow of the by-pass duct. Common configurations of AOHE (or Air-Cooled Oil Coolers, ACOC), include traditional box-shaped plate or tube types of heat exchangers, which, all in all, do not considerably differ from ordinary car radiators. Concepts for aircraft engine applications can be found in Griffin et al. (1979) or, more recently, in Schwarz and Elsaesser (2012) They are embodied in the by-pass duct of the turbofan, where a small fraction of

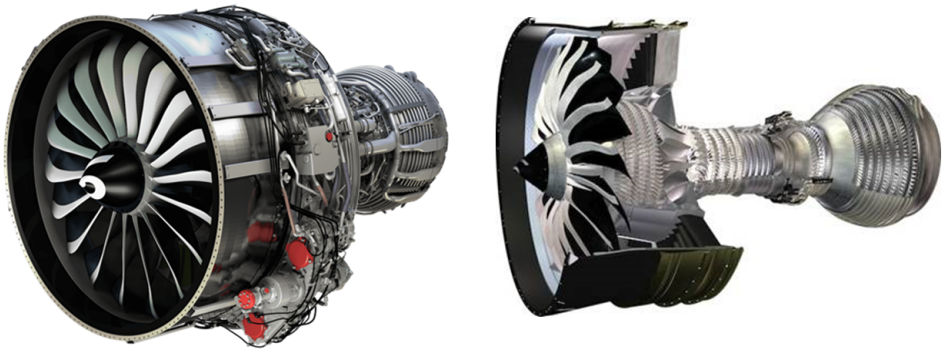

Figure 1: LEAP, by CFM International, joint-venture between Safran and General Electric.

the air flow is conveyed to the ACOC, and put in thermal contact with the lubricant oil. In addition to their weight, these systems penalise the performance of the engine through the pressure drop they generate in the air flow, which is subsequently ejected through the nozzle, and constitutes the majority of the engine's thrust.

Therefore, in recent years, attention has been drawn to a different category of AOHE, the surface air-cooled oil-cooler (SACOC), that represents the industrial configuration on which we focus in this Ph.D. work. Some concepts of SACOC can be found in Bajusz et al. (2009) or Elder (2014). These heat exchangers are usually composed of a series of staggered fins oriented along the direction of the flow, as shown in Bajusz et al. (2009) or schematically depicted in Fig. 2, but other configurations have been proposed (see, for instance, the discontinuous fins of Antel et al. (2017)). The oil flows in a complex circuit, usually made of small channels, but also continuous or discontinuous fins, which is located beneath the air fins, and connects the heat exchanger with the different engine components to be lubricated. Implemented in the by-pass duct (BPD), SACOC have the potential of introducing lower flow disturbances compared to box-shaped ACOC, thereby reducing the overall impact on the performance of the engine.

Different locations have been proposed in the patents. Bajusz et al. (2009), for instance, suggested implementing the SACOC on the air separator nose, *i.e.*, between the fan and the outlet guide vane (OGV). Elder (2014), instead, envisaged to locate it on the inner-fixed structure (IFS), downstream of the OGV. In our case of study, the configuration resembles the schematic section of Figure 3. Observe that the heat exchanger is placed on the OFS, downstream of the OGV; this location is preferable with respect to the separator nose, since the OGV delivers a straightened flow that helps orienteering the fins along its direction; furthermore, the flow disturbance induced by the SACOC is introduced into an essentially exhaust flow, which interacts with less critical aerodynamic parts of the by-pass duct compared to the OGV; finally, the OFS evidently offers a wider circumference for the SACOC panels, compared to the IFS.

Given its location, its purpose and its functioning, SACOC pose several challenges from an engineering point of view. The first three months of the Ph.D., spent in the

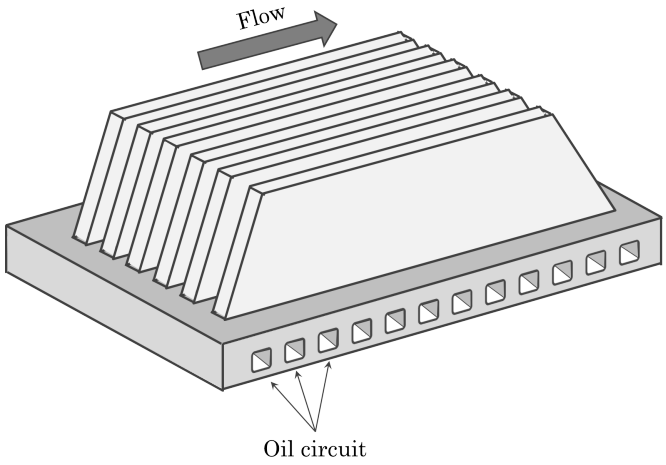

Figure 2: Schematic view of a typical SACOC.

External Aerodynamic Systems unit of Safran Arcraft Engines, have mostly been devoted to discussing with the different engineering offices, in order to make an inventory of their necessities and constraints, summarised in the following list:

— *Thermal management*: the heat exchanger must guarantee an appropriate level of heat dissipation in all phases of flight (including the low-speed phase of ground idle) and in all climatic conditions; furthermore, its transient phase should be monitored; finally, the system should be by-passed, in case the oil does not need cooling.

— *Aerodynamics*: the SACOC interacts with a complex anisotropic flow delivered by the OGV; moreover, the pressure drop it generates has a direct impact on the engine's thrust and its SFC; therefore, optimal design is required.

— *Aerothermodynamics*: thermal management and aerodynamics are coupled, since the heat exchange is generated by forced convection; an accurate assessment of the flow is fundamental to characterise the thermal performance of the SACOC; vice-versa, the heat introduced into the flow might influence its aerodynamic behaviour.

— *Integration*: the OGV and the by-pass duct are usually studied independently, yet the proximity of the heat exchanger to the OGV blades might cause aerodynamic interactions between the two, and require integrated studies.

— *Acoustics*: the air passage through the heat exchanger generates noise that, given the noise-reduction objectives set by the ACARE for 2050, should be controlled and possibly reduced.

— *Architecture*: the SACOC is arranged in circumferential panels distributed around the OFS and the oil system, constituted by circuits, pressure valves, thermal valves and by-pass ducts, is extremely complex.

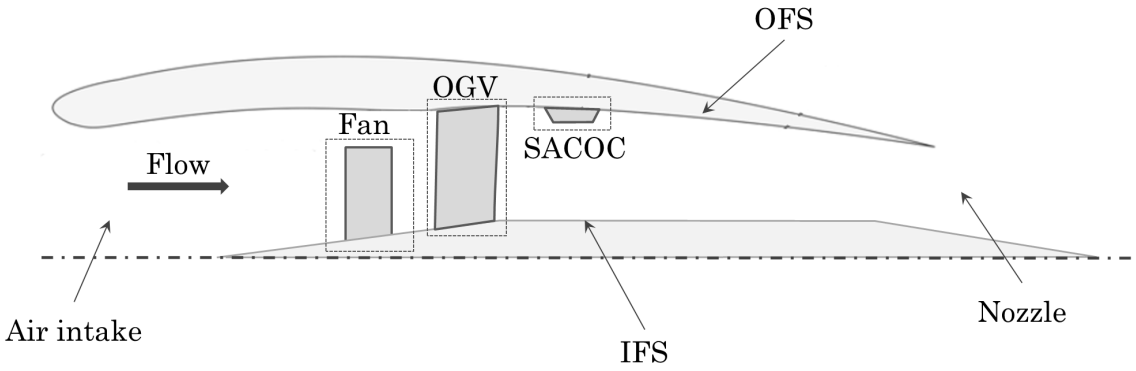

Figure 3: Schematic section of a turbofan by-pass duct with SACOC.

— *Structural integrity and vibration resistance*: any SACOC design must take into account the strong vibrations and structural load it is subjected to in the BPD.

— *Manufacturing*: SACOC geometries must take into consideration their practical feasibility.

Clearly, not all these multidisciplinary challenges can be taken up in a single Ph.D. work. Our focus is on the first three bullet-points of the list above, and the concerns of the different engineering offices have been reformulated and synthesised to yield two fundamental problems that, on the one hand, justify the necessity of a Ph.D. and that, on the other hand, should be addressed in our work.

i. *The general incomprehension of the aerothermal behaviour of the SACOC*
The SACOC operates in a challenging operating environment, which is characterised by complex flow conditions, as well as aerodynamic and aerothermal interactions, which evolve during the different phases of flight. Aerodynamically, it is not clear how these conditions influence the performance of the heat exchanger, or how the presence of the SACOC can modify the upstream flow, which is usually considered as a boundary condition in our usual simulations. Thermally, it is not clear to which extent the aerothermal interactions are strong. We do not know, for instance, if the heat introduced into the flow by the SACOC negatively affects its performance through a considerable increase of the pressure drop, or positively influences the engine's thrust through the slight stagnation temperature rise of the by-pass flow. We do not know, either, if any thermal gradients can actually be appreciated within the fins, given their reduced size, and if simplifying assumptions might be justified, such as considering the SACOC surface as isothermal. Unfortunately, experimental campaigns have not clarified all our doubts.

ii. *The lack of predictive aerothermal numerical methodologies*
In Safran Aircraft Engines (Safran AE), before this Ph.D., the thermal performances of SACOC were mainly evaluated through empiric tools of limited physical fidelity. Such tools are not completely devoid of physical meaning; furthermore, they are extremely easy to employ, and demand little to no com-

putational time and power. However, their range of validity is excessively narrow, being limited to a few fin geometries and flow conditions. Furthermore, being calibrated through experimental tests and being based, for the most part, on correlation laws, they are unable to provide any insight into the complex aerothermal interactions between the SACOC and the by-pass flow.

Furthermore, the vast majority of the Computational Fluid Dynamics (CFD) investigations carried out in Safran AE, are based on Reynolds-averaged Navier-Stokes (RANS) approaches. RANS simulations are appreciated for their reduced cost, general simplicity of setup, robustness and maturity. However, RANS turbulence modelling is well-known for failing to capture fine features of the flow which might be decisive in our study configuration. Higher-fidelity strategies, however, are either out of reach or lack of maturity.

These clearly identified issues, have led to the formulation of the two objectives of this Ph.D. thesis, *i.e.*:

1. Improving our physical understanding of aircraft engine's heat exchangers.
2. Providing predictive numerical methodologies for better investigating complex aerothermal interactions.

As can be seen, both objectives revolve around the concept of *characterisation*. We do not deal, instead, with design and, especially, *optimisation*, which represent the most natural perspectives and continuations of our work.

So as to meet the objectives of the thesis, the working plan has been organised in two sets of scientific research activities, each of them addressing *both* objectives of the Ph.D. They are characterised, however, by profoundly different methodologies of investigation and configurations of study. We propose to delve into the details of these activities.

High-fidelity study of a non-equilibrium turbulent heat transfer case

Motivation & Overview

The SACOC configuration is extremely rich from a phenomenological point of view. One could bring attention to the behaviour of a three-dimensional flow (such as the one downstream of the OGV) encountering an aerodynamic obstacle, and investigate what would change if this same flow were, instead, homogeneous. One could study the aerodynamic interaction between two consecutive bodies, *i.e.*, in this case, the SACOC and the OGV blades. One could also take an interest in the development of the velocity and thermal boundary layers between the fins (see Fig. 2), and investigate for which geometries and flow conditions the laminarisation of the flow is observed.

In this first set of activities, we focus on one particular phenomenological aspect of the SACOC, *i.e.*, the fact that an essentially temperature-homogeneous flow is put in thermal contact with a heated body. Due to the step change in wall thermal conditions, the turbulent heat transfer takes place in non-equilibrium conditions. Not only do we desire to investigate these effects, yet we also want to *isolate* them. In other words, we wish that the heated wall be the only perturbation of a temperature-homogeneous flow initially at equilibrium. Furthermore, we intend to observe how the disturbed flow gradually returns to equilibrium, once adapted to the modified wall conditions. These investigations are meant to elucidate how a temperature

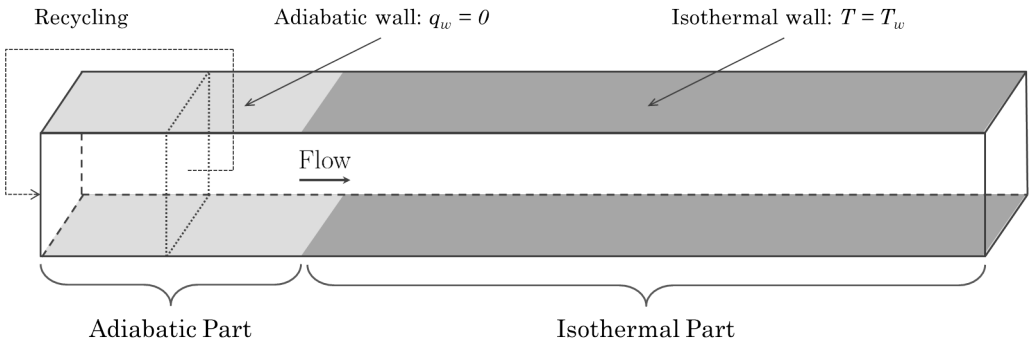

Figure 4: High-fidelity study of a non-equilibrium turbulent heat transfer case. Configuration of study.

gradient influences the behaviour of a flow, and how a turbulent thermal boundary layer evolves in such conditions.

To achieve these goals, we propose the configuration of study depicted in Figure 4. It is a long channel flow consisting of two distinct sections. The upstream section is characterised by adiabatic walls, and we want the flow to be turbulent, fully developed, temperature-homogeneous and at equilibrium. In order to do so at a moderate cost, a recycling strategy is used (see Fig. 4), thanks to which the behaviour of a bi-periodic channel flow is mimicked, and an equilibrium boundary layer is obtained. The downstream part of the domain, instead, has isothermal walls, and the temperature difference between these walls and the upcoming adiabatic flow is of the order of $\Delta T = 100$ K, *i.e.*, the same order characterising the SACOC configuration. The role of the downstream section, on the one hand, is to perturb the upcoming flow and, on the other hand, to allow the boundary layer to attain a new equilibrium state, characterised by a fully-developed thermal boundary layer.

The configuration of Figure 4 represents an extremely simplified heat exchanger. It also constitutes a non-equilibrium turbulent heat transfer case, where non-equilibrium is induced by a step change in surface temperature. Similar configurations have extensively been studied both theoretically and experimentally, with investigations which date back to the 1950s. These early works were motivated, in particular, by the interest in the behaviour of the atmospheric boundary layer (see Antonia et al., 1977), and we can cite, for instance, the experiments led by Johnson and Whippany (1957), Johnson et al. (1959) and Blom (1970), or, more recently, by Biles et al. (2019).

On the other hand, very few numerical investigations of similar flows have been carried out. In fact, interest has been given primarily to equilibrium cases of turbulent heat transfer. We can cite, for instance, the pioneering direct numerical simulation (DNS) by Kim and Moin (1989), where the transport of three passive scalars at different molecular Prandtl numbers has been considered in a fully developed bi-periodic channel flow. Dozens of similar works have been realised since then. In non-equilibrium configurations, instead, we can only cite a handful of studies. Hattori et al. (2007, 2012, 2013) performed several DNS of non-equilibrium boundary layers in the flat plate configuration, analysing the effect of discontinuities of wall thermal conditions, forward-facing steps and buoyancy. Sanchez et al. (2014) and Bellec et al. (2017), instead, performed the large-eddy simulation (LES)

of temperature-homogeneous channel flows making contact with anisothermal walls.

The first objective of these activities, in agreement with the first objective of our Ph.D. work, is thus to deepen the knowledge of non-equilibrium turbulent heat transfer, which is present in numerous industrial applications, including ours. The configuration of Figure 4 is considerably different from our industrial environment. Therefore, we focus on those physical phenomena which are expected to be encountered in both configurations, and we aim at providing the theoretical bases to understand and interpret them.

The second goal of these activities, which meets the second objective of our Ph.D., is to assess a hybrid RANS-LES approach which, despite being promising in terms of physical fidelity, lacks of maturity in non-equilibrium flows. We want to evaluate to which extent this approach can be predictive in the configuration of Figure 4 and, therefore, to which extent it can be *a priori* adapted for our industrial application, the SACOC.

Methodologies of investigation

i. *Direct numerical simulation*

The fine non-equilibrium effects that we want to describe in our physical study, demand the most precise CFD tool available. We refer to the already mentioned direct numerical simulation (DNS), in which the transport equations of mass, momentum and energy are numerically solved without introducing any approximate turbulent model. This approach requires the computational grid to provide sufficient spatial and temporal resolutions to capture all the turbulent scales of the flow. Several assumptions can still be present concerning the nature of the fluid (*e.g.*, ideal gas, Newtonian fluid, incompressible flow); nevertheless, DNS represents the highest degree of physical fidelity that can be obtained in CFD.

Ideally, all flow numerical studies would be performed using DNS, yet its Reynolds number limitation is well known. A rough estimate gives $N \sim \mathrm{Re}^{9/4}$, where N is the number of grid points and Re is the Reynolds number of the flow. Choi and Moin (2012) proposed $N \sim \mathrm{Re}^{37/14}$, which does not change the essence of these estimates, *i.e.*, that DNS is infeasible in practical applications.

These constraints force us to limit the friction Reynolds number of our flow to $\mathrm{Re}_\tau = 395$.

ii. *Wall-modelled LES*

Large-Eddy Simulation (LES) is often referred to as the *middle way* approach between DNS (all turbulent scales solved) and RANS (no turbulent scales solved). The main idea of LES is that a turbulent flow is composed of:

— Large, energetic eddies which are strongly anisotropic and case-by-case dependent; these turbulent structures, therefore, need to be solved, and the computational grid should be refined enough in both space and time to capture them;

— Small eddies which are nearly isotropic and have a similar behaviour regardless of the flow configuration; hence, these structures can easily be modelled.

Since only the large scales of the turbulent flow are solved, LES requires larger space and time resolutions with respect to DNS.

However, since the very early studies, the fact that LES can actually be almost as costly as DNS has clearly emerged. These issues relentlessly appear in high-Reynolds wall-bounded flows, and concern the near-wall region (or inner layer) of the boundary layer, where the large eddies scale with the wall distance, and are in fact small with respect to the characteristic size of the fluid domain. As an example of the level of criticality of the problem, Piomelli and Balaras (2002) estimated that in the case of a wall-bounded flow at $\mathrm{Re} \sim 10^6$, 99% of the LES grid points would be used to solve the inner layer, the thickness of which does not exceed 10% of the boundary layer. Similarly to DNS, the cost is strictly linked to the Reynolds number and, according to the estimate of Chapman (1979), the number of grid points required in LES is $N_{LES} \sim \mathrm{Re}^{9/5}$; Choi and Moin (2012), more recently, proposed $N_{LES} \sim \mathrm{Re}^{13/7}$. Both estimates show how *wall-resolved* LES is in fact not considerably more affordable than DNS, and far from being the compromise solution between RANS and DNS. These issues are usually referred to as *the near-wall problem* of LES (Larsson et al., 2016).

Alleviating the computational cost of LES to the detriment of a certain degree of its physical fidelity is still today a necessity. The way the cost of LES should be reduced has been the object of a vast debate in the scientific community, and countless methods and strategies have been proposed (see Spalart, 2009). However, two families of methods have emerged as the most popular ones, *i.e.*, Detached Eddy Simulation (DES) and Wall-Modelled LES (WMLES).

The original version of DES, introduced by Spalart (1997), has been defined as a *"three-dimensional unsteady numerical solution using a single turbulence model, which functions as a subgrid-scale model in regions where the grid density is fine enough for a large-eddy simulation, and as a Reynolds-averaged model in regions where it is not"* (see Travin et al., 2000; Spalart, 2009); in other words, the method takes advantage of the aesthetic resemblance of the Reynolds-averaged and filtered Navier-Stokes equations, to freely switch between a RANS turbulent model to a SGS model, depending on the grid resolution of each fluid cell. In practical simulations, this leads to the boundary layer being treated by RANS, and the regions of massive separation by LES; the area between these two regions, which has been called by Spalart (2009) *gray area*, can be ambiguous if the flow separation is not abrupt, and represents a major challenge that DES has faced over the years; another issue which has soon emerged, is that the original DES formulation only envisaged the use of the one-equation RANS model of Spalart and Allmaras (1992). These problems have motivated further studies and the development of several derived methods such as Scale-Adaptive Simulation (SAS) (see Menter et al., 2003), Zonal DES (ZDES) (see Deck, 2005), Delayed DES (DDES) (see Menter and Kuntz, 2004; Spalart et al., 2006) and Improved Delayed DES (DDES) (see Shu, 2008). We will not go into further detail concerning these methodologies, and the reader is referred to the cited literature.

The second family of methods is that of WMLES, which we employ in this work. The main principles of WMLES are the following: the LES is performed on a voluntarily coarse mesh which does not allow the large, energetic eddies of the flow to be captured in the near-wall region; consequently, the transport of momentum and energy within the inner layer is poorly resolved, and needs to be modelled; this is performed by a wall-model, which, according to a set of laws and/or equations which characterise its complexity and fidelity, elaborates a certain amount of flow properties extracted from the LES, and returns an estimation of the wall shear-stress and

wall heat flux; these approximate quantities are prescribed at the wall and replace the classic no-slip and temperature-imposed boundary conditions, with which the wall shear-stress and wall heat flux would be severely under-predicted. Differently from DES, in WMLES the simulation entirely remains of LES nature, and only the boundary conditions are modified. From the very first WMLES of Deardorff et al. (1970) and Schumann (1975), who used equilibrium wall-models based on the law of the wall, to the more recent computations of Park and Moin (2014), who employed a full set of three-dimensional unsteady RANS equations in the inner layer, wall-models have progressively evolved, and WMLES has been successfully applied in numerous configurations. Detailed reviews of the progress in WMLES over the years can be found in Piomelli and Balaras (2002), Piomelli (2008), Larsson et al. (2016), Moin et al. (2016) or Bose and Park (2018).

However, the WMLES community has only recently started investigating non-equilibrium flows. Furthermore, to the best of our knowledge, WMLES has never been applied to flows presenting thermal non-equilibrium effects, such as the ones we wish to describe. WMLES is a potential candidate for higher-fidelity simulations in industrial configurations, yet its lack of maturity demands more fundamental studies. In this work, we compare the results obtained by DNS and WMLES, and assess the capability of the latter to capture the evolution of the thermal boundary layer along the channel flow.

Conjugate heat transfer investigation of a surface air-oil heat exchanger

Motivation & Overview

The second set of activities of this Ph.D. thesis, involves study configurations which closely resemble the complex SACOC system we have introduced. The objective is to provide an immediate answer to some of the challenges that SACOC pose.

On the one hand, in agreement with the first objective of the Ph.D., we want to understand in which way its operating environment, *i.e.*, the by-pass duct, is to be considered *challenging*; we need to investigate, for instance, how the complex flow delivered by the fan and OGV modules affect the performance of the heat exchanger; we also need to understand if the effects observed in the BPD can be reproduced with sufficient fidelity in simpler, smaller-scale environments.

On the other hand, in agreement with the second objective of the Ph.D., we aim at providing a better methodology for predicting the aerothermal performances of the SACOC, which is supposed to replace the existing tools at Safran AE; this methodology has to be accessible, mature and robust; besides, its accuracy needs to be evaluated with respect to representative experimental results.

The first configuration subjected to our investigations, is the by-pass duct of a turbofan engine. The domain, as shown in Figure 5, actually represents an angular sector of the BPD, which can be conceptually divided into three sub-domains:

— *Fan sub-domain*: in the axial direction it extends from a plane located slightly downstream of the air-intake to the OGV sub-domain; in the azimuthal direction, the domain is large enough to include one fan blade, which rotates. The fan operates at take-off in standard conditions.

— *OGV sub-domain*: it extends from the rotor-stator interface to the entry of the BPD, while in the azimuthal direction the domain is large enough to include

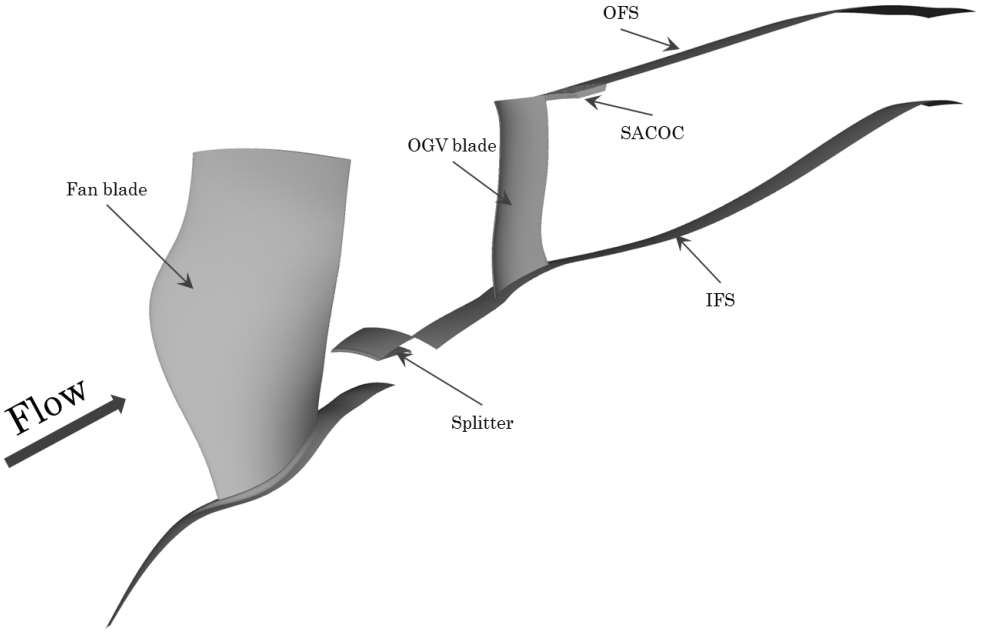

Figure 5: CHT investigation of a SACOC. By-pass duct configuration.

an entire OGV blade. As mentioned before, the role of the OGV is that of straightening the flow elaborated by the fan and delivering it to the BPD.

— *BPD sub-domain*: extending from the interface with the OGV to the nozzle, it includes the SACOC, located on the OFS as shown in Fig. 5.

Due to the presence of the fan and OGV, several aspects of the functioning of a realistic turbofan can be taken into account. In particular, the SACOC is reached by a flow of realistic complexity.

The second configuration, instead, is a more canonic wind-tunnel, shown in Figure 6. Ideally, the characterisation of the performances of SACOC would always be evaluated with engine experimental tests or simulations. However, both can be extremely expensive and time consuming, and relying on smaller-scale tests and computations is still a necessity. With this configuration, therefore, we will try to reproduce the effects observed in the engine. Furthermore, comparisons with the experiments will be carried out to evaluate the accuracy of our methodologies.

Aerothermal investigations of finned heat exchangers surely do not represent a novelty, and indeed, the literature is abundant on the matter. They have extensively been studied analytically (see Kadle and Sparrow, 1986), numerically (see Jonsson and Moshfegh, 2000; Filburn et al., 2006; Kim et al., 2014, 2016) and, of course, experimentally (see Sparrow et al., 1978; Lau and Mahajan, 1989; Wirtz et al., 1994; Manglik and Bergles, 1995). However, only a few works have investigated the behaviour of surface heat exchangers while taking into account the specificity of turbofan by-pass flows. Kim et al. (2014) performed a numerical and experimental analysis of the influence of a surface AOHE on the engine performance depending on the location and orientation of the fins, while Sousa et al. (2014) and Villafañe and Paniagua (2018) carried out experimental studies of a SACOC integrated on the

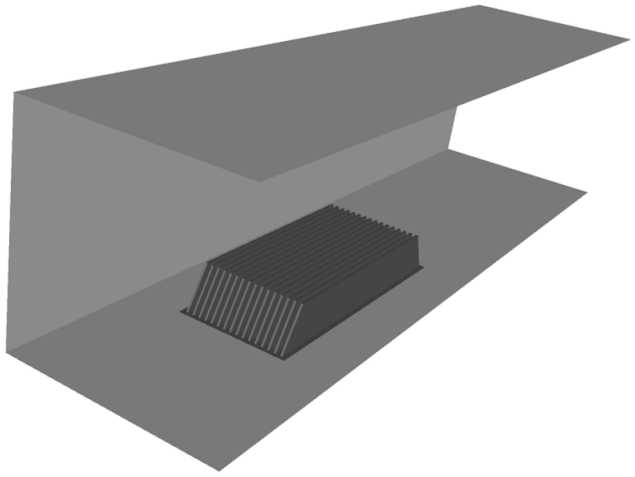

Figure 6: CHT investigation of a SACOC. Wind-tunnel configuration.

splitter of a turbofan engine, reproducing the transonic and high-swirl conditions of by-pass flows downstream of the fan. To the best of our knowledge, no numerical simulations of SACOC in a realistic turbofan can be found in the literature.

Methodologies of investigation

i. *Reynolds-averaged Navier-Stokes simulation*

The ambitious configurations described in the previous section, characterised, in particular, by extremely high Reynolds number, force us to adopt different methodologies with respect to the first set of activities. Numerical simulations will thus be carried out using Reynolds-averaged Navier-Stokes (RANS) approaches. RANS, from the point of view of turbulent modelling, represents the diametrically opposed approach with respect to DNS. Indeed, if in DNS all the turbulent structures are solved, in RANS they are all modelled.

The fundamental principle of RANS is that any fluid field ϕ can be decomposed into a mean $\overline{(\cdot)}$ and fluctuating $(\cdot)'$ field, so that $\phi = \overline{\phi} + \phi'$. Applying the operator $\overline{(\cdot)}$ to the Navier-Stokes equations yields the RANS equations, in which the mean values of the conservative fields are transported, and the different correlation terms which appear, instead, are modelled.

By solving the RANS equations, therefore, one only seeks the behaviour of the mean flow. The main inconvenient of RANS approaches is their lower physical fidelity, with respect to LES. Indeed, in RANS even the largest turbulent scales are modelled, the behaviour of which is far from being universal among turbulent flows and, in general, is case-by-case dependent. On the other hand, the main advantage of RANS methodologies is their reduced cost, since the space and time resolution requirements linearly scale with the Reynolds number, and are thus considerably less stringent compared to DNS or LES. It is the reason why RANS is still the predominant CFD strategy used in industrial applications and, according to Spalart (2010), will remain so for at least another 50 years.

ii. *Conjugate heat transfer*

Conjugate Heat Transfer (CHT) is a strategy of resolution of heat transfer problems containing two or more media, potentially governed by completely different sets of equations, which allows us to obtain a solution while taking into account the thermal interactions between the different sub-domains. It is what we need to evaluate the aerothermal performances of the SACOC.

In practical terms, most conjugate heat transfer problems and, in particular, our cases of study, deal with solid bodies partially or fully immersed in a fluid. The fluid sub-domain is governed by the Navier-Stokes equations; the heat transfer in the solid sub-domains, instead, is governed by the heat equation. From the point of view of the fluid sub-domain, the resolution of the thermal problem necessitates information at the interfaces with the solid sub-domains; in non-conjugated problems, this information is the result of assumptions concerning the behaviour of the solid domains; for instance, that the fluid-solid interface is adiabatic, or that its temperature is constant. These hypotheses are in some cases justified. In conjugate heat transfer, instead, the interactions between the different sub-domains are the result of the simultaneous resolution of all the different thermal sub-problems.

The concept of conjugate heat transfer was formulated for the first time by Perelman (1961), who solved two simple aerothermal problems analytically. The entirety of the early CHT works realised in the '60s, in fact, relied on analytical solutions (see, for instance, Soliman and Johnson, 1967; Kumar, 1968; Kumar and Bartman, 1968), and an exhaustive review can be found in Dorfman and Renner (2010).

In recent years, the scientific community has benefited from the progress of computer systems to approach aerothermal problems numerically, and more complex configurations have been investigated, making of CHT a viable option for the design and optimisation of systems of practical interest. Applications include internal combustion engines (see, for instance, Li and Kong, 2011; Wu et al., 2019), aeronautics combustion chambers (see, for instance, Jaure et al., 2013; Koren et al., 2018), gas turbines (York and Leylek, 2003; Duchaine et al., 2009) and, of course, heat exchangers (Jayakumar et al., 2008; Kim et al., 2014).

Nowadays, numerical conjugate heat transfer is approached in several ways, and there exist numerous coupling strategies and algorithms, depending on its implementation and of the thermal problem that is being addressed.

The first distinction, which is essentially numerical, is between monolithic and partitioned approaches. In monolithic CHT, the aerothermal problem is treated as a whole, and there is a single set of equations, consisting of the governing equations of every fluid or solid sub-domain, solved by a single code; examples can be found in Tiselj et al. (2013) and Shahi et al. (2014). In partitioned CHT, the different thermal sub-problems are solved by separate codes exchanging information at the common boundaries; examples can be found in Jaure et al. (2013), Koren et al. (2018) or Moretti et al. (2018). Monolithic approaches can be arduous to implement yet, once implemented, rather straightforward to use; it is the reason why these methodologies are quite common in commercial codes. On the other hand, it could be preferable to differently discretise the solid and fluid domains, since the grid requirements of the latter are normally much more stringent compared to the former; this is only possible in partitioned approaches. Besides, partitioned approaches benefit from the fact that existing and specialised codes can be used for every sub-domain; they are, therefore, generally easier to implement yet, quite often, more difficult to use, since the exchange of information between the solvers is usually performed by a third code,

and the continuity of the solution through the interfaces needs to be verified by the user. In addition, as it will be further discussed in detail, the exchange of boundary conditions can yield numerical stability issues at the interfaces even in the case where all sub-domains, for their part, are numerically stable; this problem, of course, does not exist in monolithic CHT.

The second distinction, which is of a physical nature, is between steady and unsteady conjugate heat transfer. In steady CHT, the solution at permanent regime is sought. The initial transient phase, therefore, can be artificially accelerated and later discarded to overcome the prohibitive time-scale disparity between the fluid and solid domains. In unsteady CHT, instead, the transient phase must be physical; therefore, except the case where some simplifying hypotheses are justified, the different sub-domains must coherently advance in time. Such simulations can be interesting in the case of systems operating in cycles (see, for instance, Errera et al., 2017) or in the case where the duration of the transient phase needs to be predicted (see, for instance, Schutte et al., 1992).

In this work, we perform steady conjugate heat transfer using a partitioned approach. The choice of a partitioned technique is particularly motivated by the possibility of using two specialised codes (*elsA* and *Zset*), both co-developed at ONERA. It would certainly be interesting to perform unsteady simulations, yet, since it is first of all fundamental to investigate the performances of the SACOC at permanent regime, we limit ourselves to steady computations, leaving unsteady analyses as future perspectives.

iii. *Experimental aerodynamics*

During the years of work which have led to this writing, experimental tests have been performed over a SACOC implemented in a wind-tunnel, similar to the one depicted in Figure 6. These tests, which have been carried out in the context of a very particular project we will introduce later on, have been specified and designed in collaboration with Safran AE and, in particular, with the author of this writing. Thanks to these experimental results, we are thus able to perform meticulous numerical-experimental comparisons, and to evaluate the predicting capabilities of our RANS conjugate heat transfer methodologies.

Organisation of the manuscript

This Ph.D. work is organised in three parts:

— **Part I**: The first part is dedicated to all the numerical methodologies we have used in our work.

In Chapter 1, we focus on wall-modelled LES, that we have employed for the first set of activities. An extensive review of the state of the art is proposed, with details regarding the different wall-models introduced in the literature and the challenges that WMLES has faced over the years. Then, the implementation of an equilibrium wall-model in the AVBP code is described and validated in an equilibrium channel flow configuration. Different wall boundary conditions and subgrid-scale models are tested, and the final setup is determined.

In Chapter 2, we introduce the conjugate-heat-transfer methods that we have employed for the second set of activities. After introducing the coupling algorithm, the normal-mode stability analysis for partitioned coupling

approaches by Errera and Chemin (2013) is described, discussed and validated. Then, the implementation in *elsA* and *Zset* is presented, with details concerning the governing equations, turbulence models and numerical schemes. Finally, the numerical setup and the relevance of the theoretical stability analysis are evaluated in a simple aerothermal case, *i.e.*, the laminar flat plate.

— **Part II**: The second part is devoted to the high-fidelity study of a non-equilibrium turbulent heat transfer case, *i.e.*, the first set of activities.

In Chapter 3, we present and discuss the direct numerical simulation that we have carried out with the configuration of Figure 4. The simulations allows for a detailed physical study. We focus on the strong non-equilibrium effects taking place near the leading edge of the isothermal wall, and on the gradual development of the thermal boundary layer. In particular, we show that an inner region, which we have called *equilibrium sub-layer*, can be identified along the channel flow, where several quantities are equilibrated.

In Chapter 4, the DNS data is used as reference results to assess the capability of WMLES to capture certain non-equilibrium effects. First, we employ an equilibrium wall-model, which gives inaccurate predictions of the wall heat flux as long as the modelled portion of the boundary layer exceeds the size of the aforementioned equilibrium layer. Then, thanks to the DNS data, we propose and test a non-equilibrium wall-model. We show how WMLES, once the main physical phenomena are accounted for in the wall-model, can yield very good predictions even in non-equilibrium configurations.

— **Parti III**: The third and last part, is dedicated to the conjugate-heat-transfer investigation of a surface air-oil heat exchanger, *i.e.*, the second set of activities.

In Chapter 5, we characterise the aerothermal behaviour of the SACOC in the by-pass duct, as shown in Figure 5. We show that the three-dimensional flow delivered by the OGV yields a heterogeneous distribution of the heat exchange among the fins. We also illustrate how the interaction between the SACOC and the flow generates an important flow separation downstream of the heat-exchanger, which strongly affects the global pressure drop. Finally, we attempt at reproducing these effects in a square wind-tunnel, in order to determine how precisely inflow conditions should be prescribed in usual smaller-scale test benches. The analysis shows that it is important that the SACOC be reached by, at least, a representative velocity boundary layer, and highlights the limits of representativeness of square wind-tunnels.

In Chapter 6, we perform numerical-experimental comparisons over a SACOC implemented in a wind-tunnel. The results show that our CHT methodologies allow for satisfying predictions of the global pressure drop and heat exchange, with disparities of at most 10%. However, the inability of RANS approaches to capture certain features of the flow clearly emerges. In particular, we notice that our simulations tend to underestimate and delay the flow homogenisation downstream of the SACOC.

Acknowledgements

Several chapters of this work have benefited from the help of academic, national and industrial partners, and it is the occasion to acknowledge their contribution.

The simulations performed in Part II have been carried out thanks to the HPC resources of TTGC under the allocation 2018-A0042B10159 made by GENCI, and

the HPC resources from the "Mésocentre" computing centre of CentraleSupélec and École Normale Supérieure Paris-Saclay supported by CNRS and grants from Ministry of Research via the Contrat Plan État-Région.

Special thanks for the realisation of the work described Part III go to several people of Safran. We thank Jean Bertucchi of Safran Aircraft Engines for the generation of all the meshes used in Part III, Teddy Chantrait of Safran Tech for his help in implementing the aerothermal coupling, and Thomas Hainaut of Safran Aircraft Engines for the fruitful discussions which led to the realisation of the engine simulation in Chapter 5.

We also thank the people of Universitat Politècnica de València (in particular A. Broatch, J. Tíscar and A. Felgueroso) and Universidad Politécnica de Madrid (in particular L. Gonzalez and M. Modena) for the excellent work we have carried out since 2019 to realise the Clean Sky 2 SACOC project described in Chapter 6.

We thank Lorella Palluotto, with whom the work described in Appendix B has been realised.

Finally, we thank the Association Nationale de la Recherche et de la Technologie (ANRT) and Safran Aircraft Engines for their financial support throughout the Ph.D.

List of publications

Peer-reviewed journals

— Gelain, M., Errera, M.P., Gicquel, O., *Assessment and numerical validation of a normal mode stability analysis for conjugate heat transfer*, International Journal of Heat and Mass Transfer, under review.

— Errera, M. P., Moretti, R., Mayeur, J., Gelain, M., Tessé, L., Lamet, J. M., Laroche, E. *A numerical predictive model for conjugate heat transfer with radiation*, International Journal of Heat and Mass Transfer, 2020, vol. 160, p. 120155.

— Gelain, M., Gicquel, O., Couilleaux, A., Vicquelin, R., *Physical study of the non-equilibrium development of a turbulent thermal boundary layer*, Journal of Fluid Mechanics, accepted.

— Gelain, M., Gicquel, O., Couilleaux, A., Vicquelin, R., *Wall-modelled LES of a turbulent thermal boundary layer with a non-equilibrium behaviour*, Physics of Fluids, to be submitted.

— Broatch, A., García-Tíscar, J., Felgueroso, A., Chávez-Modena, M., Valero, E., González, L., Gelain, M., *Aerodynamic upgrade of surface air-cooled oil coolersfor next generation turbofan aeroengines*, Open Research Europe, to be submitted

Conferences

— Gelain, M., Gicquel, O., Couilleaux, A., Vicquelin, R., *DNS of a turbulent thermal boundary layer spatially evolving on an isothermal wall from a fully turbulent adiabatic flow*, In : 72nd Annual Meeting of the American Physical Society-Division of Fluid Dynamics. 2019.

— Gelain, M., Gicquel, O., Couilleaux, A., Vicquelin, R., *Wall-modeled LES of a turbulent thermal boundary layer with a non-equilibrium behavior*, In : 73rd Annual Meeting of the American Physical Society-Division of Fluid Dynamics. 2020.

— Gelain, M., Couilleaux, A., Errera, M.P., Vicquelin, R., Gicquel, O., *Conjugate heat transfer analysis of a surface air-cooled oil cooler (SACOC) installed in a turbofan by-pass duct*, AIAA Aviation 2021 Forum.

Part I

Convective and conjugate heat transfer: methodology and validation

Chapter 1

Wall-modelled LES: details, implementation and validation

A brief overview of wall-modelled LES (WMLES) has already been given in the Introduction. As already mentioned, we have chosen to perform the WMLES of a turbulent, non-equilibrium boundary layer, and the objective of this chapter is to give all the details concerning the methodology, its implementation in the LES fluid solver of our choice (*i.e.*, AVBP, developed by CERFACS), and to validate our numerical setup in a canonical equilibrium boundary layer configuration.

The chapter is organised as follows. In §1.1, we combine an overview of the theory of boundary layers with a description of the main wall-modelling methods introduced in the literature, since the two are strictly linked to each other; it is also the occasion to briefly introduce all those wall-modelling strategies that have not been considered in this work. In §1.2, we describe the phenomenon of the Log-Layer Mismatch (LLM), which represents one of the main systematic problems encountered in WMLES; we provide a review of the solutions proposed in the literature underlining the advantages and drawbacks of each method. In §1.3, the way WMLES has been implemented in AVBP is illustrated, with a particular focus on the numerical setup of the wall-model and on the exchange of information between the latter and AVBP. Finally, the implementation is validated *a priori* and *a posteriori* in §1.4, followed by the conclusions in §1.5.

1.1 Theory of boundary layers and wall-modelling

As mentioned in the Introduction, WMLES is a popular strategy for overcoming the so-called *near-wall* problem of LES. The idea is that of deliberately under-resolving the inner layer by using an excessively coarse mesh in the near-wall region; by *coarse*, we refer to spatial resolutions of the order of $\Delta Y^+ \sim 10 - 100$ in wall-units, which are higher than the size of the large eddies of the inner layer. In such conditions, the transport of energy and momentum would be severely under-predicted near the wall if the LES were performed normally, for example by prescribing the classical no-slip and temperature imposed wall boundary conditions.

The purpose of the wall-model, therefore, is to estimate the actual momentum and energy transport taking place in the inner layer. The functioning of WMLES is schematically shown in Figure 1.1; first, a series of flow properties ($\widetilde{W}$ in Fig. 1.1) are

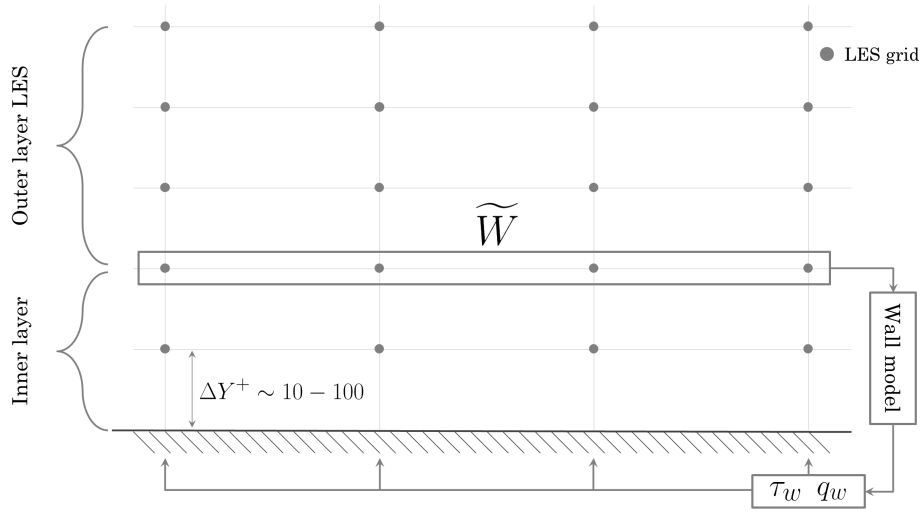

Figure 1.1: Schematic functioning of a wall-stress model.

extracted from the LES at a distance from the wall which usually amounts to 10−20% of the boundary layer, *i.e.*, the usual size of the inner layer; then, this information is elaborated by a set of simplified equations and/or laws, *i.e.*, the *wall-model*; the estimation computed by the wall-model, which operates as an independent *black box*, is then fed back to the LES under the form of wall shear-stress and wall heat flux, which are prescribed at the wall and become the new, approximate boundary conditions of the LES.

Strictly speaking, we are describing *wall-stress models*, which are based on the hypothesis of Townsend (1980) that the inner layer is connected to the outer layer through the wall stress; despite being by far the most popular and successfully employed type of wall-model, not all wall-models function in this manner; an overview of the other existing methods will be given later in the section. Unless differently specified, we will always refer to wall-stress models when talking about WMLES.

Before continuing further, two important observations should be made. First, it is easy to understand how important and binding the choice of the wall-model is; once a wall-model is chosen, it is implicitly assumed that its equations and laws faithfully represent the physics of the turbulent inner-layer and that its inputs, *i.e.*, the flow properties extracted from the LES, are the only ones the wall stress τ_w and heat flux q_w are correlated to. Second, we underline the fact that regardless of the level of sophistication of the wall-model, the only information returned to the LES are τ_w and q_w; therefore, it is implicitly assumed that the extremely complex, three-dimensional near-wall turbulent structures, which are both anisotropic and case-by-case dependent, can be replaced by a velocity and temperature gradient; this assumption is, understandably, rather simplistic; in fact, as pointed out by Piomelli and Balaras (2002) while discussing the control theory by Nicoud et al. (2001), even injecting the *exact* wall shear-stress leads to inaccuracies in the prediction of the turbulent intensities; it thus represents an intrinsic limit of WMLES which does not depend on the fidelity of the wall-model itself.

The starting point of any wall-model formulation, is of course the Navier-Stokes equations, which express the conservation of mass, momentum and energy in the

flow, and write:

$$\frac{\partial \rho}{\partial t} + \frac{\partial \rho u_i}{\partial x_i} = 0 \ , \tag{1.1.1}$$

$$\frac{\partial \rho u_i}{\partial t} + \frac{\partial \rho u_i u_j}{\partial x_j} = -\frac{\partial p}{\partial x_i} + \frac{\partial \boldsymbol{\tau}_{ij}}{\partial x_j} \ , \tag{1.1.2}$$

$$\frac{\partial \rho h}{\partial t} + \frac{\partial \rho u_j h}{\partial x_j} = \frac{\mathrm{D}p}{\mathrm{D}t} - \frac{\partial q_j^{cd}}{\partial x_j} + \boldsymbol{\tau}_{ij}\frac{\partial u_i}{\partial x_j} \ , \tag{1.1.3}$$

where ρ, u_i, p, h are respectively the mass density, velocity components, static pressure and enthalpy per mass unit of the fluid; $\boldsymbol{\tau}$ and q^{cd}, instead, are the stress tensor and conductive heat flux, respectively. Using Eqs. (1.1.1)-(1.1.3) in the boundary layer, potentially with the introduction of a Subgrid Scale (SGS) turbulent model, represents the *wall-resolved* strategy. In the following sections, we will see how, thanks to the theory of boundary layers, Eqs. (1.1.1)-(1.1.3) can be progressively manipulated and simplified to yield all the main wall-model formulations proposed in the literature.

1.1.1 Full compressible RANS wall-model

It is generally admitted that, in the context of WMLES, the inner layer can be considered in a Reynolds-averaged sense. As pointed out by Piomelli and Balaras (2002), the LES grid is so coarse in the inner layer that a single cell is supposed to contain a large number of eddies; furthermore, the time-step of the LES is several orders of magnitude larger than the characteristic time of the near-wall eddies; therefore, between two consecutive iterations, these small turbulent structures have had the time to generate, develop and dissolve several times. These arguments justify, to a certain extent, the fact that all wall-layer models are, implicitly or explicitly, based on the Reynolds-averaged Navier-Stokes (RANS) equations.

Let us consider the Reynolds-average operator $\overline{(\cdot)}$, according to which a generic fluid property ϕ can be decomposed into a mean $\overline{\phi}$ and fluctuating ϕ' field as follows:

$$\phi = \overline{\phi} + \phi' \ . \tag{1.1.4}$$

For flows with variable density, which are systematically present in this work, it is convenient to introduce the Favre average, which allows a generic field ϕ to be decomposed into a mass-weighted mean $\widetilde{(\cdot)}$ and fluctuating $(\cdot)''$ field as follows:

$$\phi = \widetilde{\phi} + \phi'' \ , \tag{1.1.5}$$

where,

$$\widetilde{\phi} = \frac{\overline{\rho\phi}}{\overline{\rho}} \ . \tag{1.1.6}$$

Given two fluid properties ϕ and ψ, the average $\overline{\rho\phi\psi}$, according to Eqs. (1.1.5) & (1.1.6), can thus be simply decomposed as $\overline{\rho\phi\psi} = \overline{\rho}\widetilde{\phi}\widetilde{\psi} + \overline{\rho}\widetilde{\phi''\psi''}$, avoiding the laborious correlations $\overline{\rho'\phi'}$ and $\overline{\rho'\psi'}$. Applying the Reynolds average to Eqs. (1.1.1)-(1.1.3), one obtains the RANS equations:

$$\frac{\partial \overline{\rho}}{\partial t} + \frac{\partial \overline{\rho}\widetilde{u}_i}{\partial x_i} = 0 \ , \tag{1.1.7}$$

$$\frac{\partial \overline{\rho}\widetilde{u}_i}{\partial t} + \frac{\partial \overline{\rho}\widetilde{u}_i\widetilde{u}_j}{\partial x_j} = -\frac{\partial \overline{p}}{\partial x_i} + \frac{\partial \overline{\boldsymbol{\tau}}_{ij}}{\partial x_j} - \frac{\partial \widetilde{\overline{\rho}u_i''u_j''}}{\partial x_j} \,, \tag{1.1.8}$$

$$\frac{\partial \overline{\rho}\widetilde{h}}{\partial t} + \frac{\partial \overline{\rho}\widetilde{u}_j\widetilde{h}}{\partial x_j} = \frac{\mathrm{D}\overline{p}}{\mathrm{D}t} - \frac{\partial \overline{q^{cd}}_j}{\partial x_j} + \overline{\boldsymbol{\tau}_{ij}\frac{\partial u_i}{\partial x_j}} - \frac{\partial \widetilde{\overline{\rho}u_j''h''}}{\partial x_j} \,, \tag{1.1.9}$$

where the correlation terms $\widetilde{\overline{\rho}u_i''u_j''}$ and $\widetilde{\overline{\rho}u_j''h''}$ are unknown and need to be modelled to close the set of equations. Models used in the literature are usually based on the Boussinesq hypothesis (Boussinesq, 1877) and, more in particular, on Prandtl's mixing length formulations (see, for instance, Cabot and Moin, 2000); occasionally, more complex RANS models are implemented, such as the dynamic, self-adjusting model of Park and Moin (2014); of course, the use of the usual two-equation RANS models such as the $k-\omega$ model of Menter (1993) is in no way precluded.

Equations Eqs. (1.1.7)-(1.1.9) constitute a first (and rather complex) example of wall-model that takes into account all the physical phenomena which might occur in a turbulent flow, from compressibility effects and pressure gradients to mean flow three-dimensionality; its resolution requires a three-dimensional grid (that adds to the preexisting LES one) and a great number of LES properties at the edge of the inner layer as boundary conditions. The major drawback of such a wall-model is undoubtedly its implementation; on the other hand, once robustly implemented, it clearly represents the most physically faithful wall-model one can have in WMLES, allowing, at least *a priori*, the study of the most complex flows. Regarding its cost, despite the complexity of the wall-model, one can still expect a significant gain with respect to a wall-resolved LES by reason of the larger time-step resulting from the coarser WMLES grid, which compensates for the additional set of equations to solve in the near-wall region.

Such wall-model is not a rarity in the literature; on the contrary, the WMLES community, which has recently started investigating more sophisticated configurations and even some industrial applications (see Bose and Park, 2018), seems to be more and more attracted to it. We can cite, for instance, the work of Park and Moin (2014), who employed it in several configurations including a separating flow over an airfoil, and reported that the wall-model required a negligible additional cost to their simulations; other examples include the works of Yang et al. (2015), Giometto et al. (2017) and Cho et al. (2020).

1.1.2 Thin boundary layer equation models

The full RANS model described in §1.1.1, because of the complexity of its implementation, has been for a long time out of reach; the WMLES community, both historically and currently, has therefore relied on further simplifications of the Navier-Stokes equations, which, in most boundary layers, are utterly justified. These simplifications are based on the following assumptions:

— That the inner layer can be considered incompressible: for the assumption to be legitimate, it is not necessary that the Mach number is low (usually, $\mathrm{M} \lessapprox 0.3$) in the whole fluid domain, but only in the modelled region, which is very often the case;

— That the inner layer can be considered quasi-bidimensional: the problem solved by the wall-model, therefore, consists of a plane, *i.e.*, the solid boundary, and

of a normal direction, along which the pressure is supposed to be constant; furthermore, only the velocity and temperature gradients along this direction are considered for the stress tensor $\boldsymbol{\tau}$ and the heat flux q^{cd}.

Applying these simplifications to Eqs. (1.1.7)-(1.1.9), yields:

$$\widetilde{v} = -\frac{1}{\overline{\rho}} \int_0^y \left(\frac{\partial \overline{\rho}}{\partial t} + \frac{\partial \overline{\rho} \widetilde{u}_i}{\partial x_i} \right) dy' \tag{1.1.10}$$

$$\frac{\partial \overline{\rho} \widetilde{u}_i}{\partial t} + \frac{\partial \overline{\rho} \widetilde{u}_i \widetilde{u}_j}{\partial x_j} + \frac{\partial \overline{\rho} \widetilde{u}_i \widetilde{v}}{\partial y} = -\frac{\partial \overline{p}}{\partial x_i} + \frac{\partial}{\partial y} \left[(\mu + \mu_t) \frac{\partial \overline{u}_i}{\partial y} \right] , \tag{1.1.11}$$

$$\frac{\partial \overline{\rho} \widetilde{h}}{\partial t} + \frac{\partial \overline{\rho} \widetilde{u}_j \widetilde{h}}{\partial x_j} + \frac{\partial \overline{\rho} \widetilde{v} \widetilde{h}}{\partial y} = \frac{\partial \overline{p}}{\partial t} + \frac{\partial}{\partial y} \left[(\lambda + \lambda_t) \frac{\partial \overline{T}}{\partial y} \right] , \tag{1.1.12}$$

where $i, j = \{1, 3\}$, assuming the solid boundary is on the $x - z$ plane and the normal direction along y; μ and λ are the dynamic viscosity and thermal conductivity, respectively, while the subscript $(\cdot)_t$, according to the Boussinesq's hypothesis, refers to their turbulent counterparts.

The set of equations (1.1.10)-(1.1.12) constitutes the so-called Thin Boundary Layer Equations (TBLE) and the vast majority of WMLES applications rely on them. With respect to Eqs. (1.1.7)-(1.1.9), the main simplification is the absence of the second momentum equation, *i.e.*, for $i = 2$. In the literature, as a matter of fact, even more simplified expressions are usually encountered; most authors, indeed, have focused on temperature-homogeneous boundary layers, for which the fluid properties are constant and the energy equation does not need to be solved. These assumptions lead to the most frequent formulation of the TBLE, that is:

$$\widetilde{v} = -\int_0^y \frac{\partial \widetilde{u}_i}{\partial x_i} dy' , \tag{1.1.13}$$

$$\frac{\partial \widetilde{u}_i}{\partial t} + \frac{\partial \widetilde{u}_i \widetilde{u}_j}{\partial x_j} + \frac{\partial \widetilde{u}_i \widetilde{v}}{\partial y} = -\frac{1}{\rho} \frac{\partial \overline{p}}{\partial x_i} + \frac{\partial}{\partial y} \left[(\nu + \nu_t) \frac{\partial \overline{u}_i}{\partial y} \right] , \tag{1.1.14}$$

where $i, j = \{1, 3\}$ and ν is the kinematic viscosity. Equations (1.1.13)-(1.1.14) have been employed, for instance, by Balaras et al. (1996) and Cabot and Moin (2000).

A wall-model based on Eqs. (1.1.10)-(1.1.12) (or Eqs. (1.1.13) & (1.1.14)) is very rich; the main contributions to the momentum and energy balances are present, and the model can take into account strong convective terms, pressure gradients and unsteadiness; furthermore, its implementation is significantly more accessible compared to the full RANS model of §1.1.1. In fact, it is common practice to construct the wall-model's grid on the LES one, as shown in Fig. 1.2; for every wall grid-point (x_i, z_k), a one dimensional grid along the wall-normal direction y is defined, and a three-dimensional connectivity is established among the surrounding wall points $(x_{i\pm1}, z_{k\pm1})$, along with the respective wall-model's grids, to compute the different velocity and temperature gradients. As we will see, a similar strategy will be used in Chapter 4.

1.1.3 The one-dimensional, equilibrium TBLE model

A major distinction lying among the different boundary layers rests upon the concept of *equilibrium*. Although there is no exact and unequivocal definition, non-equilibrium is usually associated with the idea of perturbation. A boundary layer is

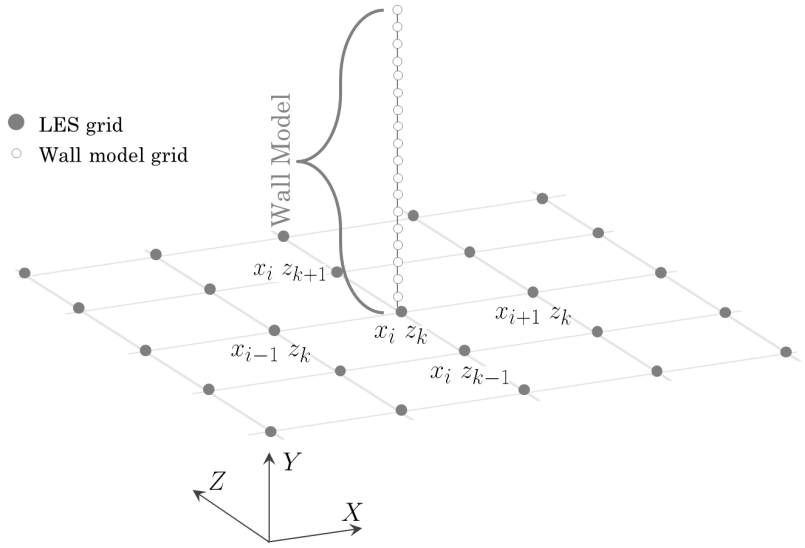

Figure 1.2: Three-dimensional TBLE model's grid.

in a non-equilibrium state, for instance, when it encounters a geometrical obstacle, or when it is subject to a strong temperature or pressure gradient. These perturbations reflect on the momentum and energy balances, and significant unsteady, convective or pressure terms may appear; accordingly, a *non-equilibrium* wall-model must account for these terms and the models described in §1.1.1 and §1.1.2 are examples of it. Fully developed turbulent boundary layers, either in external flows without pressure gradient or in established internal flows (which can be mimicked by bi-periodic channel flows), instead, are examples of equilibrium boundary layers. Because of turbulence, three-dimensional chaotic eddies still generate and develop, yet, in an averaged sense, the momentum and energy balances of such flows take a specific form.

Let us consider a fully developed periodic channel flow at a statistically steady state, *i.e.*, the classic channel flow of Kim et al. (1987); may x, y and z represent the streamwise, wall-normal and spanwise directions, respectively; may 2δ be its extension in the wall-normal direction. The averaged equation of continuity (1.1.1) writes:

$$\frac{\partial \overline{\rho}\widetilde{u}}{\partial x} + \frac{\partial \overline{\rho}\widetilde{v}}{\partial y} + \frac{\partial \overline{\rho}\widetilde{w}}{\partial z} = 0 \ . \tag{1.1.15}$$

Since the flow is homogeneous in the spanwise direction, $\widetilde{w} = \partial\overline{\rho}\widetilde{w}/\partial z = 0$; moreover, since the channel flow is fully developed, there are no mean streamwise gradients; therefore, $\partial\overline{\rho}\widetilde{u}/\partial x = 0$. According to Eq. (1.1.15), one has $\partial\overline{\rho}\widetilde{v}/\partial y = 0$, and thus:

$$\overline{\rho}\widetilde{v} = (\overline{\rho}\widetilde{v})\,|_{y=0} = (\overline{\rho}\widetilde{v})\,|_{y=2\delta} = 0 \ . \tag{1.1.16}$$

Therefore, $\widetilde{v} = 0$; it should be noted that if the mass density is variable, then $\overline{v}$ might not be zero (see Nicoud, 1999). Concerning the momentum equation, it is evident

that only the one along the streamwise direction is meaningful; Equation (1.1.2) becomes:

$$\frac{\partial \overline{\rho}\widetilde{u^2}}{\partial x} + \frac{\partial \overline{\rho}\widetilde{uv}}{\partial y} + \frac{\partial \overline{\rho}\widetilde{uw}}{\partial z} = -\frac{\partial \overline{p}}{\partial x} + \frac{\partial \overline{\tau_{1j}}}{\partial x_j} \ , \tag{1.1.17}$$

which, once the same simplifications of the mass conservation equation are applied, simply becomes:

$$\frac{\partial \overline{\rho}\widetilde{u''v''}}{\partial y} = -\frac{\partial \overline{p}}{\partial x} + \frac{\partial \overline{\tau_{1j}}}{\partial x_j} \ . \tag{1.1.18}$$

Considering that for a Newtonian fluid the stress tensor $\boldsymbol{\tau}$ can be written as:

$$\boldsymbol{\tau}_{ij} = \mu\left(\frac{\partial u_i}{\partial x_j} + \frac{\partial u_j}{\partial x_i}\right) - \frac{2}{3}\mu\left(\frac{\partial u_k}{\partial x_k}\right)\delta_{ij} \tag{1.1.19}$$

the viscous term writes:

$$\begin{aligned}\frac{\partial \overline{\tau_{1j}}}{\partial x_j} \quad = \quad & \frac{\partial}{\partial x}\left[2\mu\overline{\frac{\partial u}{\partial x}} - \frac{2}{3}\overline{\mu\left(\frac{\partial u}{\partial x} + \frac{\partial v}{\partial y} + \frac{\partial w}{\partial z}\right)}\right] + \\ & \frac{\partial}{\partial y}\left[\overline{\mu}\left(\frac{\partial u}{\partial y} + \frac{\partial v}{\partial x}\right)\right] + \\ & \frac{\partial}{\partial z}\left[\overline{\mu\left(\frac{\partial u}{\partial z} + \frac{\partial w}{\partial x}\right)}\right] \ .\end{aligned} \tag{1.1.20}$$

Considering that $\overline{v}$ and $\overline{w}$, if not zero, are negligible with respect to $\overline{u}$ and that the correlation terms $\frac{\partial}{\partial x_j}\left(\overline{\mu'\frac{\partial u_i'}{\partial x_j}}\right)$ are small compared to the dominating $\frac{\partial}{\partial y}\left(\overline{\mu}\frac{\partial \overline{u}}{\partial y}\right)$ (see Cabrit and Nicoud, 2009), Eq. (1.1.18) is thus reduced to:

$$\frac{\mathrm{d}\overline{p}}{\mathrm{d}x} = \frac{\mathrm{d}}{\mathrm{d}y}\left(\overline{\mu}\frac{\mathrm{d}\overline{u}}{\mathrm{d}y} - \overline{\rho}\widetilde{u''v''}\right) = \frac{\mathrm{d}\overline{\tau}_{tot}}{\mathrm{d}y} \ , \tag{1.1.21}$$

where the total stress $\overline{\tau}_{tot}$ is thus expressed as:

$$\overline{\tau}^{tot} = \overline{\mu}\frac{\mathrm{d}\overline{u}}{\mathrm{d}y} - \overline{\rho}\widetilde{u''v''} \ . \tag{1.1.22}$$

Equation (1.1.21) shows how the periodic channel flow is driven by the streamwise pressure gradient; if $\mathrm{d}\overline{p}/\mathrm{d}x = 0$, which is necessarily the case in a periodic flow, the pressure gradient must be replaced by a source term S_{QdM}; the momentum equation becomes:

$$\frac{\mathrm{d}}{\mathrm{d}y}\left(\overline{\mu}\frac{\mathrm{d}\overline{u}}{\mathrm{d}y} - \overline{\rho}\widetilde{u''v''}\right) = S_{QdM} \ . \tag{1.1.23}$$

Concerning the energy equation (1.1.3), the absence of mean normal and spanwise velocities $\widetilde{v}$ and $\widetilde{w}$ as well as the absence of mean streamwise gradients, also leads to a much simplified equation:

$$\frac{\mathrm{d}\overline{q}^{tot}}{\mathrm{d}y} = \frac{\mathrm{d}}{\mathrm{d}y}\left(\overline{\lambda}\frac{\mathrm{d}\overline{T}}{\mathrm{d}y} - \overline{\rho}\widetilde{v''h''}\right) = S_{ener} \ , \tag{1.1.24}$$

where q^{tot} is the total heat flux, and S_{ener} is a source term that plays a similar role of S_{QdM} in the momentum equation.

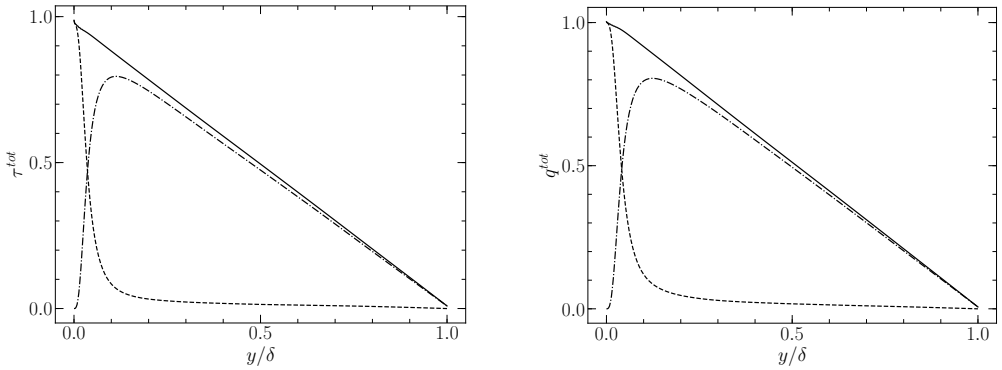

Figure 1.3: Profiles of shear stress scaled by the wall shear stress (a): —— total shear stress τ^{tot} ; - - - - viscous term $\overline{\mu}\mathrm{d}\overline{u}/\mathrm{d}y$; – · – · – turbulent term $-\overline{\rho}\widetilde{u''v''}$.
Heat fluxes scaled by the wall heat flux (b): —— total heat flux q^{tot}; - - - - conductive term $\overline{\lambda}\mathrm{d}\overline{T}/\mathrm{d}y$; – · – · – turbulent term $\overline{\rho}\widetilde{v''h''}$. Profiles taken from simulations of Appendix A.

Equations (1.1.23) & (1.1.24) are the momentum and energy equations of a boundary layer at *equilibrium*; as can be seen, both equations only present a viscous/conductive contribution and a term associated with turbulent transport, which are the so-called equilibrium terms. Figure 1.3 shows the evolution of the different momentum and energy contributions, non-dimensionalised with respect to the wall shear-stress and heat flux, respectively, along the wall-normal direction of a channel flow at equilibrium (see Appendix A for the details); as can be seen, both τ^{tot} and q^{tot} follow a straight line from unity at $y/\delta = 0$ to zero at $y/\delta = 1$.

Equations (1.1.23) (where the momentum and energy source terms S_{QdM} and S_{ener} are very often neglected[1]) and (1.1.24), with the introduction of a turbulent model for the unknown correlations $\overline{\rho}\widetilde{u''v''}$ and $\overline{\rho}\widetilde{v''h''}$, form the equilibrium TBLE wall-model, which takes the following form:

$$\frac{\mathrm{d}}{\mathrm{d}y}\left[\left(\overline{\mu}+\mu_t\right)\frac{\mathrm{d}\overline{u}}{\mathrm{d}y}\right]=0\ , \tag{1.1.25}$$

$$\frac{\mathrm{d}}{\mathrm{d}y}\left[\left(\overline{\lambda}+\lambda_t\right)\frac{\mathrm{d}\overline{T}}{\mathrm{d}y}\right]=0\ . \tag{1.1.26}$$

These equations can be very easily solved for every LES wall-grid point; as can be seen, the wall-model is, by its own nature, one-dimensional and the only information needed for its resolution is the wall-distance at which the LES flow properties are retrieved (usually called *matching-point*), as well as the values of velocity and temperature at this particular distance; in most cases, $\overline{u}$ does not refer to the streamwise velocity but to the local, instantaneous parallel velocity to the wall at the matching-point, which might have a component along the spanwise direction z; once the wall

[1] In wall units, Eq. (1.1.23) becomes $\frac{\mathrm{d}^2\overline{u}^+}{\mathrm{d}y^+}-\frac{\mathrm{d}\overline{u'v'}^+}{\mathrm{d}y^+}=\frac{1}{\mathrm{Re}_\tau}$, and, generally, $\mathrm{Re}_\tau \gg 0$.

shear stress τ_w is computed, it is also supposed to be aligned along the local direction of the flow; concerning the turbulent modelling, Prandtl's mixing lengths models (like in Cabot and Moin (2000)) are often used for μ_t.

This equilibrium wall-model has extensively been employed in the literature; the works of Bocquet et al. (2012), Kawai and Larsson (2012), Zhang et al. (2013), Larsson et al. (2015) and Giometto et al. (2017) are only a few examples of applications of such a wall-model, in some cases with some slight modifications. As we shall see, we will also employ this model in Chapter 4.

The popularity of this wall-model is motivated by several reasons. First of all, there is room for argument about whether an equilibrium wall-model could also be used in non-equilibrium flows or not. According to Larsson et al. (2016), no matter how important the non-equilibrium state of a flow is, there is always a portion of the boundary layer at equilibrium, where Eqs. (1.1.25) & (1.1.26) are representative of the local momentum and energy balance; as long as the matching-point is located in this equilibrium sub-layer, the wall-model is supposed to be pertinent, and all the non-equilibrium effects are assumed to be captured by the outer-layer LES; furthermore, still according to Larsson et al. (2016), even in the presence of non-equilibrium effects in the modelled portion of the boundary layer, these effects might, to a certain extent, balance each other, giving *net* momentum and energy balances resembling Eqs. (1.1.25) & (1.1.26). Although we will have the occasion to further discuss the arguments of Larsson et al. (2016) in Chapter 4, the possibility of using a one-dimensional equilibrium wall-model in all typologies of flows should not be prematurely discarded.

Second, it is certainly true that the WMLES community has extensively worked with equilibrium flows, both in the past and in the present; to quote the (most probably) not completely impartial opinion of Spalart (2009), the WMLES community *"seems unable to escape channel flow"*; equilibrium flows, despite being simple and very often far from being of practical interest, offer undeniable insights into the complex nature of turbulent flows, and represent a reliable reference mark for rigorously exploring slightly more complex flows presenting additional physical phenomena; Zhang et al. (2013), for instance, studied the effect of radiation on the mean flow statistics; Duprat et al. (2011) investigated favourable and adverse pressure gradients; in Chapters 3 & 4, we will study the non-equilibrium development of a thermal boundary layer. For such equilibrium or quasi-equilibrium flows, there is an *a priori* physical justification for the use of Eqs. (1.1.25) & (1.1.26) and using more complex wall-models could potentially be a futile sophistication.

Third, Eqs. (1.1.25) & (1.1.26) are extremely simple to solve numerically; because of their one-dimensional nature, every LES grid-point at the wall can be treated independently without establishing communications among them; even in the case where such a wall-model is not proposed by the chosen CFD solver, implementing these TBLE in a small, additional solver comes with (relatively) little effort.

Finally, despite the simplicity of Eqs. (1.1.25) & (1.1.26), they allow the whole profile of a velocity or temperature boundary layer to be integrated, from the viscous sub-layer to the logarithmic layer (which are introduced in the following paragraph); therefore, the user should not be too preoccupied by the location of the matching-point, as long as it is situated in the inner layer; furthermore, the wall-model can take into account flows with variable properties.

1.1.4 Algebraic models based on the logarithmic law-of-the-wall

The behaviour of thin boundary layers at equilibrium, which is described, as we have seen, by Eqs. (1.1.23) & (1.1.24), can in fact be expressed by even simpler relations, *i.e.*, the *wall functions*; these algebraic equations, which give access to the wall shear-stress and heat flux, are the basis of the very first WMLES works of Deardorff et al. (1970), Schumann (1975) and Grötzbach (1987); they are actually still very used today because of their simplicity, extremely reduced cost and, in some cases, physical relevance; however, further assumptions and simplifications are needed to obtain these relations from Eqs. (1.1.23) & (1.1.24), and their domain of validity, as we will see, is thus even narrower.

First of all, let us consider the momentum equation (1.1.23); an integration along the wall-normal direction gives:

$$\overline{\tau}_w = \overline{\mu}\frac{\mathrm{d}\overline{u}}{\mathrm{d}y} - \overline{\rho}\widetilde{u''v''} \ , \tag{1.1.27}$$

where, remember, $\tau_w = \overline{\mu}_w \left(\mathrm{d}\overline{u}/\mathrm{d}y\right)|_{y=0}$ is the wall shear-stress; the source term S_{QdM} has been neglected. Considering that the Boussinesq assumption is valid and using the Prandtl mixing-length approximation, the turbulent term can be expressed via the following turbulent viscosity μ_t[2]

$$\mu_t = \overline{\rho} l_m^2 \left(\frac{\mathrm{d}\overline{u}}{\mathrm{d}y}\right) \ , \tag{1.1.28}$$

where $l_m = \kappa y$ is the mixing-length, which in the inner layer linearly depends on the wall distance through the Von Kármán constant $\kappa \approx 0.4$ (see Pope, 2001). Accordingly, Eq. (1.1.27) becomes:

$$\overline{\tau}_w = \left(\overline{\mu} + \mu_t\right)\frac{\mathrm{d}\overline{u}}{\mathrm{d}y} = \overline{\mu}\frac{\mathrm{d}\overline{u}}{\mathrm{d}y} + \overline{\rho}\left(\kappa y\right)^2\left(\frac{\mathrm{d}\overline{u}}{\mathrm{d}y}\right)^2 \ . \tag{1.1.29}$$

We introduce the following non-dimensional wall distance and velocity:

$$y^+ = \frac{\rho_w u_\tau y}{\mu_w} \tag{1.1.30}$$

$$u^+ = \frac{u}{u_\tau} \ , \tag{1.1.31}$$

where the subscript $(\cdot)_w$ is used throughout the paragraph to denote a fluid property at the wall and $u_\tau = \sqrt{\tau_w/\rho_w}$ is the friction velocity; through Eqs. (1.1.30) & (1.1.31), Equation (1.1.29) can be rewritten as follows:

$$\frac{\overline{\mu}}{\overline{\mu}_w}\frac{\mathrm{d}\overline{u}^+}{\mathrm{d}y^+} + \frac{\overline{\rho}}{\overline{\rho}_w}\left(\kappa y\right)^2\left(\frac{\mathrm{d}\overline{u}}{\mathrm{d}y}\right)^2 = 1 \ . \tag{1.1.32}$$

Equation (1.1.32) consists of a viscous term and of a turbulent contribution, and their evolution along the wall-normal direction has been shown in Fig. 1.3a; as can

[2]Throughout the manuscript, we close turbulence models using the Reynolds average, instead of the (correct) Favre average. The choice is justified by the fact that, with our temperature ratios, mass density fluctuations can be neglected (Morkovin, 1962).

be seen, in the very near-wall region ($y/\delta \lessapprox 0.05$) the viscous term is predominant, while further away from the wall ($y/\delta \gtrapprox 0.25$), it is the turbulent one that prevails. Therefore, the boundary layer can be conceptually divided into two parts, *i.e.*, the viscous sub-layer and the logarithmic sub-layer (see Pope, 2001; Schlichting and Gersten, 2016). It is on this distinction that wall functions are based.

In the viscous sub-layer, it is possible to write:

$$\frac{\overline{\mu}}{\overline{\mu}_w}\frac{\mathrm{d}\overline{u}^+}{\mathrm{d}y^+} = 1 \ , \tag{1.1.33}$$

which, if the variation of μ is neglected, yields the simple linear relation:

$$\overline{u}^+ = y^+ \ . \tag{1.1.34}$$

Equation (1.1.34) is the first wall function and its validity is limited to $y^+ \lessapprox 5$; if the matching-point is placed in this region, Eq. (1.1.34) can be used as a wall-model as it gives access to the wall shear-stress through:

$$\overline{\tau}_w = \overline{\mu}\frac{\overline{u}|_{y=y_h}}{y_h} \ , \tag{1.1.35}$$

with y_h the wall distance of the matching-point.

In the logarithmic sub-layer, instead, Eq. (1.1.32) becomes, after some simple manipulations:

$$\left(\frac{\overline{\rho}}{\overline{\rho}_w}\right)^{\frac{1}{2}}\mathrm{d}\overline{u}^+ = \frac{\mathrm{d}y^+}{\kappa y^+} \ , \tag{1.1.36}$$

which, neglecting the variation of fluid properties, yields by integration:

$$\overline{u}^+ = \frac{1}{\kappa}\ln y^+ + C \ , \tag{1.1.37}$$

which is the well-known logarithmic law and the second wall function; in general, κ and the constant C are set to $\kappa = 0.41$ and $C = 5$, although, for low-Reynolds-number flows, Kim et al. (1987) found $\kappa = 0.4$ and $C = 5.5$. Equation (1.1.37) is valid for $y^+ \gtrapprox 30$ and if the matching-point is placed in this region, it constitutes a wall-model that gives access to the wall shear-stress by solving for u_τ, knowing $\overline{u}|_{y=h}$.

Figure 1.4 illustrates the velocity profile of a temperature-homogeneous equilibrium turbulent boundary layer obtained by DNS (see Appendix A); the friction Reynolds number is $\mathrm{Re}_\tau = u_\tau\delta/\nu = 395$; the profile is expressed in wall-units and compared to the linear law (1.1.34) and logarithmic law (1.1.37). As can be seen, the two laws accurately describe the velocity profile in their respective domains of validity; on the other hand, neither of them covers the transition zone in between (*i.e.*, for $8 \lessapprox y^+ \lessapprox 20$), which is called buffer layer; it is the part of the inner layer where the viscous and turbulent stress are of the same order of magnitude and neither of them can be removed from Eq. (1.1.32); moreover, it is the location of the main production of turbulence. If the matching-point happens to be situated in this region, neither Eq. (1.1.34) nor Eq. (1.1.37) are appropriate wall-models.

Similar relations can also be obtained for the temperature boundary layer. Integrating Eq. (1.1.24) yields:

$$\overline{q}_w = -\overline{\lambda}\frac{\partial\overline{T}}{\partial y} + \overline{\rho}\widetilde{h''v''} \ , \tag{1.1.38}$$

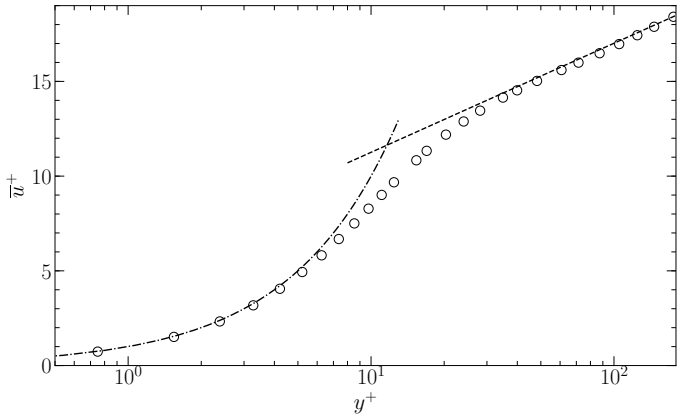

Figure 1.4: Mean velocity profile of an equilibrium turbulent boundary layer at $\mathrm{Re}_\tau = u_\tau \delta/\nu = 395$. ○, DNS profile from Appendix A; – · – · –, linear law $u^+ = y^+$; - - - - logarithmic law $u^+ = (1/0.4)\ln y^+ + 5.5$.

which, expressing the turbulent contribution through a turbulent conductivity λ_t, writes:

$$\overline{q}_w = -\left(\overline{\lambda} + \lambda_t\right) \frac{\partial \overline{T}}{\partial y} \ . \tag{1.1.39}$$

The turbulent conductivity λ_t is usually expressed as a function of μ_t through the turbulent Prandtl number Pr_t as follows:

$$\lambda_t = \frac{\mu_t \overline{c_p}}{\mathrm{Pr}_t} \ , \tag{1.1.40}$$

which, employing the mixing length model (1.1.28), becomes:

$$\lambda_t = \overline{\rho c_p} \frac{(\kappa y)^2}{\mathrm{Pr}_t} \frac{\mathrm{d}\overline{u}}{\mathrm{d}y} \ , \tag{1.1.41}$$

where Pr_t, on the basis of the Reynolds analogy (see Reynolds, 1901), can be set to a constant close-to-unity value of $0.85 - 0.9$ (see Kader, 1981; Wilcox et al., 1998) even though more complex models exist (see Kays, 1994). Replacing λ_t into Eq. (1.1.39) yields:

$$\overline{q}_w = -\overline{\lambda} \frac{\mathrm{d}\overline{T}}{\mathrm{d}y} - \overline{\rho c_p} \frac{(\kappa y)^2}{\mathrm{Pr}_t} \frac{\mathrm{d}\overline{u}}{\mathrm{d}y} \frac{\mathrm{d}\overline{T}}{\mathrm{d}y} \ , \tag{1.1.42}$$

which can be non-dimensionalised by introducing the temperature $T^+ = |T - T_w| / T_\tau$, where T_τ is the friction temperature expressed as:

$$T_\tau = \frac{|\overline{q}_w|}{\overline{c_p}_w \, \overline{\rho}_w u_\tau} \ . \tag{1.1.43}$$

Equation (1.1.42) becomes:

$$\frac{\overline{\lambda}}{\overline{c_p}_w \, \overline{\rho}_w \, \overline{\nu}_w} \frac{\mathrm{d}\overline{T}^+}{\mathrm{d}y^+} + \frac{\overline{\rho}\,\overline{c_p}}{\overline{\rho}_w \, \overline{c_p}_w} \frac{(\kappa y)^2}{\mathrm{Pr}_t} \frac{\mathrm{d}\overline{u}^+}{\mathrm{d}y^+} \frac{\mathrm{d}\overline{T}^+}{\mathrm{d}y^+} = 1 \ , \tag{1.1.44}$$

or, if the variation of fluid properties can be neglected,

$$\frac{1}{\mathrm{Pr}}\frac{\mathrm{d}\overline{T}^+}{\mathrm{d}y^+} + \frac{(\kappa y)^2}{\mathrm{Pr}_t}\frac{\mathrm{d}\overline{u}^+}{\mathrm{d}y^+}\frac{\mathrm{d}\overline{T}^+}{\mathrm{d}y^+} = 1 \ . \tag{1.1.45}$$

The thermal boundary layer, as was done for the velocity one, can be conceptually divided into two parts. In the conductive sub-layer the turbulent contribution can be neglected and Eq. (1.1.45) becomes:

$$\overline{T}^+ = \mathrm{Pr}\, y^+ \ , \tag{1.1.46}$$

which is the third wall function, giving access to the wall heat flux if the matching-point is located in the region $y^+ \lessapprox 5\mathrm{Pr}^{-1}$; note that if $\mathrm{Pr} \gg 1$, the domain of validity of Eq. (1.1.46) is extremely reduced.

In the logarithmic layer, instead, with the same assumption of constant fluid properties,

$$\overline{T}^+ = \frac{\mathrm{Pr}_t}{\kappa}\ln y^+ + C' \ , \tag{1.1.47}$$

where the constant term C' depends on the Prandtl number of the fluid. Kader (1981), for instance, proposed:

$$C' = \left(3.85\mathrm{Pr}^{1/3} - 1.3\right)^2 + 2.12\ln \mathrm{Pr} \ , \tag{1.1.48}$$

which is based on the assumption $\mathrm{Pr_t} \approx 0.85$. Equation (1.1.47) is the fourth and final wall function, which, solved iteratively for T_τ, gives access to the wall heat flux if the matching-point is located in the logarithmic region.

Equations (1.1.34), (1.1.37), (1.1.46) and (1.1.47) constitute, for all intents and purposes, a wall-model that can be used in WMLES. As mentioned at the beginning of the paragraph, the main reason of its popularity is its extreme simplicity and reduced cost, since the wall-model does not need the definition of a grid and can be solved with methods as simple as the fixed-point iteration; applications usually involve configurations where the main focus is on the far-wall regions, where the wall treatment is not supposed to have any influence, and can be carried out in a more superficial manner; it is usually the case of reactive flows (see, for instance, Moureau et al., 2004; Selle et al., 2004; Schmitt et al., 2005).

The physical relevance of wall laws, however, is not necessarily less significant than that of more complex TBLE models; if the boundary layer is temperature-homogeneous and the matching-point is located in either the viscous or logarithmic layer, Eqs. (1.1.34) & (1.1.37) give exactly the same wall shear-stress that would result from the integration of the equilibrium TBLE (1.1.25) & (1.1.26), since even the latter equations are very often constructed with a mixing-length turbulent model; in fact, in case of temperature-homogeneous flows, it is not clear how an equilibrium TBLE model may be better performing than a canonic wall law. Nevertheless, the limited physical representativeness remains the major drawback of the algebraic models; Equations (1.1.34), (1.1.37), (1.1.46) and (1.1.47) have been obtained by assuming that all fluid properties are constant; if this is not the case, wall functions can still be held to be acceptable if the wall-normal temperature gradient is not too elevated; otherwise, more sophisticated wall laws have been proposed in the literature in order to take into account stronger fluid-property variations (see Cabrit and Nicoud, 2009); despite this, TBLE wall-models are to be preferred in such cases.

1.1.5 Other wall-modelling approaches

All the wall-models introduced so far actually belong to a very precise category, *i.e.*, wall-stress models based on the RANS equations. Other strategies have been proposed for WMLES in the literature, and it is the occasion to briefly describe a few of them.

Starting from wall-stress models not employing the RANS equations, Bagwell et al. (1993) developed an approach based on the linear stochastic estimate; the idea is to provide the LES with a wall shear-stress that is estimated by correlation to a certain flow *event*; Bagwell et al. (1993), in a channel flow configuration, correlated the local shear-stress to all the velocity components of a horizontal plane, and trained the model with DNS; they obtained very good agreement with the mean and root-mean-square DNS velocity profiles, yet the model requires deep knowledge of the flow which is not *a priori* known.

The method introduced by Nicoud et al. (2001), instead, is based on suboptimal control theory; the concept of this approach is to tune the shear-stress in order to obtain a target velocity profile. This model also requires deep knowledge of the flow and, according to Nicoud et al. (2001), its cost is approximately twenty times higher than a normal LES; interestingly, Nicoud et al. (2001) reported that even in the event of a perfectly matching velocity profile, which the suboptimal control model can obtain, the turbulence intensities were still overestimated, illustrating the aforementioned intrinsic limit of wall-stress models.

A completely separate class of wall-models is that employing *off-wall* boundary conditions. The main concept of these models is that the LES grid is too coarse in the near-wall region to even remotely capture the large turbulent eddies of the flow; therefore, a promising strategy could be that of prescribing the boundary conditions at the edge of the resolved region (which is at a certain distance from the wall) rather than at the actual solid boundary as is done in wall-stress models. Consequently, in the non-resolved region an *interior* flow develops, receiving the boundary conditions from the *external* flow of the resolved region. Studies involving such wall-models can be found in Baggett (1997), Jiménez and Vasco (1998) and Nicoud et al. (1998), although all these attempts have been rather unsuccessful. Jiménez and Vasco (1998), for instance, found that the interior flow is extremely sensitive to the boundary-normal velocity component, and that spurious pressure fluctuations tend to generate; Baggett (1997) reported that spurious transition regions could only be avoided in the case where very precise turbulent structural information of the actual flow (obtained, for example, with wall-resolved LES) is prescribed at the off-wall boundary; finally, the appearance of an artificial boundary layer has also been observed in the resolved region above the off-wall boundary.

Another technique is that of virtual wall boundary conditions. The idea is that of terminating the actual LES domain at a certain distance from the wall, where a virtual boundary is thus defined; the inner layer is therefore completely removed from the flow configuration, and its resolution is carried out by integrating a set of TBLE, similar to the one introduced in §1.1.2; as a result of their integration, the velocity components at the virtual boundary are known, and can be prescribed as boundary conditions to the LES. Works involving this type of wall-models can be found in Chung and Pullin (2009), Inoue and Pullin (2011) and Cheng et al. (2015). As pointed out by Bose and Park (2018), a major concern regarding this approach is the definition of a proper virtual boundary in complex geometries.

Finally, we briefly introduce the dynamic slip-wall model of Bose and Moin (2014).

Taking a step back with respect to the resolution of turbulent structures in the inner layer, Bose and Moin (2014) focused on how boundary conditions should properly be prescribed to a LES field which is, recall, spatially filtered. In wall-resolved LES, a no-slip boundary condition is imposed at the wall; this condition is unfiltered yet justified, since the near-wall filter is small compared to the velocity gradient (see Ghosal and Moin, 1995); however, in WMLES this assumption is surely not respected and Bose and Moin (2014) derived and proposed the formal filtered boundary conditions that should be employed, *i.e.*:

$$\overline{u}_i - C\Delta_w \frac{\partial \overline{u}_i}{\partial n} = 0 \ , \tag{1.1.49}$$

where $C\Delta_w$ is the near-wall filter width and n indicates the wall-normal direction; Equation (1.1.49) is a Robin condition on the velocity at the wall, which falls back into the classic Dirichlet condition $\overline{u}_i = 0$ if $C\Delta_w \to 0$, *i.e.*, in wall-resolved LES. It is evident that according to Eq. (1.1.49), transpiration is admitted at the wall; therefore, the wall produces a finite Reynolds stress $\overline{u'v'}$, which has shown to reduce the over-prediction of the turbulence intensities near the wall. Concerning the mean velocity profiles, very good agreement with the DNS data has been obtained by Bose and Moin (2014) in a periodic channel flow configuration; further tests were carried out on a near-stall NACA 4412 airfoil, with good agreement with respect to experimental results. Further investigations of the slip model can be found in Bae et al. (2016), Yang et al. (2017a) and Lozano-Durán et al. (2017).

1.2 The log-layer mismatch

In order to well perform a wall-modelled LES, several issues have to be dealt with. In Section 1.1, we have primarily focused on the physical relevance of the wall-model to implement; we have seen that it is important to guarantee that the wall-model is representative of the mass, momentum and energy transport taking place within the inner layer and, we have explored the most popular methods. Still in §1.1, we have briefly discussed a second issue of WMLES, *i.e.*, how the information should be transferred from the wall-model to the LES; we have seen that, in the case of wall-stress models, only the wall shear-stress and heat flux are communicated to the LES, and that it represents an intrinsic limit of WMLES, which, regardless of the level of fidelity of the wall-model, leads to chronic concerns such as the over-prediction of the turbulence intensities near the wall; we have seen that other strategies exist in the literature, yet none of them has won unanimous support from the scientific community. In this section, instead, we focus on other delicate and somewhat enigmatic issues of WMLES, which are still subject to open debate in the community; these issues regard, in particular, the way boundary conditions should be transferred from the LES to the wall-model, and the way the turbulent flow behaves in the unresolved inner layer.

To better understand how important these aspects can be in WMLES, let us consider a temperature homogeneous boundary layer at equilibrium, such as the one encountered in an adiabatic, fully developed periodic channel flow; we perform the WMLES of this flow and, as explained in §1.1.4, the use of an algebraic model based on the logarithmic law is in this case completely justified. Let $\mathrm{Re}_\tau = 395$ be the friction Reynolds number of this flow and let us consider a LES grid characterised by a spatial resolution of $\Delta y^+ = 40$ in the wall-normal direction; let us couple the

wall-model with the LES at the first off-wall grid point, *i.e.*, at $y_h^+ = 40$; the non-resolved region is thus reduced to $0 < y^+ < 40$ while the outer layer extends between $y^+ \in [40, \mathrm{Re}_\tau]$. At every temporal iteration, the LES computes the wall-parallel velocity at a given first off-wall point $\widetilde{u}_{\parallel_1}$, where $\widetilde{(\cdot)}$ indicates in this case the spatial filter. According to Eq. (1.1.37), we have:

$$\frac{\overline{u}_{\parallel_1}}{u_\tau} = \frac{1}{\kappa} \ln\left(\frac{y_h u_\tau}{\nu}\right) + C \ , \tag{1.2.1}$$

where $\overline{(\cdot)}$ refers to the Reynolds average. In this case, we consider that $\widetilde{u}_{\parallel_1}$ is equivalent to $\overline{u}_{\parallel_1}$, which can be justified, as mentioned in §1.1, by the fact that the LES time-step is supposed to be several orders of magnitude higher than the time-scale of the turbulent eddies of the inner layer. In Eq. (1.2.1) the only unknown value is that of u_τ, which can be found by fixed-point iteration; the wall shear-stress τ_w can thus be deduced and prescribed as the new, approximate boundary condition of the LES. We do not provide any further details concerning the LES setup (numerical scheme, subgrid-scale model etc.) as this will be done in §1.3; for now, we limit ourselves to this qualitative description of the simulation. Details concerning the DNS data used for comparison in this section, instead, can be found in Appendix A.

Once the LES equations have been integrated in time until consolidated statistics are gathered, the mean streamwise velocity profile resembles the one illustrated in Figure 1.5. First of all, let us focus on the first LES point at $y^+ \approx 40$; as can be seen, the point perfectly stands on the DNS velocity profile, at least in wall-units. In fact, the objective of a wall-model is limited to this, *i.e.*, that its laws or equations mimic the momentum (or energy) transport taking place in the inner layer so that at the exchange location (in this case y_h) the LES mean flow is consistent with the momentum (or energy) flux at the wall; from this point of view, the wall-model represented by Eq. (1.2.1) is therefore as physically representative as a model can be. On the other hand, a wall-model cannot do anything more than this; the wall function (1.2.1) forces the first LES point on the logarithmic profile of the DNS, but has no control over all the remaining LES points, which are not constrained to follow the desired boundary layer's evolution, and can deviate. As Figure 1.5 shows, this is exactly what happens; starting from the second off-wall point, the LES seems to follow a different logarithmic law characterised by approximately the same slope and a completely different intercept; furthermore, the actual friction Reynolds number of the LES is $\mathrm{Re}_\tau \approx 340$, indicating an under-prediction of the wall shear-stress of around 26%.

This shift of the mean velocity profile, associated with an inaccurate prediction of the wall shear-stress, takes the name of *log-layer mismatch* (LLM), which represents an open challenge for the WMLES community, as both its causes and efficient remedies are still not perfectly clear. The problem has systematically been observed in both WMLES (see Mason and Thomson, 1992; Cabot and Moin, 2000; Nicoud et al., 2001; Kawai and Larsson, 2012; Lee et al., 2013) and DES (see Nikitin et al., 2000; Piomelli et al., 2003); in most cases, LLM manifests itself with an upward shift of the velocity profile, *i.e.*, with an under-prediction of the wall shear stress (see, for instance, Piomelli et al., 1989; Kawai and Larsson, 2012), yet *negative* LLM, *i.e.*, with an over-prediction of the wall-shear stress, has also occasionally been observed (see, for instance, Nicoud et al., 2001; Lee et al., 2013).

As we have seen, the causes of LLM cannot be ascribed to the wall-model or to the way the approximate boundary conditions are imposed at the wall since, in the

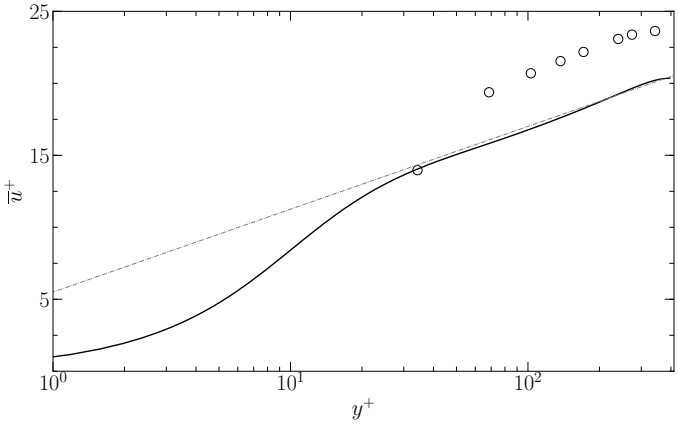

Figure 1.5: The logarithmic mismatch. Mean velocity profile of an equilibrium turbulent boundary layer at $\mathrm{Re}_\tau = 395$. ——, DNS profile from Appendix A; ○, LES results; – · – · – logarithmic law $u^+ = (1/0.4)\ln y^+ + 5.5$.

example of Fig. 1.5, the mean velocity of the first LES grid point is located where it should be. In the literature, the main arguments revolve around two fundamental questions:

— *Can the flow properties computed by the LES at the exchange locations be trusted?* The exchange locations are placed in the inner layer where, as already mentioned, the LES grid is too coarse to provide sufficient resolution; therefore, the LES could erroneously compute both the SGS viscosity and the inputs injected into the wall-model (in the example above, the wall-parallel velocity $\widetilde{u}_{\parallel_1}$); if these flow properties are contaminated, the results of the wall-model could be corrupted too.

— *Is it justified to establish such a strong correlation between the LES flow properties at the exchange locations and the wall shear-stress/heat flux?* In the example above, the wall shear-stress responds instantaneously to any variation of the first off-wall grid point velocity $\widetilde{u}_{\parallel_1}$; vice-versa, $\widetilde{u}_{\parallel_1}$ reacts to the wall boundary condition and is forced on the logarithmic law at any temporal iteration; this strong correlation between τ_w and $\widetilde{u}_{\parallel_1}$, may give birth to unphysical phenomena, disrupting the consistency of the flow and leading to bad predictions of the wall shear-stress.

In the literature, several authors have formulated assumptions regarding the origin of LLM and consistently proposed solutions; not all of these assumptions are consistent with one another, yet several of these solutions have proven to be effective. In the following paragraphs, an overview of the different strategies for solving LLM is provided, with a particular focus on the methods we have decided to test for our WMLES.

1.2.1 Correction of the subgrid-scale viscosity

Strategies based on the correction of the SGS viscosity are among the first to have been formulated and tested to remove LLM. We can cite, for instance, the works

of Sullivan et al. (1994), Porté-Agel et al. (2000) and Ding et al. (2001). The idea lying beneath these methods is that in the first LES off-wall grid point, the SGS viscosity cannot be accurately computed for both numerical and modelling reasons; these inaccuracies, combined with the momentum (or energy) flux provided by the wall-model, may thus lead to incorrect mean-velocity (or temperature) profiles.

From a numerical point of view, as pointed out by Bocquet et al. (2012), when the first off-wall point is located in the logarithmic region, one single coarse cell contains and discretises the whole viscous sub-layer, buffer layer and part of the logarithmic one. On the one hand, this leads to incoherences in the reconstruction of the velocity gradient needed for computing the SGS viscosity according to popular models such as the Wall-Adaptive Local Eddy-viscosity (WALE, see Nicoud and Ducros (1999)) or the Smagorinsky model (see Smagorinsky, 1963); Bocquet et al. (2012) estimated that the velocity gradient computed at a cell-centre located at $y^+ = 50$ can be three times as large as the actual velocity slope given by the logarithmic law, raising legitimate concern over which of the two gradients should be considered in the SGS model, since, *a priori*, both of them are acceptable. On the other hand, the velocity gradient itself could be inaccurately computed; for a logarithmic velocity profile, Wu and Meyers (2013) expressed the error of the discrete approximation of the mean velocity gradient as:

$$\frac{\delta\overline{u}}{\delta y} = \frac{\mathrm{d}\overline{u}}{\mathrm{d}y}\left(1 + (-1)^n \frac{c_n n!}{d^n}\right) , \tag{1.2.2}$$

where n is the order of discretisation, c_n a series of coefficients depending on the selected numerical scheme and $d = y/\Delta y$ is the normalised distance from the wall at which the gradient is computed. For the first grid point, $d = 1$ or $d = 1/2$ depending on where the solution variables are centred; as can be seen from Eq. (1.2.2), for these values of d the discretisation error does not vanish as the order of the numerical scheme n increases, demonstrating the inevitability of numerical errors at the first cell.

From a physical point of view, Cabot and Moin (2000) called attention to the inadequacy of SGS models in WMLES coarse grids; SGS turbulence models, indeed, are designed to mimic the behaviour of small, isotropic and quasi-universal turbulent structures, while presuming that the large, energy-bearing eddies are instead well resolved. These modelling errors, of course, only affect the near-wall cells, since far away from the wall the grid is normally designed to provide sufficient spatial and temporal resolution for meeting the assumptions of subgrid viscosity models.

The idea that these near-wall inaccuracies exist and lead to errors in the computation of the different flow fields, is widely accepted by the wall-modelling community (see Pantano et al., 2008; Kawai and Larsson, 2012). Assuming that these errors end up causing LLM is, therefore, a valid hypothesis, which explains why modifying the SGS viscosity seems a natural approach. Porté-Agel et al. (2000) introduced an improvement to the classic dynamic Smagorinsky model of Germano et al. (1991) by abandoning the scale-invariant character of the model's coefficient, and by adapting it to the actual filter-width *vs.* turbulent integral scale ratio, which is necessarily close to unity in coarse near-wall WMLES cells. Templeton et al. (2005), instead, used tabulated values of subgrid viscosity from the wall-resolved LES of a fully-developed channel flow. Bocquet et al. (2012) introduced a correction to the SGS viscosity that enforces the respect of the mean momentum balance between the first and second off-wall points. Wu and Meyers (2013) analysed the relationship between the mean velocity gradient and the turbulent kinetic energy budgets, and proposed

a self-adjusting Smagorinsky model that allows for a logarithmic velocity profile to be obtained.

All these methods brought improvements in the prediction of the mean velocity profile of equilibrium boundary layers and, in general, SGS modification approaches have always proved to be effective; however, these strategies can be burdensome to implement in practice, and can suffer from lack of robustness and generality since they are designed to meet the scope of one particular flow configuration. Finally, we also point out that the fact that modifying the SGS viscosity removes LLM, does not imply a cause-effect relationship between the two. In general, the SGS viscosity represents a degree of freedom that can be manipulated, *a priori*, to yield any sort of velocity profile; therefore, it is not surprising that adequately tuning the SGS model generates the desired logarithmic velocity distribution; whether this tuning has any actual physical meaning is, instead, questionable. All things considered, we have decided not to implement and test any of these methods.

1.2.2 Turbulence stimulation

Wall-modelling approaches suffer from the generation of artificial turbulence near the wall. These spurious structures are characterised by the de-correlation between the streamwise and wall-normal velocity fluctuations, which leads to an over-prediction of the mean velocity gradient (compensating for the lower Reynolds-stress in the momentum balance) and, possibly, to LLM. In DES, Baggett (1998) connected the lower Reynolds-stress to the presence of large streamwise vortices, the so-called *super-streaks*. In WMLES, Yang et al. (2017b) addressed the unphysical correlation between the wall shear-stress and the first off-wall point streamwise velocity, which might damp near-wall turbulence. In both DES and WMLES communities, the need of stimulating turbulence to disrupt these spurious structures has thus been identified.

An intuitive way of enhancing turbulence, is that of using stochastic forcing. Mason and Thomson (1992), arguing that stochastic subgrid stress variations are a physical process which is not present in the Smagorinsky model, introduced a backscatter model in which the energy amplitude is proportional to the dissipation. Piomelli et al. (2003) used a similar strategy, yet made use of a Gaussian distribution of lower amplitude and with a peak closer to the wall. Other turbulence-stimulating strategies have been proposed (see, for instance, Shu, 2008; Brasseur and Wei, 2010) and all these methods proved to be effective against LLM, even though the amplitude of the forcing can induce a range of different log-law intercepts (see Larsson et al., 2006), which might limit the robustness of these approaches. None of these strategies have been implemented and tested in this work.

1.2.3 Temporal and spatial filtering

A different class of solutions proposed to remove LLM are based on temporal and spatial filtering. Spatial filtering was introduced by Bou-Zeid et al. (2004), who argued that in the algebraic formulation (1.2.1) the wall shear-stress is related to the first off-wall point velocity by:

$$\langle \tau_w \rangle \propto \langle \widetilde{u}^2_{\parallel_1} \rangle \ , \tag{1.2.3}$$

where $\widetilde{(\cdot)}$ denotes the LES filter and $\langle \cdot \rangle$ represents ensemble averaging; Bou-Zeid et al. (2004) observed that, on the other hand, the law of the wall, which should be

respected in an averaged sense, yields a different relation:

$$\langle \tau_w \rangle \propto \langle \widetilde{u}_{\parallel_1} \rangle^2 \ . \tag{1.2.4}$$

Since $\langle \widetilde{u}^2_{\parallel_1} \rangle > \langle \widetilde{u}_{\parallel_1} \rangle^2$, the modelled wall stress provided by the wall-law is larger than expected. Bou-Zeid et al. (2004), therefore, proposed to apply a larger spatial filter (compared to the LES one that is already in place) to the input velocity $\widetilde{u}_{\parallel_1}$, aiming at reducing the velocity variance; the introduction of the filter removed LLM in their simulations.

The idea of filtering the wall-model's inputs has recently been revived by Yang et al. (2017b). As mentioned in the previous section, the aim of Yang et al. (2017b) was that of alleviating the strong and unphysical correlation between τ_w and $\widetilde{u}_{\parallel_1}$. They argued that due to the instantaneous response of the wall shear-stress to the velocity fluctuations, more momentum is drained in the flow when $u' > 0$ and less momentum when $u' < 0$, which has the undesired effect of inhibiting the formation of Reynolds-stress.

In order to mitigate this effect, Yang et al. (2017b) proposed to inject the following velocity u_{wm} to the wall-model:

$$u^n_{wm} = (1 - \epsilon)\, u^{n-1}_{wm} + \epsilon \widetilde{u}^n \ , \tag{1.2.5}$$

where n denotes the LES temporal iteration and $\widetilde{(\cdot)}$ the LES filter; ϵ is the weight of time averaging defined as $\epsilon = \Delta t / T_f$, where Δt is the LES time-step and T_f a filtering time-scale to be specified, normally expressed as a multiple of Δt; note that $0 < \epsilon \leq 1$. According to Eq. (1.2.5), the wall-model is provided with a velocity which combines the instantaneous velocity of the flow $\widetilde{u}$ at the first off-wall grid point with the input velocity of the previous iteration. Yang et al. (2017b) reported the progressive elimination of LLM as ϵ is reduced, which corresponds to taking less and less into consideration the fluctuations of $\widetilde{u}$ and, therefore, to disrupting the aforementioned spurious $\langle \tau'_w u' \rangle$ correlation; they also showed how an analogous spatial filter has indeed the same beneficial effect, speculating that the method of Bou-Zeid et al. (2004) is in fact equivalent to theirs.

Yang et al. (2017b) presented the remedy as the ultimate solution to LLM. Indeed, the method is physically justified, and does not require any assumptions concerning the type of wall-model or the type of flow configuration studied; furthermore, the solution is much simpler to implement compared to the other laborious strategies introduced in this section. We have therefore decided to test this methodology on an equilibrium boundary layer, as will be discussed in §1.4.

1.2.4 Location of the matching-point

The last strategy to remove LLM that we present, is the one introduced by Kawai and Larsson (2012). The starting point of the method is the same of §1.2.1, *i.e.*, that the first off-wall point is necessarily plagued by numerical and modelling errors. Kawai and Larsson (2012) proposed the following reasoning: that the size of the energy-bearing structures is proportional to the wall-distance y; that this size is, *a priori*, different in the three directions of the flow, yet still proportional to y through a constant C_i; that to accurately resolve these eddies, a grid resolution $\Delta x_i \lesssim L_i / N$ is needed, where $L_i = C_i y$ is the characteristic integral scale in the direction i and N is the number of grid-points per wavelength, which depends on the numerical scheme

employed. Therefore,

$$\frac{\Delta x_i}{y} \lesssim \frac{C_i}{N} \ . \tag{1.2.6}$$

If the first off-wall point is considered, $y = \Delta y$ and sufficient resolution would only be guaranteed if $C_i \gtrsim N$, which is, as explained by Kawai and Larsson (2012), unlikely.

As we have seen in §1.2.1, similar considerations led many authors to the conclusion that the SGS viscosity is erroneously computed and needs to be corrected. Kawai and Larsson (2012), instead, observed that there is no reason why the first off-wall grid point should systematically be used as matching-point, as long as it is positioned in the validity range of the wall-model; considering a matching-point located at a wall-distance y_h, Eq. (1.2.6) can be easily satisfied by requiring that:

$$\frac{\Delta x_i}{y_h} \lesssim \frac{C_i}{N} \ , \tag{1.2.7}$$

i.e., that the grid spacing in the three directions is a fraction of the wall-distance of the matching-point. Compared to a case where the first off-wall point is used, one can thus simply refine the grid without changing the height of the matching-point until there is a sufficient number of grid points between the wall and y_h. The reasoning is in agreement with the estimate of Wu and Meyers (2013), since the method of Kawai and Larsson (2012) amounts to increasing the value of d in Eq. (1.2.2). Note that y_h has to be designated on physical grounds, *i.e.*, taking into account the size of the inner layer and the type of wall-model used; Δx_i, instead, is a degree of freedom which can be chosen at one's discretion.

Kawai and Larsson (2012) reported that LLM is reduced as $\Delta x_i/y_h$ increases and that the behaviour of the velocity profile converges for $\Delta x_i/y_h \approx 3$. The method has proven to be effective and robust, thus gaining growing popularity over the years (see, for instance, Zhang et al., 2013; Lodato et al., 2014; Larsson et al., 2015); furthermore, the solution does not require the definition of any *ad hoc* coefficient or additional model, thus preserving the physical integrity of the pure WMLES.

However, the method can be impractical in complex flow configurations, where imposing a fixed number of points between the wall and the matching-point can be impossible; furthermore, the implementation can be arduous, especially in non-structured codes, and, in parallel computation, the wall and matching points could find themselves in different processor ranks. Another legitimate concern arises over the role of all the grid points separating the wall from the matching-point; Lodato et al. (2014) considers them as a *support for the solution* in the inner layer without any physical relevance, as they are not directly coupled to the wall shear-stress; in fact, once LLM is removed, the wall shear-stress is correctly evaluated regardless of the strategy implemented and, therefore, the additional grid points between $y \in [0, y_h]$ represent nothing more than under-resolved LES cells in which, paradoxically, the correct momentum flux in injected.

Despite the complexity of the implementation, especially in a non-structured code like the one we have used in our work, we have decided to test the solution proposed by Kawai and Larsson (2012), because of both its proved robustness and effectiveness.

1.3 Implementation in *AVBP*

In the previous sections a thorough description of WMLES and of the challenges often encountered with this approach has been given. The objective of this section,

is to present in detail the implementation of WMLES in the CFD code that we have chosen for the simulations described in Chapters 3 & 4, *i.e.*, the AVBP code. AVBP, developed at CERFACS, solves the three-dimensional Navier-Stokes equations for reactive and compressible flows on unstructured computational grids.

In §1.3.1 we will describe how the outer-layer LES is handled by AVBP, with details concerning the governing equations and numerical scheme as well as the subgrid-scale models we have employed. In §1.3.2, we will focus on the implementation of an equilibrium wall-model based on the one-dimensional thin boundary layer equations described in §1.1.3; all the details regarding the turbulence modelling, discretisation, resolution and coupling with AVBP are presented.

1.3.1 Outer-layer LES

i. *Governing equations*

The AVBP code solves the spatially-filtered, three-dimensional, compressible Navier-Stokes equations, which write:

$$\frac{\partial \overline{\rho}}{\partial t} + \frac{\partial \overline{\rho}\widetilde{u}_i}{\partial x_i} = 0 \ , \tag{1.3.1}$$

$$\frac{\partial \overline{\rho}\widetilde{u}_i}{\partial t} + \frac{\partial \overline{\rho}\widetilde{u}_i\widetilde{u}_j}{\partial x_j} = -\frac{\partial \overline{p}}{\partial x_i} + \frac{\partial \overline{\boldsymbol{\tau}}_{ij}}{\partial x_j} + \frac{\partial \boldsymbol{\tau}_{ij}^{SGS}}{\partial x_j} \ , \tag{1.3.2}$$

$$\frac{\partial \overline{\rho}\widetilde{h}}{\partial t} + \frac{\partial \overline{\rho}\widetilde{u}_j\widetilde{h}}{\partial x_j} = \frac{\mathrm{D}\overline{p}}{\mathrm{D}t} - \frac{\partial \overline{q_j^{cd}}}{\partial x_j} - \frac{\partial q_j^{SGS}}{\partial x_j} + \overline{\boldsymbol{\tau}_{ij}\frac{\partial u_i}{\partial x_j}} + \boldsymbol{\tau}_{ij}^{SGS}\frac{\partial \overline{u}_i}{\partial x_j} \ , \tag{1.3.3}$$

where $\overline{(\cdot)}$ and $\widetilde{(\cdot)}$ denote the filtered and mass-weighted filtered quantities, respectively; ρ, u_i, p, h are respectively the mass density, velocity components, static pressure and enthalpy per mass unit of the fluid; the fluid is considered to be an ideal gas with temperature-tabulated thermodynamic coefficients, with the following equation relating pressure, density and temperature:

$$p = \rho r T, \tag{1.3.4}$$

where $r = 288.18$ J/(kg K) is the mass-specific gas constant and T the fluid static temperature; gravity is neglected and not included in momentum equation (1.3.2); the viscous stress tensor $\boldsymbol{\tau}_{ij}$ is:

$$\boldsymbol{\tau}_{ij} = \mu\left(\frac{\partial u_i}{\partial x_j} + \frac{\partial u_j}{\partial x_i}\right) - \frac{2}{3}\mu\left(\frac{\partial u_k}{\partial x_k}\right)\delta_{ij} \tag{1.3.5}$$

where μ is the dynamic viscosity, computed via the Sutherland law and thus temperature-dependent:

$$\mu = \mu_{ref}\left(\frac{T}{T_{ref}}\right)^{\frac{3}{2}}\frac{T_{ref}+S_{suth}}{T+S_{suth}} \ , \tag{1.3.6}$$

with $\mu_{ref} = 1.716\times10^{-5}$ Pa s, $T_{ref} = 273.15$ K and $S_{suth} = 110.6$ K; the conductive heat flux q_i^{cd}, following Fourier's law, is:

$$q_i^{cd} = -\lambda\frac{\partial T}{\partial x_i} \ , \tag{1.3.7}$$

where λ is the fluid conductivity computed with the Prandtl number $\mathrm{Pr} = 0.71$.

ii. *Subgrid-scale modelling*

In the spatially-filtered Navier-Stokes equations (1.3.1)-(1.3.3) a subgrid-scale model needs to be introduced to take into account the small unresolved turbulent structures of the flow. As it has already been mentioned, these eddies are considered to be isotropic and, above all, independent from the flow configuration. Most of the subgrid-scale models introduced in the literature are based on the Boussinesq hypothesis, exactly like the RANS model we have introduced in §2.3.1; accordingly, the subgrid-scale Reynolds tensor

$$\boldsymbol{\tau}_{ij}^{SGS} = -\overline{\rho}\left(\widetilde{u_i u_j} - \widetilde{u}_i\widetilde{u}_j\right) \ , \tag{1.3.8}$$

is modelled as follows:

$$\boldsymbol{\tau}_{ij}^{SGS} - \frac{1}{3}\boldsymbol{\tau}_{kk}^{SGS}\delta_{ij} = 2\overline{\rho}\nu^{SGS}\left(\widetilde{S}_{ij} - \frac{1}{3}\widetilde{S}_{kk}\delta_{ij}\right) \ , \tag{1.3.9}$$

with $\widetilde{S}_{ij}$ the resolved strain tensor

$$\widetilde{S}_{ij} = \frac{1}{2}\left(\frac{\partial\widetilde{u}_i}{\partial x_j} + \frac{\partial\widetilde{u}_j}{\partial x_i}\right) - \frac{1}{3}\frac{\partial\widetilde{u}_k}{\partial x_k}\delta_{ij} \ . \tag{1.3.10}$$

Equation (1.3.9) shows how the turbulent stresses are related to the resolved strain tensor through the quantity ν^{SGS}, which is called the subgrid-scale viscosity. Concerning the turbulent heat flux

$$q_i^{SGS} = \overline{\rho}\left(\widetilde{hu_i} - \widetilde{h}\widetilde{u}_i\right) \ , \tag{1.3.11}$$

it is modelled as:

$$q_i^{SGS} = -\lambda^{SGS}\frac{\partial\widetilde{T}}{\partial x_i} \ , \tag{1.3.12}$$

which is analogous to the classic Fourier's law and exhibits another turbulent quantity λ^{SGS} called subgrid-scale conductivity; it is common practice to compute it as:

$$\lambda_{SGS} = \frac{\overline{\rho}\,\overline{c_p}\nu^{SGS}}{\mathrm{Pr}^{SGS}} \ , \tag{1.3.13}$$

where the constant subgrid-scale Prandtl $\mathrm{Pr}^{SGS} = 0.9$ is considered.

Several eddy viscosity models exist in the literature. In this work, we will consider three of them:

— *Dynamic Smagorinsky model*: it is based on the classic Smagorinsky (1963) model, which expresses the turbulent viscosity as:

$$\nu^{SGS} = \left(C_S\Delta\right)^2\sqrt{2\widetilde{S}_{ij}\widetilde{S}_{ij}} \ , \tag{1.3.14}$$

where Δ denotes the filter's characteristic length and C_S is the model's constant. The novelty of the dynamic Smagorinsky model introduced by Germano et al. (1991), is that the constant C_S is obtained on-the-fly during the simulation and is not a user-defined constant value. The expression of C_S follows the procedure of Lilly (1992), which avoids the disturbing characteristic of the classic Smagorinsky model of predicting non-zero turbulent viscosity levels in pure shear regions of the flow.

— *Wall-adapting local eddy (WALE) viscosity model*: introduced by Ducros et al. (1998) (also see Nicoud and Ducros, 1999), the model was specifically designed for wall-bounded flows, and aims at reproducing the scaling laws of the wall. The subgrid-scale viscosity is expressed as:

$$\nu^{SGS} = (C_w \Delta)^2 \frac{\left(s_{ij}^d s_{ij}^d\right)^{3/2}}{\left(\widetilde{S}_{ij}\widetilde{S}_{ij}\right)^{5/2} + \left(s_{ij}^d s_{ij}^d\right)^{5/4}} , \tag{1.3.15}$$

with $C_w = 0.5$ the model's constant and

$$s_{ij}^d = \frac{1}{2}\left(\frac{\partial \widetilde{u}_i}{\partial x_k}\frac{\partial \widetilde{u}_k}{\partial x_j} + \frac{\partial \widetilde{u}_j}{\partial x_k}\frac{\partial \widetilde{u}_k}{\partial x_i}\right) - \frac{1}{3}\left(\frac{\partial \widetilde{u}_k}{\partial x_k}\right)^2 \delta_{ij} . \tag{1.3.16}$$

— *Sigma model*: the model was introduced by Nicoud et al. (2011), and expresses the SGS viscosity as:

$$\nu^{SGS} = (C_\sigma \Delta)^2 \frac{\sigma_3 (\sigma_1 - \sigma_2)(\sigma_2 - \sigma_3)}{\sigma_1^2} , \tag{1.3.17}$$

where $C_\sigma = 1.35$ is the model's constant and $\sigma_1 \geq \sigma_2 \geq \sigma_3 \geq 0$ are the singular values of the velocity gradient tensor. The model shares the WALE model's behaviour near the wall with the additional property of vanishing in various types of laminar regions.

All these models are *a priori* adapted to the wall-bounded flow of Chapter 4 and, for this reason, they are tested in Section 1.4.

iii. *Numerical scheme*

Equations (1.3.1)-(1.3.3) are solved through the two-step Taylor-Galerkin weighed residual distribution scheme (see Colin and Rudgyard, 2000). It is a finite-element centred scheme with an explicit time integration of third order in both space and time. The scheme has very good dispersion and dissipation properties, yet is around two and a half times as expensive as a one-step time integration scheme such as the Lax-Wendroff one, which is also proposed by the code.

1.3.2 Implementation of an equilibrium wall-model

In this section all the details concerning the implementation of a one-dimensional, equilibrium TBLE wall-model are given. As we will see in Chapter 4, a non-equilibrium wall-model is also proposed, implemented and tested on a non-equilibrium boundary layer. We choose to provide a detailed description of the equilibrium one for two reasons. First, the formulation of the non-equilibrium wall-model requires a physical justification that necessitates the DNS results of Chapter 3. Second, the two models only differ slightly from a numerical point of view; these differences will be outlined and discussed in Chapter 4.

Let us recall the momentum and energy equations of the equilibrium TBLE model:

$$\frac{\mathrm{d}}{\mathrm{d}y}\left[(\overline{\mu} + \mu_t)\frac{\mathrm{d}\overline{u}}{\mathrm{d}y}\right] = 0 , \tag{1.3.18}$$

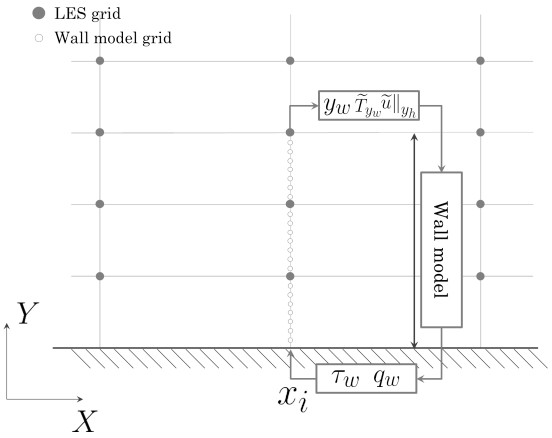

Figure 1.6: Schematic representation of the functioning of the TBLE equilibrium wall-model.

$$\frac{\mathrm{d}}{\mathrm{d}y}\left[\left(\overline{\lambda}+\lambda_t\right)\frac{\mathrm{d}\overline{T}}{\mathrm{d}y}\right]=0\ , \tag{1.3.19}$$

with the following boundary conditions:

$$\overline{u}|_{y=0}=0 \quad \text{and} \quad \overline{u}|_{y=y_h}=\widetilde{u}_{\|}|_{y=y_h}\ , \tag{1.3.20}$$

$$\overline{T}|_{y=0}=\widetilde{T}_w \quad \text{and} \quad \overline{T}|_{y=y_h}=\widetilde{T}|_{y=y_h}\ , \tag{1.3.21}$$

where, recall, y_h refers to the wall-distance of the matching-point and $u_{\|}$ indicates the wall-parallel velocity, which might have a spanwise component; $\widetilde{(\cdot)}$, in this case, denotes the LES spatial filter; the fluid properties μ and λ are computed as described in §1.3.1 for the outer-layer LES. The schematic functioning of the equilibrium wall-model is depicted in Figure 1.6; as can be seen, at a given wall grid-point x_i, the model only needs to extract three variables from the LES, *i.e.*, the wall-distance of the matching-point y_h as well as the velocity $\widetilde{u}_{\|}$ and temperature $\widetilde{T}$ at this distance.

In the following paragraphs we will present the turbulence models used for μ_t and λ_t, the way Eqs. (1.3.18) & (1.3.19) are discretised and solved numerically, and, finally, the way the wall-model is coupled with the AVBP code.

i. *Turbulence modelling*

As mentioned in §1.1.3, turbulence is usually modelled with simple algebraic models. The choice is justified by the fact that these models (such as the Prandtl's mixing length model) are sufficiently faithful in the equilibrium boundary layers that Eqs. (1.3.18) & (1.3.19) depict; furthermore, the wall-model is only used to solve the inner layer (*i.e.*, up to 20% of the boundary layer), where simple assumptions concerning the evolution of the turbulent viscosity are legitimate.

In this work, we use the model proposed by Cabot and Moin (2000) (also previously used in Cabot (1995) and Cabot (1996)), which expresses the turbulent viscos-

ity as:

$$\nu_t = \kappa y \sqrt{\frac{\tau_w}{\rho}} D \quad \text{with} \quad D = \left[1 - e^{-y^*/A^+}\right]^2 , \tag{1.3.22}$$

where, recall, $\kappa = 0.4$ is the Von Kármán constant; D is a damping function which, note, tends to zero as $y^* \to 0$, leading to zero turbulence at the wall; it contains a constant that usually takes the value of $A^+ \approx 17$; in this work we use $A^+ = 17.2$; y^*, instead, is the wall-distance expressed in semi-local scaling. Semi-local scaling (see Huang et al., 1995; Patel et al., 2015) expresses the wall distance as:

$$y^* = \frac{y u_\tau^*}{\nu} \quad \text{with} \quad u_\tau^* = \sqrt{\frac{\tau_w}{\rho}} . \tag{1.3.23}$$

As can be seen, the only difference with the classic scaling (see Eqs.(1.1.30) & (1.1.31)) is that the kinematic viscosity and the mass-density are not taken at the wall but can vary as a function of the wall distance; this new scaling helps taking into account flows with variable properties, and we use it extensively in this work. Strictly speaking, Cabot and Moin (2000) used classic scaling in Eq. (1.3.22); yet, they only analysed adiabatic flows in which classic and semi-local scaling coincide. Using semi-local scaling in Eq.(1.3.22) has proved to be effective in flows with varying properties (see, for instance, Zhang et al., 2013).

Concerning the turbulent conductivity λ_t, we compute:

$$\lambda_t = \frac{\mu_t \, \overline{c_p}}{\mathrm{Pr}_t} . \tag{1.3.24}$$

The Reynolds analogy states that Pr_t is close to unity, from which we infer $a_t \approx \nu_t$, where a_t is the turbulent diffusivity; the condition is in many cases reasonably respected, as shown experimentally, for instance, by Antonia et al. (1977), and the turbulent Prandtl number has been extensively used in RANS and LES modelling as well as, of course, TBLE (see, for instance, Benarafa et al., 2007; Bocquet et al., 2012; Zhang et al., 2013). Several algebraic models have been proposed in the literature (see Kays, 1994) and for this work we have chosen the model of Weigand et al. (1997), which expresses the turbulent Prandtl number as:

$$\mathrm{Pr}_t = \frac{1}{\frac{1}{2\mathrm{Pr}_{t_\infty}} + C\mathrm{Pr}\frac{\mu_t}{\mu}\sqrt{\frac{1}{\mathrm{Pr}_{t_\infty}}} - \left(C\mathrm{Pr}\frac{\mu_t}{\mu}\right)^2 \left[1 - \exp\left(-\frac{1}{C\mathrm{Pr}\frac{\mu_t}{\mu}\sqrt{\mathrm{Pr}_{t_\infty}}}\right)\right]} , \tag{1.3.25}$$

where we have chosen the constants $C = 0.3$ and $\mathrm{Pr}_{t_\infty} = 0.92$. Note that Pr_{t_∞} is the value of Pr_t as $\mu_t/\mu \to \infty$, *i.e.*, as $y^* \to \infty$; when $y^* \to 0$, instead, $\mu_t/\mu \to 0$ and $\mathrm{Pr}_t \to 2\mathrm{Pr}_{t_\infty}$.

All the choices we have taken concerning the turbulence models and their constants will be validated *a priori* and *a posteriori* in §1.4 on an equilibrium boundary layer configuration.

ii. *Discretisation of the wall-model equations*

Equations (1.3.18) & (1.3.19) take the form of the following differential equation:

$$\frac{\mathrm{d}}{\mathrm{d}y}\left(D_\Phi \frac{\mathrm{d}\Phi}{\mathrm{d}y}\right) = 0 , \tag{1.3.26}$$

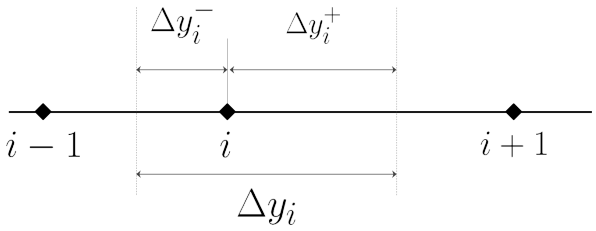

Figure 1.7: One-dimensional finite-volume discretisation.

where Φ is either the mean temperature or velocity and D_Φ either the total viscosity or conductivity. To solve Eq. (1.3.26), we use a finite-volume discretisation, schematically shown in Figure 1.7.

The integration of Eq. (1.3.26) over the control volume Δy_i (see Fig. 1.7), yields:

$$\left(D_\Phi \frac{\mathrm{d}\Phi}{\mathrm{d}y}\right)_{i+\frac{1}{2}} + \left(D_\Phi \frac{\mathrm{d}\Phi}{\mathrm{d}y}\right)_{i-\frac{1}{2}} = 0 \ , \tag{1.3.27}$$

which, with a second-order central difference scheme, writes:

$$D_{\Phi_{i+\frac{1}{2}}} \frac{\Phi_{i+1} - \Phi_i}{y_{i+1} - y_i} - D_{\Phi_{i-\frac{1}{2}}} \frac{\Phi_i - \Phi_{i-1}}{y_i - y_{i-1}} = 0 \ , \tag{1.3.28}$$

or, in a more compact form,

$$a_{i+1}\Phi_{i+1} + a_i\Phi_i + a_{i-1}\Phi_{i-1} = 0 \ , \tag{1.3.29}$$

with:

$$\begin{aligned} a_{i+1} &= \frac{D_{\Phi_{i+\frac{1}{2}}}}{y_{i+1}-y_i} \\ a_{i+1} &= \frac{D_{\Phi_{i+\frac{1}{2}}}}{y_{i+1}-y_i} \\ a_i &= -a_{i+1} - a_{i-1} \ . \end{aligned} \tag{1.3.30}$$

Finally, $D_{\Phi_{i\pm\frac{1}{2}}}$ is calculated as:

$$D_{\Phi_{i\pm\frac{1}{2}}} = \left(\frac{f_i^\pm}{D_{\Phi_i}} + \frac{1-f_i^\pm}{D_{\Phi_{i\pm1}}}\right)^{-1} \quad \text{with} \quad f^\pm = \frac{\Delta y_i^\pm}{\Delta y} \ . \tag{1.3.31}$$

Equation (1.3.29) represents a non-linear system; its non-linearity is due to the fact that the coefficients a_i are not constant and depend on the solution; furthermore, recall that the fluid properties are temperature-dependent and, therefore, Eq. (1.3.18) and Eq. (1.3.19) are coupled. The system expressed by Eq. (1.3.29) must thus be solved iteratively and, being tri-diagonal, the low-complexity algorithm of Thomas can be used (see Patankar, 2018).

Another important aspect concerning the resolution of the discrete system is the grid. In the literature, authors generally do not specify how and according to which criteria their TBLE grids are generated; yet, it is important to remember that the wall-model solves a boundary layer and, even if a RANS approach is used, it is important to guarantee that the solution is accurately computed. Hence, we have decided to implement a mesh-adapting algorithm that locates a variable number of grid points in the wall-model's range $y \in [0, y_h]$, so as to respect a criterion imposed

on the maximum gradient and curvature of the solution (more details can be found in Versaevel (1996)). The algorithm allows us to guarantee the same level of accuracy for every wall-point throughout the simulation.

As a whole, the TBLE model is solved at every LES time iteration, and for every wall grid point through the following algorithm:

1. The boundary conditions are received by the wall-model;
2. Equations (1.3.18) & (1.3.19) are solved iteratively on the TBLE grid of the previous time iteration;
3. Once the residual of the wall shear-stress and heat flux has converged, the mesh-adapting algorithm computes a new grid according to the gradient and curvature of the solution; the new grid, of course, can be more refined or coarser than the previous one;
4. Steps 2 & 3 are repeated until grid-convergence has been obtained;
5. The converged solution and the final grid are stored for the next time iteration, and the boundary conditions are transmitted to the LES.

In fact, since the final TBLE grid is stored and used at the following iteration, Steps 2 & 3 are in many cases not repeated more than once. In the last two paragraphs, we will focus on Steps 1 & 5 of the algorithm, *i.e.*, on how the wall-model is coupled with the AVBP code.

iii. *Coupling with AVBP: from the LES to the wall-model*

The TBLE wall-model that we have presented in detail in the previous paragraphs, is not available in the standard version of AVBP. Therefore, it has been implemented in the Agath library, developed at EM2C to numerically solve one-dimensional sets of partial differential equations involving convection, diffusion and reaction. The Agath library has been coupled with AVBP; in fact, the two codes have been compiled together and the wall-model thus simply acts like an additional library of AVBP. In this paragraph, we will focus on the way the boundary conditions are computed by the LES code and transmitted to the wall-model. As we have seen in §1.2, this aspect is crucial in WMLES as it can lead to the fearsome log-layer mismatch; we have also mentioned that we have decided to implement two of the strategies we have described, *i.e.*, the temporal filter of Yang et al. (2017b) and the off-wall positioning of the matching-point of Kawai and Larsson (2012). Neither of them are proposed by the standard version of the AVBP code.

Concerning the former strategy, the implementation is rather straightforward; AVBP computes the wall-parallel velocity $\widetilde{u}_{\parallel}$ at the first off-wall grid point and, following Yang et al. (2017b), the velocity injected into Eq. (1.3.18) as boundary condition is:

$$u_{wm}^{n} = (1-\epsilon)\, u_{wm}^{n-1} + \epsilon \widetilde{u}_{\parallel}^{n} \,, \tag{1.3.32}$$

where, recall, n denotes the LES temporal iteration and ϵ is the weight of time averaging. As we will see in Section 1.4, the method has in fact only been tested on an adiabatic boundary layer; therefore, it has not been implemented to take the temperature into account.

The strategy proposed by Kawai and Larsson (2012), instead, is significantly more complicated to implement; first of all, because it requires invasive coding in

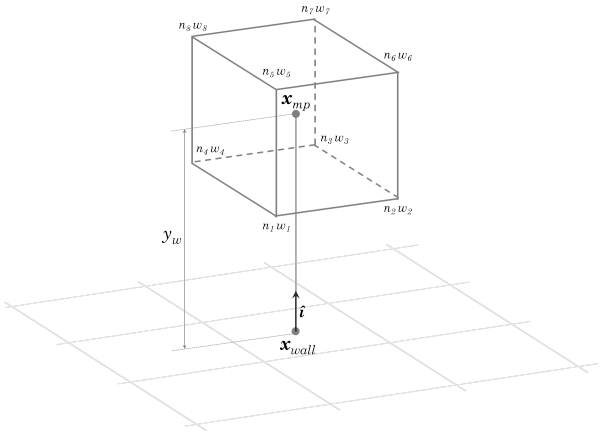

Figure 1.8: Implementation of method of Kawai and Larsson (2012).

AVBP; second, and foremost, because AVBP only uses unstructured grids in which the lack of structured connectivity hinders the search of the off-wall matching-points. We propose now, with the aid of Figure 1.8, a description of the algorithm we have implemented:

1. Let $\mathbf{x}_{wall}$ be the location of a given LES wall grid point; let y_w be the wall-distance of the matching-point (prescribed by the user) and $\hat{\mathbf{i}}$ the unit vector orthogonal to the wall at $\mathbf{x} = \mathbf{x}_{wall}$; note that y_w is a scalar quantity and that the position of the matching-point is, therefore, $\mathbf{x}_{mp} = \mathbf{x}_{wall} + y_h\hat{\mathbf{i}}$. At the beginning of the simulation, a table with the coordinates of all the respective wall- and matching-points is created.

2. Still at the beginning of the simulation, a searching algorithm (already present in AVBP) is launched for every value of $\mathbf{x}_{mp}$; the algorithm returns the cell containing the matching-point, the nodes n_i of this cell, the interpolation weights w_i of each node and the rank of the processor where the cell is located. A connectivity table is filled with all this information and the simulation starts.

3. At every temporal iteration, the velocity components and temperature at every n_i are known for every matching-point; the table is updated with these values and Message Passing Interface (MPI) communications are established between the respective wall- and matching-points, in case they are not located in the same processor.

4. For every wall-point, a given property ϕ at the matching-point is computed as follows:

$$\phi_{mp} = \sum_{i=1}^{N} \phi(n_i) w_i \ , \tag{1.3.33}$$

where N is the number of nodes of the cell containing the matching-point (eight, in the case of the cell depicted in Fig. 1.8). The wall-parallel velocity $\widetilde{u}_{\parallel}$ and the temperature $\widetilde{T}$ at the matching-point are thus known, and can be injected into Eqs. (1.3.20) & (1.3.21) as boundary conditions of the wall-model.

A few observations are due. First of all, the searching algorithm is extremely costly and scales with the number of wall-points and the number of processors; however, it is only launched once at the beginning of the simulation and, with a more efficient implementation, this step could be even effectuated in pre-processing for a given mesh. Second, the method has been implemented to function with both tetrahedral and hexahedral cells; however, in this work we only use hexahedral elements. Third, AVBP uses a *face-wise* approach for WMLES; therefore, the aforementioned wall-points $\mathbf{x}_{wall}$ are actually located at the centre of the cell's wall-face, as shown in Fig. 1.8. Fourth, the matching-point of a given wall-point could be located anywhere in the cell; this case is not considered in the theory of Kawai and Larsson (2012) who, instead, introduced a precise notion of *number of grid points* from the wall; however, in this work we only use cartesian meshes, in which it is easy to specify a wall-distance y_w so that every matching-point is precisely located on the upper or lower face of the cell. Finally, the interpolation equation (1.3.33) is of second-order in space, which is lower than the TTGC numerical scheme we use (see §1.3.1); therefore, Eq. (1.3.33) *breaks* the spatial order of the scheme; however, the standard version of AVBP uses an equivalent formula when coupling at the first off-wall point; therefore, the error we introduce is the same of the standard AVBP.

iv. *Coupling with AVBP: from the wall-model to the LES*

In this last paragraph, we describe how the approximate boundary conditions computed by the wall-model are treated by the AVBP code.

The wall heat flux is supposed to be oriented along the wall-normal direction; the wall shear-stress, instead, is considered to be aligned with the wall-parallel velocity at the matching-point. In WMLES, in general, a slip condition results from the prescription of a momentum flux; indeed, the wall-parallel velocity gradient at the wall resembles:

$$\frac{\partial \widetilde{u}_{\parallel}}{\partial y} = \frac{\tau_w}{\mu + \mu^{SGS}} \ , \tag{1.3.34}$$

which gives:

$$\widetilde{u}_{\parallel}|_{y=0} = \widetilde{u}_{\parallel}|_{y=\Delta y} - \frac{\tau_w}{\mu + \mu^{SGS}} \Delta y \ . \tag{1.3.35}$$

The value of τ_w is given by the wall-model and μ^{SGS} is given by the SGS model; therefore, in general, $\widetilde{u}_{\parallel}|_{y=0} \neq 0$. However, if $\widetilde{u}_{\parallel}|_{y=0} = 0$ is imposed and the value of μ^{SGS} is changed to:

$$\mu^{SGS} = \frac{\tau_w \Delta y}{\widetilde{u}_{\parallel}|_{y=\Delta y}} - \mu \ , \tag{1.3.36}$$

it is easy to verify that the product $\left(\mu + \mu^{SGS}\right) \partial \widetilde{u}_{\parallel}/\partial y$ is left unchanged, therefore preserving the momentum flux prescribed by the wall-model.

This is the idea of the boundary condition proposed by Nicoud et al. (2016), which is available in the standard version of AVBP[3]. We have decided to use this condition as it has not had any impact on our results (as we shall see in §1.4) whilst noticing an increased stability of our simulations (especially when combined with the WALE subgrid-scale model). Furthermore, as explained in Chapter 4, in our configuration of study it is important to avoid negative velocities near the wall, which is not guaranteed by the classic slip formulation. Finally, the boundary condition of

[3]For information, in AVBP the keyword for this boundary condition is WALL_LAW_NO_SLIP_GENERIC.

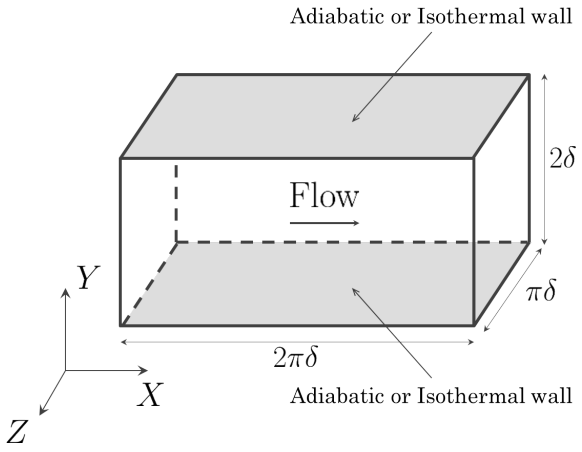

Figure 1.9: Computational domain: the bi-periodic channel flow.

Nicoud et al. (2016) does not act on the temperature; therefore, in the most general case, we will have $\widetilde{T}|_{y=0} \neq T_w$.

1.4 Validation

The objective of this section is to validate the numerical setup of our wall-modelled LES described in §1.3 in a canonical configuration, *i.e.*, an equilibrium boundary layer in a bi-periodic channel flow. As reference data, we use the direct numerical simulations described in Appendix A.

The section is organised as follows. In §1.4.1, the geometry, mesh and boundary conditions of the equilibrium configuration are presented. In §1.4.2, the *a priori* validation of the numerical setup is performed; it is the occasion to verify that the wall-model's equations are representative in the present case, and to justify the turbulence-modelling approach. In §1.4.3, the numerical setup is tested *a posteriori*; the WMLES results are compared to the DNS reference data, the influence of certain parameters on the solution is evaluated and the optimal setup is determined.

1.4.1 Presentation of the configuration: equilibrium boundary layer

The computational domain is shown in Figure 1.9. It consists of a channel flow of size $[2\pi\delta, 2\delta, \pi\delta]$, with $\delta = 0.002$ m; the domain is periodic on both the streamwise direction X and the spanwise direction Z and is, therefore, bi-periodic. Concerning the upper and lower walls, two cases are considered.

The former, is the adiabatic case; the flow is temperature-homogeneous, and the wall-model is thus reduced to the momentum equation (1.3.18); as mentioned in §1.1.3, the absence of streamwise pressure gradient requires the addition of a source term in the momentum equation (1.3.2) to drive the flow; in all the bi-periodic channel flows described in this work, we use the source terms proposed by Zhang and Vicquelin (2016) and recently extended (see Appendix B), which dynamically adapt to obtain a target bulk Reynolds number and bulk enthalpy specified by the

	Size	$\Delta X_i^{+/*}$	Re_b	T_b	$\mathrm{Re}_\tau^{+/*}$	B_q	T_w (K)	T_c (K)
Adiabatic	$[2\pi\delta, 2\delta, \pi\delta]$	$(50, 20, 25)$	7062	304.5	395	0	304.5	304.5
Isothermal walls	$[2\pi\delta, 2\delta, \pi\delta]$	$(50, 20, 25)$	7062	304.5	395	0.018	400	290

Table 1.1: Main numerical and physical parameters of fully developed channel flow with adiabatic and isothermal walls.

user. In this case, we consider $\mathrm{Re}_b = u_b\delta/\nu_b = 7062$ and $T_b = 304.5$ K, where the subscript $(\cdot)_b$ denotes the bulk value of a given property; the friction Reynolds number is correlated to Re_b and we obtain $\mathrm{Re}_\tau = u_\tau\delta/\nu \approx 395$.

The latter case, is the one with isothermal walls, both at a constant temperature of $T_w = 400$ K; also in this case we employ the source terms of Zhang and Vicquelin (2016), with the same target bulk values of the adiabatic configuration; because of the difference between T_b and T_w, a thermal boundary layer is also obtained in the channel flow, with a mean temperature at the centre of the channel of $\overline{T}_c \approx 290$ K; the friction Reynolds number, expressed with the semi-local formalism, is $\mathrm{Re}_\tau^* \approx 395$; finally, the heat flux parameter $\mathrm{B}_q = |\overline{q}_w|/\left(\rho_w C_{p_w} u_\tau T_w\right)$ (see Nicoud, 1999) is $\mathrm{B}_q \approx 0.018$.

The domain is discretised with a uniform grid of $n_X = 50$, $n_Y = 40$ and $n_Z = 50$ points in the three directions, giving a spatial resolution of $\Delta X^+ \approx 50$, $\Delta Y^+ \approx 20$ and $\Delta Z^+ \approx 25$, which clearly requires the presence of a wall-model in the inner layer. The physical and numerical parameters of the two cases are summarised in Table 1.1.

1.4.2 *A priori* validation

In this section, only the TBLE (1.3.18) & (1.3.19) are solved, without being coupled with the LES; Equations (1.3.18) & (1.3.19) are integrated between $y/\delta \in [0, 0.2]$, *i.e.*, in the inner layer; boundary conditions at $y/\delta = 0.2$ are extracted from the DNS computation described in Appendix A, which has been performed in the same conditions specified in Table 1.1; the DNS data is also used, of course, for comparison.

In the next paragraphs we will first perform grid convergence using the mesh-adapting algorithm mentioned in §1.3.2; then, using the converged grid, we will compare the velocity and temperature profiles with the DNS data.

i. *Grid convergence*

As mentioned in §1.3.2, we use a mesh-adapting algorithm which automatically generates the TBLE grid according to criteria prescribed on the gradient and curvature of the solution. These criteria impose a maximum value of scaled gradient and curvature between two consecutive points; the lower (and thus more stringent) the criterion, the more points will be introduced into the grid by the algorithm. To perform grid convergence, we analyse the evolution of the friction coefficient C_f

Scaled gradient & curvature	N	C_f $(\times 10^{-3})$	Residual
$(0.6, 0.6)$	5	1.869	41.6%
$(0.5, 0.5)$	7	2.137	33.2%
$(0.4, 0.4)$	8	2.441	23.7%
$(0.3, 0.3)$	11	2.834	11.4%
$(0.2, 0.2)$	16	3.084	3.7%
$(0.1, 0.1)$	25	3.182	0.6%
$(0.05, 0.05)$	40	3.196	0.1%
$(0.025, 0.025)$	66	3.198	0.09%
$(0.01, 0.01)$	145	3.201	-

Table 1.2: TBLE Grid convergence based on the friction coefficient C_f.

computed as follows:

$$C_f = \frac{\tau_w}{\frac{1}{2}\rho_b u_b^2} \ , \tag{1.4.1}$$

where τ_w is the wall shear-stress returned by the wall-model with a given grid, and ρ_b and u_b are the bulk mass-density and velocity of the adiabatic channel flow. Grid convergence is not performed analysing the evolution of the wall heat flux, and the choice is justified by the fact that the Prandtl number of the fluid is lower than unity; the velocity boundary layer is therefore more critical than the thermal one.

Results are shown in Table 1.2; for every value of maximum relative gradient and curvature imposed to the algorithm, the number of TBLE grid-points, the friction coefficient and the residual with respect to the most refined grid that is considered as reference. As can be seen, a good convergence level is obtained with a criterion of 0.1, with which the grid is composed of 25 points; better results could be obtained with a more stringent criterion; yet, the DNS grid is composed of 40 points in the inner layer and going beyond this value would be illogical given the RANS modelling of the TBLE. The value of 0.1 is thus the criterion we will use henceforth.

ii. *Velocity and temperature profiles*

Figure 1.10 shows the comparison between the TBLE and DNS profiles of streamwise velocity and temperature; the DNS data, in this case, are obviously taken from the channel flow with isothermal walls (see Appendix A). As can be seen, both profiles are very well predicted by the wall-model, from the viscous sub-layer to the logarithmic layer, indicating the good calibration of the different coefficients and constants of the model. These results allow us to validate *a priori* the numerical setup of the WMLES.

1.4.3 *A posteriori* validation

In this section, we perform the WMLES of the fully developed channel flows described in §1.4.1. In particular, we evaluate the influence of certain numerical and modelling

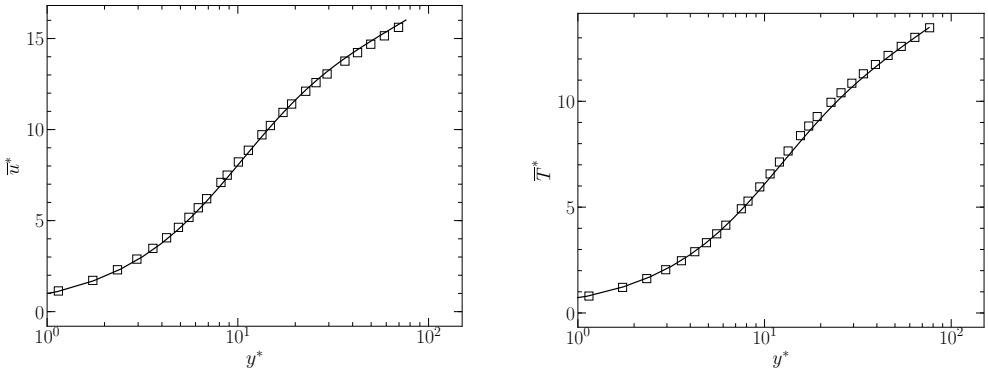

Figure 1.10: *A priori* validation. Comparison of velocity (a) and temperature (b) profiles expressed in semi-local scaling. ——, TBLE profiles; □, DNS profiles from Appendix A.

parameters that we have so far left undetermined, with the objective of defining the optimal setup which, on the one hand, must be numerically stable and, on the other hand, must not be affected by LLM. In the following paragraphs we analyse the influence of the location of the matching-point (§i.), of the temporal filter of Yang et al. (2017b) (§ii.) and of the subgrid-scale model (§iii.). Finally, results are summarised and the numerical setup of the WMLES of Chapter 4 is settled (iv.).

i. *Influence of the matching-point location*

In this paragraph we test the theory of Kawai and Larsson (2012) described in §1.2.4, which states, recall, that LLM can be removed by coupling the wall-model and the LES a few grid-points away from the wall. In this paragraph, we propose to keep the same grid and to increase y_w, which is in fact justified as long as the matching-point is located in the inner layer, *i.e.*, $y_w/\delta \in [0, 0.2]$.

We perform the WMLES of the channel flow with isothermal walls of §1.4.1, using the no-slip formulation by Nicoud et al. (2016) at the wall and the WALE subgrid-scale model; no stability issues have been encountered with this setup. We test four values of y_w, *i.e.*, $y_w^* \approx 20, 40, 60, 80$, which correspond to the first four off-wall grid points; results for the mean velocity and temperature are shown in Figure 1.11 in semi-local scaling. As can be seen, the distancing of the matching-point has a striking effect on both mean profiles; for $y_w/\Delta Y = 1$ and $y_w/\Delta Y = 2$, LLM clearly appears, with an important shift of both the mean velocity and temperature; for $y_w/\Delta Y = 3$ and $y_w/\Delta Y = 4$, instead, the LES profiles follow the reference DNS curves and LLM is completely removed; these results provide further evidence of the efficiency of the method of Kawai and Larsson (2012).

Figures 1.12a & 1.12b, instead, show the three root-mean-square (r.m.s.) velocity profiles and r.m.s. temperature obtained with $y_w/\Delta Y = 4$. As can be observed, the level of fluctuations, especially for the streamwise velocity and for the temperature, is inaccurately predicted until $y^* \approx 200$, while good agreement is obtained with the DNS results towards the centre of the channel. These results show the chronic problem of WMLES related to the over-prediction of the turbulence intensities in

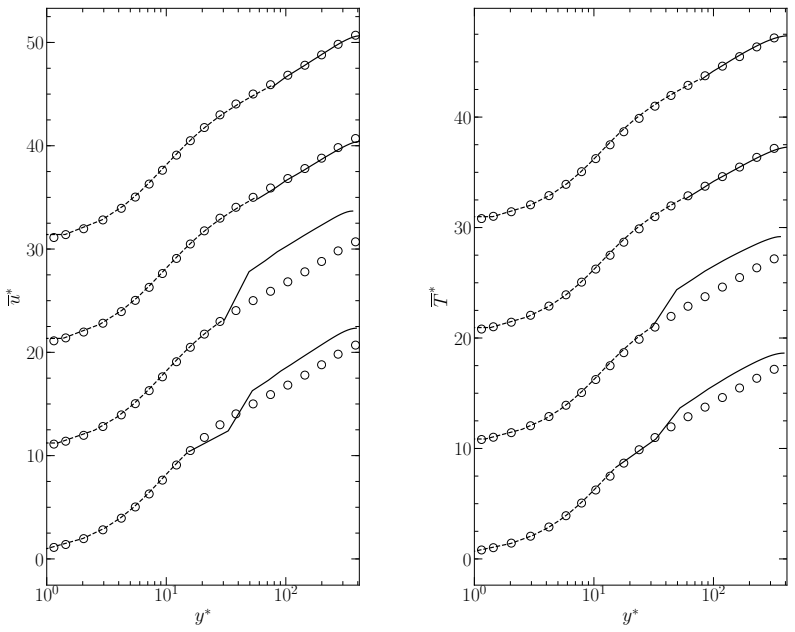

Figure 1.11: *A posteriori* tests, location of the matching-point. Mean profile of streamwise velocity (a) and temperature (b) for four matching-point locations (from bottom to top, $y_w^* = 20, 40, 60, 80$): ○ DNS profiles of Appendix A; —— present LES results; - - - - equilibrium wall-model. Profiles are shifted by ten on the vertical axis for the sake of clarity.

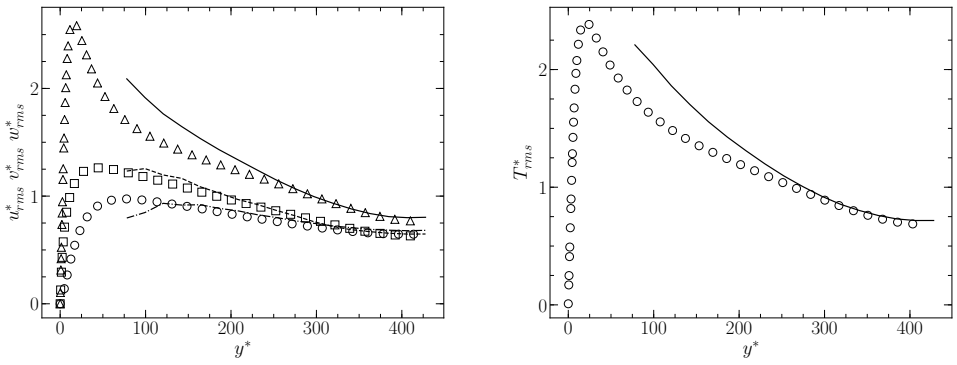

(a) (b)

Figure 1.12: *A posteriori* tests, location of the matching-point. Profiles of r.m.s. streamwise, wall-normal and spanwise velocity, respectively (a), and temperature (b): △, ○ and □ DNS profiles from Appendix A; ——, – · – · – and - - - - present LES results.

the near-wall region (see, for instance, Cabot and Moin, 2000; Lodato et al., 2014); this problem is evidently not corrected by the distancing of the matching-point.

ii. *Influence of the temporal filtering*

In this paragraph, we test the theory of Yang et al. (2017b) described in §1.2.3, which states, recall, that LLM can be removed by prescribing a temporal filter to the velocity input of the wall-model.

We perform the WMLES of the channel flow with adiabatic walls described in §1.4.1; the wall-model and the LES are coupled at the first off-wall point; therefore, we prefer in this case the classic slip formulation at the wall, with which the SGS viscosity is not modified in the first off-wall cell; finally, we use the dynamic Smagorinsky SGS model, since we have encountered numerical stability issues with WALE and Sigma combined with the slip formulation.

Figure 1.13 shows the mean velocity profile obtained for four values of the weight of time averaging $\epsilon = \Delta t/T_f$ (see §1.2.3), *i.e.*, $\epsilon = 1, 0.1, 0.01, 10^{-4}$. The case $\epsilon = 1$ corresponds to the case with no temporal filter, while $\epsilon = 10^{-4}$ corresponds to a filtering time-scale of $T_f = 10^4 \Delta t$; the range $\epsilon \in \left[10^{-4}, 1\right]$ is in agreement with the order of magnitude used by Yang et al. (2017b). As can be observed, the LLM that the velocity profile exhibits with $\epsilon = 1$, is not corrected by the progressively stronger time filtering; in fact, the mean velocity profile seems not to be affected at all.

These results are in complete disagreement with those of Yang et al. (2017b), who reported the complete elimination of LLM. We do not know if our failure is due to some code-dependency of the method (which would not be surprising, since LLM itself is code-dependent), or to some lack of information concerning the numerical setup of Yang et al. (2017b); Yang et al. (2017b), for instance, never specified which input velocity u^0_{wm} should be injected into the wall-model at the zeroth iteration; the value attributed to u^0_{wm} is fundamental in this case, since if, for instance, $\epsilon = 10^{-4}$, $u^n_{wm} \approx u^0_{wm}$ even for $n = 10^4$.

Because of the negative results obtained with the temporal filter, we have decided

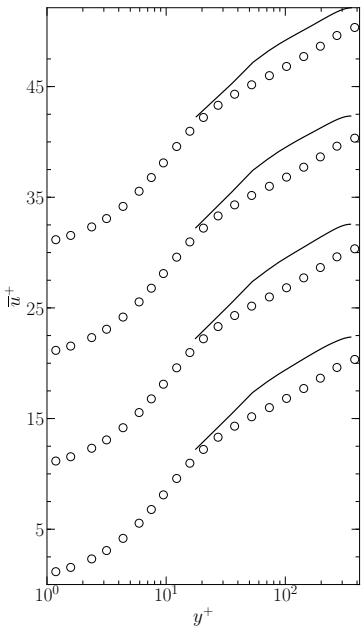

Figure 1.13: *A posteriori* tests, time filtering. Mean profile of streamwise velocity for four values of ϵ (from bottom to top, $\epsilon = 1, 0.1, 0.01, 10^{-4}$): ○ DNS profiles from Appendix A; —— present LES results.

to abandon this method, and to adopt the one proposed by Kawai and Larsson (2012) for our WMLES simulations of Chapter 4.

iii. *Influence of the subgrid-scale model*

In §1.3.1 we have introduced three subgrid-scale models, *i.e.*, dynamic Smagorinsky, WALE and Sigma; we have chosen these models because they are all supposed to accurately predict the damping of the subgrid viscosity in proximity to solid boundaries.

In this paragraph we perform the WMLES of the channel flow with isothermal walls introduced in §1.4.1 using these subgrid-scale models; the matching-point is located at $y_w/\Delta Y = 4$; concerning the wall boundary condition, we employ the classic slip formulation with dynamic Smagorinsky; with WALE and Sigma the slip formulation causes numerical instability and, therefore, we use the boundary condition of Nicoud et al. (2016).

Figures 1.14a & 1.14b show the mean velocity and temperature profiles, respectively, obtained with the three SGS models; as can be observed, the mean profiles are very well retrieved regardless of the turbulence model used, with only some small inaccuracies for the velocity near the centre of the channel with dynamic Smagorinsky. These results allow us to retain all three models for our WMLES of Chapter 4.

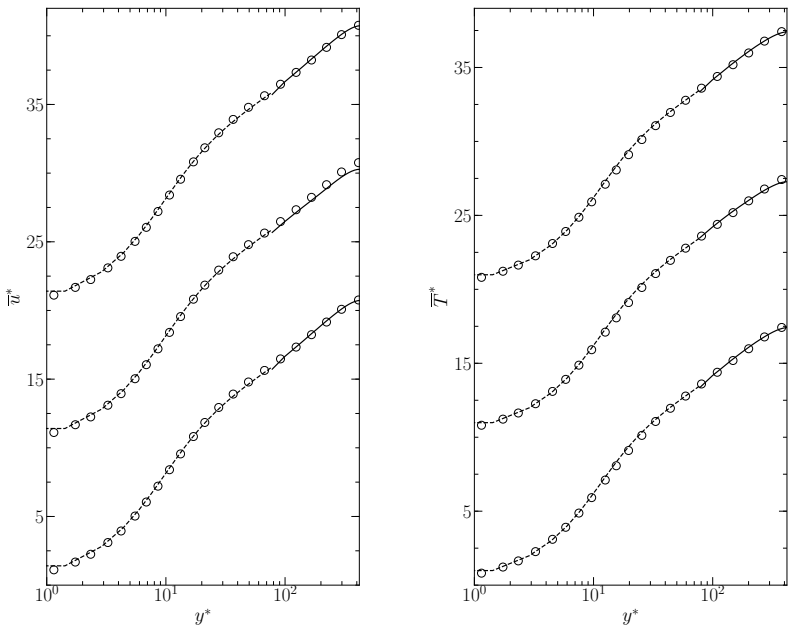

Figure 1.14: *A posteriori* tests, SGS model. Mean profile of streamwise velocity (a) and temperature (b) for three different SGS models (from bottom to top, WALE, Dynamic Smagorinsky, Sigma): ○ DNS profiles from Appendix A; —— present LES results; - - - - equilibrium wall-model. Profiles are shifted by ten on the vertical axis for the sake of clarity.

	SGS	Boundary condition	$y_w/\Delta y$	Filtering	LLM	Stability
Setup 1	Sigma	Slip	1	No	-	No
Setup 2	WALE	Slip	1	No	-	No
Setup 3	DSMA	Slip	1	No	Yes	Yes
Setup 4	WALE	No-slip	1	No	Yes	Yes
Setup 5	WALE	No-slip	2	No	Yes	Yes
Setup 6	WALE	No-slip	3	No	No	Yes
Setup 7	WALE	No-slip	4	No	No	Yes
Setup 8	WALE	Slip	1	Yes	-	No
Setup 9	Sigma	Slip	1	Yes	-	No
Setup 10	DSMA	Slip	1	Yes	Yes	Yes
Setup 11	DMSA	Slip	4	No	No	Yes
Setup 12	Sigma	No-slip	4	No	No	Yes

Table 1.3: Setups tested in this work. DMSA stands for dynamic Smagorinsky. All the numerical instabilities mentioned here led to a crash of the simulation.

iv. *Summary and final setup*

Table 1.3 summarises the ensemble of numerical setups presented in this section; we also highlight the setups we have tested but turned out to yield numerical instability. Since we have not further investigated the nature of these instabilities, we do not in any way discourage the use of these setups in other configurations. As can be seen, stability is mostly affected by the choice of SGS model and wall boundary condition; with WALE and Sigma it appears necessary to use the no-slip formulation of Nicoud et al. (2016), with dynamic Smagorinsky any boundary condition is acceptable. The log-layer mismatch, instead, is only removed by coupling the wall-model and the LES at the third or fourth off-wall point; the temporal filter of Yang et al. (2017b), on the contrary, proved to be ineffective in our case.

The acceptable setups are therefore N° 6, 7, 11 and 12. In reality, the non-equilibrium configuration of Chapters 3 & 4, as we shall see, requires the no-slip formulation at the wall in order not to yield instability at the inlet; therefore, we have finally chosen to adopt Setup 7, where the choice of the 4^{th} off-wall grid point over the 3^{rd} and of WALE over Sigma is purely arbitrary.

1.5 Conclusion

In this chapter we have presented in detail the principles of WMLES, as well as the numerical setup employed in Chapter 4.

In §1.1, we have combined an overview of the theory of boundary layers with the

description of the most common WMLES approaches introduced in the literature. We have seen that wall-models can be of extremely different levels of complexity, from simple algebraic relations of limited physical representativeness, to sophisticated three-dimensional RANS models; the choice of a wall-model depends on the typology of flow studied and, in this work, only TBLE models will be considered. These models are accessible and, if necessary, easy to implement in an external solver; in addition, they are physically more representative than algebraic models, especially in flows with variable properties, and can be adapted to take into account some non-equilibrium effects, as is done in Chapter 4.

In §1.2 we have introduced one of the chronic problems of WMLES (and DES), *i.e.*, the log-layer mismatch (LLM); LLM is a shift observed on the mean velocity and temperature profiles that implies an under-prediction (or, in some cases, over-prediction) of the wall shear-stress and heat flux. We have presented the main strategies introduced in the literature and we have decided to implement and test the temporal filter, proposed by Yang et al. (2017b), and the distancing of the matching-point proposed by Kawai and Larsson (2012).

In §1.3, we have described the LES code we have chosen for performing WMLES, *i.e.*, AVBP, and we have presented the most suitable subgrid-scale models; moreover, we have illustrated the implementation of an equilibrium TBLE wall model and the way it is coupled with AVBP.

Finally, in §1.4, we have validated *a priori* and *a posteriori* the wall-model in an equilibrium configuration, *i.e.*, a fully developed channel flow with adiabatic and isothermal walls. The *a priori* validation has confirmed the good calibration of the different coefficients and constants of the wall-model; in addition, we have analysed the TBLE grid, and found a suitable criterion to prescribe to the mesh-adapting algorithm. The *a posteriori* validation, instead, has allowed us to define the numerical setup of our WMLES; we have seen that coupling the wall-model with the LES a few grid-points away from the wall is indeed very effective for removing LLM; we have instead obtained disappointing results with the temporal filter. We have also evaluated the impact of the SGS models and we have seen how, in fact, they are all suitable. Finally, we have opted for the following setup, which will be employed in Chapter 4:

— Subgrid-scale model: WALE;

— Wall boundary condition: no-slip formulation of the wall-model;

— Matching-point: fourth off-wall point.

Chapter 2

Conjugate heat transfer: stability, implementation and validation

The objective of this chapter is to provide all the details concerning the numerical framework in which the conjugate heat transfer simulations are conducted.

It is organised as follows. In §2.1, a brief description of the coupling approach and algorithm chosen for our studies is given. In §2.2, the stability of this approach is carefully analysed and discussed. More in particular, in §2.2.1 an overview of the stability analyses performed over the years, with a particular focus on normal mode techniques, is given; in §2.2.2, the stability analysis of our coupling algorithm carried out by Errera and Chemin (2013), is presented and discussed; results concerning the stability bounds predicted by the model are validated for several test cases using a specifically designed code in §2.2.3; finally, the possibility of extending the model beyond its original assumptions is discussed in §2.2.4. In §2.3, the way CHT is implemented between the codes of our choice (*i.e.*, *elsA* and *Zset* for the fluid and solid domains, respectively) is described. Finally, test cases are performed in §2.4 with the objective of both assessing the relevance of the stability analysis presented in §2.2 in a more realistic configuration and validating the implementation with respect to reference results found in the literature.

The work of Section 2.2, has been subject of two publications:

— Gelain, M., Errera, M.P., Gicquel, O., *Assessment and numerical validation of a normal mode stability analysis for conjugate heat transfer*, International Journal of Heat and Mass Transfer, under review.

— Errera, M. P., Moretti, R., Mayeur, J., Gelain, M., Tessé, L., Lamet, J. M., Laroche, E. *A numerical predictive model for conjugate heat transfer with radiation*, International Journal of Heat and Mass Transfer, 2020, vol. 160, p. 120155.

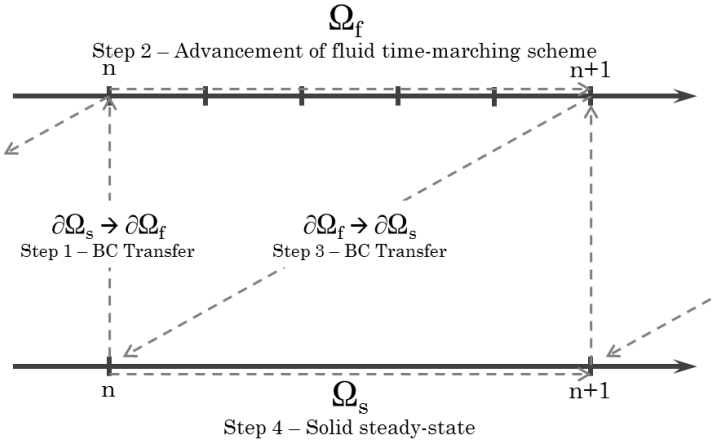

Figure 2.1: CSS (Conventional serial staggered) algorithm.

2.1 Coupling approach and algorithm

As mentioned in the Introduction, we choose for all the conjugate heat transfer (CHT) simulations performed in this work, a steady-state partitioned approach. The fluid and solid domains are therefore treated by two independent codes, which exchange the boundary conditions at a common interface until the convergence of temperature and heat-flux is attained. For the fluid domain, the Reynolds-averaged Navier-Stokes (RANS) equations are solved by the multi-purpose CFD software package *elsA* (Cambier and Gazaix, 2002) using a time-marching scheme. For the solid domain, the steady-state heat equation is solved by the software package Zset (Garaud et al., 2019) with a finite-element method. Finally, the exchange and interpolation of data between the two solvers is performed by the CWIPI coupling library (CWIPI, 2020). More details about these solvers and the way the communication between them is established are given in §2.3.

In order to obtain a fast steady solution to the aerothermal problem, the CHT is carried out through the basic four-step conventional serial staggered (CSS) algorithm (Piperno et al., 1995), which is schematically shown in Figure 2.1. The steps the algorithm consists of are the following:

1. The solid solver transfers the boundary conditions computed on the solid side of the interface $\partial\Omega_s$ to the fluid side $\partial\Omega_f$; if necessary, the boundary conditions are interpolated from one grid to the other;

2. After receiving the boundary conditions, the fluid solver's time-marching scheme advances over a pre-determined number of iterations (usually referred to as the coupling period); the use of a time-marching scheme is the first stratagem used to accelerate the convergence of the simulation since the time-step is locally computed with a predefined Courant-Friedrichs-Lewy (CFL) number, and adapts according to the acoustic and convective time-scales of every fluid cell; consequently, the transient phase is accelerated to the detriment of its physical meaning;

3. New boundary conditions are computed on the fluid interface $\partial\Omega_f$ and sent to the solid interface $\partial\Omega_s$; once again, if necessary, the boundary conditions are adequately interpolated between the two grids;

4. The solid code solves the steady-state heat equation in its domain; this is the second convergence-accelerating stratagem used, since the transient phase in the solid domain is utterly ignored.

Once the fourth step is completed, the algorithm is restarted from the first step until convergence. It is on the basis of this coupling approach and algorithm that the stability analysis described in the following section is constructed.

2.2 Stability of partitioned algorithms for conjugate heat transfer

2.2.1 Motivation and overview

One of the main disadvantages of partitioned approaches for aerothermal coupling is represented by the stability issues which the exchange of boundary conditions at the fluid-solid interface may cause, even in the case where, in both domains, the respective stability conditions are fulfilled. The way information should be exchanged between the solvers is therefore an essential question that has inspired numerous stability analyses from various points of view.

The pioneering study is that of Giles (1997), who performed a normal mode stability analysis with a hypothesis of one-dimensional diffusive fluid-solid transfer; Lindström and Nordström (2010) used a method based on the energetic equilibrium of the studied system, in order to obtain the most stable combination of boundary conditions to prescribe at the coupling interface; Roux and Garaud (2009) studied the behaviour of interface conditions at steady state using a matrix analysis based on domain decomposition methods; Verstraete and Scholl (2016) adopted a physical approach which focuses on the Biot number. These studies showed the complexity of the stability problem in partitioned CHT algorithms, and illustrated the role played by the type of boundary conditions prescribed (*i.e.*, Dirichlet, Neumann or Robin), by the thermal properties of the fluid and solid domains as well as by their numerical properties (*e.g.*, time-step, grid spacing etc.). On the whole, the most effective way of obtaining interesting and promising stability results seems to be a simplified one-dimensional coupled model based on a normal mode analysis (see Giles, 1997; Roe et al., 2008; Henshaw and Chand, 2009; Kazemi-Kamyab et al., 2014; Joshi and Leyland, 2014), and it is on this method that our study is based.

Giles (1997) focused on the most *natural* approach, *i.e.*, that of imposing Dirichlet-Neumann boundary conditions at the fluid-solid interface. These conditions can be expressed as:

$$\begin{aligned} \hat{q}_s &= -q_f \\ \hat{T}_f &= T_s \ , \end{aligned} \tag{2.2.1}$$

where T and q are the temperature and the normal heat flux, respectively; the heat flux is computed as $q = -\lambda \partial T / \partial \nu$, where λ is the thermal conductivity and ν is the inward-pointing unit normal; finally, the super-imposed hat symbol $(\hat{\cdot})$ denotes the sought value and the subscripts $(\cdot)_f$ and $(\cdot)_s$ indicate the fluid and solid domain, respectively. Therefore, at every coupling instance the solid domain receives the heat

flux computed at the fluid interface, and the fluid domain receives the temperature obtained at the solid interface. On the basis of an unsteady one-dimensional model, Giles (1997) performed a normal mode stability analysis based on the theory of Godunov and Ryabenki (1964) (see also Gustafsson, 2001) and found the following results:

— If an explicit temporal scheme is used, the partitioned coupling algorithm is stable if:

$$r < \frac{\sqrt{1 - 2\mathrm{D}_s}}{1 - \sqrt{1 - 2\mathrm{D}_f}} \ , \tag{2.2.2}$$

where $r = \left(\rho_f C_{p_f} \Delta x_f\right) / \left(\rho_s C_{p_s} \Delta x_s\right)$, with ρ the mass density, c_p the thermal capacity and Δx the grid spacing (considered uniform for each domain) and $\mathrm{D} = a\Delta t / \Delta x^2$ is the Fourier number with a the thermal diffusivity and Δt the time-step.

— If an implicit temporal scheme is used, the partitioned coupling algorithm is stable if:

$$r < \sqrt{\frac{\mathrm{D}_s}{\mathrm{D}_f}} \tag{2.2.3}$$

On the one hand, these results show why the Dirichlet-Neumann boundary conditions are considered *natural*; indeed, in order for these conditions to give a stable coupling regardless of the temporal scheme used and of the Fourier number of the two domains, r must be small which, in most fluid-solid thermal interactions, is the case. On the other hand, they show how this coupling approach is not unconditionally stable; in addition, its stability depends on physical and numerical properties that do not always belong to the degrees of freedom of the problem; in fact, these boundary conditions cause instabilities in many practical applications, including ours, as we shall see.

A straightforward way of addressing the stability issues of the coupling algorithm, is that of relaxing the Neumann condition on the solid side with a coupling coefficient; this leads to the following Dirichlet-Robin boundary conditions:

$$\begin{aligned} \hat{q}_s + \alpha_f \hat{T}_s &= -q_f + \alpha_f T_f \\ \hat{T}_f &= T_s \ . \end{aligned} \tag{2.2.4}$$

These boundary conditions are interesting because the steady-state thermal solution (if it exists) is independent of α_f; therefore, α_f represents an additional degree of freedom that does not influence the solution, and that can be freely prescribed by the user. On the contrary, a major drawback of these conditions is that, during the transient phase, the continuity of temperature and heat flux through the coupling interface is not as elementary as it is for Dirichlet-Neumann. It is the reason why the Dirichlet-Robin conditions are most adapted to steady CHT algorithms, such as the one described in §2.1, where the transient phase is in any case not physically meaningful, and can be artificially accelerated or, in this case, stabilised.

Dirichlet-Robin interface conditions have been studied in detail by Errera and Chemin (2013) (also see Errera and Duchaine, 2016), who showed how α_f can, on the one hand, positively condition stability, yet, on the other hand, affect the convergence rate of the algorithm. They demonstrated the existence of a lower stability bound, called α_f^{min}, and formulated the expression of a relaxation coefficient α_f^{opt} of

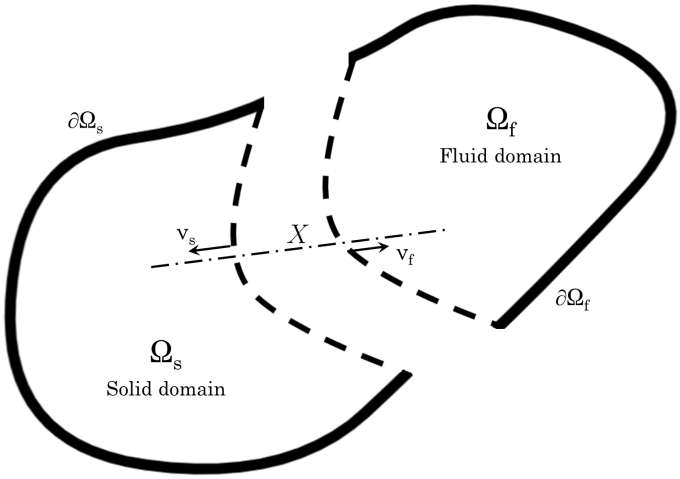

Figure 2.2: Schematic representation of a generic CHT problem.

compromise between the fast but prone-to-instability coefficients ($\alpha_f \in [\alpha_f^{min}, \alpha_f^{opt}]$), and the stable but over-relaxing coefficients ($\alpha_f \gg \alpha_f^{opt}$). The performance of these coupling coefficients has been tested in academic test cases (Errera and Duchaine, 2016) as well as in industrial applications (see El Khoury et al., 2017; Salem, 2020); furthermore, the model has recently been enriched with the inclusion of radiation (see Errera et al. (2020) or §2.2.4).

We remind the reader the organisation of the section. The stability analysis performed by Errera and Chemin (2013) is first presented and discussed in §2.2.2; then, results are validated for several test cases using a specifically designed code that respects all the assumptions of the stability analysis in §2.2.3; finally, the possibility of extending the model beyond its original validity range is discussed in §2.2.4.

2.2.2 A normal mode stability analysis

i. *Governing equations, interface treatment and discretisation*

We consider a generic aerothermal problem formed by a fluid (Ω_f) and a solid (Ω_s) domain, as depicted in Fig. 2.2. The normal stability analysis is performed over a simplified, one-dimensional sub-problem, which is extracted along the direction X orthogonal to the fluid-solid interface $\partial\Omega_{s/f}$ in any of its points. In practice, the assumption of one-dimensionality implies that the only error modes which are considered prone to instability are those varying along the normal direction of the fluid-solid interface (see Giles, 1997; Errera and Chemin, 2013). Note that it is generally admitted that this assumption is quite realistic in two- or three-dimensional configurations.

In the fluid domain Ω_f, according to the coupling algorithm, in which a time-marching scheme is employed on the fluid side (see §2.1), transient thermal conduction is considered. The domain is a semi-infinite line with $x = 0$ at the fluid-solid interface; in practice, the choice of a semi-infinite domain implies that numerical in-

stabilities, if any, are supposed to manifest in a such a short time that the fluid-solid interface does not *perceive* the other fluid boundary. Its physical properties (mass density, heat capacity etc.) are constant in both time and space. Finally, convection is neglected, implying that potential numerical instabilities are only supposed to occur in the very near-wall region, where diffusion effects prevail over convective ones. Taking into account all these hypotheses, the energy equation in the fluid domain reads:

$$\rho c_p \frac{\partial T}{\partial t} = \lambda_f \frac{\partial^2 T}{\partial x^2} \qquad x \geq 0 \ , \tag{2.2.5}$$

where λ_f is the thermal conductivity of the medium.

In the solid domain Ω_s, according to the coupling algorithm described in §2.1, steady-state conduction is considered. The domain is finite, and extends from $x = 0$ at the fluid-solid interface to $x = -\Lambda_s$ at its left boundary. The choice of a finite domain is understandably justified by the use of a steady-state equation which, as we shall see, is elliptic. Physical properties are also in this case considered constant, yielding the following heat equation:

$$\frac{\partial^2 T}{\partial x^2} = 0 \qquad x \leq 0 \ , \tag{2.2.6}$$

At the solid boundary $x = -\Lambda_s$, a generic Robin condition is imposed:

$$q = q_{ext} + \alpha_{ext} \left(T_{ext} - T \right) \qquad x = -\Lambda_s \ , \tag{2.2.7}$$

where q_{ext}, T_{ext} and α_{ext} designate a prescribed heat flux, temperature and convective coefficient, respectively.

As it has already been mentioned, Errera and Chemin (2013) considered the case of Dirichlet-Robin boundary conditions at the fluid-solid interface. The Dirichlet condition applied on the fluid side of the interface yields:

$$\hat{T}_f = T_s \qquad x = 0 \ , \tag{2.2.8}$$

while the Robin condition applied on the solid side of the interface writes:

$$\hat{q}_s + \alpha_f \hat{T}_s = -q_f + \alpha_f T_f \qquad x = 0 \ . \tag{2.2.9}$$

Both fluid and solid domains are spatially discretised with a uniform grid of spacing Δx_f and Δx_s, respectively, as shown in Figure 2.3. The time-step Δt is also uniform, giving the following space and time discretisation:

$$\begin{aligned} x_j &= j \Delta x_f \qquad && j = 0, 1, 2, ... \\ x_j &= j \Delta x_s \qquad && j = 0, -1, ..., -J \\ t^{n+1} &= t^n + \Delta t \qquad && n = 0, 1, 2, ... \end{aligned} \tag{2.2.10}$$

Concerning the fluid domain, Eq. (2.2.5) is solved with a backward implicit time scheme of second order in space and, in discretised form, reads:

$$\frac{\rho c_p}{\Delta t} \left(T_j^{n+1} - T_j^n \right) = \frac{\lambda_f}{\Delta x_f^2} \left(T_{j+1}^{n+1} - 2T_j^{n+1} + T_{j-1}^{n+1} \right) \quad j > 0 \ , \tag{2.2.11}$$

which can be rewritten as:

$$\left(T_j^{n+1} - T_j^n \right) = \mathrm{D}_f \left(T_{j+1}^{n+1} - 2T_j^{n+1} + T_{j-1}^{n+1} \right) \quad j > 0 \ , \tag{2.2.12}$$

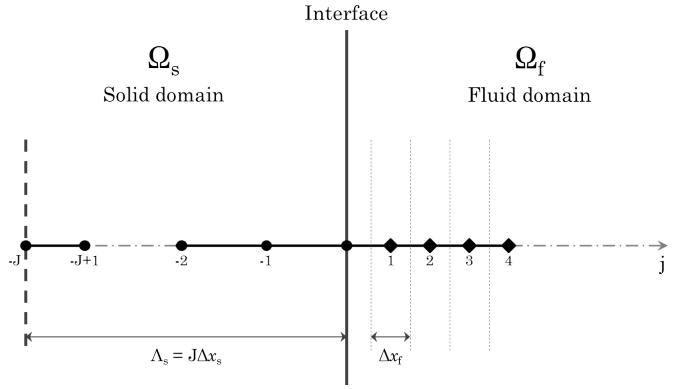

Figure 2.3: Schematic representation of the discretised fluid ($x > 0$) and solid ($x < 0$) one-dimensional domains (reproduction of figure from Errera and Chemin (2013)).

where the mesh Fourier number $\mathrm{D}_f = a_f \Delta t / \Delta x_f^2$ introduced in §2.2.1 appears. It should be noted that the choice of a numerical scheme is binding, as the results of the stability analysis depend on it. In this work, no other temporal or spatial schemes are explored.

Concerning the solid domain, a similar spatial scheme is used for Eq. (2.2.6):

$$T_{j+1}^{n+1} - 2T_j^{n+1} + T_{j-1}^{n+1} = 0 \quad j < 0 \ , \tag{2.2.13}$$

even if, in reality, no discretisation is actually needed since the medium is at steady-state and its thermal conductivity λ_s is constant, giving a linear distribution of the temperature between $x \in [-\Lambda_s, 0]$, which can be found analytically. At the $x = -\Lambda_s$ boundary, the Robin condition (2.2.7) becomes:

$$-\frac{\lambda_s}{\Delta x_s}\left(T_{-J+1}^{n+1} - T_{-J}^{n+1}\right) = q_{ext} + \alpha_{ext}\left(T_{ext} - T_{-J}^{n+1}\right) \quad j = -J \ , \tag{2.2.14}$$

or, considering the domain's steady-state,

$$-\frac{\lambda_s}{\Lambda_s}\left(T_{0^-}^{n+1} - T_{-J}^{n+1}\right) = q_{ext} + \alpha_{ext}\left(T_{ext} - T_{-J}^{n+1}\right) \quad j = -J \ , \tag{2.2.15}$$

giving:

$$T_{-J}^{n+1} = \left(\frac{\lambda_s}{\Lambda_s} T_{0^-}^{n+1} + \alpha_{ext} T_{ext} + q_{ext}\right) \Big/ \left(\frac{\lambda_s}{\Lambda_s} + \alpha_{ext}\right) \ . \tag{2.2.16}$$

The two media exchange their boundary conditions at every fluid iteration n (the way this choice affects the stability of the coupling process will be seen in detail in §2.2.4). The Dirichlet boundary condition on the fluid side of the interface, therefore, is simply expressed by:

$$T_{0^+}^{n+1} = T_{0^-}^{n} \quad j = 0^+ \ , \tag{2.2.17}$$

while the Robin condition on the solid side writes:

$$\frac{\lambda_s}{\Lambda_s}\left(T_{0^-}^{n+1} - T_{-J}^{n+1}\right) + \alpha_f T_{0^-}^{n+1} = \frac{\lambda_f}{\nu \Delta x_f}\left(T_1^{n+1} - T_{0^+}^{n+1}\right) + \alpha_f T_{0^+}^{n+1} \quad j = 0^- \ , \tag{2.2.18}$$

where $\nu = 1/2$ if a cell-centred scheme, as in Fig. 2.3, is used for Eq. (2.2.5), since the heat flux is in this case expressed as $q = \frac{2\lambda_f}{\Delta x_f}(T_{j+1} - T_j)$; $\nu = 1$, instead, in case of a cell-vertex scheme. Now, inserting (2.2.16) into (2.2.18), we obtain after some elementary algebraic operations:

$$\left(\frac{\beta\lambda_s}{\Lambda_s} + \alpha_f\right) T_{0^-}^{n+1} = \frac{\lambda_f}{\nu\Delta x_f} T_1^{n+1} - \left(\frac{\lambda_f}{\nu\Delta x_f} - \alpha_f\right) T_{0^-}^{n} + \frac{\beta\lambda_s}{\Lambda_s}\left(T_{ext} + \frac{q_{ext}}{\alpha_{ext}}\right) , \tag{2.2.19}$$

where:

$$\beta = \frac{\alpha_{ext}}{\frac{\lambda_s}{\Lambda_s} + \alpha_{ext}} . \tag{2.2.20}$$

As a whole, the discrete system of equations governing the aerothermal problem is:

$$\begin{aligned}
&\left(T_j^{n+1} - T_j^n\right) = \mathrm{D}_f\left(T_{j+1}^{n+1} - 2T_j^{n+1} + T_{j-1}^{n+1}\right) && j > 0 \\
&T_{j+1}^{n+1} - 2T_j^{n+1} + T_{j-1}^{n+1} = 0 && j < 0 \\
&T_{0^+}^{n+1} = T_{0^-}^{n} && j = 0^+ \\
&\left(\tfrac{\beta\lambda_s}{\Lambda_s} + \alpha_f\right) T_{0^-}^{n+1} = \tfrac{\lambda_f}{\nu\Delta x_f} T_1^{n+1} - \left(\tfrac{\lambda_f}{\nu\Delta x_f} - \alpha_f\right) T_{0^-}^{n} + \tfrac{\beta\lambda_s}{\Lambda_s}\left(T_{ext} + \tfrac{q_{ext}}{\alpha_{ext}}\right) && j = 0^-
\end{aligned} \tag{2.2.21}$$

ii. *A stability bound for the Dirichlet-Robin coupling coefficient*

Errera and Chemin (2013) performed a normal mode stability analysis over the discrete system of equations (2.2.21). Following Gustafsson et al. (1972), the temperature can be expressed in space and time as:

$$T(x,t) = \sum_{p=-\infty}^{+\infty} A_p e^{\mathrm{i}(k_p x + \omega_p t)} = \sum_{p=-\infty}^{+\infty} A_p e^{\left(\mathrm{i}k_p x - k_p^2 t\right)} , \tag{2.2.22}$$

where k is the wave number, ω the angular frequency and A the complex amplitude. The frequency ω can be expressed as a function of the wave number through the dispersion relation $\omega = \omega(k)$ and, in the case of the heat equation, $\omega = \mathrm{i}k^2$. In discrete form and considering only a single harmonic, Eq. (2.2.22) becomes:

$$T_j^n = A e^{\mathrm{i}(k x_j + \omega t_n)} = A e^{\mathrm{i}(kj\Delta x + \omega n \Delta t)} = A\kappa^j z^n , \tag{2.2.23}$$

where $\kappa = e^{\mathrm{i}k\Delta x}$ and $z = e^{\mathrm{i}\omega\Delta t}$ are the spatial and temporal amplification factors, respectively. For the aerothermal problem described in §2.2.2, and assuming $A = 1$ without loss of generality, we can therefore write:

$$T_j^n = \begin{cases} z_f^{n-1}\kappa_f^j & j > 0 \\ \\ z_s^n \kappa_s^j & j < 0 \end{cases} , \tag{2.2.24}$$

where the subscripts $(\cdot)_f$ and $(\cdot)_s$ are necessary since κ and z are, *a priori*, different for the two domains; furthermore, the exponent $(n-1)$ is applied to the fluid temporal amplification factor z_f, as we shall see, to simplify the Dirichlet condition (2.2.17).

The discrete system (2.2.21) is stable under Godunov and Ryabenki (1964) if no solutions of the form (2.2.24) are admitted with $|\kappa_f| < 1$ and $|\kappa_s| > 1$, which are necessary conditions for the *spatial* stability of the problem, while $|z_{f/s}| > 1$ as $j \to \pm\infty$. It is also important to exclude neutrally stable modes with $|z_{f/s}| = 1$. The objective of the stability analysis by Errera and Chemin (2013) is thus to determine for which coupling coefficients α_f the abovestated stands.

Inserting (2.2.24) into the Dirichlet condition (2.2.17), we obtain:

$$z_f = z_s \ , \tag{2.2.25}$$

which indicates that the Dirichlet condition is automatically satisfied if a single temporal amplification factor is considered for the two domains. Hence, we can drop the use of the subscripts $(\cdot)_{s/f}$ in the following. Substituting (2.2.24) into the discretised diffusion equation for the solid domain, we obtain:

$$\kappa_s^2 - 2\kappa_s + 1 = 0 \quad j < 0 \ , \tag{2.2.26}$$

which gives the solutions $\kappa_s \pm 1$; in other words, the solid domain's diffusion provides a *neutral* contribution to the stability of the problem, which is a direct consequence of the use of a steady-state equation.

Inserting (2.2.24) into the discretised diffusion equation for the fluid domain (2.2.12), we obtain:

$$\kappa_f^2 - \left(2 + \frac{z-1}{z\mathrm{D}_f}\right)\kappa_f + 1 = 0 \quad j > 0 \ , \tag{2.2.27}$$

which gives the solutions:

$$\kappa_f = \frac{1}{2}\left(2 + \frac{z-1}{z\mathrm{D}_f} \pm \sqrt{\left(2 + \frac{z-1}{z\mathrm{D}_f}\right)^2 - 4}\right) \ , \tag{2.2.28}$$

even though only the minus-sign root is considered in order to respect the condition $|\kappa_f| < 1$.

Finally, injecting (2.2.24) into the Robin condition (2.2.19) gives:

$$\left(\frac{\beta\lambda_s}{\Lambda_s} + \alpha_f\right) z^{n+1} = \frac{\lambda_f}{\nu\Delta x_f} + z^n\kappa_f - \left(\frac{\lambda_f}{\nu\Delta x_f} - \alpha_f\right) z^n \ , \tag{2.2.29}$$

where the constant term $(\beta\lambda_s/\Lambda_s)\,(T_{ext} + q_{ext}/\alpha_{ext})$ has no impact on the stability analysis and can therefore be removed.

As a whole, the only meaningful relations are Eqs. (2.2.28) and (2.2.29), indicating that only the heat diffusion in the fluid domain and the Robin condition at the interface play an active role in the numerical stability of the coupling problem considered. Combining these two equations to eliminate κ_f, we obtain:

$$z = \frac{\frac{1}{2}\frac{\lambda_f}{\nu\Delta x}\left[2 + \frac{z-1}{\mathrm{D}_f z} - \sqrt{\left(2 + \frac{z-1}{\mathrm{D}_f z}\right)^2 - 4}\right] - \left(\frac{\lambda_f}{\nu\Delta x} - \alpha_f\right)}{\frac{\beta\lambda_s}{\Lambda_s} + \alpha_f} = g(z) \ , \tag{2.2.30}$$

which is a non-linear relation governing the stability of the whole discrete system (2.2.21). For every $\alpha_f \in \Re$, there exists a z^* giving $z^* = g(z^*)$, and, if $|z^*| < 1$ the

coupling problem is stable under Godunov and Ryabenki (1964); in other words, in order to show if for certain value of α_f the process is stable, it would be necessary to demonstrate that $z \neq g(z)$ for every $|z| > 1$. Yet, as pointed out by Errera and Chemin (2013), the analysis of the relation $z = g(z)$ for every $\alpha_f \in \Re$ can actually be limited to the unit circle $|z| = 1$. Indeed, it can be shown that $g(z)$ is a holomorphic function for $|z| > 1$ and, according to the maximum modulus principle in complex analysis (see Cartan, 1995), the maximum of its modulus can only be attained at its boundary[1], *i.e.*, $|z| = 1$. Consequently, if for a given α_f we can show that $|g(z)| < 1$ for $|z| = 1$, it will be guaranteed that $z \neq g(z)$ for every $|z| > 1$. Yet, the analysis can be simplified even more; indeed, it can be shown that the maximum of $|g(z)|$ can only be situated on either $z = -1$ or $z = 1$. More precisely, we have (see Errera and Chemin, 2013):

$$\max(|g(z)|) = \begin{cases} \frac{K_f\left[1+\mathrm{D}_f-\sqrt{1+2\mathrm{D}_f}\right]-(K_f-\alpha_f)}{K_s+\alpha_f} & \alpha_f \leq \alpha_f^* \\ \\ \frac{\alpha_f}{K_s+\alpha_f} & \alpha_f \geq \alpha_f^* \end{cases} , \tag{2.2.31}$$

where $K_f = \frac{\lambda_f}{\nu \Delta x_f}$ and $K_s = \frac{\beta \lambda_s}{\Lambda_s}$; finally,

$$\alpha_f^* = \frac{K_f}{\left(1+\sqrt{1+2\mathrm{D}_f}\right)} , \tag{2.2.32}$$

is a remarkable coupling coefficient on which we will focus later on.

As can be seen from Eq. (2.2.31) or, visually, from Fig. 2.4, the maximum of the amplification factor $\max(|g(z)|)$ evolves along two distinct branches. The former, for $\alpha_f \leq \alpha_f^*$, depends on the Fourier number D_f, and is a decreasing function of α_f; this branch always crosses the stability bound $\max(|g(z)|) = 1$, potentially for $\alpha_f ll 0$; for any given α_f for which $\max(|g(z)|) > 1$, there are potentially solutions to $z = g(z)$ with $|z| > 1$ and the stability of the process is not guaranteed. The latter branch, for $\alpha_f \geq \alpha_f^*$, does not depend on D_f; despite increasing with α_f, this branch never crosses the stability bound, as $\max(|g(z)|) \to 1^-$ for $\alpha_f \to \infty$; therefore, any $\alpha_f > \alpha_f^*$ will guarantee the stability of the coupling algorithm; this also implies that, as could be expected, there is no upper stability bound for α_f .

The value of α_f at which the left branch crosses the stability bound, can easily be determined. Imposing $z = -1$ into $z = g(z)$ (see Eq. (2.2.30)), we obtain:

$$\boxed{\alpha_f^{min} = \frac{K_f}{\left(1+\sqrt{1+2\mathrm{D}_f}\right)} - \frac{K_s}{2}} . \tag{2.2.33}$$

Several observations can be made regarding this remarkable result:

— The coupling coefficient α_f^{min} represents a lower stability bound; in other words, the coupling process is guaranteed to be stable for any $\alpha_f \in]\alpha_f^{min}, +\infty[$; this coefficient has been found analytically and, therefore, is exact;

— The expression for α_f^{min} is extremely rich as it includes, through D_f, K_f and K_s, all the relevant physical and numerical properties of the aerothermal problem;

[1]The principle actually applies to holomorphic functions defined on an open set. Rigorously, Errera and Chemin (2013) performed the change of variable $Z \to 1/z$, operated a branch-cut on $\kappa_f(Z)$ along the path $[1, +\infty]$ and worked in the open set $|Z| < 1$, where $g(Z)$ is holomorphic (details in Errera and Chemin (2013)).

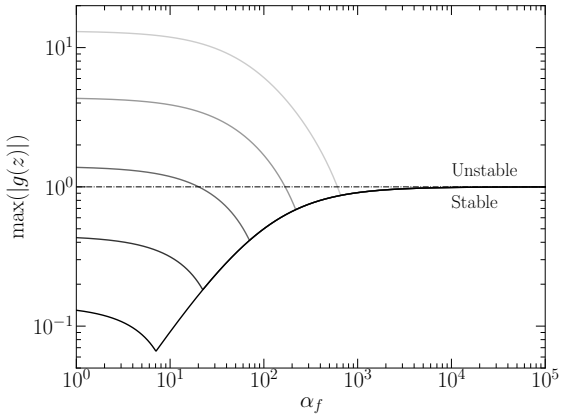

Figure 2.4: Evolution of $\max(|g(z)|)$ as a function of α_f for $K_f = 10^4$, $K_s = 100$ and different values of D_f. From lighter to darker: $\mathrm{D}_f = 10^2, 10^3, 10^4, 10^5, 10^6$.

— It can be noticed that if $K_s = \beta\lambda_s/\Lambda_s \to 0$, $\alpha_f^{min} \to \alpha_f^*$; in other words, for a given fluid domain (represented by D_f and K_f), α_f^* is the highest α_{min} possible; therefore, regardless of the conductivity of the solid domain or, in other words, regardless of how challenging the coupling process is, α_f^* guarantees stability. It is the reason why this coefficient is remarkable, and why Errera and Chemin (2013) called this coefficient α_f^{opt}, *i.e.*, the optimal coefficient. We will see in §2.2.3 how α_f^{opt} can be interesting in practice.

— It can be seen from Eq. (2.2.33) that α_f^{min} can be negative; when this happens, any coefficient $\alpha_f \in]\alpha_f^{min}, 0]$ will guarantee stability, indicating that, at least in the context of this particular aerothermal problem, there is no intrinsic mathematical reason why α_f should be greater than or equal to zero; the only conditions which needs to be satisfied is $\alpha_f > \alpha_f^{min}$; it is also obvious that when $\alpha_f^{min} < 0$, imposing the *classical* Neuman-Dirichlet boundary conditions at the fluid-solid interface would guarantee the stability of the process.

— When $\alpha_f \to \alpha_f^{min^+}$, the solution to $z = g(z)$ is $z \to -1^+$; since $z = T_j^{n+1}/T_j^n$ (see Eq. (2.2.24)), if $z \approx -1$ the solution strongly varies and oscillates between two consecutive iterations; the coupling process is, therefore, likely to converge fast, yet prone to instability. On the other hand, when $\alpha_f \gg \alpha_f^{min}$, the solution to $z = g(z)$ is $z \approx 1$; since $z = T_j^{n+1}/T_j^n$, if $z \approx 1$ the solution essentially does not evolve between two temporal iterations; the coupling process is therefore over-stable. It is the reason why it is essential, in practice, to choose a compromise coupling coefficient between the fast but prone to instability coefficients ($\alpha_f \approx \alpha_f^{min}$), and the stable but over-relaxing ones ($\alpha_f \gg \alpha_{min}$); this aspect will be further discussed at the end of this chapter (see §2.5).

iii. *Nature of the CHT process*

It is possible to rewrite the stability bound α_f^{min} in a more compact manner by introducing a numerical Biot number defined as follows (see Moretti et al., 2018):

$$\mathrm{Bi}_\nu = \frac{K_f}{K_s}\frac{2}{1+\sqrt{1+2\mathrm{D}_f}} \ , \tag{2.2.34}$$

where K_f/K_s can be regarded as the ratio of the thermal conductance of a fluid cell over the thermal conductance of the whole solid domain. Using Eq. (2.2.34) we have:

$$\alpha_f^{min} = \frac{K_s}{2}\left(\mathrm{Bi}_\nu - 1\right) \ . \tag{2.2.35}$$

The newly introduced Biot number, being non-dimensional, is actually more meaningful than α_f^{min} which, instead, is dimensionally equivalent to a convective coefficient; furthermore, Bi_ν is always positive. The numerical Biot number Bi_ν gives key insight into the nature of the fluid-solid interaction, allowing us to quantify its intensity:

— *Weak interaction,* $\mathrm{Bi}_\nu \leq 1$: if this condition is met, the *transient* thermal resistance of a fluid cell is greater than the resistance of the whole solid domain. This happens, for instance, when the conductivity of the solid domain λ_s is very elevated, or when that of the fluid domain λ_f is very low; when $\mathrm{Bi}_\nu \leq 1$, $\alpha_f^{min} \leq 0$ and Dirichlet-Neumann boundary conditions can be prescribed at the fluid-solid interface. Note that a sufficient condition for $\mathrm{Bi}_\nu < 1$ is given by $K_f < K_s$.

— *Moderate interaction,* $\mathrm{Bi}_\nu \gtrsim 1$: the thermal resistance of the fluid is of the same order of magnitude of that of the solid domain; a necessary condition for $\mathrm{Bi}_\nu > 1$ is $K_f > K_s$, and when this happens D_f becomes decisive for determining the intensity of the aerothermal interaction, which is *artificially* damped if D_f increases. In any case, when $\mathrm{Bi}_\nu \gtrsim 1$, then $\alpha_f^{min} \gtrsim 0$, and Dirichlet-Robin boundary conditions need to be used.

— *Strong interaction,* $\mathrm{Bi}_\nu \gg 1$: when this happens, there is a major stability restriction; it is usually the case of extreme coupling processes featuring very low-conducting solid materials or very low Prandtl number fluids; although Dirichlet-Robin boundary conditions, as long as $\alpha_f > \alpha_f^{min}$, guarantee numerical stability, a very high coupling coefficient is needed; this is the reason why it could actually be advisable to *switch* the fluid and solid domains and use either Neumann-Dirichlet or Robin-Dirichlet boundary conditions (with an analogous coupling coefficient α_s) at the interface.

The relevance of Bi_ν in the study of aerothermal processes, will be further elucidated in §2.2.4.

2.2.3 Numerical validation of the stability analysis

In the previous section, a lower stability bound for the coupling coefficient α_f has been found analytically. The objective of this section is to verify its validity in a numerical environment which fully respects the assumptions of the aerothermal problem considered in §2.2.2. For this purpose, a one-dimensional computational code has been designed *ad hoc* and is briefly described; finally, the results obtained for two test cases are presented.

Computational code

The computational code designed *ex novo* to meet the needs of the current study, solves the discrete system (2.2.21) which we rewrite here:

$$\begin{aligned}
&\left(T_j^{n+1} - T_j^n\right) = \mathrm{D}_f \left(T_{j+1}^{n+1} - 2T_j^{n+1} + T_{j-1}^{n+1}\right) && j > 0 \\
&T_{j+1}^{n+1} - 2T_j^{n+1} + T_{j-1}^{n+1} = 0 && j < 0 \\
&T_{0^+}^{n+1} = T_{0^-}^n && j = 0^+ \\
&\left(\tfrac{\beta\lambda_s}{\Lambda_s} + \alpha_f\right) T_{0^-}^{n+1} = \tfrac{\lambda_f}{\nu\Delta x_f} T_1^{n+1} - \left(\tfrac{\lambda_f}{\nu\Delta x_f} - \alpha_f\right) T_{0^-}^n + \tfrac{\beta\lambda_s}{\Lambda_s}\left(T_{ext} + \tfrac{q_{ext}}{\alpha_{ext}}\right) && j = 0^-
\end{aligned} \tag{2.2.36}$$

The discretised equation of the heat diffusion in the fluid domain, since it leads to a tridiagonal matrix, is easily solved through the Thomas algorithm (exactly like in §1.3 for the equilibrium wall-model); we use a cell-vertex scheme and, therefore, $\nu = 1$. The main difference with respect to the theoretical study, is that the fluid domain cannot be semi-infinite; its length is Λ_f and the grid has J_f points, so that $\Delta x_f = \Lambda_f / J_f$; in order for the $x = \Lambda_f$ boundary not to be perceived by the fluid-solid interface at $x = 0$ and, therefore, to meet the assumptions of the stability analysis, simulations are performed over a total time τ_{tot} so that:

$$\mathrm{Fo} = \frac{a_f \tau_{tot}}{\Lambda_f^2} \ll 1 \ , \tag{2.2.37}$$

where Fo represents the Fourier number of the whole fluid domain.

Concerning the solid domain, no actual grid is defined as the thermal conductivity λ_s is considered to be constant, and the domain is at steady-state; an analytical solution for T_{0^-} can thus be obtained:

$$T_{0^-} = \frac{\frac{K_s}{\alpha_{ext}}\left(q_{ext} + \alpha_{ext} T_{ext}\right) - q_f + \alpha_f T_f}{K_s + \alpha_f} \ , \tag{2.2.38}$$

where q_f and T_f are respectively the heat flux and temperature on the fluid side of the interface and, therefore, are known; for the temperature at the boundary $x = -\Lambda_s$, instead:

$$T_{x=-\Lambda_s} = \frac{q_{ext} + \alpha_{ext} T_{ext} + \frac{\lambda_s}{\Lambda_s} T_{0^-}}{\frac{\lambda_s}{\Lambda_s} + \alpha_f} \ , \tag{2.2.39}$$

from which the heat flux, keeping in mind that for every domain it is oriented along the inward-pointing normal, can easily be calculated:

$$q_s = -\frac{\lambda_s}{\Lambda_s}\left(T_{x=-\Lambda_s} - T_{0^-}\right) \tag{2.2.40}$$

At first, we will consider the case where the two domains exchange their boundary conditions at every fluid time iteration, which is in agreement with the stability model. The case where the coupling period is greater than unity will be analysed in §2.2.4 using the same computational code.

Fluid				Solid					Numerics			
λ_f	a_f	Λ_f	$T_{x=\Lambda_f}$	λ_s	Λ_s	α_{ext}	T_{ext}	q_{ext}	Δx_f	Δt	CHT period	Fo
0.02	2^{e-05}	0.05	300	20	1	∞	500	-	1.25^{e-04}	0.01	1	0.08

Table 2.1: Moderate mesh Fourier number case: physical and numerical parameters.

K_f	K_s	D_f	β	Bi_ν	α_f^{min}	α_f^{opt}
160	20	12.74	1	2.6	16.04	26.04

Table 2.2: Moderate mesh Fourier number case: fundamental parameters.

Test cases and results

i. *Moderate mesh Fourier number*

The CHT computations of the first test case are performed using the values of the fluid and solid data expressed in SI units in Table 2.1, where the same nomenclature employed in §2.2.2 is adopted. The resulting fundamental parameters of the aerothermal problem are summarised in Table 2.2. As can be seen, $\mathrm{Bi}_\nu > 1$, indicating a rather strong aerothermal interaction which necessitates a Dirichlet-Robin condition at the interface. The value of α_f^{opt}, calculated as $\alpha_f^{opt} = K_f/\left(1+\sqrt{1+2\mathrm{D}_f}\right)$ is also given; as pointed out in §2.2.2, this value represents the highest stability bound which is obtained if $K_s \to 0$.

A set of six different calculations are obtained by simply adopting six different coupling coefficients, strategically located in the spectrum of $\alpha_f \in \Re$. At this stage, it is worth remembering that, at convergence, $T_j^n = T_j^{n+1} = T_j^\infty$ for $j \in [-J_s, J_f]$ and T_j^∞ does not depend on the value of α_f as pointed out in §2.2.1 when discussing Eq. (2.2.4); furthermore, the evolution of the temperature across the two domains at convergence can easily be obtained analytically and can therefore be used as a reference for evaluating the convergence rate of every computation.

Figure 2.5 shows the evolution of the temperature at the fluid-solid interface non-dimensionalised as follows: $T_f^* = \left|T_f - T_f^\infty\right| / (T_{ext} - T_{x=\Lambda_f})$. The analysis highlights the following main points:

— $\alpha_f = \alpha_f^{min} - \epsilon$: this coefficient is slightly lower than α_f^{min}, more precisely $\alpha_f = 0.99\alpha_f^{min}$. According to the stability analysis described in §2.2.2, the coupling process is supposed to be unstable. This is exactly what happens, as illustrated in Fig. 2.5: this coupling coefficient produces oscillations that grow without bound, leading to a rapid divergence.

— $\alpha_f = \alpha_f^{min} + \epsilon$: this coefficient is slightly greater than α_f^{min}, more precisely $\alpha_f = 1.01\alpha_f^{min}$. According to the theoretical model, the CHT computation should be stable. These predictions are indeed verified since the strong oscil-

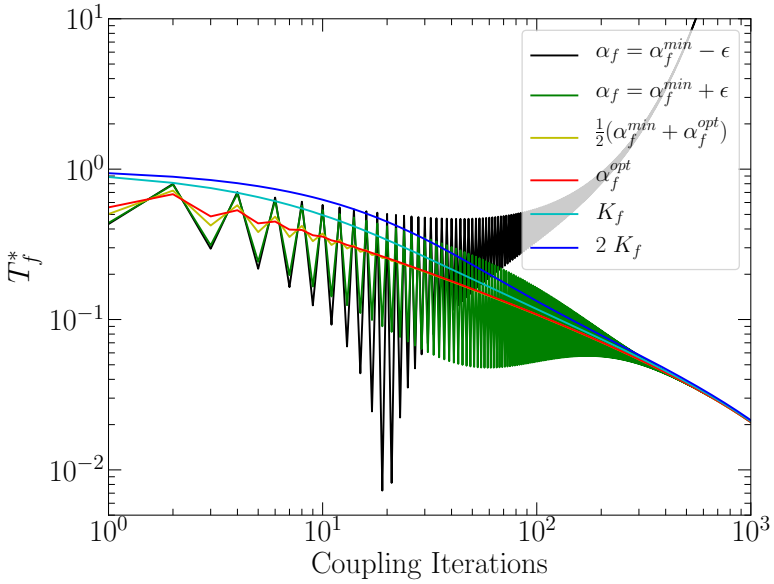

Figure 2.5: Moderate mesh Fourier number case: convergence history of the interface temperature with six different coupling coefficients.

lations observed during the initial iterations diminish and eventually die out; as explained in §2.2.2, these oscillations are due to the fact that the temporal amplification factor is in this case $z \gtrsim -1$.

— $\alpha_f = \left(\alpha_f^{min} - \alpha_f^{opt}\right)/2$: moving a little away from the stability limit, whilst remaining with $\alpha_f < \alpha_f^{opt}$, an oscillatory behaviour is still noted, but the amplitude of these oscillations is small and a monotonic convergence occurs rapidly.

— $\alpha_f = \alpha_f^{opt}$: here, the optimal coefficient defined by Errera and Chemin (2013) is implemented. A very small oscillatory behaviour is again initially observed, then this oscillation dies out rapidly and a stable and fast convergence occurs.

— $\alpha_f = K_f$: this coefficient is remarkable for two reasons; first, it is a static coefficient that is extremely easy to compute in practical CHT simulations, and that guarantees the stability of the simulation; second, it is easy to verify that injecting $\alpha_f = K_f$ into Eq. (2.2.30), $z = 0$ is a solution to $z = g(z)$; it can also be shown that, in general, $z^* \leq 0$ for $\alpha_f \leq K_f$, and $z^* \geq 0$ for $\alpha_f \geq K_f$, where z^* satisfies $z^* = g(z^*)$; since $z = T_j^{n+1}/T_j^n$, when $\alpha_f \geq K_f$ and $z \geq 0$, no oscillations should be observed in the solution. As can be seen from Fig. 2.5, this is exactly what happens. One major drawback of this coupling coefficient, on the other hand, is that it often leads to an excessively low convergence rate and, therefore, $\alpha_f = K_f$ is acceptable only if the fluid domain's dynamic effect is low, *i.e.*, the Fourier number D_f is relatively small.

— $\alpha_f = 2K_f$: as in the previous case, no oscillations are observed. However, as expected, this coefficient produces a very slow speed of the convergence process; this coefficient represents an emblematic case of over-relaxation.

Fluid				Solid					Numerics			
λ_f	a_f	Λ_f	$T_{x=\Lambda_f}$	λ_s	Λ_s	α_{ext}	T_{ext}	q_{ext}	Δx_f	Δt	CHT period	Fo
0.02	$2.^{e-05}$	0.05	300	20	1	∞	500	-	5^{e-05}	0.05	1	0.19

Table 2.3: Large mesh Fourier number case: physical and numerical parameters.

K_f	K_s	D_f	β	Bi_ν	α_f^{min}	α_f^{opt}
400	20	398	1	1.37	3.68	13.68

Table 2.4: Large mesh Fourier number case: fundamental parameters.

ii. *Large mesh Fourier number*

For the second test case, only two important parameters were changed compared to the previous one. The size of the fluid cells is reduced while the time step is increased. This has the desired effect of considerably increasing the mesh Fourier number D_f. The main physical, numerical and aerothermal parameters are summarised in Tables 2.3 and 2.4. The direct consequences of the modifications made are:

— Since the solid domain's properties remain the same, the difference $\alpha_f^{opt} - \alpha_f^{min} = K_s/2$ does not change;

— The distance between α_f^{opt} and K_f has considerably increased;

— The aerothermal interaction has been weakened since Bi_ν has decreased.

With this in mind, let us briefly analyse the computed results obtained in this test case using the same six coefficients. Figure 2.6 illustrates the convergence history and we can see that:

— $\alpha_f = \alpha_f^{min} - \epsilon$: this coefficient is equal to $\alpha_f = 0.99\alpha_f^{min}$. As before, an unstable computation is expected. Large oscillations are observed and they grow without bound, leading to a rapid divergence.

— $\alpha_f = \alpha_f^{min} + \epsilon$: this coefficient is equal to $\alpha_f = 1.01\alpha_f^{min}$. The same stability behaviour observed in the previous test case is observed here.

— $\alpha_f = \left(\alpha_f^{min} - \alpha_f^{opt}\right)/2$: an oscillatory behaviour is noted at the initial phase, with a small amplitude. Then, a monotonic convergence occurs rapidly.

— $\alpha_f = \alpha_f^{opt}$: there are very weak oscillations that die out rapidly, and a stable and fast convergence is obtained. Note that from the 10^{th} iteration, all the three previous curves are coincident.

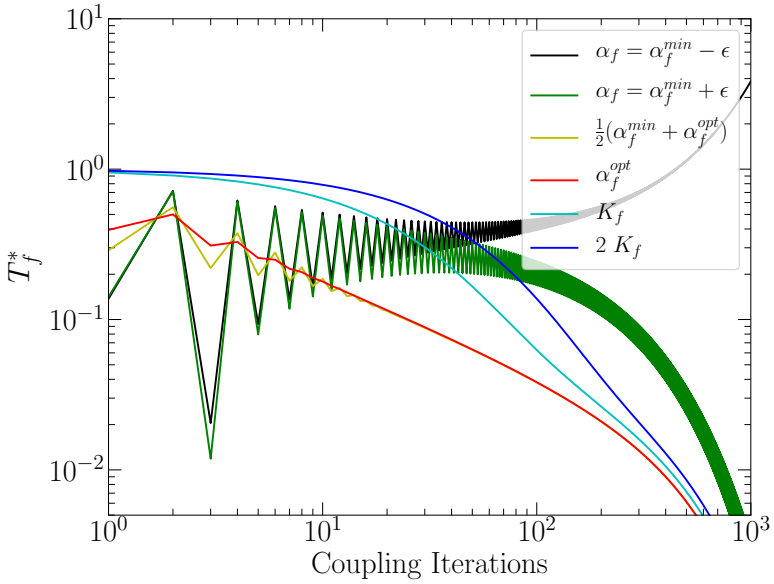

Figure 2.6: Large mesh Fourier number case: convergence history of the interface temperature with six different coupling coefficients.

— $\alpha_f = K_f$: the large Fourier number D_f leads to a significant heat penetration into the fluid domain. As a result, a slow rate of convergence is observed (see Fig. 2.6). Clearly, this coefficient produces an overstable solution and the coupling process is not efficient.

— $\alpha_f = 2K_f$: the same overall conclusions of $\alpha_f = K_f$ can be drawn.

As a whole, the results obtained for the two test cases allow us to validate the theoretical stability analysis described in §2.2.2. The coupling coefficient α_f^{min} clearly represents a bifurcation for the stability of the aerothermal problem of §2.2.2: any coefficient slightly lower than α_f^{min} leads to divergence while any coefficient slightly greater than α_f^{min} leads to convergence. The numerical study also proves the importance of choosing an adequate coupling coefficient for practical CHT computations. One the one hand, if $\alpha_f \gtrsim \alpha_f^{min}$ the coupling process is theoretically stable yet, as the results show, strong oscillations are likely to be observed; although these temporary instabilities eventually disappear in the simplistic computational code we used in these test cases, they could be amplified and lead to divergence in a realistic, three-dimensional CHT simulation employing actual CFD; therefore, α_f needs to be sufficiently far from its stability bound. On the other hand, if an excessively elevated coefficient α_f is chosen for the sake of safety, the convergence rate of the coupling process can be significantly penalised; thus, α_f needs to be sufficiently low. The issue of accurately choosing a coupling coefficient will be further discussed in the conclusion§2.5.

2.2.4 Extension of the stability analysis to more general cases

In section §2.2.2 the stability analysis of a simplified aerothermal problem has been presented and later validated in §2.2.3. A lower stability bound for the coupling coefficient α_f has been found and the result is exact. On the other hand, as it has already been mentioned in the previous sections, the analytical results have been found with several restrictive assumptions, which might limit its relevance in practical CHT simulations; we can name, in particular, the following:

— The aerothermal problem considered in §2.2.2 is one-dimensional; consequently, the characteristic length of the solid domain Λ_s is easily determined; in more complex geometries, identifying a characteristic length is not an easy task and calculating α_f^{min} is more arduous.

— Both domains are supposed to have constant physical properties; furthermore, the fluid domain is discretised with a uniform grid, which is almost never the case in actual CFD.

— On the fluid side, only the conductive heat flux is considered; in some practical applications, other contributions, like radiation, might be present.

— For the fluid domain, a very specific numerical scheme is used, *i.e.*, a time-implicit finite-volume scheme of second order in space; this choice leads to the definition of the mesh Fourier number D_f which perfectly describes and mimics the dynamics of the fluid domain; if another scheme were chosen, a different relation $z = g(z)$ would be obtained instead of Eq. (2.2.30), leading to a different stability bound α_f^{min}.

— The two domains exchange boundary conditions at every fluid iteration, which is never done in practice; the effect of the coupling period on the stability of the coupling process might be important.

— The solid domain is considered to be at steady-state; the stability analysis, therefore, does not cover the case where the transient phase of the CHT simulation needs to be accurately captured.

The objective of this section is to extend, either analytically or empirically, the validity of the theoretical analysis by removing some of the assumptions listed above. In particular, we will focus on the solid domain's heterogeneity (§i.), on the presence of other heat contributions at the fluid-solid interface (§ii.) and on the coupling period (§iii.). Comments concerning the remaining open issues and perspectives are also given (§iv.).

i. *Influence of the solid domain heterogeneity*

In many practical applications, the solid material is not homogeneous and its conductivity might vary from one point to another. It is the case, for instance, of solid domains protected by a thermal barrier coating. Thermal barrier coatings (TBC) are usually composed of ceramic materials and it is the most advanced technology in terms of thermal stability, and its potential of obtaining surface temperature reduction.

Let us replace the homogeneous solid domain of sections §2.2.2 and §2.2.3 with a more complex material, composed of a metallic plate of thickness Λ_s and conductivity

λ_s, and a ceramic top-coat of thickness e and conductivity λ_{TBC}. The temperature distribution between $x = 0$ and $x = -(\Lambda_s + e)$ is no longer a straight line and, at first glance, the aerothermal problem is more complicated. However, we can take advantage of the fact that the domain is at steady-state to express the heat flux penetrating the solid medium as:

$$q_s = \frac{\lambda_{TBC}}{e}\left(T_{0^-} - T_{x=-e}\right) = \frac{\lambda_s}{\Lambda_s}\left(T_{x=-e} - T_{x=-(\Lambda_s+e)}\right) \ . \tag{2.2.41}$$

It is possible to eliminate $T_{x=-e}$ from Eq. (2.2.41) and to express the heat flux only as a function of T_{0^-} and $T_{x=-(\Lambda_s+e)}$ as follows:

$$q_s = \frac{\left(T_{0^-} - T_{x=-(\Lambda_s+e)}\right)}{\frac{e}{\lambda_{TBC}} + \frac{\Lambda_s}{\lambda_s}} \ . \tag{2.2.42}$$

In other words, the heterogeneous domain formed by two distinct materials can be replaced by an equivalent material of total thermal resistance:

$$\frac{1}{K_{tot}} = \frac{\Lambda_s}{\lambda_s} + \frac{e}{\lambda_{TBC}} \ . \tag{2.2.43}$$

It can be easily verified that replacing λ_s/Λ_s with K_{tot} in Eq. (2.2.15), leads to the exact same development of the stability analysis and, therefore, to the exact same results concerning α_f^{min}. The reasoning can of course be extended to any solid domain formed by a series of N materials of different thickness and conductivity:

$$\frac{1}{K_{tot}} = \sum_{j=1}^{N} \frac{e_i}{\lambda_i} \ , \tag{2.2.44}$$

or, in case of a continuous distribution of $\lambda(x)$,

$$\frac{1}{K_{tot}} = \int_0^{\Lambda_{tot}} \frac{\mathrm{d}x}{\lambda(x)} \ . \tag{2.2.45}$$

ii. *Influence of other heat contributions*

In §2.2.2, only the heat conduction is considered in the fluid domain. However, other heat contributions may be present and need to be taken into account, since they might have an impact on both the physical solution of the aerothermal problem and its stability. It is the case, for instance, of radiation. Radiation can play a key role in the design and optimisation of applications, since it is the dominant mode of heat transfer involving high temperatures. Thus, thermal radiation coupled with convection and conduction can have extensive real-world applications when accurate heat transfer predictions are needed, such as re-entry vehicles, turbomachinery, high temperature heat exchangers, combustion chambers, furnaces, etc. The analysis that follows has been the object of the recent publication by Errera et al. (2020) that we have mentioned at the beginning of the chapter, and all the details can be found there.

Let us consider a new aerothermal problem, identical to the one described in §2.2.2 except for the fact that the fluid medium is crossed by radiation of non negligible intensity. Let the solid medium be opaque, and the fluid one fully transparent; with

these assumptions, the heat diffusion equation of both domains remains the same, *i.e.*, identical to Eqs. (2.2.5) and (2.2.6). In fact, the only equation modified by the presence of an additional heat contribution is in this case the Robin condition at the fluid-solid interface, which becomes:

$$\hat{q}_s + \alpha_f \hat{T}_s = -q_f + \alpha_f T_f - \Phi^R \ , \tag{2.2.46}$$

where q_f is the conductive flux at the first fluid cell and Φ^R is the radiative flux. Supposing that radiation originates from a source at a constant temperature T_{ref}, and supposing that the difference with the fluid temperature at the interface T_f always remains small, it is possible to linearise Φ^R and to express it as follows:

$$\Phi^R = h^R \left(T_f - T_{ref} \right) \ , \tag{2.2.47}$$

where h^R is the coefficient of radiant heat transfer. In discretised form, the Robin condition (2.2.19) becomes after some arrangements:

$$\left(K_s + \alpha_f \right) T_{0^-}^{n+1} = K_f T_1^{n+1} + \left(\alpha_f - K_f - h^R \right) T_{0^+}^{n+1} + K_s \left(T_{ext} + \frac{q_{ext}}{\alpha_{ext}} + h^R T_{ref} \right) \ , \tag{2.2.48}$$

while all the remaining equations forming the discrete system (2.2.21) remain identical. Injecting the normal modes (2.2.24) into Eqs. (2.2.12) and (2.2.48), we obtain a new $z = g(z)$ relation:

$$z = \frac{\frac{K_f}{2} \left[2 + \frac{z-1}{\mathrm{D}_f z} - \sqrt{\left(2 + \frac{z-1}{\mathrm{D}_f z} \right)^2 - 4} \right] + \left(\alpha_f - K_f - h^R \right)}{K_s + \alpha_f} = g(z) \ , \tag{2.2.49}$$

which, with $z = -1$, gives a new stability bound α_{f-R}^{min} that can be expressed as:

$$\alpha_{f-R}^{min} = \frac{K_f}{1 + \sqrt{1 + 2\mathrm{D}_f}} - \frac{K_s}{2} + \frac{h^R}{2} \ . \tag{2.2.50}$$

Since, by definition, $h^R \geq 0$, we can see that α_{f-R}^{min} is always greater than the classical α_f^{min} (see Eq. (2.2.33)), indicating that radiation always plays a destabilising effect on the coupling process. If $h^R \approx K_s$, we can actually see that $\alpha_{f-R}^{min} \approx \alpha_f^{opt}$; in other words, if radiation is physically and numerically present, but not taken into account for choosing a proper α_f, a suitable coupling coefficient like α_f^{opt} that would normally enhance stability, could actually become unstable.

Finally, if following Eq. (2.2.35) we have:

$$\alpha_f^{min} = \frac{K_s}{2} \left(\mathrm{Bi}_\nu - 1 \right) \ , \tag{2.2.51}$$

we can also define a new Biot number which includes the effect of radiation:

$$\mathrm{Bi}_\nu = \frac{K_f}{K_s} \frac{2}{1 + \sqrt{1 + 2\mathrm{D}_f}} + \frac{h^R}{K_s} \tag{2.2.52}$$

iii. *Influence of the coupling period*

In the theoretical study of §2.2.2, only the case where the fluid and solid domains exchange boundary conditions at every time-step is considered. As we have seen,

this choice enables us to perform a stability analysis and to find numerous interesting (and, above all, exact) results. However, in the vast majority of CHT computations of interest, the *coupling period*, *i.e.*, the number of temporal iterations between two consecutive coupling instances, is much greater than unity. This is understandably justified by the fact that the fluid time-step is usually very small in actual CFD computations. In this section, we aim at better understanding the impact of the coupling period on the stability of CHT problems. These results have been the object of a recent publication (currently under review) that we have mentioned at the beginning of the chapter.

First of all, let us analyse the problem from a mathematical point of view. We consider the exact same aerothermal problem of §2.2.2, except for the fact that the two domains exchange boundary conditions every p fluid iterations. Let Δt_f be the fluid time-step and Δt_c the coupling time-step, so that $\Delta t_c = p\Delta t_f$. The temperature of a generic grid point j at a generic time index n, can therefore be written as:

$$T_j^n = T_j^{Np+k} \ , \tag{2.2.53}$$

where $N = \{0, 1, 2, ...\}$ represents the coupling iteration and $k = \{1, 2, 3, ..., p\}$ denotes the fluid sub-iteration. The Dirichlet condition on the fluid side of the interface can thus be written as:

$$T_{0^+}^{Np+k} = T_{0^-}^{Np} \quad k = \{1, 2, 3, ..., p\} \ , \tag{2.2.54}$$

indicating that T_{0^+} remains constant throughout the fluid sub-iterations between two consecutive coupling instances. Note that on T_{0^-} there is no index k, since in the solid domain there are no sub-iterations, and the temperature does not change before the following exchange of boundary conditions. The heat diffusion equation in the fluid domain can be written as:

$$T_j^{Np+k+1} - T_j^{Np+k} = \mathrm{D}_f \left(T_{j-1}^{Np+k+1} - 2T_j^{Np+k+1} + T_{j+1}^{Np+k+1} \right) \quad j = \{1, 2, 3, ...\} \ , \tag{2.2.55}$$

with $\mathrm{D}_f = a_f \Delta t_f / \Delta x_f^2$, while in the solid domain we have:

$$T_{j-1}^{p(N+1)} - 2T_j^{p(N+1)} + T_{j+1}^{p(N+1)} = 0 \quad j = \{-1, -2, ... - J\} \ , \tag{2.2.56}$$

where we can observe once more that the absence of the sub-iteration index k. Finally, the Robin condition can be rewritten as follows:

$$\frac{\lambda_s}{\Lambda_s} \left(T_{0^-}^{p(N+1)} - T_{-J}^{p(N+1)} \right) + \alpha_f T_{0^-}^{p(N+1)} = \frac{\lambda_f}{\nu \Delta x_f} \left(T_1^{p(N+1)} - T_{0^+}^{p(N+1)} \right) + \alpha_f T_{0^+}^{p(N+1)} \ . \tag{2.2.57}$$

Mathematically, the challenge is to propose a new decomposition in normal modes of the temperature T_j^{Np+k}, as in Eq. (2.2.24) for the case $p = 1$, which would allow us to perform a similar stability analysis. It is not clear if such normal modes exist and if a new analytical expression for α_f^{min} can be found for $p > 1$.

In the following, we propose to get a better insight of the effect of $p > 1$ on the stability of the coupling process numerically. For this purpose, the same computational code described in §2.2.3 is used. We consider an aerothermal problem the fundamental parameters of which are summarised in Table 2.5. The reader will notice that this test case is identical to the first one analysed in §2.2.3, except for the fact that $p = 10$ and the time-step has been divided by ten, so that the coupling

Fluid				Solid					Numerics			
λ_f	a_f	Λ_f	$T_{x=\Lambda_f}$	λ_s	Λ_s	α_{ext}	T_{ext}	q_{ext}	Δx_f	Δt_f	CHT period	Fo
0.02	$2.^{e-05}$	0.05	300	20	1	∞	500	-	1.25^{e-04}	0.001	10	0.08

Table 2.5: Test case with $p = 10$: physical and numerical parameters.

period, expressed in seconds, is the same between the two cases. In other words, we attempt to maintain the same level of aerothermal interaction between the two cases.

As was done in §2.2.3, we perform six different calculations using six coupling coefficients, strategically located with respect to the value of α_f^{min}. Of course, for $p = 10$, we have no analytical expression of the lower stability bound. As a first hypothesis, we might consider calculating the mesh Fourier number as $\mathrm{D}_f = a_f \Delta t_c / \Delta x_f^2$, which, injected into Eq. (2.2.33) together with the physical and numerical parameters of Table 2.5, gives $\alpha_f^{min} = 16.04$, *i.e.*, the same value of §2.2.3. This hypothesis implies that dividing Δt_c into $p = 10$ sub-iterations has no effect on the stability of the coupling process, as long as Δt_c remains the same. The convergence history of the interface temperature, non-dimensionalised as in §2.2.3, for the six coupling coefficients is shown in Fig. 2.7. As can be seen, the CHT simulation always converges, and only some weak oscillations are observed for $\alpha_f \approx \alpha_f^{min}$. These results clearly indicate that the lower stability bound has moved, and, more precisely, decreased; therefore, the value of p has a strong impact on the stability of the coupling process and the theoretical study of §2.2.2 is no longer valid.

So as to systematically study the influence of p on stability, we perform a series of numerical simulations which aim at determining an empirical law for α_f^{min}. We consider, in particular, three study cases, which are presented in Table 2.6, where all the coupling parameters are obtained considering $p = 1$, *i.e.*, using the results of the stability analysis of §2.2.2. As can be seen, the three cases exhibit very disparate parameters and, therefore, different stability limits. However, for all cases the mesh Fourier number D_f is the same. For each of these cases, eight different splitting levels of the coupling period Δt_c have been adopted, namely $p = \{1, 2, 4, 5, 10, 20, 40, 50\}$; for each p, a different fluid time-step $\Delta t_f = \Delta t_c / p$ is obtained; for each case and for each value of p, we perform a dichotomic search of the coefficient α_f^* such that the coupling is unstable for $(1 - 0.01\mathrm{sign}(\alpha_f^*))\alpha_f^*$, and stable for $(1 + 0.01\mathrm{sign}(\alpha_f^*))\alpha_f^*$; this α_f^* represents the empirical lower stability bound, *i.e.*, the actual α_f^{min}.

Figure 2.8 presents the evolution of α_f^{min} as a function of p. It can be noticed that:

— As expected, for $p = 1$ the value of α_f^{min} coincides with the theoretical one of Eq. (2.2.33) shown in Table 2.6.

— α_f^{min} is always a decreasing function of p, which means that splitting the coupling period always has a stabilising effect;

— All the curves seem to exhibit a horizontal asymptote for approximately $p = 20$. This indicates that stability is affected only until a certain value of p, and that

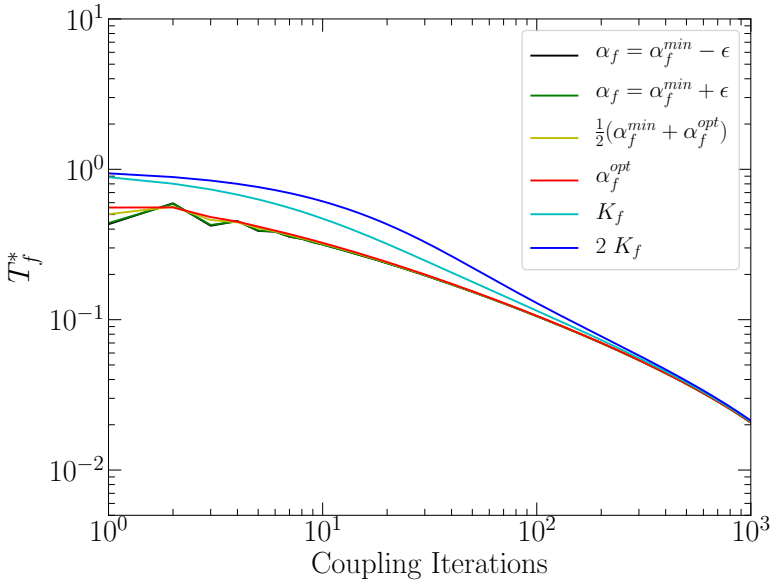

Figure 2.7: Test case with $p = 10$: convergence history of the interface temperature with six different coupling coefficients.

	Fluid		Solid			Numerics			Coupling		
	a_f	Λ_f	λ_s	Λ_s	β	Δx_f	Δt_c	Fo	D_f	Bi_ν	α_f^{min}
Case 1	$2.^{e-05}$	0.5	2	2	1	0.0001	0.1	0.008	1.99	12.37	5.69
Case 2	1.59^{e-05}	0.5	5	0.21	1	0.002	0.05	0.032	1.99	1.04	0.47
Case 3	7.59^{e-05}	1	1	0.1	1	0.004	0.4	0.0318	1.99	0.62	-1.91

Table 2.6: Study cases for $p > 1$: physical, numerical and coupling parameters.

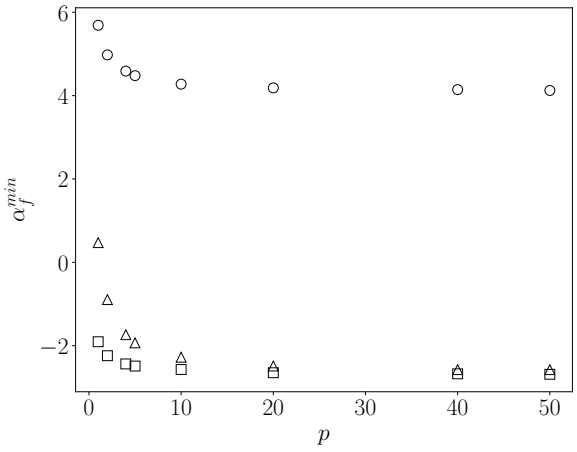

Figure 2.8: Evolution of the stability limit as a function of p: ○, Case 1; △, Case 2; □ Case 3.

it is futile to split the coupling period beyond that limit;

— Increasing p can radically change the nature of the CHT process; Case 2, for instance, exhibits a Biot number $\mathrm{Bi}_\nu > 1$ indicating that a coupling coefficient $\alpha_f^{min} > 0$ is necessary for stability; when $p = 2$, it can be seen from Fig. 2.8 that the actual stability bound is lower than zero, indicating that even Dirichlet-Neumann conditions would guarantee stability.

Another way of examining the modification of the stability bound is to analyse the Biot number $\mathrm{Bi}_\nu(p) = 2\alpha_f^{min}(p)/K_s + 1$; since $\mathrm{Bi}_\nu > 0$, it is possible to calculate a normalised value $\overline{\mathrm{Bi}}_\nu(p) = \mathrm{Bi}_\nu(p)/\mathrm{Bi}_\nu(p=1)$, which is shown in Figure 2.9 for the same three test cases. As can be seen, numerical uncertainties aside, all the points coincide. Since the only common parameter to all these cases is the mesh Fourier number D_f, it can be reasonably assumed that $\overline{\mathrm{Bi}}_\nu$ only depends on D_f and p.

So as to corroborate this hypothesis, several other test cases are performed with different physical and numerical properties; the results obtained for the normalised Biot number are shown in Figure 2.10. We can observe that:

— Some values of D_f occur twice; it is the case of $\mathrm{D}_f = 2$ and $\mathrm{D}_f = 80$, for which two simulations with very different parameters were performed whilst keeping the same Fourier number, as was done for the three test cases of Table 2.6. As can be seen, in both cases the evolution of $\overline{\mathrm{Bi}}_\nu$ is the same, empirically showing that the evolution of the normalised Biot number only depends on p and D_f. If this is true, keeping in mind the definition of Bi_ν (see Eq. (2.2.34)), it is thus possible to write:

$$\overline{\mathrm{Bi}}_\nu = \frac{\mathrm{Bi}_\nu(p)}{\mathrm{Bi}_\nu(p=1)} = \frac{1+\sqrt{1+2\mathrm{D}_f}}{2} f(p, \mathrm{D}_f) \ , \tag{2.2.58}$$

where $f(p, \mathrm{D}_f)$ is a function that remains, unfortunately, unknown.

— For a given p, $\overline{\mathrm{Bi}}_\nu$ is a decreasing function of D_f; this indicates that dividing the coupling period into several sub-iterations is particularly advantageous when

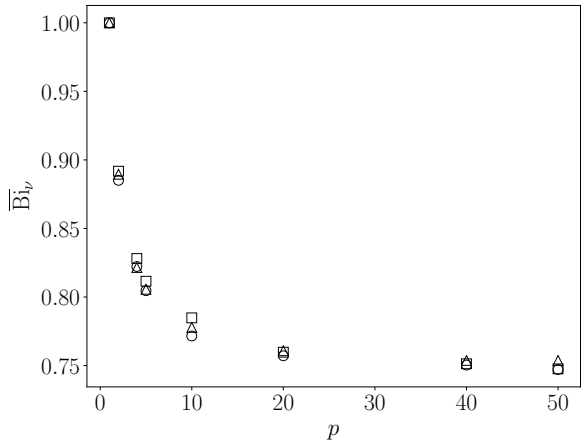

Figure 2.9: Evolution of the normalised Biot number $\overline{\mathrm{Bi}}_\nu$ as a function of p: ○, Case 1; △, Case 2; □ Case 3.

the Fourier number is large. Indeed, a large $\mathrm{D}_f = a_f \Delta t_f / \Delta x_f^2$ indicates that the time-step is significant with respect to the cell size Δx_f; it is intuitive to imagine that if Δt_f is reduced by increasing p, the nature of the CHT process might considerably change; as can be seen from Fig. 2.10, when $\mathrm{D}_f \approx 1000$, the normalised Biot number is reduced by half for $p = 40$. On the other hand, a small D_f indicates that the time-step is small compared to Δx_f; it is intuitive to imagine that reducing Δt_f even more might have no impact on the nature of the aerothermal coupling; as can be seen from Fig. 2.10, when $\mathrm{D}_f \approx 0.1$, $\overline{\mathrm{Bi}}_\nu$ essentially remains the same as p increases.

— The asymptote of $\overline{\mathrm{Bi}}_\nu$ is always obtained from the same value of p, namely $p \approx 20$, regardless of the Fourier number. This is somewhat counter-intuitive: it could be expected that the stability of the coupling process benefits from an increasing p as long as Δt_f is reduced to the point that $\mathrm{D}_f = a_f \Delta t_f / \Delta x_f^2 \sim 1$. It is evidently not the case, and a possible cause might be the limited spatial order of the numerical scheme used for the fluid diffusion.

— The curves for $\mathrm{D}_f = 800$ and $\mathrm{D}_f = 50000$ are extremely similar; this suggests that not only is there an asymptote for $p \to \infty$ but also for $\mathrm{D}_f \to \infty$. The curves seem to show that $\lim_{p\to\infty} \lim_{\mathrm{D}_f \to \infty} \overline{\mathrm{Bi}}_\nu = 0.5$.

In conclusion, no exact expression for α_f^{min} when $p > 1$ has been found. Instead, a numerical investigation has been performed, showing, however, some interesting results. The evolution of the normalised Biot number, which only depends on the Fourier number and on p, appears to be too curious for an analytical result not to exist. Leaving this mathematical challenge aside, it can be noticed that the lower stability bound α_f^{min} for $p = 1$ is in any case the most elevated and, therefore, a conservative choice if $p > 1$ and $\alpha_f^{min}(p)$ is not known. For the time being, α_f^{min} can be computed through Eq. (2.2.33) replacing the fluid time-step Δt_f in the definition of D_f with the coupling time-step Δt_c; this will lead to an inevitable over-estimation of the stability bound, yet will guarantee stability. This is what is done in the remaining of this work, whenever $p > 1$.

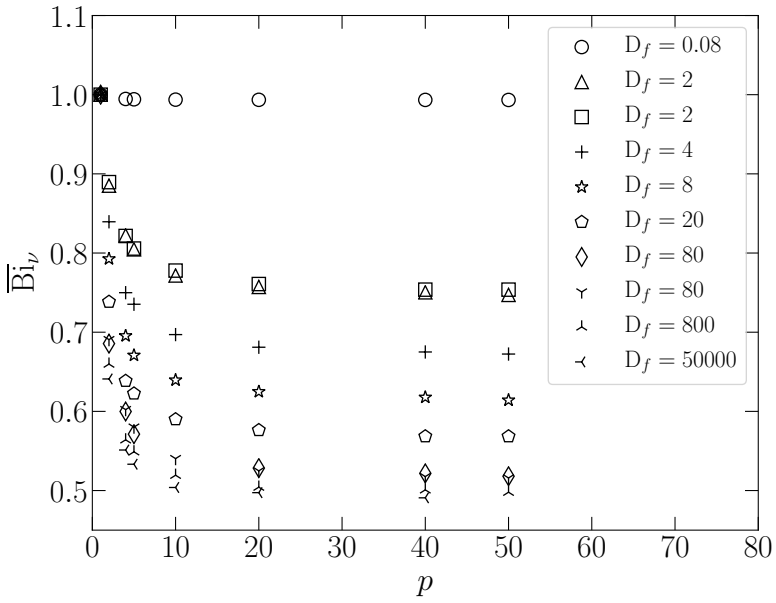

Figure 2.10: Evolution of the normalised Biot number $\overline{\mathrm{Bi}}_\nu$ as a function of p for several test cases exhibiting different mesh Fourier numbers D_f.

iv. *Open issues and perspectives*

In the previous paragraph several analyses have been performed, leading us to a better understanding of how the theoretical results obtained in §2.2.2 can be either extended or used in practice. Nevertheless, several issues remain open as future perspectives.

The main limit of the stability analysis is the one-dimensional character of the study. This limit does not really seem to concern the fluid domain, for which very local physical and numerical properties are used for calculating the coupling coefficients of interest such as α_f^{min} and α_f^{opt}; assuming, for instance, that on the fluid side the main error mode impacting the stability of the coupling process is the one orthogonal to the exchange surface, and that the characteristic length is, therefore, the first cell size, seems to be a realistic assumption. On the other hand, since the solid domain is at steady-state, what happens at the fluid-solid interface is perceived by the whole medium; therefore, the characteristic length of the solid (called Λ_s, in this chapter) needs to be carefully chosen, as it must represent the entire domain; in a one-dimensional problem, the task is straightforward, and Λ_s is simply the length of the domain; in the case of a complex geometry such as the one of the SACOC that we will discuss in Part III, choosing a representative Λ_s is not as easy. It is certainly possible, for the sake of safety, to choose the largest dimension, leading to the largest possible value of α_f^{min}; otherwise, it is possible to rely on the value of α_f^{opt} which, as pointed out in §2.2.2, does not depend on any solid property; despite this, attention needs to be paid, since if the thermal resistance of the solid domain is very important, α_f^{opt} might be very close to the stability bound. A possible way of commencing to address the issue, might be to increase the complexity of the code described in §2.2.3, in order to perform some simple two-dimensional diffusion problems with a solid of

varying thickness; numerical investigations similar to those carried out in §iii., might help finding the most suitable characteristic length for the solid domain.

Another limit of the stability analysis is the use of a very specific numerical scheme for the heat diffusion in the fluid domain. More precisely, since the work of Errera and Chemin (2013), we have always adopted a time-implicit scheme of second order in space and first order in time, which CFD codes do not always employ; the scheme was obviously chosen because it gives a direct relation for the spatial amplification factor κ_f, once the temperature is expressed in normal mode form. Of course, if more complex schemes are used, it could be arduous or even impossible to obtain any analytical results; on the other hand, with a systematic numerical study it would at least be possible to understand if the α_f^{min} we currently calculate is a safe choice or not if a higher-order scheme is employed.

Finally, we must stress that the results obtained for the normalised Biot number as a function of the splitting of the coupling period suggest the existence of an analytical solution. Our attempts, however, have not been fruitful.

2.3 CHT implementation in *elsA* - *Z-set*

The previous section has allowed us to lay the theoretical foundations of the coupling approach, described in §2.1, that we have chosen for our simulations. Now, the objective is to describe in detail the numerical environment in which our actual CHT computations have been performed. In §2.3.1 the fluid solver *elsA* is presented, the Reynolds-averaged Navier Stokes equations are detailed as well as the numerical schemes and turbulence models used for the different study configurations. In §2.3.2 the same is done for the solid solver *Z-set*. Finally, in §2.3.3, details about the treatment of the fluid-solid interface are given.

2.3.1 Fluid solver: *elsA*

For the fluid domain we have chosen the multi-purpose CFD software package *elsA* (see Cambier and Gazaix, 2002) for solving the steady-state Reynolds-Averaged Navier Stokes (RANS) equations; the choice of this fluid modelling is motivated by both the fact that our primary interest is to investigate the performance of the SACOC at permanent regime, and for its reduced cost, which allows us to simulate complex industrial configurations at elevated Reynolds numbers.

In form of partial derivative equations, the compressible RANS conservation laws for mass, momentum and energy write:

$$\frac{\partial \overline{\rho}}{\partial t} + \nabla \cdot \overline{\rho}\widetilde{\mathbf{v}} = 0 \ , \tag{2.3.1}$$

$$\frac{\partial \overline{\rho}\widetilde{\mathbf{v}}}{\partial t} + \nabla \cdot \left(\overline{\rho}\widetilde{\mathbf{v}} \otimes \widetilde{\mathbf{v}}\right) = \nabla \cdot \left(\overline{\boldsymbol{\tau}} + \boldsymbol{\tau}^t - \overline{p}\mathbb{I}\right) \ , \tag{2.3.2}$$

$$\frac{\partial \overline{\rho}\left(\widetilde{E}+k\right)}{\partial t} + \nabla \cdot \left[\overline{\rho}\left(\widetilde{E}+k\right)\right] = \nabla \cdot \left[\left(\overline{\boldsymbol{\tau}} + \boldsymbol{\tau}^t\right) \cdot \widetilde{\mathbf{v}} - \left(\overline{\mathbf{q}} + \mathbf{q}^t\right)\right] \ . \tag{2.3.3}$$

In these equations, $\mathbf{v}$ indicates the absolute velocity field; ρ, p, $\boldsymbol{\tau}$ and $\mathbf{q}$ represent the mass density, the static pressure, the stress tensor and the heat flux vector, respectively; E is the total energy per mass unit, *i.e.*, the sum of the internal energy

e and kinetic energy $1/2\mathbf{v}^2$. The fluid is considered to be a calorifically perfect gas with heat capacity ratio $\gamma = 1.4$ and specific gas constant $R = 287$ J/(kg K); the internal energy is therefore expressed as:

$$e = c_v T \ , \tag{2.3.4}$$

where c_v is the specific heat at constant volume, and T the static temperature; the pressure, instead, is calculated as:

$$p = R\rho T \ . \tag{2.3.5}$$

Furthermore, the fluid is Newtonian and the stress tensor is given by the law:

$$\boldsymbol{\tau} = 2\mu\boldsymbol{\mathcal{D}} - \frac{2}{3}\mu\nabla\cdot\mathbf{v} \ , \tag{2.3.6}$$

where $\boldsymbol{\mathcal{D}}$ is the tensor of the rates of deformation, and μ is the dynamic viscosity calculated through the Surhterland law and, therefore, temperature dependent; the heat flux vector, instead, is given by the Fourier law:

$$\mathbf{q} = -\lambda\nabla T \ , \tag{2.3.7}$$

where λ is the thermal conductivity computed with $\mathrm{Pr} = 0.72$.

Equations (2.3.1)-(2.3.3) are obtained by applying the Reynolds average $\overline{(\cdot)}$ to the instantaneous Navier-Stokes equations (1.1.1)-(1.1.3). For flows with variable density, as seen in §1.1.1, it is convenient to introduce the Favre average $\widetilde{(\cdot)}$. Due to the introduction of these averages into the Navier-Stokes equations, a series of additional terms of correlation appear, namely:

— Turbulent kinetic energy: $k = \frac{1}{2}\overline{\rho\mathbf{v}''^2}/\overline{\rho}$;

— Reynolds tensor: $\boldsymbol{\tau}^t = -\overline{\rho\mathbf{v}''\otimes\mathbf{v}''}$;

— Enthalpy turbulent diffusion flux: $\mathbf{q}^t = \overline{\rho\mathbf{v}''h''}$.

These unknown terms represent the effect of turbulence on the mean flow, and they need to be modelled to close the system of RANS equations (2.3.1)-(2.3.3). The Reynolds tensor, considering the Boussinesq hypothesis, is expressed as:

$$\boldsymbol{\tau}^t = 2\mu^t\boldsymbol{\mathcal{D}} - \frac{2}{3}\left(\rho k + \mu^t\nabla\cdot\mathbf{v}\right) \ , \tag{2.3.8}$$

where μ^t is the so-called turbulent viscosity; the turbulent heat flux, instead, can be written as:

$$\mathbf{q}^t = -\frac{c_p\mu^t}{\mathrm{Pr}^t}\nabla T \ , \tag{2.3.9}$$

where c_p is the heat capacity at constant pressure, and Pr^t is the turbulent Prandtl number. Thanks to the Boussinesq hypothesis, it is thus possible to close the RANS equations by modelling three scalar quantities, *i.e.*, k, μ^t and Pr^t. For the turbulent Prandtl number, we simply consider a constant value of $\mathrm{Pr}^t = 0.9$. For the turbulent kinetic energy and the turbulent viscosity, we employ instead two different transport models.

The former is the $k-\omega$ model of Menter (1993) with Shear-Stress Transport (SST) correction. With this model, two additional transport equations are added to

Eqs. (2.3.1)-(2.3.3), one for the turbulent kinetic energy k and one for the specific rate of dissipation $\omega = \epsilon/(C_\mu k)$ (see Wilcox, 1988), where ϵ is the turbulent dissipation rate and C_μ a constant. Once the equations are solved and k and ω are known, the turbulent viscosity is simply calculated as $\mu^t = \rho k/\omega$. The $k-\omega$ of Menter (1993) preserves the good behaviour of the model of Wilcox (1988) in the inner region of the boundary layer, while switching to the $k-\epsilon$ model of Launder and Sharma (1974) in the outer region and in wakes; the SST correction, instead, allows to correct the ratio $\tau/(\rho k)$ which, in case of positive pressure gradients, can be over-estimated when two-equation turbulent models are used. This model has been used in the simulations described in §6.

The latter is the $k-\ell$ model of Smith (1990), later corrected and improved by Smith (1994). It is a two-equation model transporting the turbulent kinetic energy k and the characteristic length of the large turbulent scales ℓ. Once k and ℓ are known, μ^t can be easily deduced. According to Smith (1995), the model has a low sensitivity to the distribution of the near-wall grid points, and allows to take into account compressibility effects better than $k-\epsilon$ models. This model has been used in the simulations described in §5, characterised by a high Mach number in the fan dub-domain.

The transport equations are solved by a time-implicit cell-centred finite-volume scheme on structured grids. Integration in time is carried out with the backward Euler scheme; since only a steady-state solution is sought, it is a time-marching scheme in which the time-step is locally computed in every fluid cell according to a Courant-Friedrichs-Lewy (CFL) number. Spatially, convective fluxes are computed with a second-order centred Jameson scheme.

In case of no-slip walls, on which the zero-velocity $\mathbf{v} = 0$ boundary condition is prescribed, the meshes are always refined in the wall-normal direction so that, in wall-units, the first grid point is at a distance of $y^+ = y\rho u_\tau/\mu \sim 1$. The boundary layer is thus fully solved and no wall-models are needed.

2.3.2 Solid solver: *Z-set*

For the solid domain we have chosen the software package *Z-set* (see Garaud et al., 2019), which can solve a large variety of problems of material and structural mechanics; in this work, we use a very small part of the software since we are only interested in the steady-state heat diffusion of a non-deformable, isotropic and homogeneous solid domain.

In this context, the evolution of the internal energy contained into an arbitrary volume $\mathcal{V}$ delimited by the surface $\mathcal{S}$ can be written as follows:

$$\int_{\mathcal{V}} \rho \frac{\partial E}{\partial t} \mathrm{d}\mathcal{V} = \int_{\mathcal{V}} \phi \mathrm{d}\mathcal{V} + \int_{\mathcal{S}} \mathbf{q} \cdot \hat{\boldsymbol{n}} \mathrm{d}\mathcal{S} \ , \tag{2.3.10}$$

where ρ is the mass density, ϕ represents the internal volumetric sources, $\mathbf{q}$ the heat flux crossing the surface and $\hat{\boldsymbol{n}}$ the inward-pointing normal of the surface $\mathcal{S}$. As can be seen, the energy equation is independent and decoupled from the mechanics of the medium. Assuming that there are no chemical or physical transformations of the material, it is possible to relate the internal energy to its temperature through the equation:

$$\frac{\partial E}{\partial t} = C \frac{\partial T}{\partial t} \ , \tag{2.3.11}$$

where C is the thermal capacity of the material; furthermore, according to Fourier's law, we have:

$$\mathbf{q} = -\lambda \nabla T \ , \tag{2.3.12}$$

which is identical to Eq. (2.3.7); since the medium is supposed to be isotropic and homogeneous, the thermal conductivity λ is a scalar constant; finally, the volumetric sources ϕ are supposed to be everywhere zero. Equation (2.3.10) thus becomes:

$$\int_{\mathcal{V}} \rho C \frac{\partial T}{\partial t} \mathrm{d}\mathcal{V} = \int_{\mathcal{S}} (-\lambda \nabla T) \cdot \hat{\boldsymbol{n}} \mathrm{d}\mathcal{S} \ , \tag{2.3.13}$$

or, transforming the surface integral into a volumetric one by applying the divergence theorem,

$$\int_{\mathcal{V}} \left[\rho C \frac{\partial T}{\partial t} + \nabla \cdot (-\lambda \nabla T) \right] \mathrm{d}\mathcal{V} = 0 \ . \tag{2.3.14}$$

Since the volume $\mathcal{V}$ is arbitrary and the thermal conductivity is assumed to be a constant, we can write:

$$\rho C \frac{\partial T}{\partial t} = \lambda \nabla^2 T \ , \tag{2.3.15}$$

which, once the steady-state of the medium is considered, takes its well-known final form:

$$\nabla^2 T = 0 \ . \tag{2.3.16}$$

Equation (2.3.16) is rather simple; the mass density ρ and the thermal capacity C of the material do not play any role in the thermal problem and, therefore, do not need to be defined; on the other hand the thermal conductivity λ, although not present in Eq. (2.3.16), is of fundamental importance, since it determines the intensity of the temperature gradient ∇T at the boundary once an external heat flux $\mathbf{q}$ is imposed through a Neumann or Robin boundary condition. Equation (2.3.16) is solved by *Z-set* using the finite-element method.

2.3.3 Interface treatment

At every coupling instance, the solid and fluid domain exchange their boundary conditions at the interface. The stability analysis described in §2.2 has shown that Dirichlet-Robin boundary conditions are likely to stabilise any aerothermal problem provided that the relaxation coefficient is sufficiently elevated. In all the CHT simulations performed in this work, we therefore always employ the following interface conditions:

$$\begin{aligned} \hat{q}_s + \alpha_f \hat{T}_s &= -q_f + \alpha_f T_f \\ \hat{T}_f &= T_s \ , \end{aligned} \tag{2.3.17}$$

where the same notation of §2.2.1 for Eq. (2.2.4) is used here. As seen in §2.2, the choice of α_f is of fundamental importance. In this work, we compute α_f according to Eq. (2.2.32) that we rewrite here:

$$\alpha_f^{opt} = \frac{K_f}{\left(1 + \sqrt{1 + 2\mathrm{D}_f}\right)} \ . \tag{2.3.18}$$

The choice is motivated by the following considerations:

— According to the stability analysis (see §2.2.2), the relation $\alpha_f^{opt} > \alpha_f^{min}$, where α_f^{min} is the lower stability bound, is always verified; in other words, α_f^{opt} guarantees the stability of the coupling process.

— As seen in §2.2.2, $\alpha_f^{opt} - \alpha_f^{min} = K_s/2$, where $K_s \propto \lambda_s/\Lambda_s$ with λ_s the thermal conductivity of the solid medium and Λ_s its characteristic length; now, since in all our CHT cases $\lambda_s \sim 100$ W/(m K) and $\Lambda_s \sim 0.01$ m, α_f^{opt} thus ensures a sufficient margin of safety.

— As seen in the test cases of §2.2.3, not only does α_f^{opt} offer stability yet also a fast convergence characterised by low oscillations of the solution.

— The coupling coefficient α_f^{opt} only depends on physical and numerical properties of the fluid domain, namely: the mesh grid size at the wall Δy, the time-step Δt_f and the thermal diffusivity $a_f = \lambda_f / \left(\rho_f C_{p_f}\right)$; these properties are locally defined and generally vary from one fluid cell to the other (even Δt_f since we employ a time-marching scheme, see §2.3.1); therefore, α_f^{opt} is a local coupling coefficient which adjusts to the stability requirements of every fluid cell.

The transfer of information between *Zset* and *elsA* is performed by the coupling library *CWIPI* (see CWIPI, 2020). As mentioned in the Introduction, one of the main advantages of using partitioned algorithms in CHT is that the fluid and solid domains can be separately discretised, which generally allows for a much less refined grid for the solid domain to be employed; at the interface, therefore, *CWIPI* aggregates the information received by the two solvers (both parallelised), and performs spatial interpolation from one grid to the other, while taking into account the different numerical methods used by the two codes. In this work, for the benefit of simplicity and to the detriment of computing efficiency, we only use coincident meshes for the two domains; note that a small interpolation is nevertheless needed to transfer the solid properties from the cell nodes (since *Z-set* employs a finite-element scheme) to the centres (since *elsA* employs a cell-centred finite-volume scheme) and vice-versa.

Considering the governing equations of the fluid domain (2.3.1)-(2.3.3), the governing equation of the solid domain (2.3.16), the Robin-Dirichlet boundary conditions (2.3.17) and the coupling coefficient (2.3.18), the coupling algorithm described in §2.1 can be rewritten more in detail:

1. The temperature on the solid side of the coupling interface computed by *Z-set* is interpolated and transferred by *CWIPI* to the fluid interface, where a Dirichlet boundary condition is prescribed.

2. The fluid solver *elsA* integrates Equations (2.3.1)-(2.3.3) over a pre-determined number of time iterations (usually between 10 and 100); then, on the fluid side of the interface, the wall heat flux and the coupling coefficient (according to Eq. (2.3.18)) are computed.

3. The wall heat flux and the coupling coefficient are transferred by *CWIPI* to the solid side of the interface, where the Robin condition (2.3.17) is prescribed.

4. *Z-set* solves Eq. (2.3.16) and determines a new temperature field on the solid side of the coupling interface.

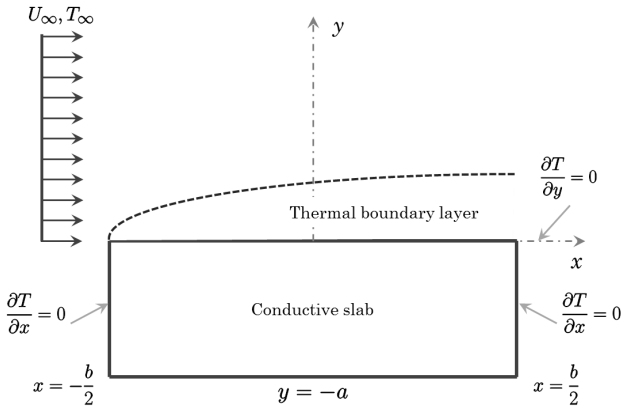

Figure 2.11: Laminar flat plate (reproduction of figure by Vynnycky et al. (1998)).

2.4 Validation

The objective of this section is to validate the numerical set-up described in §2.3 in a simple aerothermal case, *i.e.*, the laminar flat plate. The section is organised as follows; in §2.4.1 the configuration, which is the same used by Vynnycky et al. (1998), is described in detail; in §2.4.2, the relevance of the theoretical stability bound obtained in §2.2 is first evaluated in a practical CHT simulation; then, results for the temperature and Nusselt number are compared to the results obtained by Vynnycky et al. (1998).

2.4.1 Presentation of the configuration: laminar flat plate

The study configuration is the same of Vynnycky et al. (1998) and is shown schematically in Fig. 2.11. It is a two-dimensional aerothermal case where the X axis represents the direction of the flow and the Y axis the wall-normal direction; the fluid domain extends between $x \in]-\infty, \infty[$ and $y \in [0, \infty[$ while the solid domain is defined between $x \in [-b/2, b/2]$ and $y \in [0, -a]$, the length of the conductive slab thus being b and the thickness a.

The flow is characterised by a uniform free-stream velocity U_∞ and temperature T_∞; at $y = 0$ a slip, adiabatic condition is imposed for $|x| > b/2$, with U_∞ and T_∞ thus being the velocity and temperature with which the flow attains the leading edge of the conductive slab; for $|x| < b/2$, a no-slip condition is prescribed and the flow is at thermal contact with the solid domain; on its surface, the development of both a velocity and thermal boundary layer is thus observed; every fluid property is considered to be constant. Concerning the solid domain, the two side walls at $x \pm b/2$ are both adiabatic with $\partial T/\partial x|_{x=\pm b/2} = 0$, while at the lower wall $y = -a$ an isothermal condition $T = T_c$ is prescribed; the thermal conductivity of the medium is constant.

Mathematically, the aerothermal problem is entirely determined by four non-dimensional numbers, which are:

— The Reynolds number, defined as $\mathrm{Re} = bU_\infty/\nu$, with ν the kinematic viscosity of the flow;

— The Prandtl number, defined as $\mathrm{Pr} = \mu c_p/\lambda_f$, with μ the dynamic viscosity, c_p the heat capacity and λ_f the thermal conductivity of the flow;

— The aspect-ratio $\eta = a/b$;

— The ratio of the fluid and solid thermal conductivities $\kappa = \lambda_s/\lambda_f$.

Vynnycky et al. (1998) treated a total number of thirty-two cases using different combinations of parameters and, in particular, exploring the cases where $\mathrm{Pr} \ll 1$ and $\mathrm{Pr} \gg 1$. Vynnycky et al. (1998) solved the aerothermal problems using two strategies, the former being numerical and based on the Keller-Box method (see Cebeci and Bradshaw, 2012), the latter involving approximate analytical one-dimensional solutions.

Our simulations are instead based on the numerical set-up described in §2.3; so as to simulate an infinite domain, the fluid medium extends between $x \in [-b, 2b]$ and $y \in [0, 10a]$ while the conductive slab remains defined between $x \in [-b/2, b/2]$ and $y \in [0, -a]$; furthermore, since *elsA* can only treat three-dimensional grids, a third dimension along the Z axis is added, along which the domain extends between $z \in [0, b]$; at $z = 0$ and $z = b$ a periodical boundary condition is prescribed, thanks to which the aerothermal problem remains, in fact, two-dimensional. The fluid domain is discretised with a structured grid of $[156, 43, 7]$ points in the x, y and z directions, respectively; along the X direction the grid is refined near the leading edge of the conductive slab so that $\Delta x^+ \sim 1$ in wall-units; the same is done along the Y direction, where $\Delta y^+ \approx 0.3$ near the wall. The solid domain has the same point distribution along the X and Z directions, so that the fluid and solid grids are coincident at the coupling interface, while in the wall-normal direction a uniform discretisation of 23 points is used. Since the flow is laminar, no turbulent model is used; furthermore, so as to limit the temperature dependence of the fluid properties, a temperature difference of $\Delta T = T_c - T_\infty = 2$ K is considered.

2.4.2 Results

i. *Stability bound*

The stability analysis described in §2.2 showed that when Dirichlet-Robin boundary conditions are prescribed at the fluid-solid interface (see Eq. (2.2.4)), there exists a lower stability bound for the coupling coefficient α_f which we have called α_f^{min}. As pointed out in §2.2.4, the theoretical study is based on several restrictive assumptions, and the validity of α_f^{min} is not guaranteed out of that particular context. Despite the simplicity of the configuration described in §2.4.1, it is nevertheless the opportunity to test the robustness of the theoretical study in an actual CHT simulation employing a real CFD code.

For this purpose, we present two test cases, the fundamental parameters of which are summarised in Table 2.7. As can be seen, the first case presents a low numerical Biot number which, being lower than unity, gives a negative α_f^{min}; the second case, instead, presents a high Biot number, a low K_s and, as a consequence, $\alpha_f^{min} \sim \alpha_f^{opt}$; for both test cases the exchange of boundary conditions takes place at every fluid iteration, which is one of the most important hypotheses of the theoretical model.

	Re	Pr	η	κ	K_f	K_s	D_f	Bi_ν	α_f^{min}	α_f^{opt}
Case 1	$\sim 2^{e+05}$	0.71	0.05	$\sim 4^{e+03}$	$\sim 7^{e+03}$	20^{e+03}	2.16	0.20	−7987.27	2012.73
Case 2	$\sim 2^{e+05}$	0.71	0.05	~ 800	50^{e+03}	4^{e+03}	2.02	7.68	13365.3	15365.3

Table 2.7: Validation of stability bound: fundamental physical and numerical parameters.

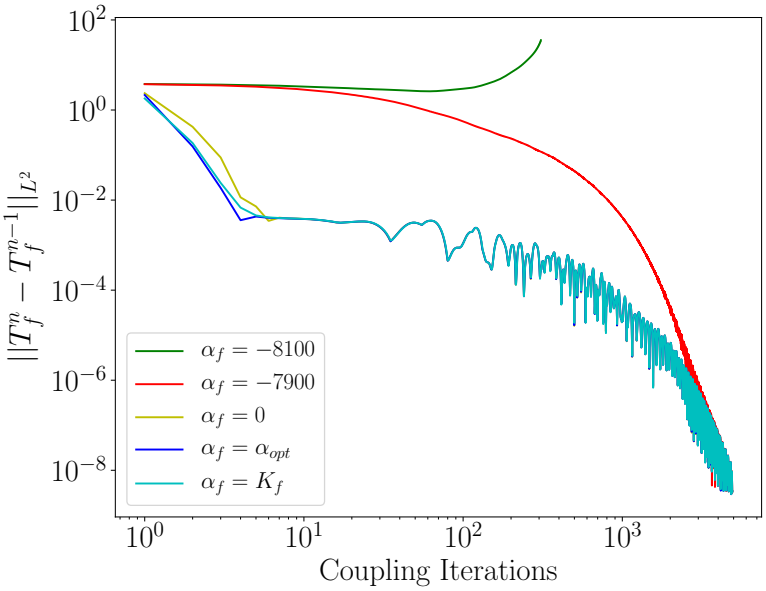

Figure 2.12: Validation of stability bound, Case 1: convergence history of the interface temperature with five different coefficients.

Figure 2.12 shows the convergence history, expressed as the L^2-norm of the interface temperature T_f between two consecutive coupling iterations, for the first test case and with five different coupling coefficients. The first two coefficients, *i.e.*, $\alpha_f = -8100$ and $\alpha_f = -7900$, are respectively slightly lower and greater than α_f^{min}; as can be seen, the former leads to divergence while the second allows to stabilise the coupling process, showing how α_f^{min} is a reasonable stability bound for this test case; all the remaining coefficients lead to stability with a rather similar convergence rate, even when $\alpha_f = K_f$.

Figure 2.13 shows the convergence history of the second test case with four different coupling coefficients. As can be seen, even for $\alpha_f = 13500 \gtrapprox \alpha_f^{min}$ the interface temperature diverges, showing the limits of the theoretical stability analysis; however, the actual stability bound is not far away as with $\alpha_f = 14200$, after some rather strong oscillations, the temperature converges; it can also be noticed that for all the stable coefficients the convergence rate is the same after around 100 coupling iterations.

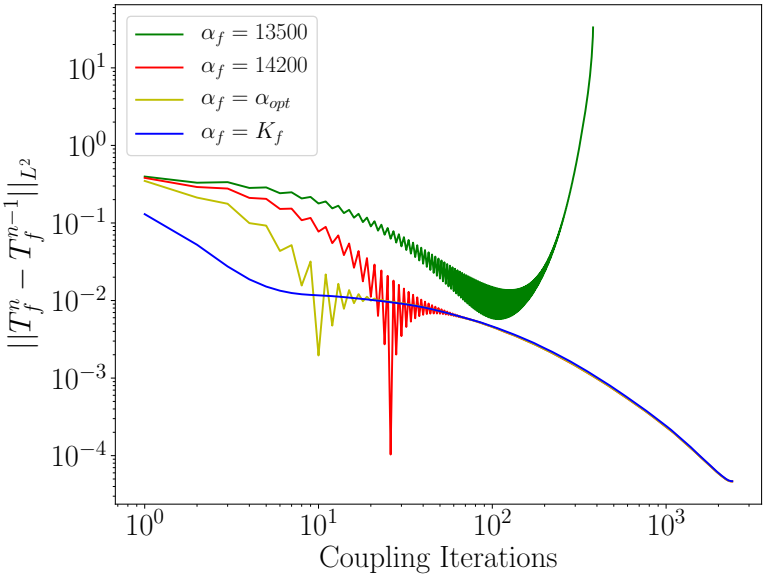

Figure 2.13: Validation of stability bound, Case 2: convergence history of the interface temperature with four different coefficients.

Re	Pr	η	κ
10000	0.01	0.25	20

Table 2.8: Comparison with Vynnycky et al. (1998): fundamental parameters of the test case.

As a whole, these results illustrate the relevance of the theoretical stability bound in simple yet realistic CHT simulations which do not strictly respect the assumptions of the theoretical study; understandably, α_f^{min} does not represent a pivotal coefficient as it has been demonstrated in §2.2.3 with a one-dimensional assumption, and in aerothermal problems of practical interest a certain safety margin has to be taken. Further considerations concerning the choice of a coupling coefficient are given in the concluding section of this chapter §2.5.

ii. *Temperature profiles and Nusselt number*

In this paragraph we present a last test case in the laminar flat plate configuration, with the objective of comparing our results to the ones obtained numerically and analytically by Vynnycky et al. (1998). The fundamental parameters of the simulation are summarised in Table 2.8. So as to stabilise the coupling process, we prescribe Dirichlet-Robin boundary conditions at the fluid-solid interface, as described in §2.3.3, and we adopt the relaxation coefficient α_f^{opt} (see Eq. (2.3.18)).

Figure 2.14 shows the temperature iso-lines in the two domains; the temperature

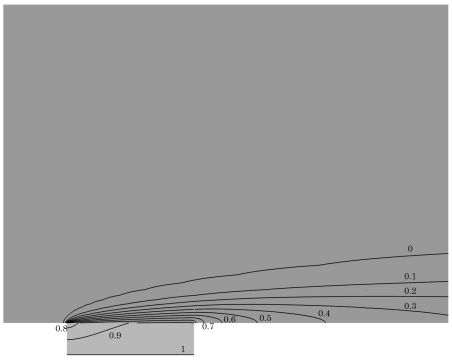

Figure 2.14: Temperature iso-lines ($\Delta\theta = 0.1$).

θ is non-dimensionalilsed as follows:

$$\theta = \frac{T - T_\infty}{T_c - T_\infty} \ , \tag{2.4.1}$$

and, therefore, varies between zero and unity. As can be seen, because of the elevated conductivity ratio κ, the temperature gradient is concentrated in the fluid domain, where almost all the iso-lines are situated; in the solid domain, on the contrary, the temperature is basically constant.

Figure 2.15, instead, shows the profiles of temperature (2.15a) and Nusselt number (2.15b) at the fluid-solid interface, compared to the numerical and analytical results of Vynnycky et al. (1998). The Nusselt number is computed as:

$$\mathrm{Nu} = b\frac{\phi}{\lambda_f \left(T_c - T_\infty\right)} = -\frac{\partial\theta}{\partial y}|_{y=0} \ , \tag{2.4.2}$$

where ϕ is the wall heat-flux. For the non-dimensional temperature θ, an overall good agreement is obtained; the greatest uncertainties are localised near the leading edge of the conductive slab, where the temperature we have obtained is anyway situated between the profiles of Vynnycky et al. (1998); near the trailing edge, our CHT simulation predicts a higher temperature, yet the error is of the same order of magnitude of the difference between the analytical and numerical results of Vynnycky et al. (1998). Concerning the Nusselt number, instead, excellent agreement is obtained throughout the length of the fluid-solid interface, even though Vynnycky et al. (1998) do not provide any values in proximity of the leading edge. These results allow us to validate the numerical set-up introduced in §2.3.

2.5 Conclusion

In this chapter, we have provided a thorough description of the numerical methods employed in our conjugate heat transfer simulations.

In §2.1, a brief overview of the coupling approach and algorithm has been given; we adopt a partitioned approach with a basic four-step CSS algorithm and we seek a steady-state solution; this allows us to neglect the transient phase which we accelerate using a time-marching scheme in the fluid domain and steady-state heat diffusion in the solid domain.

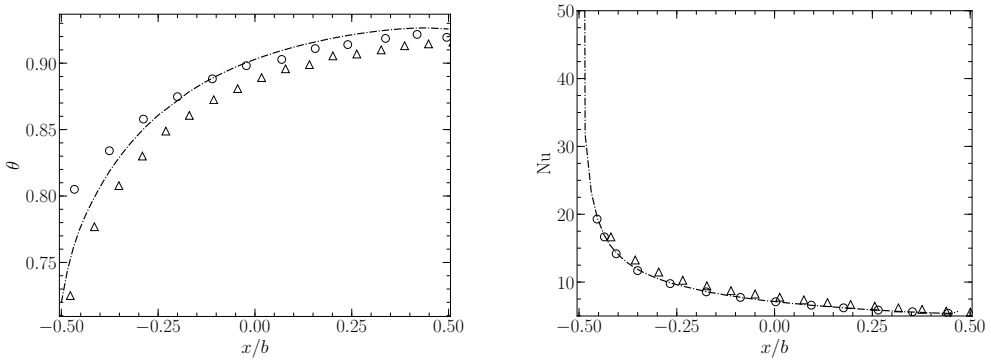

(a) (b)

Figure 2.15: Comparison with Vynnycky et al. (1998), temperature (a) and Nusselt (b) profiles at the fluid-solid interface. – · – · –, present results; △, approximate analytical results from Vynnycky et al. (1998); ○, numerical results from Vynnycky et al. (1998).

In §2.2, an exhaustive stability analysis of the coupling algorithm has been given; we have focused on Dirichlet-Robin boundary conditions at the fluid-solid interface and, following the work of Errera and Chemin (2013), we have introduced a lower stability bound for the relaxation coefficient added to the Robin condition, which we have called α_f^{min}; the stability analysis has been performed using the normal-mode theory of Godunov and Ryabenki (1964), and is based on a hypothesis of one-dimensional diffusive fluid-solid transfer. Furthermore, in §2.2.3 , we have provided a numerical validation of the stability bound using a specifically designed computational code; finally, in §2.2.4, several extensions of the stability analysis have been proposed. These two sections represent an original contribution, which has been published in the two articles mentioned at the beginning of the chapter.

In §2.3, abandoning the one-dimensional formalism, the implementation of conjugate heat transfer in the fluid and solid solvers of our choice, *i.e.*, *elsA* and *Z-set*, has been described in detail. Finally, in §2.4, the numerical set-up has been validated in a simple aerothermal configuration, *i.e.*, the laminar flat plate, with respect to results found in the literature.

To conclude this chapter, we wish to take advantage of the ensemble of analyses and test cases performed in this work, to provide some guidelines for choosing an adequate coupling coefficient in a conjugate heat transfer problem of practical interest.

In the stability analysis, three fundamental parameters defining the nature of the coupling process have clearly emerged:

1. α_f^{min} (see Eq. (2.2.33)) or, equivalently, the numerical Biot number Bi_ν; α_f^{min} represents the lower stability bound, and includes all the information of the coupling process: the solid domain (through K_s), the fluid domain (through K_f) and the coupling dynamics (through D_f); as pointed out in §2.2.4, it is not an easy coefficient to calculate in three-dimensional configurations; nevertheless, a conservative estimation can be provided, allowing to determine at least

the order of magnitude of α_f^{min}.

2. α_f^{opt} (see Eq. (2.2.32)); it represents the limit of α_f^{min} for $K_s \to 0$; therefore, it does not depend on any physical or numerical property of the solid domain, yet includes information concerning the fluid domain and the coupling dynamics through K_f and D_f. This coupling coefficient should guarantee stability regardless of the solid domain considered.

3. K_f; observe that $K_f/2 = \lim_{\mathrm{D}_f \to 0} \lim_{K_s \to 0} \alpha_f^{min}$, where both $\mathrm{D}_f \to 0$ and $K_s \to 0$ clearly represent the worst case scenario from a numerical point of view; a coefficient $\alpha_f \sim K_f$ should therefore guarantee stability regardless of the aerothermal problem considered and of the numerical scheme implemented.

When choosing a coupling coefficient, all these parameters need to be calculated or at least estimated, as they represent three points of reference in the spectrum $\alpha_f \in]-\infty, +\infty[$. Depending on their values, four different scenarios can appear:

— $\alpha_f^{min} \ll 0$: the coupling coefficient $\alpha_f = 0$, with which the Dirichlet-Robin conditions of Eq. (2.2.4) fall back into the classical Dirichlet-Neumann ones, can be chosen without hesitation; as shown in §2.4.2, even a coefficient $\alpha_f < 0$ can be stable as long as $\alpha_f > \alpha_f^{min}$, yet there is no practical interest in using a negative coupling coefficient.

— $\alpha_f^{opt} - \alpha_f^{min} \gg 0$: the stability margin of α_f^{opt} is elevated and $\alpha_f = \alpha_f^{opt}$ should guarantee both stability and a satisfying convergence rate.

— $\alpha_f^{opt} \sim \alpha_f^{min}$ and $K_f \gg \alpha_f^{opt}$: the stability margin of α_f^{opt} is narrow and $\alpha_f = \alpha_f^{opt}$ should be avoided; $\alpha_f = K_f$ is also to avoid since it could lead to a very slow convergence. In this case, it could be advisable to take a coefficient $\alpha_f \propto \alpha_f^{opt}$; Errera et al. (2019), for instance, suggest taking $\alpha_f = \sqrt{3}\alpha_f^{opt}$.

— $\alpha_f^{opt} \sim \alpha_f^{min}$ and $K_f \approx 2\alpha_f^{opt}$: as above, $\alpha_f = \alpha_f^{opt}$ should be avoided; on the contrary, $\alpha_f = K_f$ could be a viable coupling coefficient as it guarantees stability and, in this case, the convergence rate should not be excessively penalised.

As mentioned and motivated in §2.3.3, in this work we have chosen to use α_f^{opt} for all the conjugate heat transfer cases which will be described in Chapters §5 and §6. All our cases, as we shall see, fall into the second scenario.

Part II

High-fidelity study of a non-equilibrium turbulent heat transfer case

Chapter 3

Physical study of the non-equilibrium development of a turbulent thermal boundary layer

With this chapter, we inaugurate the second part of this work, in which we discuss the first set of activities introduced in the Introduction.

As mentioned, we aim at investigating one of the (many) phenomenological aspects of the surface air-oil heat exchanger, *i.e.*, the perturbation of a flow subjected to a temperature gradient. In particular, our goal is to isolate this effect, so that the temperature gradient is the only disturbance in the configuration. Therefore, we have introduced a study configuration in which a fully developed turbulent temperature-homogeneous channel flow at equilibrium makes contact with an isothermal wall; the abrupt change of wall thermal conditions generates non-equilibrium effects which slowly vanish as the thermal boundary layer develops and attains its fully developed state at the exit of the channel. This configuration represents an elementary heat exchanger. Phenomenologically, it represents a non-equilibrium turbulent heat transfer case.

In this chapter, we perform the physical study of this flow by means of direct numerical simulation (DNS). We aim at gaining insight into its nature and throw light on those physical phenomena that are expected to appear in similar non-equilibrium configurations. Besides, our objective is to obtain clear indications of how the flow should be treated in wall-modelled LES, which is the object of the next chapter.

The results we have obtained and that we detail in this chapter, have been presented in the following paper, which has been accepted by *Journal of Fluid Mechanics*:

— Gelain, M., Gicquel, O., Couilleaux, A., Vicquelin, R., *Physical study of the non-equilibrium development of a turbulent thermal boundary layer*, Journal of Fluid Mechanics, accepted.

The results have also been presented at the 72$^{\text{nd}}$ Meeting of the Division of Fluid Dynamics of the American Physical Society in 2019:

— Gelain, M., Gicquel, O., Couilleaux, A., Vicquelin, R., *DNS of a turbulent thermal boundary layer spatially evolving on an isothermal wall from a fully turbulent adiabatic flow*, In : 72nd Annual Meeting of the American Physical Society-Division of Fluid Dynamics. 2019.

3.1 Introduction

Turbulent heat transfer is encountered in numerous industrial applications, and in most cases the turbulent heat exchange takes place in non-equilibrium flows. It is the case, for instance, of the surface air-oil heat exchangers we have presented in the Introduction, where an essentially temperature-homogeneous flow makes contact with a heated surface, and is therefore abruptly subjected to a temperature gradient.

It is the interest in the behaviour of the atmospheric boundary layer, however, which drew first attention to turbulent heat transfer in non-equilibrium flows, both theoretically and experimentally (see Antonia et al., 1977). The case where non-equilibrium is induced by a step change in surface temperature is the simplest example of non-equilibrium turbulent heat transfer, and numerous experimental works can be found in the literature. Johnson and Whippany (1957) studied the development of a thermal boundary layer on a smooth flat plate, and presented mean temperature and velocity profiles, while focusing on fluctuating profiles in a later work (Johnson et al., 1959). Blom (1970) carried out a similar study, comparing mean temperature profiles to the theoretical predictions of Spalding (1961), and presenting the evolution of the turbulent Prandtl number. Similar experimental works can be found in Fulachier (1972), Hoffmann and Perry (1979), Ng et al. (1982), Taylor et al. (1990) and, more recently, Biles et al. (2019), while Antonia et al. (1977) and Teitel and Antonia (1993) studied the case of a step change in wall heat flux in a flat plate and turbulent channel flow configuration, respectively.

In spite of its Reynolds number limitation, direct numerical simulation (DNS) is undoubtedly the most accurate tool available for the investigation of turbulent heat transfer, since all the turbulent scales are solved. The first DNS addressing turbulent heat transfer is that of Kim and Moin (1989), where the transport of three passive scalars at different molecular Prandtl numbers is considered in a fully developed channel flow at a friction Reynolds number of $\mathrm{Re}_\tau = 180$. Several works followed, aiming at understanding the influence on the flow statistics of the Reynolds number and molecular Prandtl number (e.g. Papavassiliou and Hanratty, 1997; Kawamura et al., 1999; Abe et al., 2001), as well as of the isothermal or iso-flux boundary conditions (e.g. Kasagi et al., 1992; Kawamura et al., 2000). Other authors focused on the coupling between turbulence and temperature gradient, an analysis which is possible only if temperature is handled as an active scalar. Most of these DNS were performed in supersonic channel flows (see Coleman et al., 1995; Huang et al., 1995; Morinishi et al., 2004; Tamano and Morinishi, 2006) while only a few focused on low speed flows with high temperature gradients (see Nicoud, 1999; Toutant and Bataille, 2013).

All the numerical works mentioned so far represent cases of equilibrium flows, and are undoubtedly the reference for understanding turbulent heat transfer in all its aspects (flow statistics, turbulent Prandtl number, wall scaling and much more). Nevertheless, questions arise concerning the validity of these findings in non-equilibrium configurations. Once more, DNS can be a powerful tool for the analysis of such flows, yet the literature is extremely less abundant on the matter. Seki and Kawa-

mura (2005) performed the DNS of a fully developed channel flow with temperature as a passive scalar, where the wall temperature is constant everywhere but in a small fraction of the bottom wall, where it evolves along the streamwise direction attaining a peak. The step change of wall temperature significantly perturbs the mean and fluctuating temperature, as well as turbulent Prandtl number. Hattori et al. (2007), Hattori et al. (2012) and Hattori et al. (2013) performed several DNS of non-equilibrium thermal boundary layers in the flat plate configuration. Hattori et al. (2007) analysed the effects of buoyancy on mean and fluctuating properties, as well as on the turbulent budgets for a turbulent boundary layer at equilibrium facing a step change in wall temperature. In Hattori et al. (2012), non-equilibrium is induced through the sudden vanishing of wall-heat flux and, in one of the two cases presented, with the addition of a forward facing step. Similar analyses are carried out in Hattori et al. (2013), yet temperature, in this case, is not handled as a passive scalar. Large-eddy simulation (LES) is certainly another valid tool for studying non-equilibrium turbulent heat transfer yet, despite the large turbulent scales being solved, a certain degree of modelling is needed for the smaller scales. Sanchez et al. (2014) and Bellec et al. (2017) performed the LES of a temperature-homogeneous fully developed channel flow making contact with anisothermal walls for $\mathrm{Re}_\tau = 180$ and $\mathrm{Re}_\tau = 395$, respectively. They showed the evolution of the mean and fluctuating temperature profiles, as well as the impact on the mean and fluctuating velocity components.

The objective of this chapter, is to deepen the knowledge of turbulent non-equilibrium heat transfer, which, as the literature review shows, has been investigated in a limited number of studies, especially in the case of flows with temperature-dependent properties. The intention is not only to describe and characterise a non-equilibrium flow, but also its gradual evolution towards a new equilibrium state.

To achieve the scope of the study, as already mentioned, we perform the direct numerical simulation of a channel flow, where a turbulent, fully developed, temperature-homogeneous flow at $\mathrm{Re}_\tau = 395$ makes contact with an isothermal wall. The step change in surface temperature leads to the development of a thermal layer, and, since temperature is an active scalar, the velocity boundary layer is also modified. The length of the isothermal wall allows the boundary layer to reach a new equilibrium state, characterised by a fully developed thermal boundary layer. The simulation is performed under one single flow regime, in terms of Reynolds number, Mach number and temperature gradient, and the non-equilibrium nature of the flow does not allow for a straightforward generalisation of our findings. Therefore, the study primarily aims at identifying the physical phenomena that are expected to be encountered in comparable non-equilibrium flows, while providing the theoretical means to understand them.

The chapter is organised as follows. In section 3.2, the problem is described in detail; the governing equations are presented as well as details about the study configuration and initialisation are given. In section 3.3, the numerical set-up and the proposed configuration are validated with respect to reference results found in the literature for equilibrium flows. In section 3.4, the results are presented. In §3.4.1, the behaviour of the flow is analysed in what appears to be the most perturbed region, *i.e.*, the leading edge of the isothermal wall. In §3.4.2, an equilibrium region which characterises the development of the thermal boundary layer is identified and quantitatively defined. In §3.4.3, the findings of §3.4.2 are contrasted to the evolution of several turbulent quantities. This is followed by the conclusions, in §3.5.

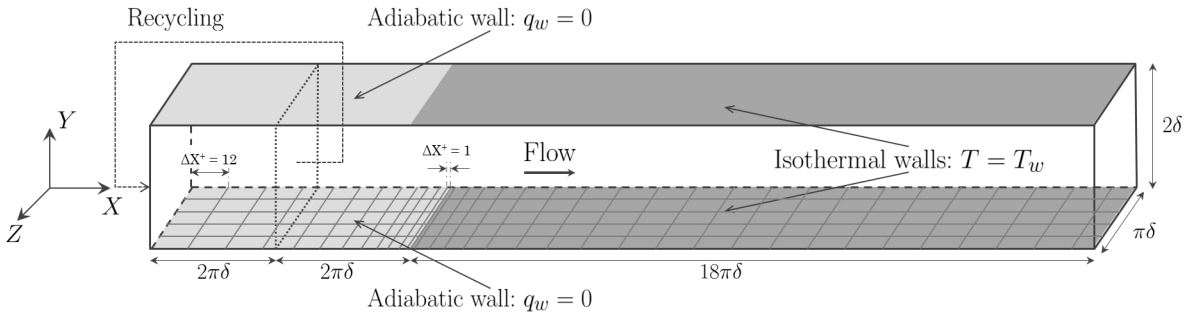

Figure 3.1: Computational domain of the present study.

3.2 Problem description

In this section, details about governing equations and numerical scheme (§3.2.1), geometry, mesh and boundary conditions (§3.2.2) as well as initialisation (§3.2.3) are given.

3.2.1 Governing equations and numerical scheme

The full compressible Navier-Stokes equations are solved in the fluid without any turbulence model. The set of equations has already been introduced in Chapter 1, and we rewrite it here:

$$\frac{\partial \rho}{\partial t} + \frac{\partial \rho u_i}{\partial x_i} = 0 \ , \tag{3.2.1}$$

$$\frac{\partial \rho u_i}{\partial t} + \frac{\partial \rho u_i u_j}{\partial x_j} = -\frac{\partial p}{\partial x_i} + \frac{\partial \boldsymbol{\tau}_{ij}}{\partial x_j} \ , \tag{3.2.2}$$

$$\frac{\partial \rho h}{\partial t} + \frac{\partial \rho u_j h}{\partial x_j} = \frac{\mathrm{D}p}{\mathrm{D}t} - \frac{\partial q_j^{cd}}{\partial x_j} + \boldsymbol{\tau}_{ij}\frac{\partial u_i}{\partial x_j} + S_{ener} \ . \tag{3.2.3}$$

The reader can refer to §1.3.1 for the laws governing the behaviour of the fluid properties. Notice the presence of S_{ener} in the energy equation. It is a source term the role of which is clarified in the next section.

The set of equations is solved by the parallel code AVBP (Schonfeld and Rudgyard, 1999; Moureau et al., 2005) using a time-explicit finite-element two-step Taylor-Galerkin scheme (Colin and Rudgyard, 2000) which provides third-order accuracy in space and time.

3.2.2 Geometry, mesh and boundary conditions

The geometry of the configuration studied is shown in Figure 3.1. The computational domain is a channel flow of size $22\pi\delta \times 2\delta \times \pi\delta$ (where $\delta = 0.002$ m) which is made of two parts in the streamwise direction.

The upstream part has size $4\pi\delta \times 2\delta \times \pi\delta$, the upper and lower walls (with respect to the Y direction) are adiabatic, and a no-slip boundary condition is prescribed, while periodic boundary conditions are applied in the spanwise direction Z.

Differently from what happens in bi-periodic channel flows, in this case the flow is driven by a streamwise pressure gradient compensating the head losses generated along the whole domain shown in Figure 3.1. In the Z direction the mesh is uniform; in the wall-normal direction the mesh size, expressed in wall units, varies from $\Delta Y^+ = 0.75$ at the upper and lower walls, to $\Delta Y^+ = 7$ at the centre of the channel; along the streamwise direction, the mesh size varies with a constant ratio 1.05 from $\Delta X^+ = 12$ at the inlet to $\Delta X^+ = 1$ at the interface with the downstream part of the channel flow (see Fig. 3.1). The role of this part of the domain is to generate a temperature-homogeneous boundary layer at equilibrium, with the regime conditions specified in Table 3.1. In order to do so at a moderate cost, a recycling strategy is used: the three velocity components and the temperature imposed at the domain inlet via the Navier-Stokes Characteristic Boundary Condition (NSCBC) formalism (Poinsot and Veynante, 2005; Moureau et al., 2005) are extracted from a recycling plane situated downstream at a distance of $2\pi\delta$.

Despite the low Mach number (see Table 3.1), compressibility effects, which are fully considered in Equations (3.2.1), (3.2.2) and (3.2.3), impact the recycling procedure. Similarly to a subsonic Fanno flow (see Ockendon et al., 2001), if inlet conditions were recycled without any sort of correction, the presence of wall friction would make the flow accelerate and the temperature diminish until the sonic condition is attained. It is thus necessary to normalise the values extracted at the recycling plane with respect to a target average temperature $\langle T \rangle_{target}$ and streamwise velocity $\langle U \rangle_{target}$, which allow us to obtain the regime specified in Table 3.1. For every time iteration one has:

$$u_i(x,y,z,t)|_{x=0} = u_i(x,y,z,t)|_{x=2\pi\delta} \frac{\langle U \rangle_{target}}{\langle U \rangle_{x=2\pi\delta}} \ , \tag{3.2.4}$$

as well as,

$$T(x,y,z,t)|_{x=0} = T(x,y,z,t)|_{x=2\pi\delta} \frac{\langle T \rangle_{target}}{\langle T \rangle_{x=2\pi\delta}} \ , \tag{3.2.5}$$

where $\langle U \rangle_{x=2\pi\delta}$ is the average streamwise velocity and $\langle T \rangle_{x=2\pi\delta}$ the average temperature at the recycling plane at instant t. Given the low Mach number and the short distance between the inlet and the recycling plane, the correction applied to the temperature and the velocity components is minimal,

$$\left(1 - \langle U \rangle_{target} \,/\, \langle U \rangle_{x=2\pi\delta}\right) \sim 10^{-7},$$

$$\left(1 - \langle T \rangle_{target} \,/\, \langle T \rangle_{x=2\pi\delta}\right) \sim -10^{-7},$$

and yet necessary. Without, the bulk velocity drifts away and eventually diverges.

The energy source term S_{ener} added to Equation (3.2.3), is zero in this portion of the channel flow.

The downstream part of the domain has size $[18\pi\delta, 2\delta, \pi\delta]$, the upper and lower walls are isothermal, both at temperature $T_w = 400$ K, and a no-slip boundary condition is prescribed, while, analogously to the upstream part, the domain is periodic in the spanwise direction. At the outlet, pressure is imposed via the NSCBC formalism. The mesh has the same point distribution of the upstream sub-domain along the Y and Z directions, while the mesh size varies with a constant ratio 1.05 from $\Delta X^+ = 1$ at the adiabatic-isothermal interface until $\Delta X^+ = 12$ further downstream, where wall units are still referred to the adiabatic conditions of the upstream

Size	$n_X \times n_Y \times n_z$	ΔX^+	ΔY^+	ΔZ^+	Re_τ	M	T_b (K)
$[4\pi\delta, 2\delta, \pi\delta]$	$420 \times 179 \times 200$	$[1.0 - 12.0]$	$[0.75 - 7.0]$	6.2	395	0.16	304.5

Table 3.1: Size, mesh, spatial resolution and regime conditions of upstream (adiabatic) sub-domain: n_i is the number of grid points and ΔX_i^+ the spatial resolution in wall-units; Re_τ is the friction Reynolds number, M the average Mach number and T_b the bulk temperature.

Size	$n_X \times n_Y \times n_z$	ΔX^+	ΔY^+	ΔZ^+
$[18\pi\delta, 2\delta, \pi\delta]$	$1771 \times 179 \times 200$	$[1.0 - 12.0]$	$[0.75 - 7.0]$	6.2

Table 3.2: Size, mesh and spatial resolution of downstream (isothermal) sub-domain.

sub-domain. This refinement along the streamwise direction serves to well capture the very first development region of the thermal boundary layer at the leading edge of the isothermal wall, where streamwise gradients can be important. The role of the downstream part is to allow the thermal boundary layer to be fully developed and to attain a new equilibrium state before the exit. The fully developed regime is characterized by a scaled mean temperature profile which is homogeneous in the streamwise direction. The role of the source term S_{ener} added to the energy equation (3.2.3), is that of guaranteeing that a temperature gradient is preserved between the wall and the centre of the channel, allowing for a better appreciation of the fully developed regime. The mean temperature profile, therefore, results from the balance between the prescribed source term and the wall heat fluxes of the established flow $\overline{q_w}^{eq}$:

$$\overline{q_w}^{eq} \approx -S_{ener}\delta \ . \tag{3.2.6}$$

The source term S_{ener} takes a constant value specifically designed to obtain at equilibrium a bulk temperature of $T_b^{eq} = 304.5$ K, *i.e.*, the same of the upstream part of the domain (see Table 3.1), which yields a temperature of $T_c^{eq} \approx 290$ K at the centre of the channel. Thanks to Equation (3.2.6), the value at equilibrium of the heat flux parameter B_q and of the Nusselt number Nu can be deduced:

$$\mathrm{B}_q^{eq} = -\frac{\overline{q_w}^{eq}}{\rho_w c_{p_w} u_\tau T_w} \qquad \mathrm{Nu}^{eq} = -2\delta\frac{\overline{q_w}^{eq}}{\lambda_w\left(T_w - T_c\right)} \ , \tag{3.2.7}$$

where $u_\tau = \sqrt{\tau_w/\rho_w}$, with τ_w the wall shear stress, is the friction velocity, c_p is the constant-pressure specific heat and the subscript $(\cdot)_w$ denotes a fluid quantity taken at the wall.

Table 3.2 summarises the size and the mesh resolution, while Table 3.3 details the regime conditions of the downstream part of the domain.

T_w (K)	B_q^{eq}	Nu^{eq}	Re_τ^{eq}	$\left(\frac{T_w}{\overline{T}_c}\right)^{eq}$	$\frac{T_w}{\overline{T}_{in}}$
400	0.018	26.6	292	1.38	1.31

Table 3.3: Regime conditions of downstream (isothermal) sub-domain. $T_w/\overline{T}_{in}$ is the temperature ratio between the wall and the inlet.

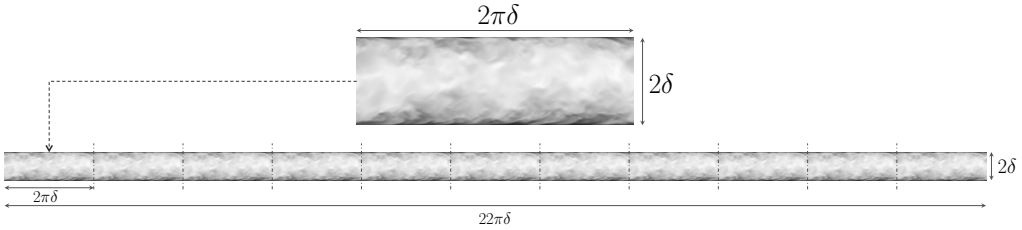

Figure 3.2: Schematic representation of the initial solution. The conservative fields (in this case ρu) of a $2\pi\delta \times 2\delta \times \pi\delta$ adiabatic channel flow at equilibrium is repeated periodically in the streamwise direction eleven times.

3.2.3 Initialisation and computing time

So as to minimise the transient period necessary for the flow to reach the statistically steady state, the initial conservative fields are extracted from a smaller bi-periodic adiabatic channel flow at equilibrium, the same that will be mentioned later in §3.3.1. The size of this channel flow being $[2\pi\delta, 2\delta, \pi\delta]$, the same solution is put in sequence eleven times in the streamwise direction to cover the whole length of $22\pi\delta$, as shown in Figure 3.2. In this manner, not only is the initial solution periodic along the Z axis, but also between the inlet and the recycling plane.

The velocity boundary layer is then already fully developed at the start of the simulation, but in order for the thermal boundary layer to develop and attain steady state, the initial solution is integrated during a transient time $\tau_{trans} = 18\pi\delta/\overline{u}$, *i.e.*, the time the average flow needs to cross the whole downstream part of the domain. Once the steady state is reached, flow statistics are collected over the duration $56\delta/u_\tau$, with u_τ the friction velocity computed at the outlet.

3.3 Equilibrium states and validation

This study is characterised by two distinct equilibrium states, between which the flow evolves along the streamwise direction. The former is an adiabatic, fully developed turbulent flow in the upstream part of the domain; the latter is a fully developed turbulent thermal boundary layer at the outlet.

The objective of this section is twofold: first, to validate the numerical setup introduced in §3.2.1 with respect to reference results of the literature; second, to verify that the configuration described in §3.2.2 allows us to to meet the scope of the study, *i.e.*, to observe the evolution of the boundary layer between the aforementioned equilibrium states.

In the following, $\overline{(\cdot)}$ and $\widetilde{(\cdot)}$ denote Reynolds and Favre averages, while $(\cdot)'$ and $(\cdot)''$ denote their respective fluctuating parts. Spatially, quantities are only averaged along the Z axis, which is the only homogeneous direction for this configuration. Given the streamwise evolution of the boundary layer, unless specified, scaling of quantities (dimensionless numbers included) has to be intended *locally* with respect to the X coordinate. The origin of the axes is placed at the interface between the adiabatic and isothermal walls, so that the adimensionalised X coordinate x/δ is defined in the range $[-4\pi, 18\pi]$ between the inlet and the outlet. The subscripts $(\cdot)_w$ and $(\cdot)_c$ indicate that the given property is evaluated at the wall and at the centre of channel, respectively. The superscript $(\cdot)^+$ denotes classic wall scaling, that is:

$$y^+ = \frac{\rho_w y u_\tau}{\mu_w} \quad \text{and} \quad u_i^+ = \frac{u_i}{u_\tau} \quad \text{with} \quad u_\tau = \sqrt{\frac{\tau_w}{\rho_w}} \,, \tag{3.3.1}$$

$$T^+ = \frac{|T - T_w|}{T_\tau} \quad \text{with} \quad T_\tau = \frac{|q_w|}{\rho_w c_{p_w} u_\tau} \,. \tag{3.3.2}$$

The superscript $(\cdot)^*$, instead, denotes semi-local scaling (see Huang et al., 1995; Patel et al., 2015), which uses *local* values (with respect to the wall-normal direction Y) of ρ, μ and c_p, instead of their values at the wall.

In the following sections, the behaviour of the flow is analysed at two streamwise locations: at $x/\delta \approx 0$ in §3.3.1, where an adiabatic, fully developed turbulent flow is expected; at $x/\delta \approx 18\pi$ in §3.3.2, where the development of the thermal boundary layer should be concluded.

3.3.1 Upstream equilibrium state

Figure 3.3 shows the mean streamwise velocity and the three root-mean square (r.m.s.) velocity profiles at $x/\delta = -0.1\pi$, *i.e.*, slightly downstream of the leading edge of the isothermal wall. Results at $x/\delta \approx 0$, represented by the black solid lines, are compared with two reference data. The former, represented by the gray lines, have been obtained by simulating a classic bi-periodic channel flow of size $[2\pi\delta, 2\delta, \pi\delta]$ with the regime conditions of Table 3.1; the latter, represented by the symbols, are taken from Kawamura et al. (2000).

The harmony between the small channel flow results and Kawamura et al. (2000), is required to validate the numerical setup of §3.2.1; as can be seen, good agreement is obtained for both the mean streamwise velocity and the r.m.s. velocities.

The accord between the small channel flow and the present results at $x/\delta \approx 0$, instead, is required to validate the study configuration described in §3.2.2; excellent agreement is obtained on the mean streamwise velocity, which shows that the flow reaching the downstream part of the domain is a fully developed turbulent temperature-homogeneous boundary layer as desired; on the other hand, even though good agreement is obtained for the wall-normal and spanwise r.m.s. velocities, a disparity of around 10% is observed for the streamwise component in the log-layer; a possible explanation for this behaviour is given in the following section.

3.3.2 Downstream equilibrium state

At $x/\delta \approx 18\pi$, the flow is expected to have evolved towards a new equilibrium state, characterised by a fully developed thermal boundary layer.

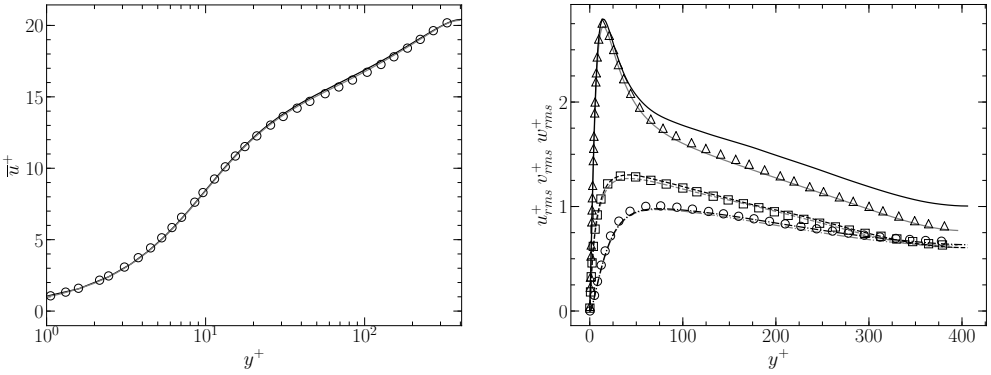

Figure 3.3: Upstream equilibrium state. Mean profile of streamwise velocity (a): —— present results with small channel flow (gray) and at $x/\delta \approx 0$ (black); ○ results from Kawamura et al. (1999). Profiles of r.m.s. streamwise, wall-normal and spanwise velocity respectively (b): ——, – · – · – and - - - - present results (colors as above); △, ○ and □ results from Kawamura et al. (1999).

Figure 3.4 shows the mean streamwise and r.m.s. velocities at $x/\delta = 287/16\pi$ compared to both the results of Kawamura et al. (1999) and, similarly to what is done in §3.3.1, to the results obtained with a classic bi-periodic channel flow at the regime conditions of Table 3.3. Note that, in this case, semi-local scaling is used. As can be seen, good agreement is obtained for all the profiles, and even the streamwise r.m.s. velocity is considerably closer to the reference results. The disparity illustrated in Figure 3.3b, can thus be attributed to some local perturbation of the upstream flow, most probably induced by the recycling method described in §3.2.2, the effects of which disappear further downstream.

The profiles of mean and r.m.s. temperature are instead shown in Figure 3.5. Good agreement is obtained among all the curves for the mean temperature, while a slight discrepancy is observed on the r.m.s. profile. Therefore, if on the one hand the average thermal boundary layer seems to be fully developed at the outlet, on the other hand a longer isothermal wall would have been necessary to observe the same level of convergence for the temperature fluctuations.

Both Figures 3.4 & 3.5 also illustrate how, thanks to semi-local scaling, fluid property variations in the wall-normal direction are properly taken into account, with all velocity and temperature profiles collapsing to those obtained by Kawamura et al. (1999) with a passive scalar. Fluid mean property variations, at least at equilibrium, seem thus to be the only remarkable impact of the heated wall on the flow, as suggested by Morkovin (1962) and seen in several studies involving compressible flows (e.g. Huang and Coleman, 1994; Huang et al., 1995; Nicoud, 1999).

However, the effects of the temperature gradient on the flow can be much more important in other portions of the channel, namely in proximity of the leading edge of the isothermal wall. This can be seen in Figure 3.6, which plots the evolution of the Nusselt number and of the heat flux parameter along the channel; both are very important near the leading edge, and the behaviour of the flow needs to be investigated in that region. The later convergence of Nu and B_q towards the values of

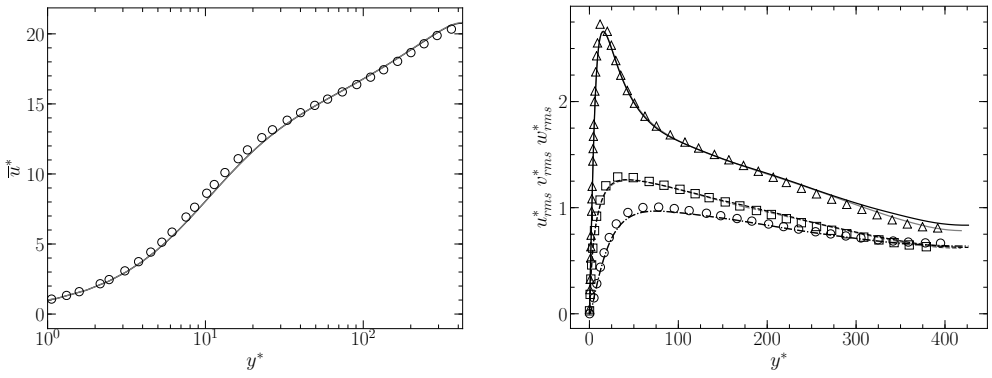

(a) (b)

Figure 3.4: Downstream equilibrium state. Profiles of mean streamwise (a) and r.m.s. streamwise, wall-normal and spanwise velocities (b) at $x/\delta \approx 18\pi$. See Figure 3.3 for a reference to colours and symbols.

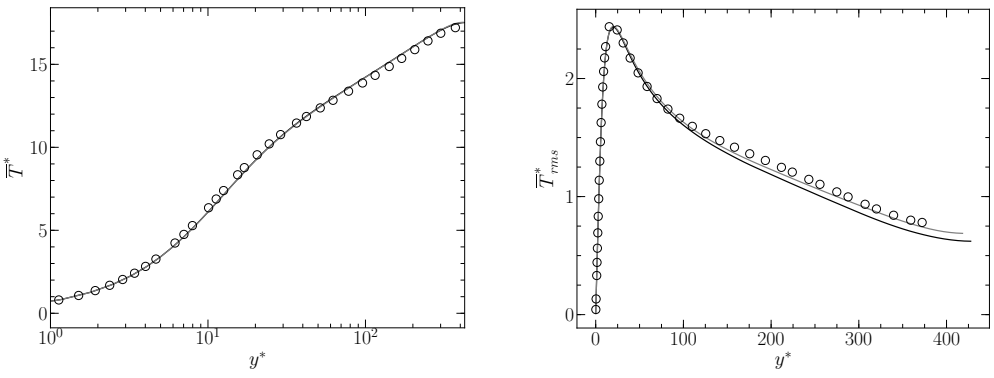

(a) (b)

Figure 3.5: Downstream equilibrium state. Profiles of mean (a) and r.m.s. (b) temperature: —— present results with small channel flow (gray) and at $x/\delta \approx 18\pi$; ○ results from Kawamura et al. (1999).

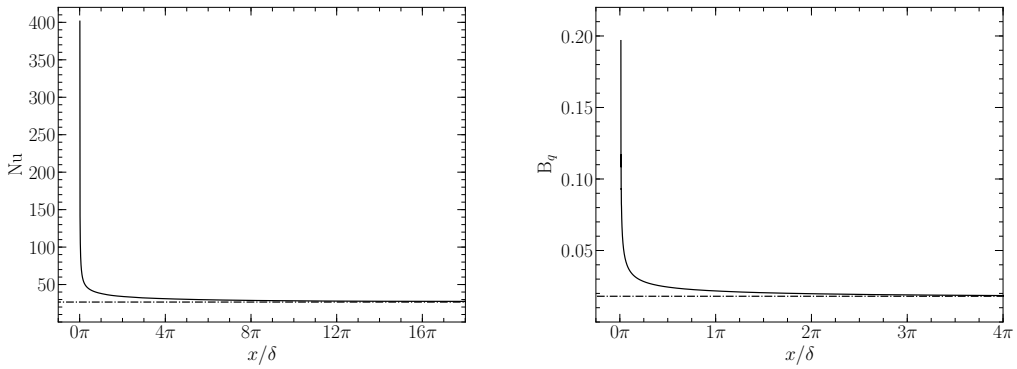

Figure 3.6: Nusselt number Nu (a) and heat flux parameter B_q (b) as a function of x/δ: —— present results; – · – · – equilibrium values of table 3.3.

table 3.3, instead, provides further confirmation of the evolution towards equilibrium of the thermal boundary layer.

As a whole, thanks to the results of §3.3.1 and of this section, it is possible to conclude that the given configuration and the numerical setup allow us to meet the aim of the study.

3.4 Results

This work aims at analysing the non-equilibrium evolution of an adiabatic, equilibrium boundary layer towards a new equilibrium state, which is characterised by a fully developed thermal boundary layer. These two equilibrium states have been presented and analysed in §3.3. The objective of this section, instead, is to investigate the most relevant phenomena which can be identified in the non-equilibrium phase of the flow. Although the DNS is performed at one single flow regime, certain physical events and flow characteristics are expected to be distinguishable in phenomenologically similar non-equilibrium flows, regardless of the particular regime. We aim at identifying these phenomena, and at providing the theoretical tools to investigate them.

In §3.4.1, the region in proximity of the leading edge is analysed, where due to the abrupt change of boundary conditions, non-equilibrium effects are the strongest. Particular attention is devoted to the velocity profiles and to the momentum balance, which, at $x/\delta \approx 0$, are significantly perturbed by the temperature gradient. Figure 3.7, for instance, shows some instantaneous contours of the wall shear stress near the leading edge. Observe how the contours are condensed around $x/\delta = 0$ to the point that the interface becomes clearly visible, signalling a discontinuity.

In §3.4.2, the gradual development of the thermal boundary layer is investigated. Along the isothermal wall, the edge of the growing thermal layer (of which an instantaneous visualisation is given in Figure 3.8) is at a non-equilibrium state. Yet, in a more inner region, a sub-layer can be identified, where several quantities are equilibrated. The notion of equilibrium and non-equilibrium layers are clarified in this section, and a definition based on the mean energy balance is proposed.

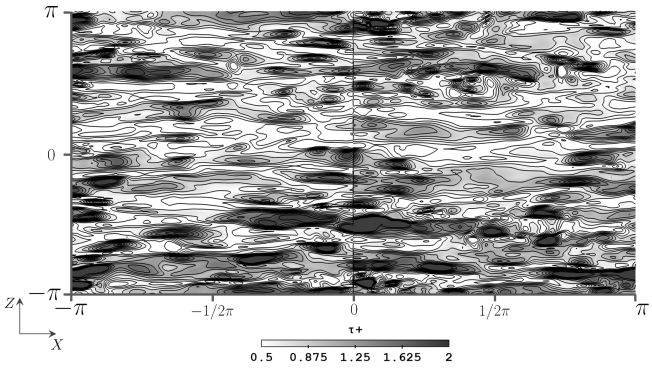

Figure 3.7: Leading edge effects. Contours of wall shear stress (τ_w) near the leading edge of the isothermal wall. Values are non-dimensionalised with respect to the average τ_w.

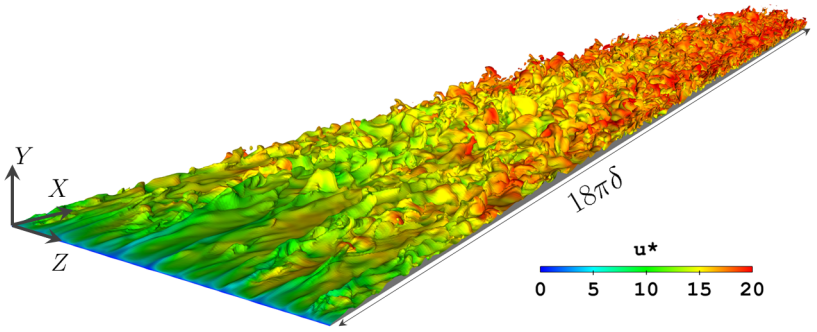

Figure 3.8: Instantaneous iso-temperature $\theta = \left(T - \overline{T}_{in}\right) / \left(T_w - \overline{T}_{in}\right) = 0.9$ along the channel, coloured by the friction velocity u^*.

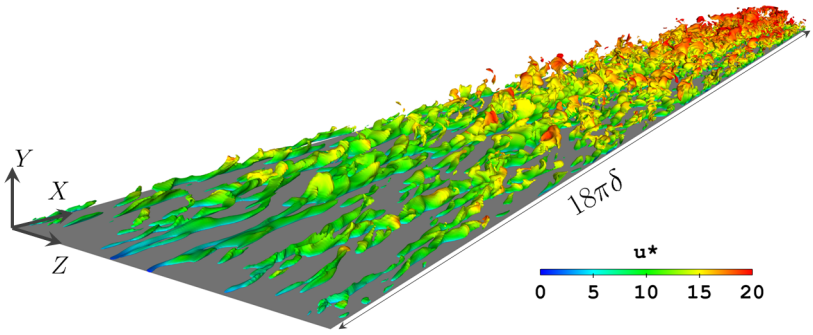

Figure 3.9: Instantaneous iso-surface of fluctuating temperature $(T^*)' = \left|T^* - \overline{T}^*\right| / T_\tau = 2$, coloured by the friction velocity u^*.

However, the analysis of Section 3.4.2 is effectuated in a mean sense and, therefore, the findings concerning the equilibrium sub-layer need to be contrasted to the evolution of several turbulent quantities. This is done in §3.4.3, where the behaviour of the fluctuating temperature (of which an instantaneous field is provided in Figure 3.9), turbulent heat flux and turbulent Prandtl number is investigated.

In the following, the same notation of Section 3.3 is used.

3.4.1 Analysis of the leading edge

The abrupt change of boundary conditions taking place at $x/\delta = 0$ generates enduring non-equilibrium effects which, as will be seen more in detail in §3.4.2, do not vanish completely even at the distance of $x/\delta = 18\pi$. However, there is a portion of the channel where these effects are so strong that the flow has a behaviour of its own that needs to be carefully investigated. This region is the leading edge, where the temperature gradient is the most elevated, as a consequence of the sudden change of thermal wall conditions (see the evolution of Nu and B_q in Figure 3.6). Since the temperature is not treated as a passive scalar in our simulation, an impact on the velocity fields and momentum balance is expected. On the other hand, in this region the thermal boundary layer is too thin for any appreciable phenomenon to be observed on the temperature.

Figure 3.10 shows the mean streamwise velocity for x/δ ranging between $[-0.06, 0.18]$ compared to the canonical profiles seen in §3.3. Even if semi-local scaling is used, none of the profiles agrees with the equilibrium ones, showing that, at these close distances from the leading edge, the perturbation cannot be ascribed to the only variation of mean fluid properties. This is particularly true for the profile at $x/\delta = 0.015$, for which the velocity boundary layer seems to be at equilibrium only for $y^* \lesssim 2$, *i.e.*, in the viscous sub-layer. The discrepancy of the profile at $x/\delta = -0.06$ with respect to the equilibrium profile of §3.3.1, instead, shows how the perturbation slightly propagates upstream.

A similar impact on the streamwise velocity has been observed by Sanchez et al. (2014) with a higher B_q, arguing that the perturbation should be ascribed to the increase of the wall-normal velocity induced by the temperature gradient. It is certainly true that the wall-normal velocity considerably increases near the leading edge, as it can be seen in Figure 3.11. Yet, the wall-normal velocity is also important at

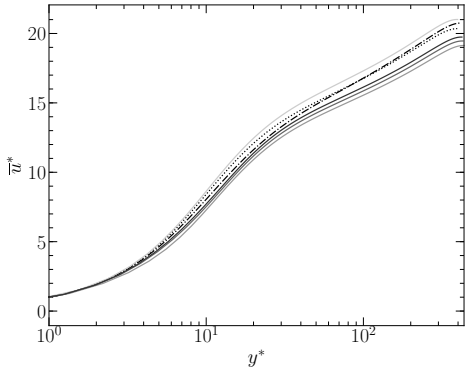

Figure 3.10: Mean streamwise velocity profile for different x/δ in semi-local scaling: —— present results at $x/\delta = -0.06,\ 0.015,\ 0.09,\ 0.18$ (from lightest to darkest respectively); ····· equilibrium profile of §3.3.1; – · – · – equilibrium profile of §3.3.2.

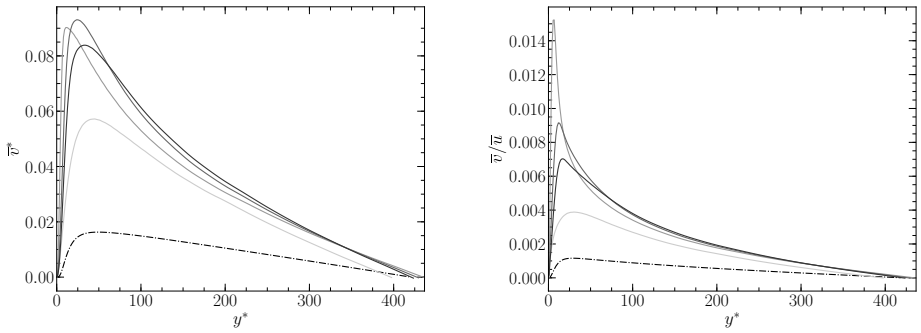

(a) (b)

Figure 3.11: Wall-normal velocity profile for different x/δ in semi-local scaling (a) and normalised with the mean streamwise velocity (b): —— present results at $x/\delta = 0.015, 0.18, 0.73$ (from lightest to darkest); – · – · – equilibrium profile.

$x/\delta = -0.06$, and, above all, always greater than zero. If the wall-normal velocity were the only responsible for the deviation of the streamwise velocity, the impact would be expected to be similar to the one observed downstream of the leading edge, where the normal velocity is also always positive and of the same order of magnitude. Instead, as can be seen in Figure 3.10, it is not the case, since an upper and lower shift is respectively observed at $x/\delta = -0.06$ and, for example, $x/\delta = 0.18$.

Hence, we propose a different interpretation, *i.e.*, that the destabilisation of the boundary layer is due to to the abrupt variation of the wall shear stress. Figure 3.12a shows the evolution of the skin friction coefficient $C_f = \overline{\tau_w}/\left(\frac{1}{2}\rho_b u_b^2\right)$, where ρ_b and u_b are respectively the bulk density and the bulk velocity. At $x/\delta = 0^+$, the skin friction coefficient is at its maximum, which can be explained by the abrupt increase of the fluid dynamic viscosity at the leading edge of the isothermal wall. Then, the following relaxation and adaptation of the velocity gradient at the wall to the increased viscosity, leads to a quickly decreasing C_f until it attains a plateau.

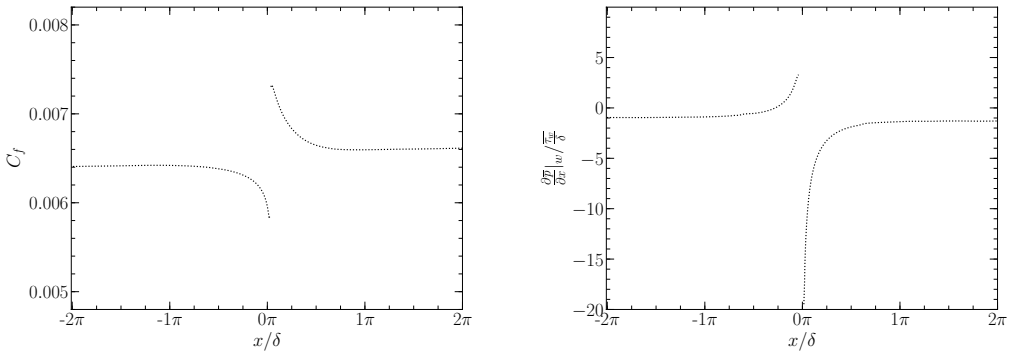

(a) (b)

Figure 3.12: Skin friction coefficient C_f (a) and non-dimensionalised wall pressure gradient (b) along the channel flow.

At $x/\delta = 0^-$, instead, the skin friction coefficient is at its minimum. This is due to the fact that the flow, being subsonic, perceives the upcoming isothermal wall, and adapts by decreasing the gradient of streamwise velocity at the wall, while the dynamic viscosity remains constant since the wall is adiabatic. This perturbation, limited to a very small portion of the channel flow between $x/\delta \in [-1/2\pi, 1/2\pi]$, results in a local perturbation of the wall streamwise pressure gradient, as it can be seen in Figure 3.12b. While $\frac{\partial \overline{p}}{\partial x}|_w / \frac{\overline{\tau_w}}{\delta} \approx -1$ far from the leading edge, a positive (and thus adverse) and strongly negative (and thus favourable) pressure gradient is observed at $x/\delta = 0^-$ and $x/\delta = 0^+$, respectively.

In order to take the effect of the streamwise pressure gradient into account, we introduce, following Simpson (1983), the velocity scale u_p defined as:

$$u_p = \left| \frac{\mu}{\rho^2} \frac{\partial p}{\partial x}\Big|_w \right|^{\frac{1}{3}} \tag{3.4.1}$$

which, combined with the classic friction velocity $u_\tau = |\tau_w/\rho|^{\frac{1}{2}}$, gives as proposed by Manhart et al. (2008):

$$u_{\tau p} = \sqrt{u_\tau^2 + u_p^2} \ . \tag{3.4.2}$$

We propose here a slight modification of this definition, which distinguishes positive and negative pressure gradients:

$$u_{\tau p} = \sqrt{u_\tau^2 + \text{sign}\left(\frac{\partial p}{\partial x}\Big|_w\right) u_p^2} \ . \tag{3.4.3}$$

In this manner, the decrease of u_τ in case of adverse pressure gradient, and its increase in case of favourable pressure gradient, are compensated by u_p, correcting the upward and downward deviation of the streamwise velocity at $x/\delta = 0^-$ and $x/\delta = 0^+$, respectively.

We can thus introduce the following wall scaling:

$$y^*_{\tau p} = \frac{y u_{\tau p}}{\nu} \qquad u^*_{\tau p} = \frac{u}{u_{\tau p}} \ , \tag{3.4.4}$$

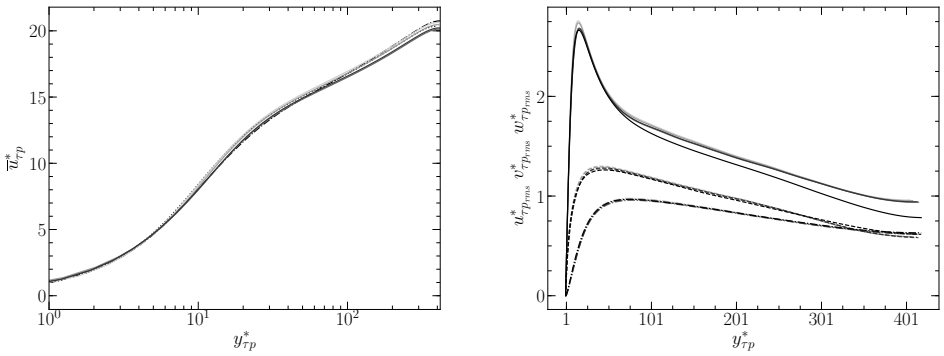

(a) (b)

Figure 3.13: Mean streamwise velocity profile for different x/δ in the newly introduced wall scaling (a). See Figure 3.10 for a reference to lines and colours.
Profiles of r.m.s. streamwise, wall-normal and spanwise velocity, respectively (b): ——, – · – · – and - - - - present results at $x/\delta = -0.06,\ 0.015,\ 0.09,\ 0.18$ and equilibrium (see §3.3).

where, analogously to semi-local scaling, fluid properties depend on the wall-normal direction in order to take the effect of the temperature gradient into account.

Figure 3.13a shows the same velocity profiles of Figure 3.10 in the newly introduced wall scaling, while Figure 3.13b illustrates the r.m.s. velocity profiles. Very good agreement is obtained between the different profiles in every region of the boundary layer, with the only exception of the r.m.s. streamwise velocity, for which the upward shift in the log layer has in any case to be ascribed to what is explained in §3.3.2.

The fact that the velocity profiles are corrected by adopting a different wall-scaling, suggests that, in our case, the perturbation is confined in the near-wall region and does not propagate towards the core of the flow. In the most general case, however, the leading edge effects are expected to become more important as B_q increases, with, in particular, larger wall-normal velocities and stronger variations of the pressure gradient. In these conditions, a modified wall-scaling might not suffice to correct these effects.

In order to corroborate our interpretation of the leading edge perturbations, the evolution of the different contributions to the momentum balance is analysed. For every crosswise section, integrating along the wall-normal direction the streamwise

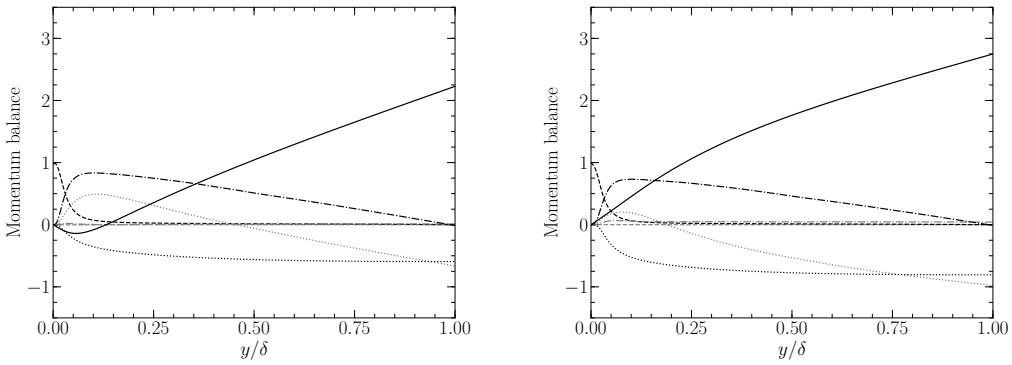

Figure 3.14: Momentum flux balance at $x/\delta = -0.06$ (a) and 0.18 (b): —— pressure gradient; - - - - streamwise (gray) and wall-normal (black) viscous terms; ····· streamwise (gray) and wall-normal (black) mean convective terms; – · – · – streamwise (gray) and wall-normal (black) turbulent terms.

momentum balance yields (see Appendix C.1 for the details):

$$\begin{aligned}\overline{\tau}_w(x) \;=\; & -\underbrace{\int_0^y \left(\overline{\rho}\widetilde{u}\frac{\partial \widetilde{u}}{\partial x}\right)\mathrm{d}y}_{I_x} - \underbrace{\int_0^y \left(\overline{\rho}\widetilde{v}\frac{\partial \widetilde{u}}{\partial y}\right)\mathrm{d}y}_{I_y} - \underbrace{\int_0^y \left(\frac{\partial \overline{p}}{\partial x}\right)\mathrm{d}y}_{II} + \\ & + \underbrace{\int_0^y \left(\frac{\partial \overline{\boldsymbol{\tau}_{xx}}}{\partial x}\right)\mathrm{d}y}_{III_x} + \underbrace{\overline{\boldsymbol{\tau}_{xy}}(y)}_{III_y} + \\ & - \underbrace{\int_0^y \left(\frac{\partial}{\partial x}\left(\overline{\rho}\widetilde{u''u''}\right)\right)\mathrm{d}y}_{IV_x} - \underbrace{\overline{\rho}\widetilde{u''v''}(y)}_{IV_y}\,, \end{aligned} \tag{3.4.5}$$

where on the right-hand side of the equation there are two mean convective terms (I_x and I_y), the pressure gradient (II), two viscous terms (III_x and III_y) and two terms associated with turbulent transport (IV_x and IV_y). Figure 3.14 shows the different terms non-dimensionalised with respect to the average local wall shear stress $\overline{\tau_w}$ as a function of y/δ for two values of x/δ, slightly upstream and downstream of $x/\delta = 0$.

Figure 3.14a is relative to $x/\delta = -0.06$. At this close distance from the leading edge, the terms of Eq. (3.4.5) are strongly perturbed. The pressure gradient flux does not follow a straight line, showing that $\partial\overline{p}/\partial x$ is not uniform along the wall-normal direction and that the pressure field is bidimensional; it is also evident how the streamwise pressure gradient is positive (and thus adverse) until $y/\delta \approx 0.05$. Both mean convective terms are important; note the positive slope of the streamwise convective term near the wall, indicating that $\partial\widetilde{u}/\partial x$ is negative and resulting in the aforementioned decrease of τ_w. The remaining terms seem not to be significantly modified, indicating that the perturbation of the pressure gradient is fully compensated by the two convective terms. This is in agreement with the hypothesis that the non-equilibrium contributions to the momentum balance tend to self-compensate (see Larsson et al., 2016).

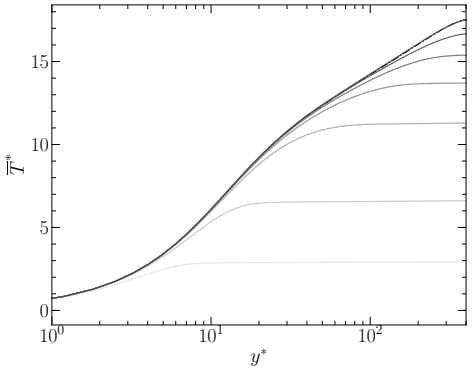

Figure 3.15: Profiles of mean temperature for different x/δ: —— present results at $x/\delta = 0.015$ - 0.21 - $\frac{1}{2}\pi$ - $\frac{3}{2}\pi$ - 3.6π - 7.75π - 17.9π (from lighter to darker); – · – · – equilibrium profile of §3.3.2.

Figure 3.14b is relative to $x/\delta = 0.18$. The pressure gradient flux still does not follow a straight line and the pressure field is thus two-dimensional; the positive slope of the pressure gradient term indicates that $\partial\overline{p}/\partial x$ is now negative for every y/δ. Both mean convective terms are still important; near the wall, like at $x/\delta = -0.06$, $\partial\widetilde{u}/\partial x < 0$, indicating that τ_w is decreasing. The perturbation of the momentum fluxes becomes negligible at $x/\delta \approx \pi/2$, and completely disappears by $x/\delta \approx 3\pi$, where the canonic momentum fluxes are finally retrieved, and the effects of the leading edge can be considered fully dissipated (not shown here).

Note that the results described in this section can only be observed if the temperature is not handled as a passive scalar, *i.e.*, if the momentum and energy equations are coupled.

3.4.2 Identification of an equilibrium sub-layer

Observe the behaviour of the instantaneous temperature iso-surface illustrated in Figure 3.8. Near the leading edge of the isothermal wall, the thermal layer is extremely thin, and the heated pockets are entirely located in the purely shear region of the flow. As the distance increases, these pockets thicken, breach through the viscous region and gradually become turbulent, until a fully developed state is attained at the outlet. The goal of this section is to describe the development of the thermal boundary layer from the leading edge to the outlet, and to identify, thanks to the mean energy balance, the different non-equilibrium regions of the flow.

The progressive development of the thermal boundary layer is shown in Figure 3.15, where several mean temperature profiles are plotted at different x/δ, and compared to the equilibrium profile of Section 3.3.2. For every x/δ, three distinct parts of the developing thermal boundary layer can be clearly identified. The first is the near wall region where, for $y^* \in [0, h^*_{eq}]$, where h^*_{eq} depends on and increases with x/δ, the thermal boundary layer is fully developed and the mean temperature profile agrees with the one at equilibrium; note that this equilibrated behaviour is visible even at $x/\delta = 0.015$, where the leading edge effects described in §3.4.1 are very much present. The second, for $y^* \in [h^*_{n-eq}, \delta^*]$, where h^*_{n-eq} also increases with x/δ, is a region that is still not affected by the isothermal wall and the temperature profile is flat. The third, for $y^* \in [h^*_{eq}, h^*_{n-eq}]$, is instead the actual non equilibrium devel-

oping portion of the thermal boundary layer, where the mean temperature profile is neither flat nor agreeing with the equilibrium one. As x/δ increases, both h^*_{eq} and h^*_{n-eq} tend towards the mid-height of the channel δ^*, and the non equilibrium region disappears.

The existence of an equilibrium region in the development of the thermal boundary layer has been shown experimentally, for example by Blom (1970) (who called this zone *adapted region*) or Teitel and Antonia (1993). The objective is to analyse the evolution of the equilibrium layer (delimited by h^*_{eq}) and of the non-equilibrium region (delimited by h^*_{n-eq}), yet it is first necessary to quantitatively define the notions of *equilibrium* and *non-equilibrium*.

We propose to do so through the analysis of the different terms of the energy balance. The integration along the wall-normal direction of the local averaged energy equation gives a local heat budget for every crosswise section (see Appendix C.2) for the details:

$$\begin{aligned}\overline{q}_w(x) \;=\; & \underbrace{\int_0^y \left(\overline{\rho}\widetilde{u}\frac{\partial \widetilde{h}}{\partial x}\right)\mathrm{d}y}_{I_x} + \underbrace{\int_0^y \left(\overline{\rho}\widetilde{v}\frac{\partial \widetilde{h}}{\partial y}\right)\mathrm{d}y}_{I_y} + \underbrace{\int_0^y \left(\frac{\partial \overline{q_x^{cd}}}{\partial x}\right)\mathrm{d}y}_{II_x} + \underbrace{q_y^{cd}}_{II_y} + \\ & + \underbrace{\int_0^y \left(\frac{\partial}{\partial x}\left(\overline{\rho}\widetilde{u''h''}\right)\right)\mathrm{d}y}_{III_x} + \underbrace{\overline{\rho}\widetilde{v''h''}}_{III_y} + \\ & - \underbrace{\int_0^y \left(\frac{\mathrm{D}\overline{p}}{\mathrm{D}t} + \overline{\boldsymbol{\tau} : \nabla \mathbf{v}}\right)\mathrm{d}y}_{IV} - \underbrace{yS_{ener}}_{V}\,, \end{aligned} \tag{3.4.6}$$

where on the right-hand side of the equation there are two mean convective terms (I_x and I_y), two mean conductive terms (II_x and II_y), two terms associated with turbulent heat transport (III_x and III_y), one flux combining compressibility effects (IV), and the source term contribution (V). The evolution of these terms, normalised by $\overline{q}_w$, is shown for several x/δ in Figure 3.16.

Figures 3.16a & 3.16b are relative to $x/\delta = 0.73$ and $x/\delta = 2\pi$, respectively. At these short distances from the leading edge, many contributions which do not appear in equilibrium channel flows, are important. It is the case, for example, of the wall-normal convective flux since, as illustrated in Figure 3.11, the mean vertical velocity is considerably higher compared to equilibrium. It is also the case of the streamwise turbulent flux, indicating that the correlation $\widetilde{u''h''}$ is evolving and increasing (in module). Yet, the preponderant contribution is that of the streamwise convective flux. Its positive slope near the wall indicates that the thermal boundary layer is developing and, as can be seen, the wall-normal conductive and turbulent fluxes are active. Farther away from the wall, its slope is negative and linear; since all the other contributions are constant, it is evident that the only active phenomenon is the uniform cooling caused by the source term. It is thus a portion of the boundary layer which still has not perceived the presence of the heated wall.

Further away from the leading edge, the canonic heat fluxes are gradually retrieved. At $x/\delta = 5.7\pi$ (see Fig. 3.16c), $\overline{\rho}\widetilde{v''h''} > 0$ everywhere but at $y/\delta = 1$, suggesting that the impact of the heated wall has by now reached the centre of the channel. At $x/\delta = 16.5\pi$ (see Fig. 3.16d), the thermal boundary layer seems to be at equilibrium. However, notice how at $y/\delta \approx 1$ the streamwise convective flux is negative and decreasing, indicating that the temperature at the centre of the channel is

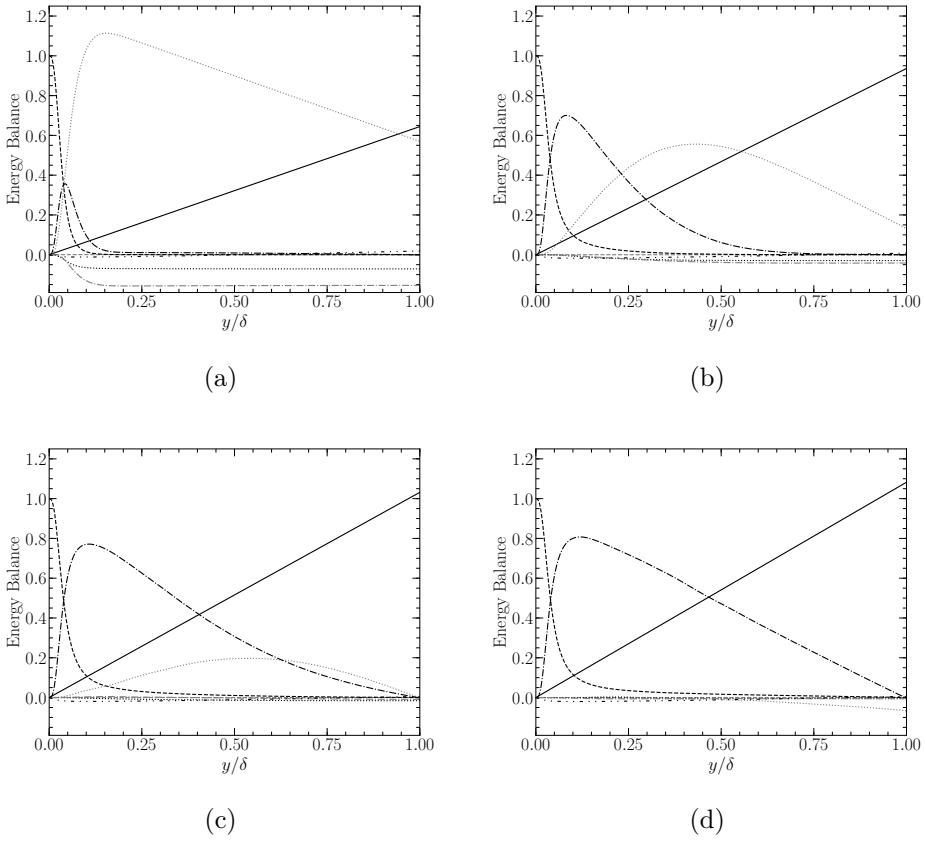

Figure 3.16: Energy flux balance at $x/\delta = 0.73$ (a), 2π (b), 5.7π (c) and 16.5π (d): —— source term; - - - - streamwise (gray) and wall-normal (black) conductive fluxes; ····· streamwise (gray) and wall-normal (black) convective fluxes; – · – · – streamwise (gray) and wall-normal (black) turbulent fluxes; – · · – compressibility effects.

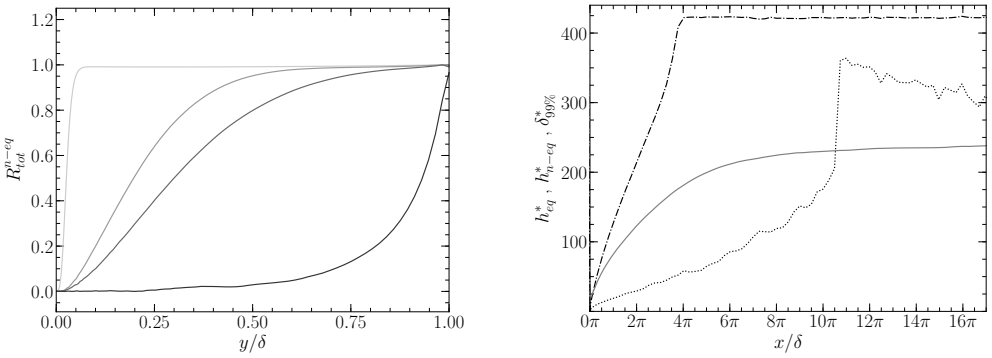

(a) (b)

Figure 3.17: Evolution of R_{tot}^{n-eq} with respect to y/δ for $x/\delta = 0.18$, 1.5π, 2.5π and 16.5π (from light gray to black) (a). Evolution of h_{eq}^*, h_{n-eq}^* and $\delta_{99\%}^*$ along the channel flow: $\cdots\cdots$ h_{eq}^*; $- \cdot - \cdot -$ h_{n-eq}^*; —— $\delta_{99\%}^*$ (b).

still cooling under the action of the source term. This signals that even at the outlet the thermal boundary layer is not perfectly developed, given the limited extent of the simulated channel.

The evolution of the different contributions to the energy balance shows that the fluxes can be divided into two categories. The former is that of the *equilibrium* terms, which tend to become more and more important with x/δ until stabilisation. The contributions that belong to this category are the wall-normal conductive flux and the wall-normal turbulent flux, which, summed, form the mean equilibrium flux q^{eq}. The latter is that of the *non-equilibrium* terms which, even if potentially preponderant near the leading edge, tend to become negligible and disappear with x/δ. The contributions belonging to this category are the streamwise and wall-normal convective terms as well as the streamwise turbulent flux, which form the mean non-equilibrium flux q^{n-eq}. The remaining contributions, at least in the present case, are always negligible.

Now, defining the average total heat flux q^{tot} as:

$$q^{tot} = \overline{q_w}(x) + yS_{ener} \ , \tag{3.4.7}$$

Equation (3.4.6) can be rearranged in the following form:

$$q^{tot} = q^{eq} + q^{n-eq} \ , \tag{3.4.8}$$

where the compressibility effects and the streamwise conductive flux have been neglected. For every x/δ and y/δ, it is thus possible to define the ratio:

$$R_{tot}^{n-eq} = \frac{|q^{n-eq}|}{|q^{eq}| + |q^{n-eq}|} \ , \tag{3.4.9}$$

quantifying the importance of the non-equilibrium terms in the energy balance.

Figure 3.17a shows the evolution of R_{tot}^{n-eq} along the wall-normal direction for different x/δ. The ratio R_{tot}^{n-eq} allows to define a quantitative criterion for distinguishing the three aforementioned regions of the developing thermal boundary layer. Indeed, as it can be seen in Figure 3.17a, for every x/δ there is a near-wall portion

of the boundary layer where the equilibrium fluxes are predominant with respect to the non-equilibrium ones; consequently $R_{tot}^{n-eq} \approx 0$ and the energy equation can be simply approximated as

$$\overline{q_w} + yS_{ener} \approx q_y^{cd} + \overline{\rho}\widetilde{v''h''} \ .$$

The equilibrium region of the boundary layer, delimited by $h_{eq}^*(x)$, can thus be defined as the region laying beneath an isoline of R_{tot}^{n-eq} in the $x-y$ plane, for example $R_{tot}^{n-eq} = 0.1$. For every x/δ, there is also a portion of the boundary layer adjacent to the centre of the channel, where the non-equilibrium terms are predominant; consequently $R_{tot}^{n-eq} \approx 1$, the only active physical phenomenon is the cooling caused by the source term and the mean temperature profile is flat along the wall-normal direction. This region of the boundary layer, delimited by $h_{n-eq}^*(x)$, can thus be defined as the region laying above an isoline of R_{tot}^{n-eq}, for example $R_{tot}^{n-eq} = 0.9$. Finally, for every x/δ and for $y^* \in [h_{eq}^*, h_{n-eq}^*]$, the equilibrium and non-equilibrium fluxes are of the same order of magnitude, and the thermal boundary layer is in development.

Figure 3.17b shows the evolution of h_{eq}^* (defined as the isoline $R_{eq}^{n-eq} = 0.1$) and h_{n-eq}^* (defined as the isoline $R_{eq}^{n-eq} = 0.9$) compared to the wall-scaled thermal boundary layer thickness $\delta_{99\%}^* := h^* \ : \ \left|T_w - \overline{T}(h^*)\right| / \left|T_w - \overline{T}_c(x)\right| = 0.99$.

The iso-line h_{n-eq}^* is defined by a very loose criterion on R_{tot}^{n-eq}. Therefore, the advance of h_{n-eq}^* towards the centre of the channel can benefit from the slightest expansion of the wall-normal heat flux, which takes place in regions of the flow where heat transport is efficiently carried out by turbulence. Consequently, the region beyond h_{n-eq}^* quickly decays and disappears before $x/\delta = 4\pi$. Downstream of this crosswise section, the effect of the heated wall has reached the centre of the channel and, as shown in Figure 3.15, the mean temperature profile is nowhere flat any more.

The iso-line h_{eq}^*, instead, is defined by a very stringent criterion on the development of the equilibrium terms. Therefore, its growth is initially driven by the slow development of the wall-normal conductive flux, which takes place in regions of the flow where heat transport is essentially carried out by diffusion. As h_{eq}^* grows and reaches the most turbulent parts of the boundary layer, its expansion accelerates, and, as can be qualitatively seen in Figure 3.17b, at $x/\delta \approx 10\pi$ its growth rate is similar to that of h_{n-eq}^* at $x/\delta \approx 3\pi$, where $h_{eq}^* \approx h_{n-eq}^* \approx 300$. However, h_{eq}^* does not reach the centre of the channel, and attains a peak at $y^* \approx 350$ before slowly decreasing. The criterion $R_{tot}^{n-eq} = 0.1$ is thus so stringent that the slight cooling of the source term at the centre of the channel (recall Figure 3.16d) becomes appreciable at a certain x/δ. With a higher criterion for h_{eq}^*, the same behaviour of h_{n-eq}^* would be observed. However, note that $h_{eq}^* > \delta_{99\%}^*$, indicating that the equilibrium sub-layer attains in any case an essentially temperature-homogeneous region.

The evolution of h_{eq}^* and h_{n-eq}^*, is understandably case-dependent. However, note that their definition, based on R_{tot}^{n-eq}, is general and can be used in all cases. By computing or estimating the size of h_{eq}^* and comparing it with respect to a characteristic length of a given flow configuration, one can thus quantify the importance of the thermal non-equilibrium effects in the flow.

Finally, Figure 3.18a shows the evolution of R_{tot}^{n-eq} as a function of x/δ for several wall distances. The intersection of every iso-y^* with the isoline $R_{tot}^{n-eq} = 0.1$ can be seen as the non-equilibrium distance associated to that wall distance, *i.e.*, the distance from the leading edge which is necessary for the thermal boundary layer

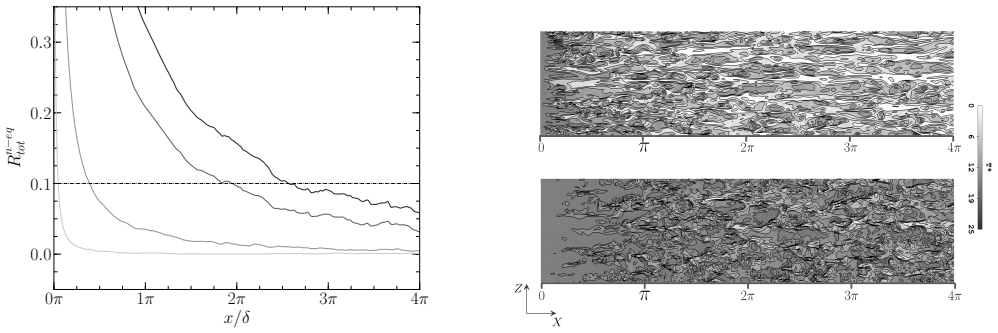

(a) (b)

Figure 3.18: Evolution of R_{tot}^{n-eq} as a function of x/δ for several wall distances: —— R_{tot}^{n-eq} for $y^* = 5$, 12.5, 30 and 40 (from light gray to black respectively); – · – · – isoline $R_{tot}^{n-eq} = 0.1$ (a). Instantaneous contours of temperature at $y^* = 12.5$ (above) and $y^* = 40$ (below) (b).

to be at equilibrium between the wall and the specified y^*. Some contours of T^* are given in Figure 3.18b at $y^* = 12.5$ (above) and $y^* = 40$ (below). By comparing Figures 3.18a and 3.18b, one can appreciate the correspondence between the values of R_{tot}^{n-eq} at these wall distances and the development of the heated turbulent structures as x/δ increases.

3.4.3 Development of turbulent heat transfer

The previous section has allowed us to appreciate and quantitatively define an equilibrium sub-layer, where both the mean temperature and the mean energy balance are equilibrated. In this section, we investigate its relevance with respect to the evolution along the isothermal wall of several turbulent quantities.

Figure 3.19 shows the evolution of the temperature fluctuations and of the wall-normal turbulent heat flux for different crosswise sections compared to equilibrium. Observe how both quantities progressively grow with x/δ, and how the peak shifts towards the higher y^*, until it stabilises at $y^* \approx 20$ for the r.m.s temperature and $y^* \approx 45$ for the turbulent heat flux.

The wall-normal turbulent heat flux (see Figure 3.19b) clearly exhibits an equilibrated behaviour in the near-wall region for every x/δ. Interestingly, the same cannot be said about the fluctuating temperature (see Figure 3.19a), which starts agreeing with equilibrium only at a certain distance from the leading edge ($x/\delta \approx 3/2\pi$). This illustrates how the r.m.s. temperature has a stronger inertia, and needs a larger distance to settle, an aspect which has also been observed experimentally (see Teitel and Antonia, 1993). Also observe, in Figure 3.9, the scant fluctuating structures near the leading edge. Figure 3.19b also outlines the fast wall-normal expansion of the turbulent heat flux during the early boundary layer development. As suggested in §3.4.2, this explains the fast decay of the region $y^* > h_{n-eq}^*$ seen in Figure 3.17b.

The turbulent budgets of the enthalpy variance are now analysed. The time-averaged transport equation of $\widetilde{h''^2}$ reads (see Appendix C.3 for the detailed devel-

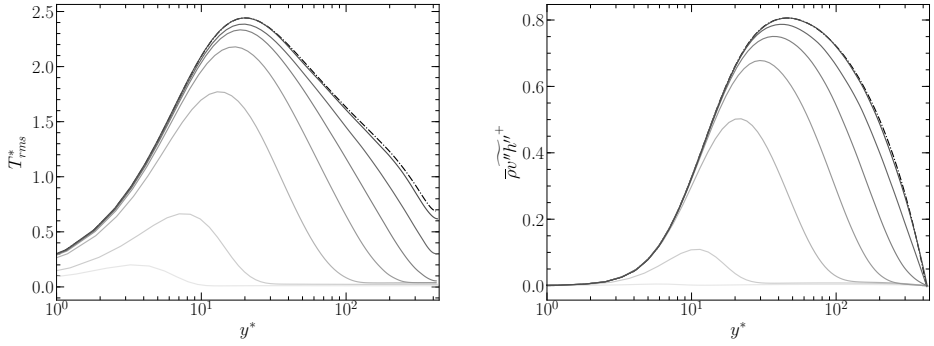

(a) (b)

Figure 3.19: Profiles of r.m.s temperature (a) and wall-normal turbulent heat flux (b) for different x/δ: —— present results at $x/\delta = 0.015$ - 0.21 - $\frac{1}{2}\pi$ - $\frac{3}{2}\pi$ - 3.6π - 7.75π - 17.9π (from lighter to darker); – · – · – equilibrium profiles of §3.3.2.

opment):

$$
\begin{aligned}
0 \;=\; & \underbrace{-\frac{\partial}{\partial x}\left(\overline{\rho}\widetilde{u}\widetilde{\frac{h''^2}{2}}\right)}_{I_x} \underbrace{-\frac{\partial}{\partial y}\left(\overline{\rho}\widetilde{v}\widetilde{\frac{h''^2}{2}}\right)}_{I_y} \underbrace{-\frac{\partial}{\partial x}\left(\overline{q_x^{cd'}h'}\right)}_{II_x} \underbrace{-\frac{\partial}{\partial y}\left(\overline{q_y^{cd'}h'}\right)}_{II_y} + \\
& \underbrace{+\overline{q_x^{cd'}\frac{\partial h'}{\partial x}} + \overline{q_y^{cd'}\frac{\partial h'}{\partial y}} + \overline{q_z^{cd'}\frac{\partial h'}{\partial z}}}_{III} + \underbrace{\overline{h'N'}}_{IV} \underbrace{-\overline{\rho}\widetilde{u''h''}\frac{\partial \widetilde{h}}{\partial x}}_{V_x} + \\
& \underbrace{-\overline{\rho}\widetilde{v''h''}\frac{\partial \widetilde{h}}{\partial y}}_{V_y} \underbrace{-\frac{1}{2}\frac{\partial}{\partial x}\left(\overline{\rho}\widetilde{u''h''h''}\right)}_{VI_x} \underbrace{-\frac{1}{2}\frac{\partial}{\partial y}\left(\overline{\rho}\widetilde{v''h''h''}\right)}_{VI_y} + \\
& \underbrace{+\overline{h''}\left(-\frac{\partial\overline{q_x^{cd}}}{\partial x} - \frac{\partial\overline{q_y^{cd}}}{\partial y} + \overline{N}\right)}_{VII},
\end{aligned}
\tag{3.4.10}
$$

composed of the streamwise and wall-normal mean convective terms (I_x and I_y) and molecular diffusion (II_x and II_y), molecular dissipation (III), a term of correlation between the enthalpy and N (IV), where $N = \frac{\mathrm{D}p}{\mathrm{D}t} + \boldsymbol{\tau}_{ij}\frac{\partial u_i}{\partial x_j} + S_{ener}$ regroups the compressibility effects and the source term, the streamwise and wall-normal production (V_x and V_y) and turbulent diffusion terms (VI_x and VI_y), and, finally, a term related to the enthalpy-density correlation (VII). Figure 3.20 shows the evolution of the different terms (scaled with respect to $\overline{q_w}(x)^2/\overline{\mu_w}(x)$) for different crosswise sections. For each x/δ, the values of h^*_{eq} and h^*_{n-eq} defined in §3.4.2 are put into evidence. Some terms (IV and VII), being always small and negligible, are not plotted.

Figure 3.20a is relative to $x/\delta = 0.73$. At this close distance from the leading edge, the different terms of (3.4.10) are active only in a small portion (approximately 10%) of the boundary layer, delimited by h^*_{n-eq}, beyond which the flow is still not affected by the heated wall. Observe how it is between h^*_{eq} and h^*_{n-eq} that the non-equilibrium

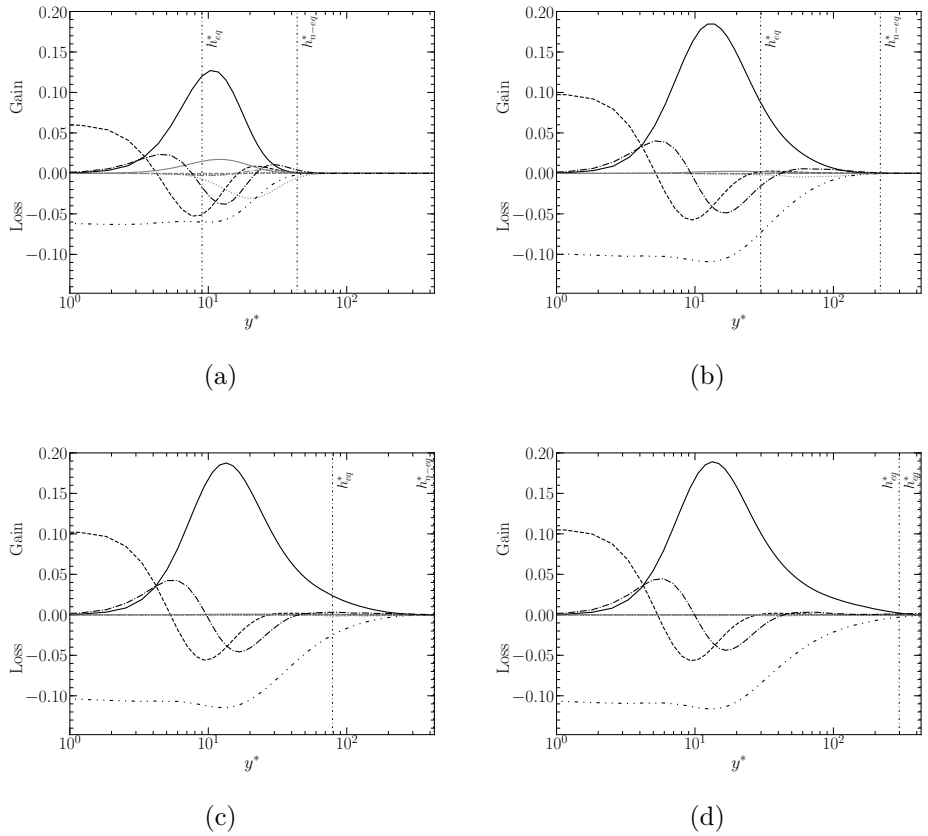

Figure 3.20: Budgets of enthalpy variance at $x/\delta = 0.73$ (a), 2π (b), 5.7π (c) and 16.5π : —— streamwise (V_x: gray) and wall-normal (V_y: black) production; - · · · · - molecular dissipation III; - - - - - streamwise (II_x: gray) and wall-normal (II_y: black) molecular diffusion; – · – · – streamwise (VI_x: gray) and wall-normal (VI_y: black) turbulent diffusion; ····· streamwise (I_x: gray) and wall-normal (I_y: black) mean convective terms.

effects are located, with non-negligible streamwise convective and production terms. The classic contributions (wall-normal production, molecular dissipation and wall-normal turbulent and molecular diffusion), instead, appear to be under-developed. This is true even between the wall and h^*_{eq}, which is in agreement with the low level of r.m.s. temperature observed near the leading edge.

Figure 3.20b is relative to $x/\delta = 2\pi$. It is interesting to notice how all the streamwise non-equilibrium terms in the temperature variance budget have vanished. In the region between h^*_{eq} and h^*_{n-eq}, while the mean energy balance presents strong non-equilibrium terms as seen in §3.4.2, the enthalpy variance budget seems to merely feature the gradual development of the classic terms. Observe how in the equilibrium sub-layer, instead, the different contributions controlling the r.m.s. temperature have by now settled, as can be seen by comparing figures 3.20b, 3.20c and 3.20d for $y^* < h^*_{eq}$. Accordingly, the r.m.s. temperature exhibits an equilibrated behaviour for $y^* < h^*_{eq}$ at these crosswise sections (see figure 3.19a).

Concerning the wall-normal turbulent heat flux, the time-averaged transport equation reads (see Appendix C.4 for the detailed derivation):

$$
\begin{aligned}
0 \;=\; & \underbrace{-\frac{\partial}{\partial x}\left(\overline{\rho}\widetilde{u}\widetilde{v''h''}\right)}_{I_x} \underbrace{-\frac{\partial}{\partial y}\left(\overline{\rho}\widetilde{v}\widetilde{v''h''}\right)}_{I_y} + \underbrace{\frac{\partial}{\partial x}\left(\overline{\tau'_{2,1}h'} - \overline{q_x^{cd'}u'}\right)}_{II_x} + \underbrace{\frac{\partial}{\partial y}\left(\overline{\tau'_{2,2}h'} - \overline{q_y^{cd'}v'}\right)}_{II_y} + \\
& \underbrace{-\left(\overline{\tau'_{2,1}\frac{\partial h'}{\partial x}} + \overline{\tau'_{2,2}\frac{\partial h'}{\partial y}} + \overline{\tau'_{2,3}\frac{\partial h'}{\partial z}}\right) + \left(\overline{q_x^{cd'}\frac{\partial v'}{\partial x}} + \overline{q_y^{cd'}\frac{\partial v'}{\partial y}} + \overline{q_z^{cd'}\frac{\partial v'}{\partial z}}\right)}_{III} + \qquad (3.4.11) \\
& \underbrace{-\overline{h'\frac{\partial p'}{\partial y}}}_{IV} + \underbrace{\overline{v'N'}}_{V} \underbrace{-\overline{\rho}\widetilde{u''h''}\frac{\partial \widetilde{v}}{\partial x} - \overline{\rho}\widetilde{u''v''}\frac{\partial \widetilde{h}}{\partial x}}_{VI_x} \underbrace{-\overline{\rho}\widetilde{v''h''}\frac{\partial \widetilde{v}}{\partial y} - \overline{\rho}\widetilde{v''v''}\frac{\partial \widetilde{h}}{\partial y}}_{VI_y} \underbrace{-\frac{\partial}{\partial x}\left(\overline{\rho}\widetilde{u''v''h''}\right)}_{VII_x} + \\
& \underbrace{-\frac{\partial}{\partial y}\left(\overline{\rho}\widetilde{v''v''h''}\right)}_{VII_y} + \underbrace{\overline{h''}\left(-\frac{\partial \overline{p}}{\partial y} + \frac{\partial \overline{\tau_{2,1}}}{\partial x} + \frac{\partial \overline{\tau_{2,2}}}{\partial y}\right) + \overline{v''}\left(\overline{N} - \frac{\partial \overline{q_x^{cd'}}}{\partial x} - \frac{\partial \overline{q_y^{cd'}}}{\partial y}\right)}_{VIII},
\end{aligned}
$$

composed of the mean streamwise and wall-normal convective terms (I_x and I_y) and molecular diffusion (II_x and II_y), the molecular dissipation (III), the enthalpy-pressure-gradient correlation (IV), the correlation between the wall-normal velocity and N (V), the streamwise and wall-normal production (VI_x and VI_y) and turbulent diffusion (VII_x and VII_y), and, finally, two terms related to the enthalpy-density and wall-normal-velocity-density correlations ($VIII$). Figure 3.21 shows the evolution of the different terms (scaled with respect to $\overline{q_w}(x)\overline{\tau_w}(x)/\overline{\mu_w}(x)$) for different crosswise sections with the respective h^*_{eq} and h^*_{n-eq} defined in §3.4.2. The terms V and $VIII$ are always small and negligible, and are not plotted. Most of the observations made concerning the budgets of enthalpy variance are still valid. The non-equilibrium region $h^*_{eq} < y^* < h^*_{n-eq}$ manifests itself with a gradual development of the classic terms (including, in this case, the enthalpy-pressure-gradient), rather than with the presence of strong streamwise terms as seen in §3.4.2 for the mean energy balance. In this case, the only streamwise terms that are important near the leading edge are the streamwise production and convection, as illustrated in figure 3.21a. Yet, even these terms become negligible at $x/\delta = 2\pi$ (see figure 3.21b).

The only difference with the enthalpy variance budget, is the behaviour for $y^* < h^*_{eq}$. For the wall-normal turbulent heat flux, the classic budgets have settled in

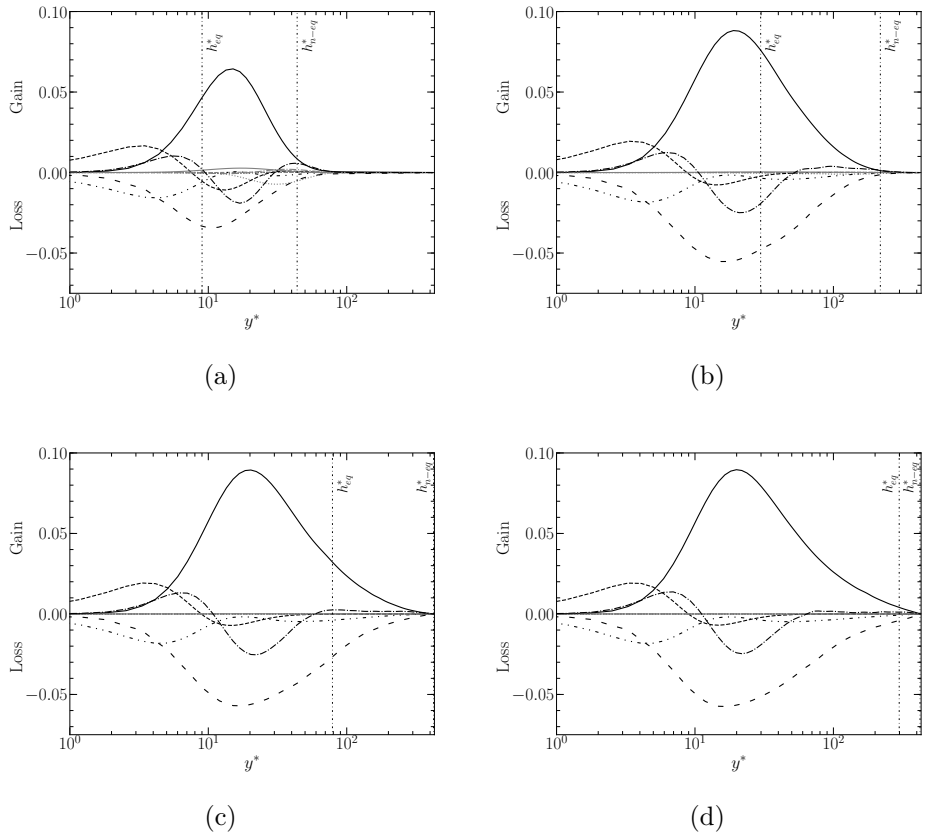

Figure 3.21: Budgets of wall-normal turbulent heat flux at $x/\delta = 0.73$ (a), 2π (b), 5.7π (c) and 16.5π: —— streamwise (VI_x: gray) and wall-normal (VI_y: black) production; - · · - · · - molecular dissipation III; - - - - - streamwise (II_x: gray) and wall-normal (II_y: black) molecular diffusion; – · – · – streamwise (VII_x: gray) and wall-normal (VII_y: black) turbulent diffusion; ····· streamwise (I_x: gray) and wall-normal (I_y: black) convective terms; - - - - - enthalpy-pressure-gradient correlation IV.

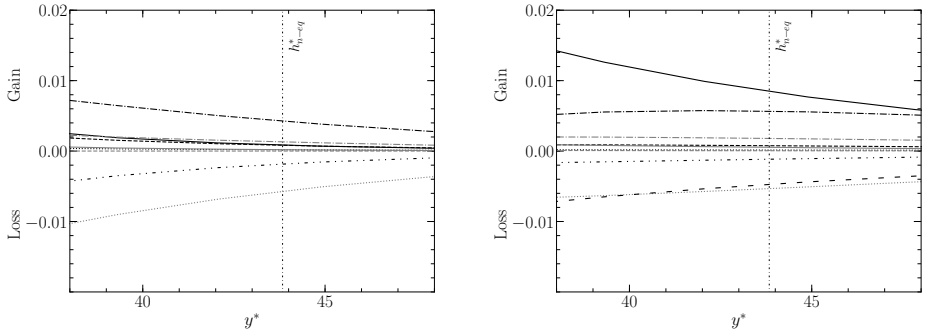

Figure 3.22: Budgets of enthalpy variance (a) and wall-normal turbulent heat flux (b) at $x/\delta = 0.73$ zoomed at $y^* \sim h^*_{n-eq}$. See Figures 3.20 and 3.21 for the notation.

the equilibrium sub-layer even for the smallest x/δ, which is in agreement with the equilibrated profiles observed for $y^* < h^*_{eq}$ in figure 3.19b.

Figure 3.22 shows the details of the budgets of enthalpy variance and wall-normal turbulent heat flux for $y^* \approx h^*_{n-eq}$ at $x/\delta = 0.73$, *i.e.*, the same crosswise section of figures 3.20a and 3.21a. In both figures 3.22a and 3.22b, it can be seen how the turbulent diffusion plays an important role in the development of both $\widetilde{h''^2}$ and $\widetilde{v''h''}$. In the case of the enthalpy variance, turbulent diffusion is actually the only term inducing a gain of enthalpy fluctuations, mostly counterbalanced by the mean streamwise convective term. The presence of non-negligible turbulent diffusion around $y^* \approx h^*_{n-eq}$ corroborates the hypothesis formulated in §3.4.2, *i.e.*, that the fast decay of the temperature-homogeneous region beyond $y^* > h^*_{n-eq}$ might be due to the efficient heat transport carried out by turbulence.

Finally, the behaviour of the turbulent Prandtl number Pr_t is investigated. Pr_t offers a simple way of relating the turbulent kinematic viscosity ν_t and conductivity λ_t in Reynolds-averaged Navier-Stokes (RANS), LES or wall-modelled LES (WMLES) turbulence modelling, and, analogously to the molecular Prandtl number, Pr_t is defined as:

$$\mathrm{Pr}_t = \frac{\overline{\rho}\nu_t\overline{c_p}}{\lambda_t} = \frac{-\overline{\rho}\widetilde{u''v''}}{-\overline{\rho}\widetilde{v''h''}/\overline{c_p}}\frac{\mathrm{d}\overline{T}/\mathrm{d}y}{\mathrm{d}\overline{u}/\mathrm{d}y} \ . \tag{3.4.12}$$

Experimentally, Blom (1970) analysed the evolution of the turbulent Prandtl number in a developing thermal boundary layer, and found that it varies in both wall-normal and streamwise directions, while suggesting that a universal distribution of Pr_t can only be expected in the near-wall region. Antonia et al. (1977) carried out similar investigations, and found that the turbulent Prandtl number is generally in the order of magnitude of one, thus showing the overall validity of the Reynolds analogy; according to their experimental results, values of Pr_t strongly exceeding unity can only be found near the leading edge of the thermal boundary layer.

Figure 3.23 displays the evolution of Pr_t for different x/δ, compared to its equilibrium profile. The latter, is represented by the dashed-dotted line. It can be seen that Pr_t is slightly greater than unity at the wall, before decreasing and attaining $\mathrm{Pr}_t \approx 0.7$ in the channel core flow. Its mild gradient along the wall-normal direction can justify the use of a constant average turbulent Prandtl number (usually

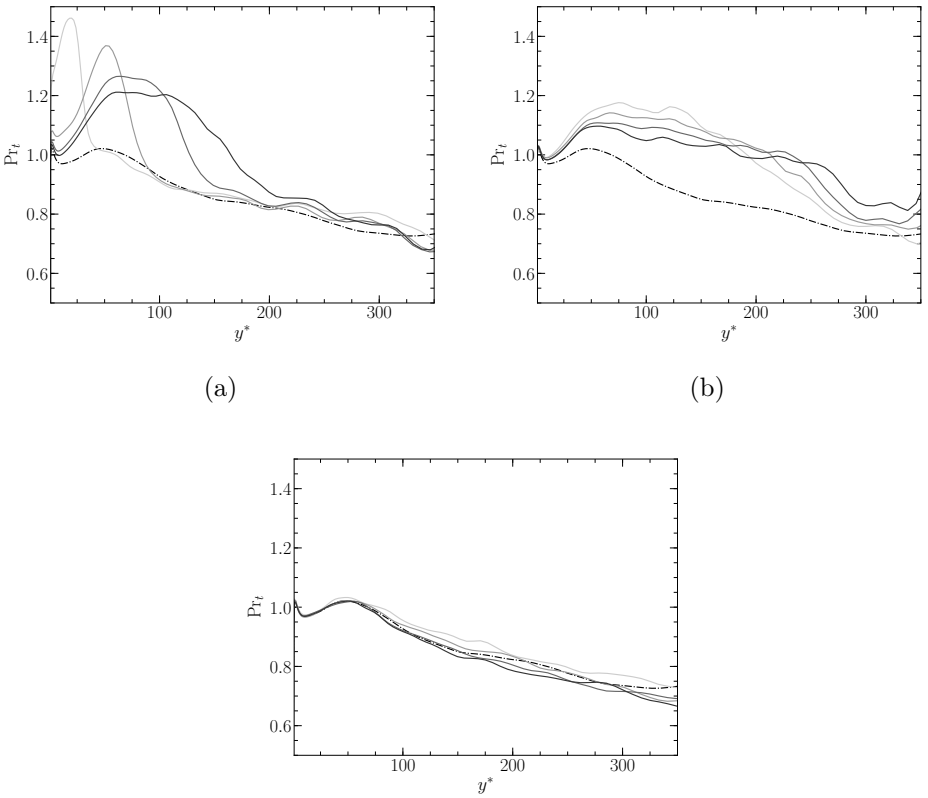

Figure 3.23: Evolution of turbulent Prandtl number in the wall-normal direction for different x/δ: —— present results at (from light to dark gray) $x/\delta = 0.18$, 0.73 0.5π and 0.75π (a), at $x/\delta = \pi$, 1.25π, 1.5π and 1.75π (b); at $x/\delta = 5.67\pi$, 8.25π, 10.8π and 16.5π (c); – · – · – equilibrium profile.

$\mathrm{Pr}_t \approx 0.9$), at least in equilibrium boundary layers (see, for instance, Kawai and Larsson, 2012).

Figure 3.23a shows the evolution of Pr_t for four crosswise sections which are relatively close to the leading edge. As can be seen, the turbulent Prandtl number does not exhibit an equilibrated behaviour in the near-wall region, where its value largely exceeds unity. Given the proximity to $x/\delta = 0$, this might represent another leading-edge effect caused by the abrupt variation of the fluid properties, in this case c_p. Further away from the leading edge, $\mathrm{Pr_t}$ remains for the most part greater than unity and, as x/δ increases, its perturbation expands in the wall-normal direction, while its intensity decreases. This tendency is particularly evident in Figure 3.23b, for x/δ ranging between $[\pi, 1.75\pi]$. The profiles of Fig. 3.23c, instead, illustrate how the turbulent Prandtl number essentially returns to equilibrium at $x/\delta \approx 5\pi$.

The larger values of Pr_t during the development of the thermal boundary layer, are explained by the fact that its numerator, ν_t, is already well-established with the incoming fully developed adiabatic flow; its denominator λ_t, instead, is initially small, since heat transfer is essentially carried out by mean convection, as seen in §3.4.2. The results are, therefore, in qualitative agreement with those of Antonia et al. (1977). On the other hand, there is no evidence of the existence of a universal distribution in the near-wall region, as indicated in Blom (1970). It appears to be quite the opposite since the highest values of Pr_t can be found near the leading edge in the very proximity of the wall.

3.5 Conclusion

The direct numerical simulation of a non-equilibrium turbulent thermal boundary layer is performed in a channel flow. Non-equilibrium is induced by a step-change in wall temperature, which perturbs a turbulent adiabatic flow initially at equilibrium. The flow later evolves towards a new equilibrium state, characterised by a fully developed thermal boundary layer. The simulation is performed under one single flow regime, in terms of Reynolds number, Mach number and temperature gradient. The study throws light on several physical phenomena which are expected to appear in phenomenologically similar non-equilibrium flows, providing the bases to understand them.

The leading edge of the isothermal wall appears to be the most perturbed region of the flow, with effects that also slightly propagate upstream. The temperature step-change causes a discontinuity of the wall shear stress and of the pressure gradient, which modify the velocity profiles. In our case, these modifications seem to be fully corrected by the adoption of a new wall-scaling, which takes into account both the mean fluid property variations and the pressure gradient. This suggests that the disturbance is confined in the very near-wall region, and does not propagate to the core of the flow. In the most general case, these effects are expected to appear at any discontinuity of thermal wall condition and, being regulated by the heat flux parameter B_q, to expand and aggravate as B_q increases, *i.e.*, for stronger temperature gradients or lower friction velocities. In these conditions, one should anticipate larger wall-normal velocities and stronger pressure gradient discontinuities astride the leading edge, the effects of which might not be corrected by only adopting a different wall-scaling.

The study has allowed for the identification of an equilibrium region, where several quantities are equilibrated. These quantities are the mean temperature, the energy

fluxes, the wall-normal turbulent heat flux and its budgets. Defined as the region of the flow where the equilibrium contributions to the energy balance are preponderant, the equilibrium sub-layer is initially confined in the shear region and slowly driven by heat diffusion, before it reaches the most turbulent part of the flow. Experimentally observed by several authors, there is reason to believe that it might be identifiable in any comparable non-equilibrium flow, where the same criterion on the energy balance contributions can be adopted to analyse it.

Other quantities do not have the expected behaviour in the equilibrium sub-layer. Low levels of temperature fluctuations, for instance, have been observed in the early development of the thermal boundary layer, accompanied by under-developed budgets of enthalpy variance. This illustrates the stronger inertia of the r.m.s. temperature, and it is an aspect that has also been observed experimentally. Finally, the turbulent Prandtl number exceeds unity in a relatively large portion of the flow, which includes part of the equilibrium sub-layer. The perturbation is due to the fact that heat transfer is initially carried out by mean convection, and only to a minor extent by turbulence. An important role is also played by the abrupt variation of fluid properties at the beginning of the isothermal wall, thus representing another leading edge effect. Even in the present case, characterised by a mild temperature gradient, different models for the turbulent Prandtl number might be required to take into account its modified behaviour in RANS or LES modelling of turbulent heat transfer.

Finally, we wish to draw a parallel with our industrial configuration, in order to understand what this physical study reveals to us about the aerothermal interactions taking place between the SACOC and the by-pass duct flow.

Concerning the leading edge effects, we have estimated (thanks to the conjugate-heat-transfer simulations that we will introduce in Part III) that the heat flux parameter amounts to $\mathrm{B}_q \sim 0.1$ at the leading edge. Note that it is the same order of magnitude that we have obtained in the channel flow described in this chapter. Indeed, the temperature difference between the wall and the upcoming adiabatic flow is similar in the two configurations; on the other hand, the heat flux is understandably higher for the SACOC, since the Reynolds number is more elevated; however, the higher Re is accompanied by a higher friction velocity u_τ; consequently, $\mathrm{B_q} = q_w/\rho_w c_{p_w} u_\tau T_w$ is all-in-all of the same order of magnitude. Therefore, we can reasonably conclude that in the by-pass duct we do not expect a stronger impact of the temperature gradient on the flow, compared to the channel investigated in this chapter.

The most important result of the chapter, is undoubtedly the identification of an equilibrium sub-layer. Its existence might be of fundamental importance for turbulence modelling, as simplifying equilibrium assumptions might be justified in the near-wall region, the resolution of which, as explained in the Introduction as well as in Chapter 1, constitutes the main impediment of wall-resolved LES. Our findings may *a priori* justify, for instance, the use of equilibrium wall-models in the WMLES of non-canonic flows, as long as the modelled portion of the flow lays within the aforesaid equilibrium layer. However, two major observations are due. First, we have seen that the equilibrium sub-layer exists, yet, we have also seen that near the leading edge it is extremely thin, and confined in the inner layer for quite some time; the use of equilibrium assumptions, therefore, might require extremely refined meshes to be legitimate; we will analyse this aspect in detail in the next chapter. Second, the development of the equilibrium sub-layer might be delayed, or even completely

disrupted, by other non-equilibrium effects penetrating every region of the boundary layer; in this case, only the most complex three-dimensional non-equilibrium wall-models or detached eddy simulation approaches can *a priori* yield accurate predictions. In Chapter 5, we will have the opportunity to investigate the behaviour of a developing thermal boundary layer in a realistic industrial configuration.

Chapter 4

Wall-modelled LES of a turbulent thermal boundary layer with a non-equilibrium behaviour

In this chapter, we proceed with the wall-modelled LES of the non-equilibrium thermal boundary layer studied in Chapter 3. The results that we have obtained have been the subject of the following scientific article which, at the time of writing, has been written and awaits submission to the journal *Physics of Fluids*:

— Gelain, M., Gicquel, O., Couilleaux, A., Vicquelin, R., *Wall-modelled LES of a turbulent thermal boundary layer with a non-equilibrium behaviour*, Physics of Fluids, to be submitted.

The results have also been presented at the 73$^{\text{rd}}$ Meeting of the Division of Fluid Dynamics of the American Physical Society in 2020:

— Gelain, M., Gicquel, O., Couilleaux, A., Vicquelin, R., *Wall-modeled LES of a turbulent thermal boundary layer with a non-equilibrium behavior*, In : 73rd Annual Meeting of the American Physical Society-Division of Fluid Dynamics. 2020.

4.1 Introduction

In Chapter 3, we have performed the physical study of a non-equilibrium heat transfer case, representing a simplified heat exchanger configuration. The use of direct numerical simulation (DNS) has enabled us to capture every aspect of the perturbation of a temperature gradient on an equilibrium flow. The study, in particular, has thrown light on the peculiar behaviour of the leading edge, where an appreciable disturbance of the velocity profiles has been observed, on the existence of an equilibrium sub-layer, where several mean quantities are equilibrated, and on the evolution of several turbulent properties of the flow, some of which have a behaviour of their own even in the equilibrium sub-layer. The analysis has allowed us to deepen our

knowledge of non-equilibrium flows, and represents a significant advancement of the state of the art.

Unfortunately, as we have already mentioned in the Introduction, in the most general case we cannot rely on DNS for investigating such flows, due to its severe Reynolds number limitation. Even Large-eddy Simulation (LES), as discussed in Chapter 1, does not constitute a sufficiently low-cost alternative, at least in the case of high-Reynolds wall-bounded flows. Given the current computer power limitations, alleviating the computational cost of LES to the detriment of a certain degree of its physical fidelity is still today a necessity. In the Introduction, we have mentioned two families of methods, which allow to considerably reduce the resolution cost of the near-wall region. The former is Detached Eddy Simulation (DES), that we have briefly presented and will not examine more in depth. The latter, is wall-modelled LES (WMLES), to the description of which we have dedicated the entire Chapter 1, and that we have decided to implement and test in this work.

These two methods, despite being conceptually very different, have similar advantages and drawbacks, and represent serious candidates for replacing or juxtaposing RANS modelling for concrete industrial applications. Historically, however, WMLES has mainly been applied to equilibrium boundary layers; we can cite, for instance, the works by Benarafa et al. (2007), Kawai and Larsson (2012), Bocquet et al. (2012) and Lodato et al. (2014). The interest of the community has only recently been increasingly drawn to more complex, non-equilibrium configurations. The main non-equilibrium effects which have been considered are pressure gradients and mean-flow three-dimensionality, which are of undeniable importance in most industrial applications, including ours; we can cite, for instance the works by Duprat et al. (2011), Park and Moin (2014), Giometto et al. (2017) and Cho et al. (2021). In this chapter, we propose to address a different class of non-equilibrium effects, *i.e.*, that of turbulent boundary layers presenting thermal non-equilibrium effects, which are also very common in many flows of practical interest, not least the SACOC. Yet, to the best of our knowledge, the capability of WMLES to accurately describe any sort of thermal non-equilibrium effect has never been assessed before.

In this chapter, we consider the same configuration of Chapter 3, and we aim at evaluating the prediction capability of two wall-models with respect to the DNS results. The former is a classic equilibrium model based on one-dimensional thin boundary layer equations (TBLE) for the momentum and energy, *i.e.*, the model implemented and validated in Sections 1.3 and 1.4. The latter, is a new *ad hoc* non-equilibrium wall-model that we construct by identifying, thanks to the DNS, the most influential non-equilibrium effects not taken into account by the equilibrium wall-model.

The chapter is organised as follows. In §4.2, the problem is briefly described, as a lot of information has been given in both Chapters 1 and 3. In §4.3, the results obtained with the equilibrium wall-model are presented. In §4.4, a new-equilibrium wall-model is constructed, validated *a priori* and tested *a posteriori*. This is followed by the conclusions, which are discussed in §4.5.

4.2 Problem description

The studied configuration is identical to the one described in Chapter 3. Therefore, we limit ourselves to reminding the fundamental features of the study case and to underlining any remarkable difference from the DNS setup illustrated in §3.2.2.

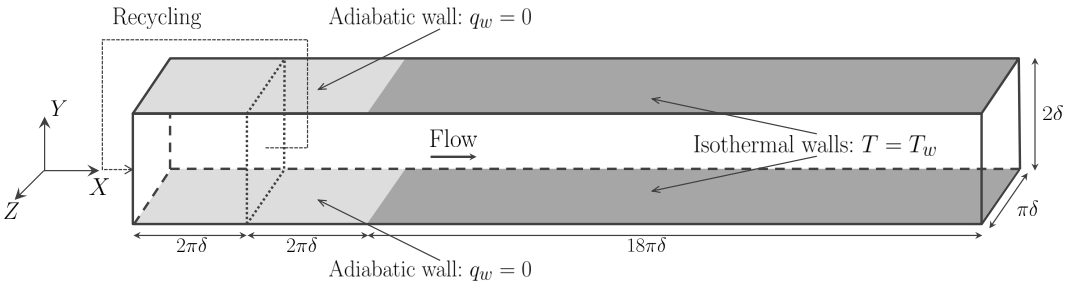

Figure 4.1: Computational domain of the present study.

Size	Re_τ	M	T_b (K)
$[4\pi\delta, 2\delta, \pi\delta]$	395	0.16	304.5

Table 4.1: Size and regime conditions of upstream (adiabatic) sub-domain.

The computational domain, illustrated in Figure 4.1, is a channel flow of size $22\pi\delta \times 2\delta \times \pi\delta$ (where $\delta = 0.002$ m) which is made of two parts in the streamwise direction.

The upstream part has size $4\pi\delta \times 2\delta \times \pi\delta$, the upper and lower walls (with respect to the Y direction) are adiabatic while periodic boundary conditions are applied in the spanwise direction Z. The role of this part of the domain is to generate a temperature-homogeneous boundary layer at equilibrium with the regime conditions specified in Table 4.1. In order to do so at a moderate cost, a recycling strategy is used: the three velocity components and the temperature imposed at the domain's inlet are extracted from a recycling plane situated downstream at a distance of $2\pi\delta$. It is because of the recycling strategy that, as mentioned in §1.3.2, we have preferred using the no-slip formulation by Nicoud et al. (2016); in fact, with the classic slip formulation, negative streamwise velocities can appear at the wall, which, once re-injected at the inlet, lead the simulation to a crush.

The downstream part of the domain has size $[18\pi\delta, 2\delta, \pi\delta]$, the upper and lower walls are isothermal, both at temperature $T_w = 400$ K. The role of the downstream part is to allow the thermal boundary layer to be fully developed and to attain a new equilibrium state before the exit. In order to prevent the mean temperature from asymptotically approaching the fixed wall temperature, which would make the identification of the established regime tedious, a (negative) source term S_{ener} is added to the energy equation, thanks to which a non-homogeneous temperature profile is maintained along the wall-normal direction. The value prescribed to the energy source term is the same specified in §3.2.2. The regime conditions of the downstream part of the domain are given in Table 4.2.

The computational domain of Fig. 4.1 is discretised with a mesh composed of 551, 41 and 51 points uniformly distributed in the streamwise, wall-normal and spanwise direction, respectively, giving, in wall-units and with respect to the regime conditions specified in Table 4.1, a spatial resolution of $\Delta X^+ \approx 50$, $\Delta Y^+ \approx 20$ and $\Delta Z^+ \approx 25$. The mesh is undoubtedly too coarse for the inner-layer's turbulent structures to be

Size	T_w (K)	B_q^{eq}	Nu^{eq}	Re_τ^{eq}	$\left(\frac{T_w}{\overline{T}_c}\right)^{eq}$	$\frac{T_w}{\overline{T}_{in}}$
$[18\pi\delta, 2\delta, \pi\delta]$	400	0.018	26.6	292	1.38	1.31

Table 4.2: Size and regime conditions of downstream (isothermal) sub-domain. $T_w/\overline{T}_{in}$ is the temperature ratio between the wall and the inlet.

adequately resolved by the LES, regardless of the sub-grid scale model implemented. As a consequence, as explained in Chapter 1, imposing the classic no-slip boundary condition $\widetilde{\mathbf{v}} = \mathbf{0}$ at the upper and lower walls (with the addition of $\widetilde{T} = T_w$ for the isothermal part of the domain) would incur important inaccuracies in the prediction of the mean flow statistics. Hence, the near-wall turbulent eddies need to be differently modelled and we propose to do so by employing a wall-model, which provides approximate boundary conditions for every grid point on the lower and upper walls of the fluid domain.

Also note that, differently from what is done in Chapter 3, the mesh is not refined near the leading edge in the streamwise direction. Thus, we renounce trying to capture the leading edge effects that we have observed in Section 3.4.1, which are located in a very limited portion of the channel ($x/\delta = [-\pi/2, \pi/2]$). The choice is motivated by the fact that a resolution of $\Delta X^+ \sim 1$ in the streamwise direction would have excessively penalised the time-step of the simulation.

Concerning the set of equations, laws, numerical scheme and turbulence model used for the outer-layer LES, the reader is referred to §1.3.1.

4.3 Equilibrium wall-modelling: setup, validation and results

In this section, we assess the capability of an equilibrium wall-model to describe the non-equilibrium development of a thermal boundary layer. The use of an equilibrium model in this configuration may seem counter-intuitive. However, as we have shown in Chapter 3, there is a portion of the developing thermal layer where several quantities, especially the contributions to the energy balance, are equilibrated, and where a canonic wall-model could well mimic the energy transport.

The section is organised as follows. In §4.3.1, we briefly recall the equations constituting the wall-model that we have already thoroughly described in §1.3 and §1.4. In §4.3.2, the setup is validated with respect to the configuration of Fig. 4.1; in particular, we need to verify if the velocity boundary layer is at equilibrium at $x/\delta = 0$, and if the temperature one is fully developed at $x/\delta = 18\pi$. In §4.3.3, results are presented and compared to the DNS of Chapter 3. Finally, in §4.3.4, conclusions upon the use of equilibrium wall-models in non-equilibrium flows are drawn.

4.3.1 Numerical setup

We only remind the reader the momentum and energy equations constituting the equilibrium wall-model used in this section:

$$\frac{\mathrm{d}}{\mathrm{d}y}\left[(\overline{\mu}+\mu_t)\,\frac{\mathrm{d}\overline{u}}{\mathrm{d}y}\right]=0\ , \tag{4.3.1}$$

$$\frac{\mathrm{d}}{\mathrm{d}y}\left[(\overline{\lambda}+\lambda_t)\,\frac{\mathrm{d}\overline{T}}{\mathrm{d}y}\right]=0\ , \tag{4.3.2}$$

where, as can be seen, only the equilibrium contributions defined in §3.4.2 are present. For all the details concerning the turbulence model, discretisation, numerical resolution, coupling algorithm *etc.*, the reader is referred to Sections 1.3 and 1.4. Recall, in particular, that we place the matching-point at the fourth off-wall point, according to the LLM-removing strategy by Kawai and Larsson (2012).

4.3.2 Validation

Our WMLES setup has already been validated in §1.4 with respect to an equilibrium configuration, *i.e.*, the fully developed bi-periodic channel flow. However, validation with respect to the configuration of Fig. 4.1 is required to verify that the recycling method functions as desired, and that a fully developed thermal boundary layer is obtained near the outlet.

Figure 4.2 shows the mean streamwise and r.m.s. velocities at $x/\delta \approx 0$, compared to the DNS profiles of the upstream equilibrium state of §3.3.1. Excellent agreement is obtained for the mean streamwise velocity (see Fig. 4.2a), illustrating that the velocity boundary layer is fully developed at the leading edge of the isothermal wall. On the other hand, a significant upward shift is observed for the r.m.s. streamwise velocity (see Fig. 4.2b). We suspect, as in §3.3.1, that this effect is due to the ongoing perturbation of the recycling method, which appears to be even more important in this case, with respect to the DNS. For the remaining r.m.s. velocity components, instead, the usual behaviour is retrieved, with only a slight over-prediction near the matching-point.

Similar profiles are shown for $x/\delta \approx 18\pi$ in Figure 4.3, compared to the DNS profiles of the downstream equilibrium state of §3.3.2. Once again, excellent agreement is obtained for the mean streamwise velocity (see Fig. 4.3a). Also observe that most of the upward shift of the r.m.s. streamwise velocity (see Fig. 4.3b) has also been absorbed, showing how the disturbance of the recycling method disappears downstream. The inaccuracies near the matching-point, instead, have to be ascribed to the usual over-prediction of the turbulent intensity in WMLES, which has also been observed in §1.4.

Finally, Figure 4.4a and 4.4b illustrate the mean and r.m.s. temperature profiles, respectively, at $x/\delta \approx 18\pi$. Excellent agreement is obtained for the mean temperature, while a slight under-prediction of the r.m.s. temperature is observed near the centre of the channel, showing, similarly to the conclusions drawn in §3.3.2 for the DNS, that a longer isothermal wall would have been necessary to allow the boundary layer to fully converge towards equilibrium.

As a whole, both equilibrium states are well retrieved at $x/\delta \approx 0$ and $x/\delta \approx 18\pi$, allowing us to validate the numerical setup.

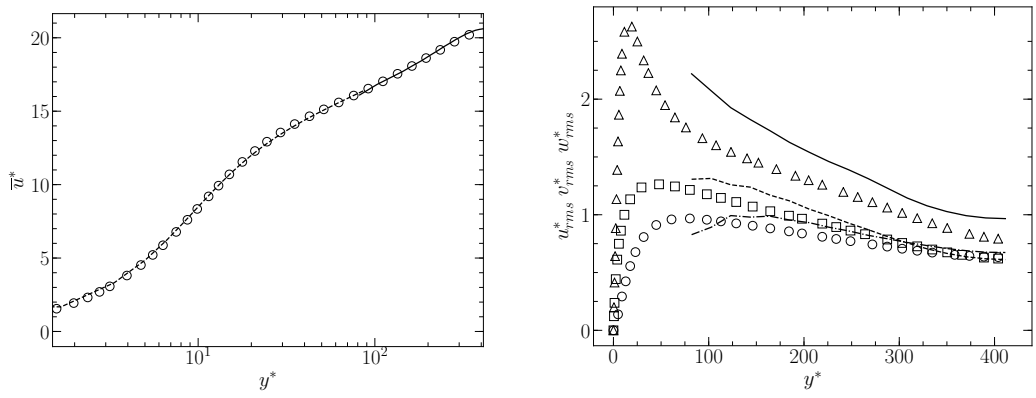

(a) (b)

Figure 4.2: Validation of equilibrium wall-model. Profiles of mean streamwise velocity at $x/\delta \approx 0$ (a): —— present LES results; - - - - present TBLE profile; ○ DNS results from §3.3.1.
Profiles of r.m.s. streamwise, wall-normal and spanwise velocities at $x/\delta = 0$ (b): ——, – · – · – and - - - - present LES results; △, ○ and □ DNS results from §3.3.1.

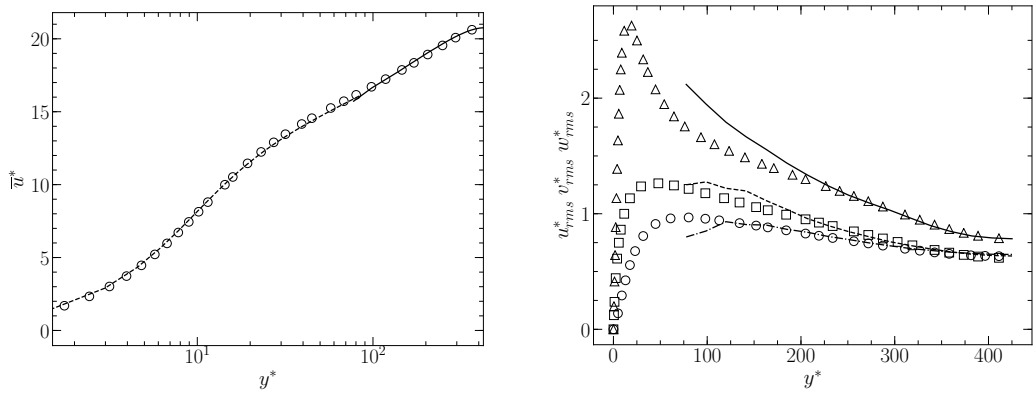

(a) (b)

Figure 4.3: Validation of equilibrium wall-model. Profiles of mean streamwise (a) and r.m.s. (b) velocities at $x/\delta = 18\pi$. DNS profiles from §3.3.2. See Figure 4.2 for a reference to lines and symbols.

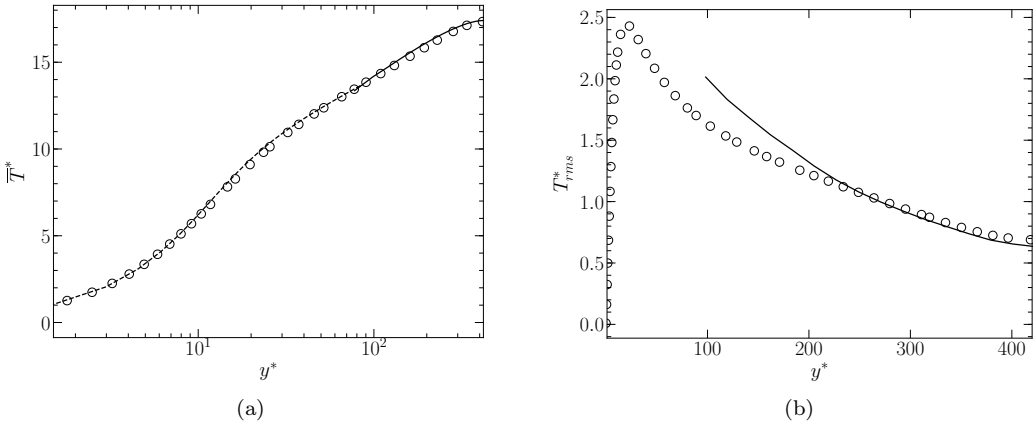

Figure 4.4: Validation of equilibrium wall-model. Profiles of mean (a) and r.m.s. (b) temperature at $x/\delta = 18\pi$: —— present LES results; - - - - present TBLE profiles; ○ DNS results from §3.3.2.

4.3.3 Results

The results obtained with the equilibrium wall-model on the configuration described in §4.2 are now presented. In the following, $\overline{(\cdot)}$ denotes Reynolds average. Spatially, quantities are only averaged along the Z axis, which is the only homogeneous direction for this configuration. Apex $(\cdot)^*$ denotes semi-local scaling. The wall-distance y_h^*, refers, as in Chapter 1, to the location of the matching-point. The origin of the axes is placed at the interface between the adiabatic and the isothermal wall so that the adimensionalised X coordinate x/δ is defined within the range $[-4\pi, 18\pi]$ between the inlet and the outlet. Finally, unless differently specified, every value at the wall or at the centre of the channel flow, respectively denoted as $(\cdot)_w$ and $(\cdot)_c$, has to be intended locally with respect to the X coordinate.

Figure 4.5 shows the mean temperature profiles obtained with the equilibrium wall-modelled LES along the channel flow, compared to the DNS results of §3.4.2. The profiles of Fig. 4.5a are taken from four locations that are relatively close to the leading edge of the isothermal wall. As can be observed from the DNS profiles, especially at $x/\delta = \pi/4$, the thermal boundary layer is extremely thin and characterised by the three distinct regions we have introduced in §3.4.2: the *equilibrium* near-wall region, where the thermal boundary layer is fully developed, the *non-equilibrium* region, where the boundary layer grows, and, finally, the *adiabatic* region, which still has not been perturbed by the isothermal wall and the temperature profile is flat. From the WMLES profiles of Fig. 4.5a, it can be seen how the second of these regions is completely missing, and the equilibrium region (for $y^* \in [0, y_h^*]$) abruptly switches to the *adiabatic* one (for $y^* \in [y_h^*, \delta^*]$). This, of course, is due to the equilibrium wall-model which, between the wall and the matching-point, cannot but return the temperature profile of a fully developed boundary layer. Consequently, the temperature plateau predicted by the WMLES is at a higher value, which indicates that the wall-heat flux is underestimated.

Further away from the leading edge of the isothermal wall (see Fig. 4.5b), however, the equilibrium region grows, even if spuriously, since the wall heat flux is badly predicted, and, at $x/\delta \approx 2\pi$, attains the matching-point. The non-equilibrium por-

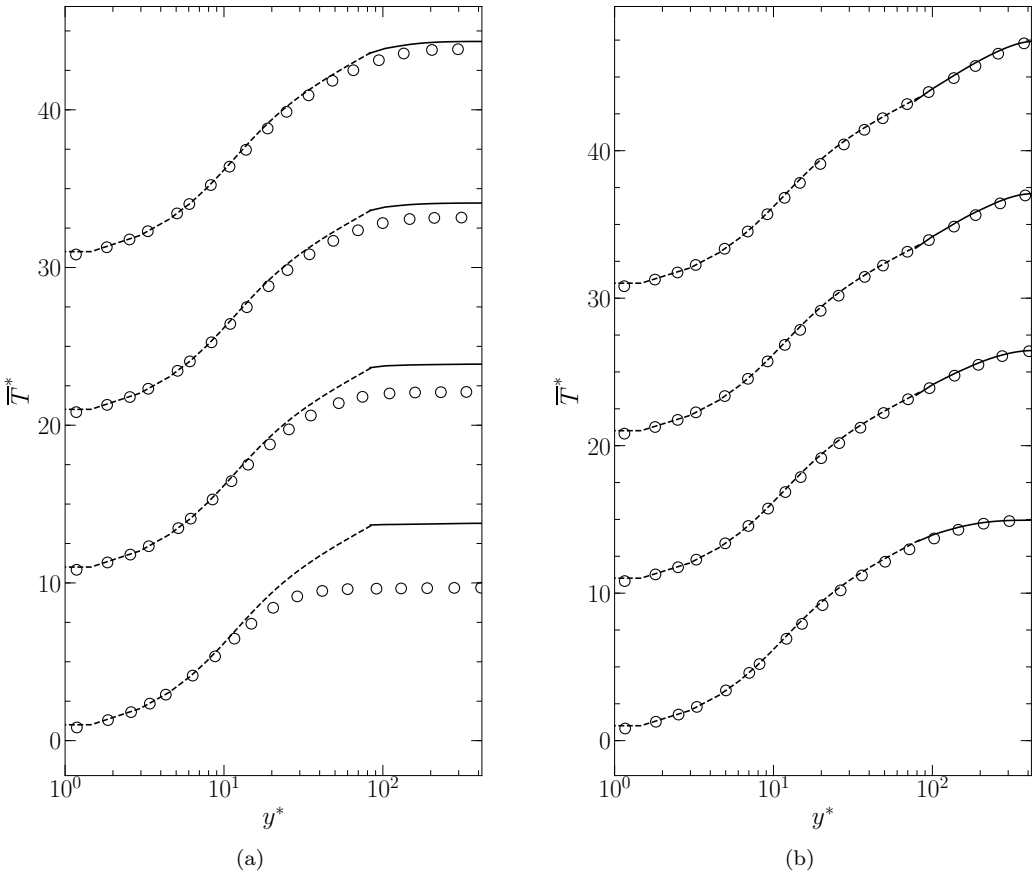

Figure 4.5: *A posteriori* results with equilibrium wall-model. Mean temperature profile for eight streamwise locations: from bottom to top, $x/\delta = \frac{\pi}{4}, \frac{3}{4}\pi, \frac{5}{4}\pi, \frac{7}{4}\pi$ (a) and $x/\delta = 3\pi, 7\pi, 11\pi, 17\pi$ (b) ; ○ DNS profile from §3.4.2; —— present LES results; - - - - equilibrium wall-model. Profiles are shifted by ten on the vertical axis for the sake of clarity.

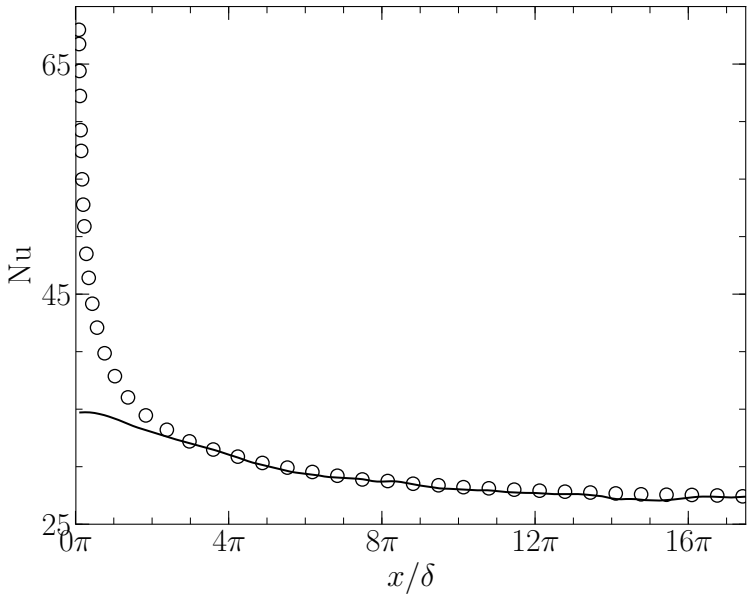

Figure 4.6: Equilibrium wall-model. Evolution of the Nusselt number along the channel flow: —— DNS profile from §3.3.2; ○ present LES results.

tion of the boundary layer, as well as what remains of the vanishing adiabatic one, are now entirely located in the outer-layer, and the non-dimensional temperature profile is well retrieved from the wall to the centre of the channel.

The overall accuracy of the WMLES in describing the development of the thermal boundary layer is well summarised by the evolution of the Nusselt number, defined as

$$\mathrm{Nu} = 2\delta \frac{q_w}{\lambda_w \left(T_w - \overline{T}_c\right)} \ ,$$

which is shown in Figure 4.6. According to the DNS profile, the Nusselt number is very important near the leading edge, and later decreases until convergence as the thermal boundary layer develops and establishes; on the other hand, the profile obtained with the WMLES is essentially flat, presenting a barely visible leading edge effect. In other words, the Nusselt number abruptly changes from zero at $x/\delta = 0^-$, to approximately its established value at $x/\delta = 0^+$, illustrating how the wall-model fails to capture the strong non-equilibrium effects occurring near the leading edge. Satisfactory agreement with the DNS profile is only attained at $x/\delta \approx 2\pi$, where, as previously mentioned, the matching-point is located in the equilibrium region of the thermal boundary layer.

So as to fully understand the behaviour of the wall-model in the present case, we need to recall the definition of equilibrium sub-layer. As seen in §3.4.2, we have proposed a quantitative definition of equilibrium based on the analysis of the energy balance, the contributions of which can be split into two categories: the equilibrium terms (*i.e.*, the terms of Eq. (4.3.2)) and the non-equilibrium terms (*i.e.*, the terms neglected in Eq. (4.3.2)); once the ratio between the equilibrium terms and the whole energy content is calculated, the equilibrium sub-layer has been defined as the region laying beneath an iso-line (or iso-surface) of this ratio, the value of which is, *a priori*,

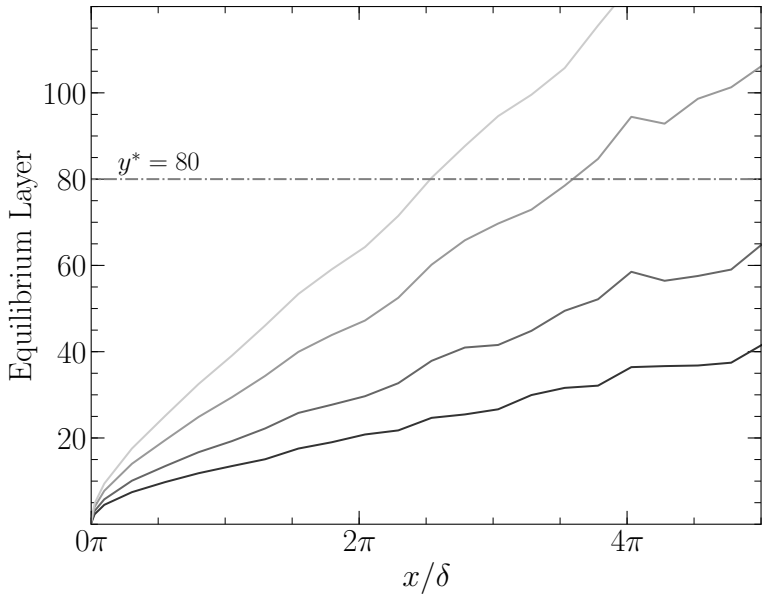

Figure 4.7: Evolution of the equilibrium sub-layer according to four different criteria: 70%, 80%, 90% and 95% (from lighter to darker).

purely arbitrary. Figure 4.7 shows the evolution of several equilibrium sub-layers in semi-local scaling, each one defined according to a different criterion: below the 90% iso-line, for instance, the equilibrium terms represent at least 90% of the energy content.

As previously mentioned, at $x/\delta \approx 2\pi$ the WMLES provides accurate results for both the mean temperature and Nusselt number. As can be seen from Fig. 4.7, at $x/\delta = 2\pi$ and $y^* = 80$, which represents the wall-distance of the matching-point, the equilibrium terms constitute around 70% of the energy balance. Consequently, it is possible to draw the conclusion that the corresponding iso-line can be considered, at least in the context of WMLES, an appropriate representation of the equilibrium sub-layer, and that the matching-point should be placed in this region in order for such a wall-model to perform well in non-equilibrium flows.

To corroborate these statements, an additional simulation is performed, where the matching-point is placed at $y_w^* \approx 20$. In order to keep the exchange location at the fourth off-wall grid-point and avoid LLM, the mesh is refined in the wall-normal direction, along which the resolution, expressed in wall-units, is now $\Delta Y^+ = 5$. According to Figure 4.7, the matching-point should be immersed in the equilibrium layer at $x/\delta \approx \pi/2$, starting from which the prediction of the wall-heat flux is expected to be accurate. Figure 4.8 shows the mean temperature profiles obtained with this grid at the same four streamwise locations of Figure 4.5a. While a small difference between the LES and DNS plateaus can still be observed at $x/\delta = \pi/4$, excellent agreement is obtained from $x/\delta = 3\pi/4$, showing that it is between these crosswise sections that the equilibrium sub-layer attains the matching-point.

Finally, returning to the original mesh introduced in §4.2 (*i.e.*, with $\Delta Y^+ = 20$), temperature fluctuations are shown in Figure 4.9 for four different streamwise locations. Surprisingly, the closer to the leading edge, the better the level of fluctuations

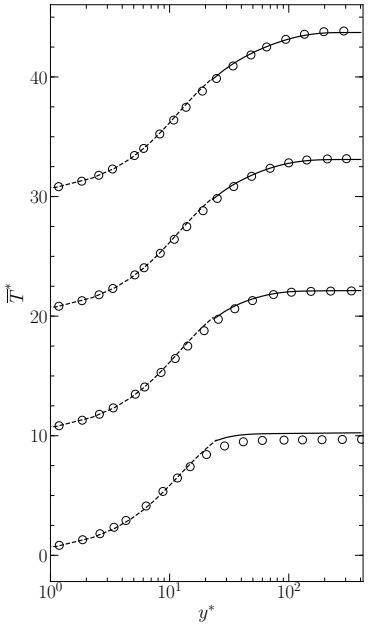

Figure 4.8: Results with equilibrium wall-model and refined mesh ($\Delta Y^+ = 5$). Mean temperature profile at four streamwise locations: from bottom to top, $x/\delta = \frac{\pi}{4}, \frac{3}{4}\pi, \frac{5}{4}\pi, \frac{7}{4}\pi$. See Figure 4.5 for a reference to symbols.

seems to be predicted, which is the opposite of what happens for the mean temperature profile and for the Nusselt number. However, further away from the leading edge (see profile at $x/\delta = 11\pi$ in Fig. 4.9), the r.m.s. temperature is affected by the same level of overestimation observed in Fig. 4.4b at equilibrium. Good agreement with the DNS profiles, instead, is obtained for every crosswise section at the centre of the channel. We will further discuss these profiles in §4.4.

4.3.4 On the use of equilibrium wall-models in non-equilibrium flows

In conclusion to this section, it is interesting to draw a parallel with the arguments of Larsson et al. (2016) concerning the accuracy of equilibrium wall-models in non-equilibrium flows. Larsson et al. (2016), in the case of an adiabatic velocity boundary layer subject to a pressure-gradient, speculated that since in WMLES at least 80% of the boundary layer is resolved, the majority of the non-equilibrium effects are expected to be captured by the LES and that even in the event of strong non-equilibrium contributions in the modelled-layer, these terms may, at least to a certain extent, balance each other. Consequently, an equilibrium wall-model is likely to provide fairly accurate results in most non-equilibrium configurations.

One the one hand, our results confirm that, as long as the modelled portion of the boundary layer, limited by the matching-point, lays within an equilibrium sub-layer, the outer-layer LES is capable of capturing all the non-equilibrium effects, and both the mean temperature and Nusselt number are indeed well retrieved. On the other hand, the use of an equilibrium wall-model for describing the development of

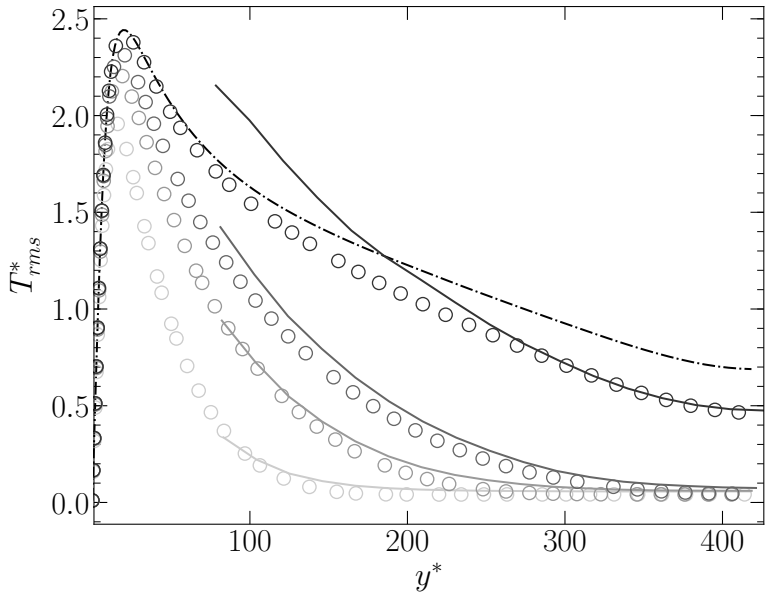

Figure 4.9: Equilibrium wall-model. Profiles of r.m.s. temperature for four streamwise locations: $x/\delta = \frac{3}{4}\pi, \frac{7}{4}\pi, 3\pi, 11\pi$ (from lighter to darker); – · – · – equilibrium profile from §3.3.2; ○ DNS profile from §3.4.3; —— present LES results.

a thermal boundary layer inevitably exposes to a certain level of error, regardless of the importance of the perturbation (*i.e.*, the temperature gradient the flow is subject to). Indeed, when an adiabatic flow makes contact with a heated wall, an event that takes place in numerous practical applications, including ours, the entirety of the boundary layer is inescapably affected by non-equilibrium effects; furthermore, as discussed in detail in §4.4, these non-equilibrium terms give a net contribution to the energy balance, without any sort of auto-compensation. The most emblematic manifestation of these errors, in our case of study, is the inaccurate prediction of the Nusselt number evolution, as shown in Figure 4.6. It should also be noted that even if the non-dimensional temperature and Nusselt number are well retrieved further away from the leading edge, the poor prediction of the wall heat flux in the early development phase of the thermal boundary layer irremediably compromises the estimation of the total heat exchanged between the inlet and the outlet of the channel flow. Therefore, if the isothermal wall were indeed a heat exchanger of which we want to evaluate the thermal performance, the global heat dissipated would be under-predicted with an equilibrium wall-model.

If such a wall-model is employed, two options are available. The first, is to simply neglect the error committed near the leading edge and admit, at least temporarily, an underestimated heat flux. This is definitely a possibility, yet it is imperative to estimate the evolution of the equilibrium sub-layer, to compare it to the wall-distance of the matching point, and to verify that the former attains the latter at a distance from the leading edge which can be considered small. In practice, such an estimate could be carried out through a preliminary RANS simulation, for instance.

The second option, as pointed out in the results section, is to improve the quality of the WMLES results by reducing the modelled part of the boundary layer, *i.e.*,

by placing the matching-point closer to the wall. However, reducing the modelled layer to a wall-distance of compromise may require a strong mesh refinement, and the WMLES could become prohibitively expensive.

Therefore, if neither option is acceptable, increasing the complexity of the wall-model seems to be the only viable solution for providing accurate results in a wide range of configurations. This, is the object of the next section.

4.4 Non-equilibrium wall-modelling: construction, validation and results

The chapter is organised as follows. In §4.4.1, an *ad hoc* non-equilibrium wall-model is constructed using the DNS data of Chapter 3. In§4.4.2, the equations of the new wall-model are presented, and the numerical setup is validated *a priori*. Finally, in section §4.4.3, the *a posteriori* results are presented and discussed.

4.4.1 Construction of a non-equilibrium wall-model

The results presented in §4.3, as pointed out in §4.3.4, show the necessity of a more sophisticated wall-model. The objective of this section is to identify, thanks to the DNS data, the most relevant non-equilibrium effects to be included into a new set of equations replacing Eqs. (4.3.1) and (4.3.2).

In Chapter 3, we have explained how the perturbation of the heated wall primarily manifests through the presence of strong non-equilibrium contributions to the momentum and energy balances. Figure 4.10 shows the different energy budgets in the near-wall region $y/\delta \in [0, 0.2]$ at $x/\delta = 0.73$, *i.e.*, at a very close distance from the leading edge of the isothermal wall, where the equilibrium wall-model fails to accurately predict the wall heat flux, as discussed in §4.3.3. As can be observed, the dominating contribution is given by the streamwise convective term, while the equilibrium terms (*i.e.*, the wall-normal conductive and turbulent fluxes) are actually negligible for $y/\delta \gtrapprox 0.1$. Besides, one can notice the significant contribution of the streamwise turbulent flux and of the wall-normal convective term. It is evident how, at $x/\delta = 0.73$, the equation used for the equilibrium wall-model (4.3.2) cannot be representative of the actual energy balance but in an extremely limited near-wall region ($y/\delta \lessapprox 0.02$). Concerning the momentum balance (not shown here), in §3.4.1 we have also identified a significant perturbation of the pressure gradient near the leading edge, which, despite being compensated by the presence of important streamwise and wall-normal convective fluxes, as suggested by Larsson et al. (2016), modifies the mean streamwise velocity. However, as we have already pointed out, the perturbation is localised in an extremely limited part of the channel flow ($0 < x/\delta \lessapprox \pi/2$), and the mesh resolution in the streamwise direction ($\Delta X^+ = 50$, see §4.2) is not sufficient to capture these effects. Consequently, leaving the momentum equation (4.3.1) unchanged seems justified.

Moreover, in §3.4.3, we have also observed a perturbation of the turbulent Prandtl number Pr_t. As can be seen in Figure 4.11, the turbulent Prandtl number exceeds unity in the near-wall region, and the return to equilibrium (see §3.4.3) is not observed before $x/\delta \approx 5\pi$. Therefore, the pertinence of the modelling of Pr_t according to Eq. (1.3.25) has to be evaluated in the present case.

So as to assess the importance of each non-equilibrium effect on the development of the thermal boundary layer, the following momentum and energy equations are

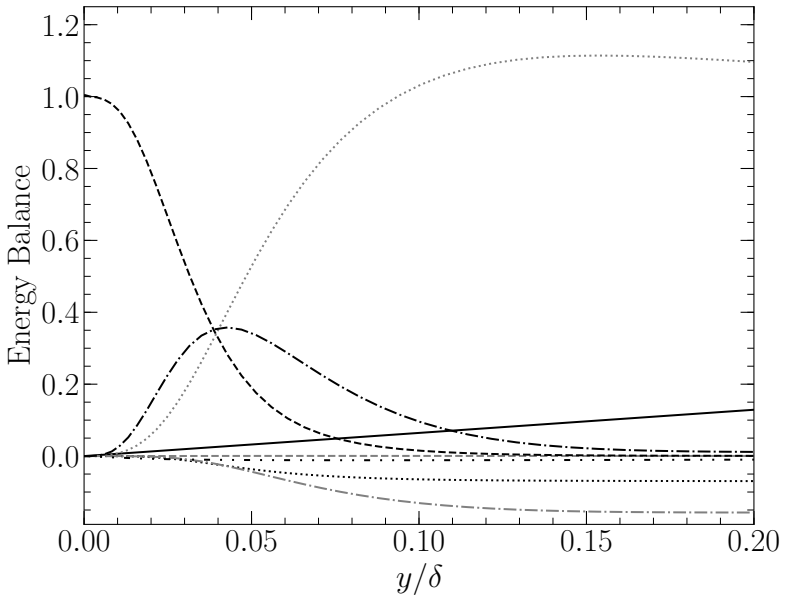

Figure 4.10: Energy flux balance at $x/\delta = 0.73$, non-dimensionalised with respect to the wall heat flux: —— energy source term S_{ener}; - - - - streamwise (gray) and wall-normal (black) conductive fluxes; ····· streamwise (gray) and wall-normal (black) convective fluxes; – · – · – streamwise (gray) and wall-normal (black) turbulent fluxes; – · · – compressibility effects. Data taken from §3.4.2.

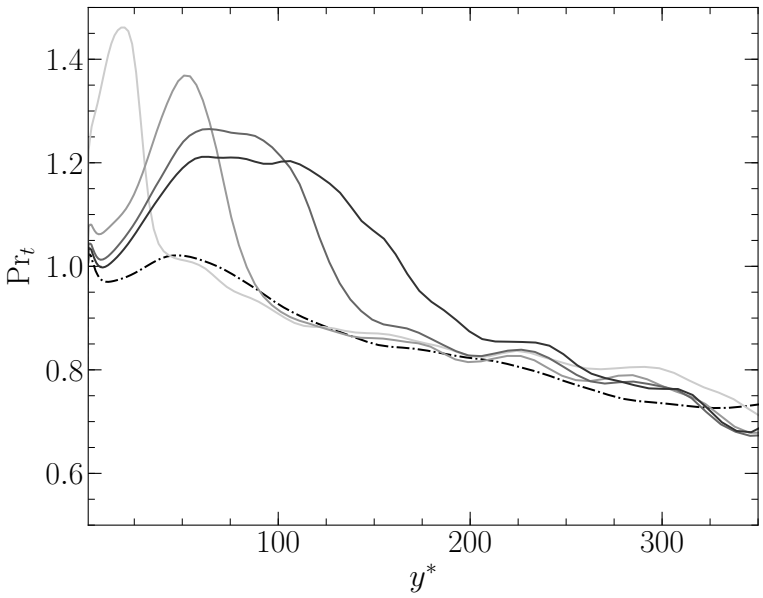

Figure 4.11: Evolution of turbulent Prandtl number in the wall-normal direction for different x/δ: —— DNS data from §3.4.3 at (from light to dark gray) $x/\delta = 0.18$, 0.73, 0.5π and 0.75π; – · – · – equilibrium profile.

considered:

$$\frac{\mathrm{d}}{\mathrm{d}y}\left[(\overline{\mu}+\mu_t)\,\frac{\mathrm{d}\overline{u}}{\mathrm{d}y}\right]=0\ , \tag{4.4.1}$$

$$\underbrace{\overline{\rho}\widetilde{u}\frac{\partial\widetilde{h}}{\partial x}}_{C_x(x,y)}+\underbrace{\overline{\rho}\widetilde{v}\frac{\partial\widetilde{h}}{\partial y}}_{C_y(x,y)}-\frac{\partial}{\partial y}\left[(\overline{\lambda}+\lambda_t)\,\frac{\partial\overline{T}}{\partial y}\right]+\underbrace{\frac{\partial}{\partial x}\left(\overline{\rho}\widetilde{u''h''}\right)}_{T_x(x,y)}=0\ , \tag{4.4.2}$$

where $C_x(x,y)$, $C_y(x,y)$ and $T_x(x,y)$ are three energy source terms in which the streamwise convective term, wall-normal convective term and streamwise turbulent term, respectively, are injected directly from the DNS; besides, μ_t and λ_t are either modelled through Eqs. (1.3.22), (1.3.24) and (1.3.25) or taken from the DNS. Equations (4.4.1) and (4.4.2) are solved between $y/\delta\in[0,0.2]$ and $x/\delta\in[0,3\pi]$ on a two-dimensional grid with the same point-distribution of the DNS, from which the boundary conditions at the matching point are also extracted.

Figure 4.12 shows the mean temperature profiles at several x/δ obtained through the integration of Eqs. (4.4.1) and (4.4.2) with different source terms. In Fig. 4.12a, only C_x is considered, *i.e.*, the streamwise convective term; the top profiles are obtained using the turbulent viscosity and conductivity of the DNS. As can be seen by comparing the bottom and top profiles, injecting μ_t and λ_t from the DNS does not bring any appreciable benefit, showing that the perturbation of Pr_t illustrated in §3.4.3 can be neglected. The development of the thermal boundary layer is overall well captured, even though at $x/\delta=0.01\pi$ and $x/\delta=0.2\pi$, no real plateau is observed for $y^*\gtrapprox 10$. This is evidently due to the lack of the remaining non-equilibrium energy budgets, since the effect is corrected by the introduction of the wall-normal convective term C_y (Fig. 4.12b, bottom) and of the streamwise turbulent term T_x (Fig. 4.12b, top).

These results indicate that the most important non-equilibrium effect not taken into account by the equilibrium wall-model is the streamwise convective term, which cannot be neglected at any stage of the boundary layer's development. The remaining terms, *i.e.*, the wall-normal convective term and streamwise turbulent term, play a minor role in close proximity to the leading edge ($x/\delta\lessapprox\pi/2$), a region which is anyway under-resolved given the resolution of the LES grid ($\Delta X^+\approx 50$). Finally, despite the alteration of the turbulent Prandtl number observed in §3.4.3, the turbulence modelling introduced in §1.3 does not seem to need any adjustment in the present case. These arguments allow us to justify the construction of a new wall-model, which is introduced in the next section.

4.4.2 Numerical setup and validation

On the basis of the *a priori* results shown in §4.4.1, we propose to test a non-equilibrium wall-model consisting of the following momentum and energy equations:

$$\frac{\mathrm{d}}{\mathrm{d}y}\left[(\overline{\mu}+\mu_t)\,\frac{\mathrm{d}\overline{u}}{\mathrm{d}y}\right]=0\ , \tag{4.4.3}$$

$$\overline{\rho}\,\overline{c_p}\,\overline{u}\frac{\partial\overline{T}}{\partial x}-\frac{\partial}{\partial y}\left[(\overline{\lambda}+\lambda_t)\,\frac{\partial\overline{T}}{\partial y}\right]=0\ , \tag{4.4.4}$$

where the eddy viscosity μ_t and conductivity λ_t are expressed through the same models described in §1.3. With respect to Equation (4.3.2), Eq. (4.4.4) presents an additional mean streamwise convective term.

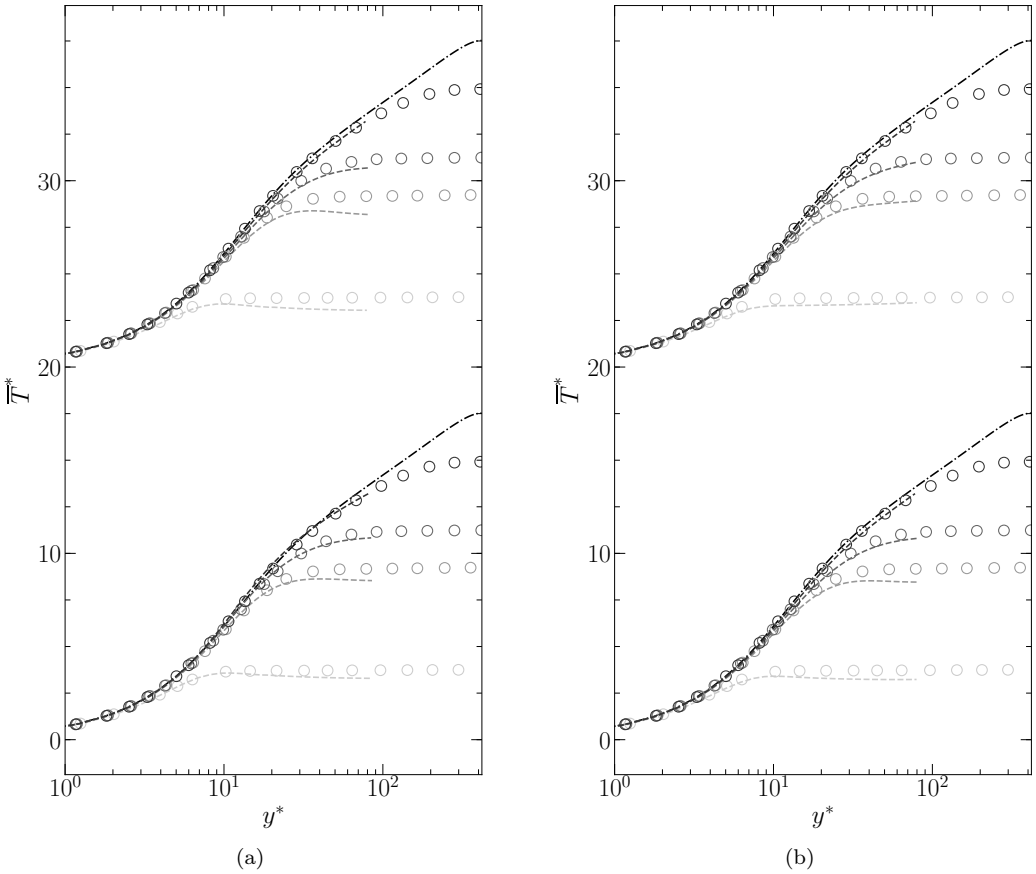

Figure 4.12: Construction of a non-equilibrium wall-model. Mean temperature profiles at $x/\delta = 0.01\pi, 0.2\pi, \pi/2, 3\pi$ (from light to dark gray) for different source terms extracted from the DNS. Source terms: (a) C_x (bottom) and C_x with μ_t and λ_t from DNS (top); (b) $C_x + C_y$ (bottom) and $C_x + C_y + T_x$ (top). Symbols : ○ DNS results; - - - - results from wall-model; – · – · – equilibrium profile. Profiles are shifted by twenty on the vertical axis for the sake of clarity.

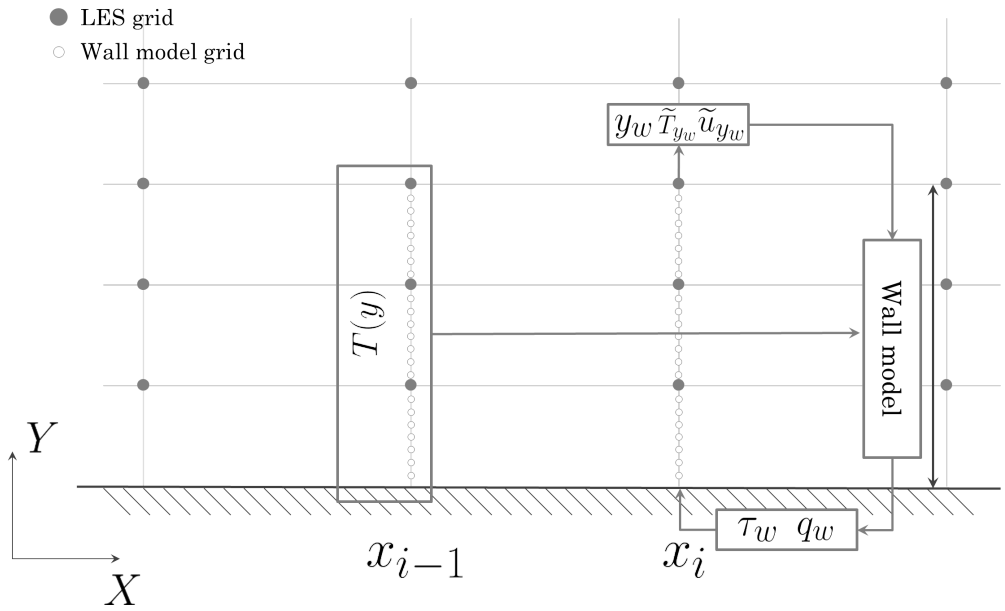

Figure 4.13: Schematic representation of the coupling of the non-equilibrium wall-model with the outer-layer LES.

Figure 4.13 schematically shows the functioning of the non-equilibrium wall-model. Because of the gradients along both the streamwise and wall-normal directions, the wall-model is bi-dimensional and, therefore, can be arduous to implement and noticeably more costly than a standard equilibrium model. Yet, since Eq. (4.4.4) is parabolic, it can be solved using an explicit scheme with respect to the streamwise coordinate x. Thus, for a given wall-point at a generic $x = x_i$, only the temperature profile $\overline{T}(y)$ at $x = x_{i-1}$ is needed to solve the wall model's equations. Still, the straightforward explicit integration of Eq. (4.4.4) would require a strictly sequential update of transverse wall-model profiles from the leading edge to increasing x-coordinates, which would stall the WMLES parallel performance. This is here alleviated by locally updating the profiles at $x = x_i$, without necessarily waiting for an update of profiles at $x = x_{i-1}$. This is repeated at each flow solver iteration: this assembles a scalable iterative approach to solve Eq. (4.4.4) that converges with the resolved turbulent flow in steady-state regime. Therefore, the wall-model is in practice *quasi*-unidimensional.

The mean temperature profiles obtained by integrating Eqs. (4.4.3) and (4.4.4) on the same bi-dimensional grid used in §4.4.1 are shown in Figure 4.14; note that in this case, differently from what has been done in §4.4.1, no data is injected from the DNS, except for the boundary conditions at the matching-point. As can be seen, the development of the thermal boundary layer is *a priori* well described by the newly introduced wall-model, with only some small discrepancies which remain within the order of magnitude of those observed in Fig. 4.12.

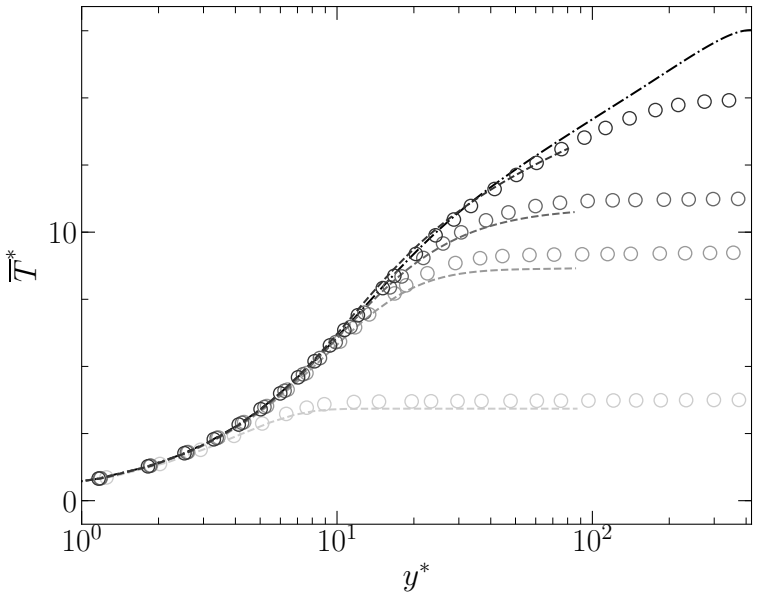

Figure 4.14: *A priori* results with non-equilibrium wall-model (Eqs. (4.4.3) and (4.4.4)). Mean temperature profiles at $x/\delta = 0.01\pi, 0.2\pi, \pi/2, 3\pi$ (from light to dark gray): ○ DNS results; - - - - results from wall-model; – · – · – equilibrium profile.

4.4.3 Results

The *a posteriori* results obtained with the non-equilibrium wall-model on the configuration of Figure 4.1 are now presented. The same notation used in §4.3.3 is adopted; furthermore, as in §4.3, the matching-point is located at the fourth LES off-wall grid-point.

Figure 4.15 shows the mean temperature profiles obtained at different x/δ compared to the DNS results. As can be seen, the non-equilibrium wall-model leads to a significant improvement of the mean temperature prediction near the leading edge with respect to the results shown in §4.3.3. The presence of a streamwise convective term in the energy equation (4.4.4), indeed, allows the wall-model to capture all three sub-regions of the developing thermal boundary layer mentioned in §4.3.3, *i.e.*, the equilibrium, non-equilibrium and adiabatic regions. At $x/\delta = \pi/4$ (see bottom profiles in Fig. 4.15a), all three are present in the modelled layer $[0, y_h^*]$ and the temperature profile returned by the wall-model ends with a plateau; as x/δ increases, the equilibrium sub-layer thickens and, at $x/\delta = \frac{3}{4}\pi$ or $x/\delta = \frac{5}{4}\pi$, the matching-point finds itself in the very middle of the non-equilibrium region; finally, at $x/\delta \approx 2\pi$, the entirety of the modelled layer is at equilibrium, the streamwise convective term disappears from Eq. (4.4.4) and the non-equilibrium wall-model is, in practice, equivalent to the equilibrium one.

The capability of the wall-model to capture the main non-equilibrium effects appears even more clearly in Figure 4.16 from the evolution of the Nusselt number, which is accurately predicted all along the channel flow but at $x/\delta = 0$, where the limited spatial resolution of the LES grid in the streamwise direction does not allow to capture the peak value.

More qualitatively, yet more strikingly, the two wall-models are compared to

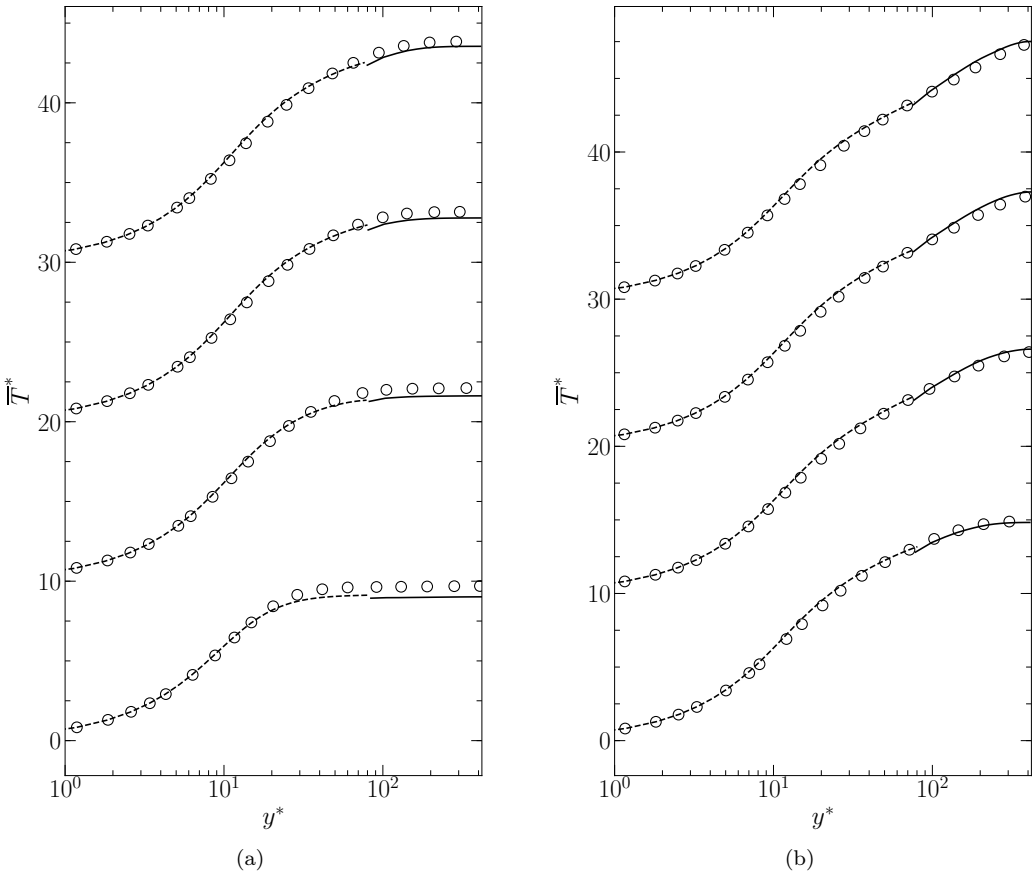

Figure 4.15: *A posteriori* results with non-equilibrium wall-model. Mean temperature profile for eight streamwise locations: from bottom to top, $x/\delta = \frac{\pi}{4}, \frac{3}{4}\pi, \frac{5}{4}\pi, \frac{7}{4}\pi$ (a) and $x/\delta = 3\pi, 7\pi, 11\pi, 17\pi$ (b) ; ○ DNS profiles; —— present LES results; - - - - non-equilibrium wall-model. Profiles are shifted by ten on the vertical axis for the sake of clarity.

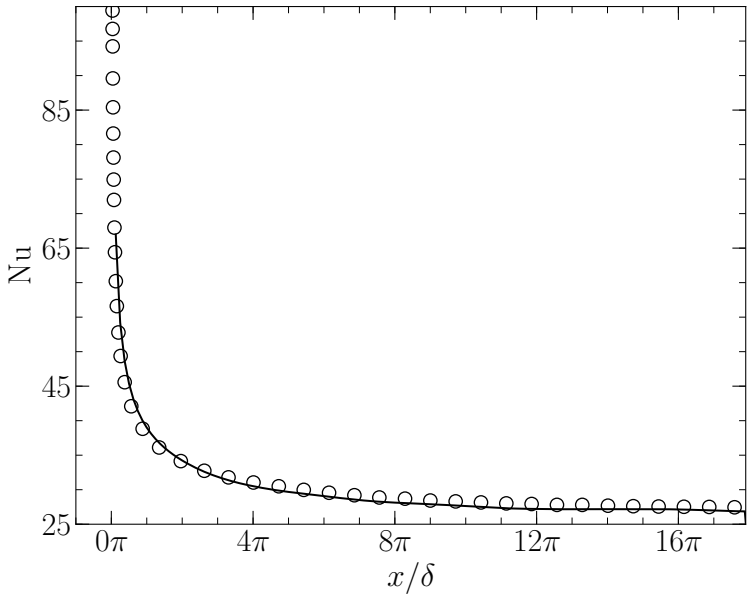

Figure 4.16: Non-equilibrium wall-model. Evolution of the Nusselt number along the channel flow: ○ DNS profile; —— present LES results.

the DNS in Figure 4.17, where some instantaneous contours of temperature at the wall-distance of the matching-point are plotted. With the equilibrium wall-model (Fig. 4.17, top), the temperature gradients are particularly scant until approximately $x/\delta \approx 3\pi$ (where the equilibrium sub-layer has finally attained y_h^*), signalling a delayed development of the thermal boundary layer. This delay, instead, is not observed with the non-equilibrium wall-model (Fig. 4.18, middle); note how the first heated turbulent structures appear at approximately the same distance from the leading edge, compared to the DNS.

Figure 4.18, instead, offers a three-dimensional visualisation of the thermal boundary layer, defined as the temperature iso-surface $\theta = 0.9$, where

$$\theta = \left(T - \overline{T}_{in}\right) / \left(T_w - \overline{T}_{in}\right) \ .$$

Once again, it is evident how the development of the thermal layer is delayed with an equilibrium wall-model (see Fig. 4.18, top). In particular, observe how the temperature iso-surface does not adhere to the leading edge of the isothermal wall; this indicates that the flow is unaware of the modified wall thermal condition until further downstream. The non-equilibrium wall-model (Fig. 4.18, middle), instead, allows the flow to *perceive* the heated wall since $x/\delta = 0$.

Finally, the r.m.s. temperature is shown in Figure 4.19 at the same crosswise sections as Fig. 4.9, for comparison. As can be seen, with the non-equilibrium wall-model good agreement with the DNS results is only obtained towards the centre of the channel, while the r.m.s. intensity is affected by over-prediction at every x/δ. This leads to the surprising conclusion that, although the non-equilibrium wall-model outperforms the equilibrium one in the prediction of the thermal boundary layer's development, the r.m.s. temperature is actually better captured by the latter. However, this is only observed at the low x/δ, since at $x/\delta = 11\pi$ the same profile is

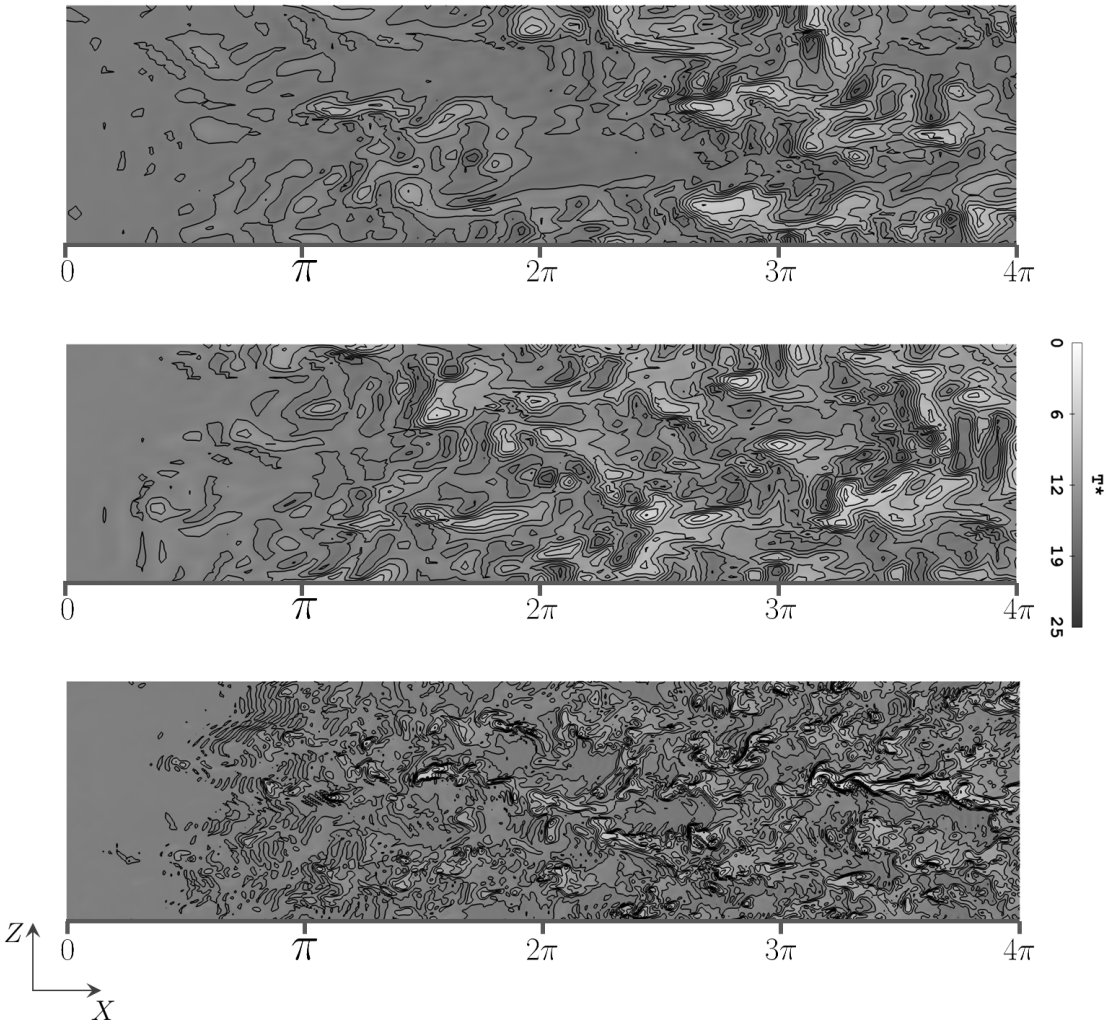

Figure 4.17: Instantaneous contours of temperature T^* at $y^* = 80$ obtained with the equilibrium (top) and non-equilibrium (middle) wall-model WMLES, compared to the DNS (bottom).

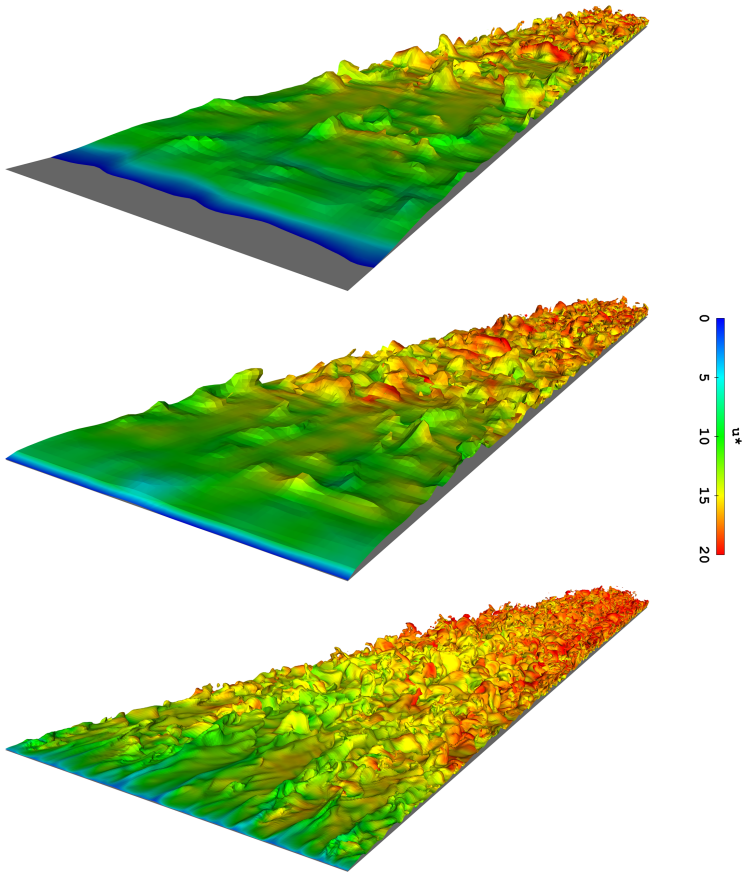

Figure 4.18: Instantaneous iso-temperature $\theta = \left(T - \overline{T}_{in}\right) / \left(T_w - \overline{T}_{in}\right) = 0.9$ along the channel, coloured by the friction velocity u^*. WMLES with equilibrium (top) and non-equilibrium (middle) wall-model and DNS (bottom).

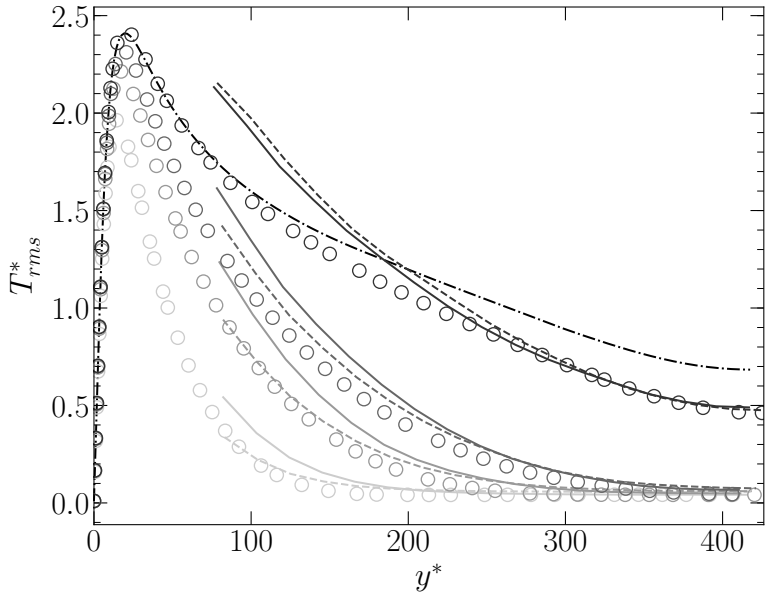

Figure 4.19: Profiles of r.m.s. temperature for four streamwise locations, equilibrium *vs.* non-equilibrium wall-model: $x/\delta = \frac{3}{4}\pi, \frac{7}{4}\pi, 3\pi, 11\pi$ (from lighter to darker); – · – · – equilibrium profile from §3.3.2; ○ DNS profiles; —— present LES results with non-equilibrium wall-model; - - - - present LES results with equilibrium wall-model

obtained with the two wall-models (see Fig. 4.19). As it is indeed near the leading edge that the equilibrium wall-model is the least reliable, it is plausible that the counter-intuitive behaviour of the temperature fluctuations might be simply fortuitous. On the other hand, it is certainly possible to conclude that in the present case the use of a non-equilibrium wall-model does not seem to bring any improvement to the prediction of the turbulent intensity.

4.5 Conclusion

The wall-modelled LES of a non-equilibrium turbulent thermal boundary layer has been performed in a channel flow. Non-equilibrium is induced by a step-change in surface temperature, and a fully turbulent temperature-homogeneous flow evolves towards a new equilibrium state characterised by a fully developed thermal boundary layer. The studied configuration is identical to the direct numerical simulation realised by Chapter 3, where we have analysed the main non-equilibrium effects and identified a near-wall region, called equilibrium sub-layer, where the essential contribution to the energy balance is given by the equilibrium terms, and several mean quantities are equilibrated. In this chapter, two wall-models have been tested and the results have been compared to the DNS.

The former model, is a classic equilibrium wall-model. Results show that good agreement with the DNS for the mean temperature and Nusselt number is obtained only at a certain distance from the leading edge of the isothermal wall, before which the wall heat flux is strongly underestimated. This distance must allow for the

modelled layer to be fully immersed in the equilibrium sub-layer, which is identified, at least in the context of WMLES, as the region where the equilibrium contributions represent approximately 70% of the whole energy content. Surprisingly, the r.m.s. temperature intensity is better captured where the wall heat flux is worse predicted, while further away from the leading edge, where the mean temperature is in good agreement with the DNS, the usual over-prediction of the temperature fluctuations is observed.

The latter model, is a non-equilibrium wall-model. It has been constructed *ad hoc* by identifying, thanks to the DNS data, the most influential non-equilibrium effects not taken into account by the equilibrium wall-model. We have found that the most important contribution is that of the streamwise convective term, while all the other effects, including the perturbation of the turbulent Prandtl number, can be neglected. The non-equilibrium wall-model outperforms the equilibrium one in the prediction of the mean temperature and Nusselt number all along the channel flow. On the other hand, significant over-estimation of the r.m.s. temperature is observed in this case even near the leading edge, showing that the use of a non-equilibrium wall-model does not bring any benefit to the prediction of the turbulent fluctuations.

The study allows us to draw several conclusions. First of all, our work marks another step towards the inevitable retirement of equilibrium wall-models, which are revealing more and more evidently their inadequacy in non-equilibrium configurations. We believe, given the increasing number of works involving three-dimensional RANS wall-models, that the community has come to similar conclusions. In general, we are maybe assisting to some sort of convergence between WMLES and DES methods. On the one hand, as just said, WMLES is progressively abandoning simplistic wall-models, and adopting more complex ones which resemble the inner-layer treatment of DES; on the other hand, DES studies of shallowly separated or attached flows have highlighted the necessity of reducing the ratio of RANS *vs.* LES areas of competence in the boundary layer (see Deck and Renard, 2020), attaining a ratio of the order of 20% vs 80%, which is typical of WMLES, and presumably recognising that, in the most general case, the entirety of the boundary layer cannot be simulated in RANS with impunity.

Equilibrium wall-models, of course, remain pertinent if equilibrium assumptions hold in the inner-layer. As we will illustrate in Chapter 5, this can sometimes be the case even in the most challenging configurations. However, the validity of equilibrium assumptions needs to be verified case by case. This is evidently not necessary with tree-dimensional all-inclusive wall-models, for which an equilibrium inner-layer is nothing but a particular case of flow.

The two-dimensional wall-model that we have introduced, is certainly not the ultimate solution for non-equilibrium thermal boundary layers. Indeed, it has been constructed using very detailed information about the flow which, in the most general case, is not known. Our work has attempted to illustrate the benefits that non-equilibrium wall-models can bring to WMLES, and to prove that its major current limitation is its lack of maturity. Once the appropriate physical phenomena are taken into account by the wall-model, WMLES, as we have seen, has indeed the potential of successfully simulating complex flows of practical interest. However, in perspective, a real effort is required to build a solid LES framework giving access to the most complete three-dimensional wall-models. This would mark a decisive advancement towards a satisfying level of maturity of WMLES, which cannot rely on slightly modified, quasi-bidimensional non-equilibrium wall-models to progress

(like ours or the one proposed by Duprat et al. (2011), for instance).

Part III

Conjugate heat transfer investigation of a surface air-oil heat-exchanger

Chapter 5

Conjugate heat transfer analysis of a surface air-cooled oil cooler installed in a turbofan by-pass duct

This chapter marks the beginning of the third and last part of this work. It also marks a radical change of both the object of our study and the tools used for our investigations.

In Part II, we have privileged the most reliable fluid simulation strategies, with the objective of finely characterising the non-equilibrium effects which occur when an adiabatic flow makes contact with a heated body. The use of direct numerical simulation (DNS) has allowed us to identify even the smallest perturbations of the flow, as well as to faithfully describe its gradual return to equilibrium. The assessment of wall-modelled large-eddy simulation (WMLES), instead, has shown how it can be a valuable and, above all, more accessible tool to capture these effects, with which future applications to more complex geometries and flows can clearly be envisaged. However, the excessive cost of DNS on the one hand, and the lack of maturity of WMLES on the other, have constrained us to focus on an extremely simplified aerothermal case, characterised by a basic heat exchanger (*i.e.*, an isothermal wall in a channel) and a limited Reynolds number, which is far from the usual regimes of industrial applications.

In this last part of the work we adopt a different approach, with the objective of providing an immediate answer to the scientific challenges posed by the studied industrial configuration. On the one hand, we will considerably increase the complexity of both the geometry and flow conditions of our aerothermal cases; we will therefore abandon the channel flow configuration, and focus on the behaviour of realistic surface air-cooled oil coolers (SACOC) mounted in their operating environment (*i.e.*, the by-pass duct of a modern turbofan) and in their typical test-bench configuration (*i.e.*, the square wind tunnel); concerning the flow regime, it will be characterised by mean-flow three-dimensionality, in some cases by flow separation and, of course, by higher Mach and Reynolds numbers; finally, we will consider the heat conduction inside the SACOC and, therefore, perform conjugate heat transfer

(CHT). On the other hand, we are constrained to abandon the sophisticated numerical tools of Part II and to adopt more accessible modelling strategies, at the cost of some degree of physical fidelity. In the following two chapters, therefore, we will make use of the methodologies introduced in Chapter 2, which are based, recall, on Reynolds-averaged Navier-Stokes (RANS) fluid modelling.

In this chapter, we perform the CHT analysis of a SACOC in its operating environment, *i.e.*, the turbofan by-pass duct. This work has been the subject matter of a recent publication to the 2021 AIAA Aviation Forum:

— Gelain, M., Couilleaux, A., Errera, M.P., Vicquelin, R., Gicquel, O., *Conjugate heat transfer analysis of a surface air-cooled oil cooler (SACOC) installed in a turbofan by-pass duct*, AIAA Aviation 2021 Forum.

The paper has been published and orally presented on the 3rd of August, 2021.

5.1 Introduction

A first presentation of the industrial application of interest has been provided in the Introduction. We have seen that the implementation of Air/Oil Heat Exchangers (AOHE) in turbofan by-pass ducts is a consequence of the growing lubricant-cooling demand of modern engines, that is exacerbated by the constant increase of the by-pass ratio. Surface air-cooled oil coolers (SACOC) represent today's technology of reference, as they have the potential to introduce lower aerodynamic disturbances to the flow that is later ejected through the nozzle. As we have seen, a typical SACOC (see Bajusz et al., 2009; Elder, 2014) is composed of a series of staggered fins aligned with the direction of the main flow, which dissipate the heat transferred from an oil circuit placed beneath the heat exchanger.

Finned heat exchangers surely do not represent a novelty, and indeed, the literature is abundant on the matter. They have extensively been studied analytically (see Kadle and Sparrow, 1986), numerically (see Jonsson and Moshfegh, 2000; Filburn et al., 2006; Kim et al., 2014, 2016) and, of course, experimentally (see Sparrow et al., 1978; Lau and Mahajan, 1989; Wirtz et al., 1994; Manglik and Bergles, 1995). However, only a few works have investigated the behaviour of surface heat exchangers while taking into account the specificity of turbofan by-pass flows. Kim et al. (2014) performed a numerical and experimental analysis of the influence of a surface AOHE on the engine performance depending on the location and orientation of the fins, while Sousa et al. (2014) and Villafañe and Paniagua (2018) carried out experimental studies of a SACOC integrated on the splitter of a turbofan engine, reproducing the transonic and high-swirl conditions of by-pass flows downstream of the fan.

The characterisation of SACOC in representative functioning conditions represents a major challenge for Safran Aircraft Engines. Ideally, their performances would always be assessed in their operating environment, *i.e.*, in engine tests. However, such full-scale tests are extremely expensive and time-consuming, especially in the design and optimisation process, where a great number of different SACOC configurations need to be evaluated. In fact, even steady-state RANS numerical investigations demand important resources and are difficult to implement when the whole by-pass duct (from the air intake to the nozzle) is simulated, thereby becoming impractical. Therefore, relying on smaller-scale experimental tests and simulations is still today a necessity, and it is fundamental to understand to which extent a simplified environment can be representative of the real engine conditions. The objective

of this chapter is thus twofold.

First, we aim at characterising the behaviour of a realistic heat exchanger in its operating environment, and to achieve this goal we perform the CHT numerical simulation of a SACOC directly installed in the by-pass duct (BPD) of a turbofan. More precisely, the SACOC is placed on the outer-fixed structure (OFS) of the engine, slightly downstream of the outlet guide vane (OGV). The flow making contact with the heat exchanger is thus characterised by a complex, three-dimensional, non-equilibrium boundary layer with residual swirl coming from the fan, the presence and rotation of which are also simulated. We aim at characterising the behaviour and interaction of this flow with the heat exchanger, and studying the performances of the SACOC in terms of the heat dissipated, of its drag coefficient and of the global pressure drop it generates.

Second, we aim at understanding how these engine integration effects should be reproduced in small-scale experiments and simulations. To reach this objective, we introduce a second study configuration in which the SACOC is installed in a square wind tunnel, which is the most common testing configuration. Boundary conditions at the inlet are extracted from the engine simulation with different degrees of fidelity. The results obtained with the two configurations are compared and guidelines are given about the level of representativeness required in test rigs and numerical investigations to reproduce realistic engine conditions.

Note that this work is purely numeric. The experimental assessment of the methodologies introduced in Chapter 2 on a surface heat exchanger, is left for the last chapter of this work.

The chapter is organised as follows. In §5.2, the problem is described; first, the geometry and characteristics of surface heat exchanger are introduced (§5.2.1); then, we illustrate in detail the engine and wind tunnel configurations (§5.2.2). In §5.3, the numerical setup, which has been extensively described in Chapter 2, is briefly presented to highlight the specificities of this work; furthermore, the main stability parameters of Section 2.5 are estimated and the choice of a coupling coefficient for the Robin fluid-solid condition is motivated. Finally, results are shown and discussed in §5.4 for the engine configuration and in §5.5 for the test-bench cases, followed by the conclusions in §5.6.

5.2 Problem description

The study aims at analysing and comparing the aerothermal behaviour of a surface air-oil heat exchanger in two fluid environments, that is the by-pass duct of a turbofan engine and the square tunnel of a typical test bench. The section is organized as follows: in §5.2.1 the surface air-cooled oil cooler (SACOC) is introduced and details about geometry, physical properties and boundary conditions are given; Section 5.2.2 is dedicated to the fluid domain and the turbofan by-pass duct and test bench configurations are described in detail. In the following, $(\cdot)^H$ denotes a variable of length non-dimesionalised with respect to the fin height H.

5.2.1 Solid domain: surface air-cooled oil cooler (SACOC)

Figure 5.1 shows a schematic representation of the geometry of the surface heat exchanger while its characteristic dimensions, normalised with respect to the fin height H, are specified in Table 5.1.

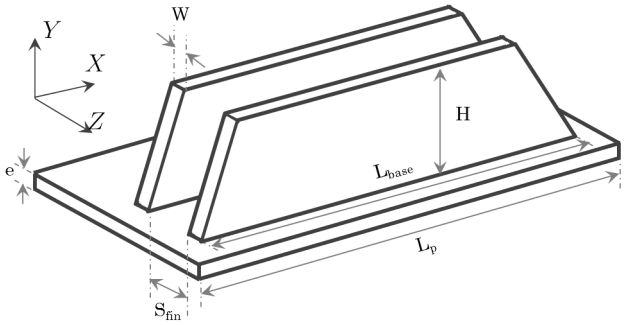

Figure 5.1: Schematic representation of two fins of SACOC with dimensions.

L^H_{base}	L^H_p	H^H	W^H	S^H_{fin}	e^H
6.67	7.33	1	0.0533	0.133	0.1

Table 5.1: SACOC's dimensions (normalized with respect to the fin height H).

The SACOC consists of a series of staggered fins oriented along the direction of the main flow (i.e. the X-axis in Figure 5.1). The cold sink of the heat exchanger is the airstream flowing through the fins; the surface in contact with the air is the CHT in thermal contact with the fluid domain; at this surface, a Robin condition is imposed on the temperature as extensively described in Chapter 2, and the coupling coefficient α_f^{opt} is prescribed. This choice will be justified in §5.3. The hot source of the exchanger, in practical applications (see Bajusz et al., 2009, , for instance), consists of a complex system of channels and winglets placed beneath the air-fins, in which the oil of the engine circuit flows. In this work, in order to simplify the numerical simulations, the oil circuit is not taken into account and the hot source is simply represented by a temperature-imposed surface (with $T_p = 400$ K) situated at the base of a platform of thickness e^H (see Figure 5.1).

The inner part of the domain is discretised with a structured mesh (interpreted as unstructured by *Zset*) of around 300,000 nodes per fin; for both fluid configurations, the solid and fluid grids coincide at the coupling interface, thereby removing all interpolation errors. The material is considered to be an isotropic aluminium alloy of constant thermal conductivity $\lambda_s = 150$ W/(m K). The steady-state energy equation is thus reduced to:

$$\nabla^2 T = 0 \ , \tag{5.2.1}$$

which is solved by the solid solver at every coupling instant.

5.2.2 Fluid domains

i. *Turbofan by-pass configuration*

The aim of the turbofan configuration is to reproduce the real engine conditions at which a surface heat exchanger normally operates, as they may have a strong

impact on its performance, in terms of both heat exchange and head losses. For this purpose, a series of 50 fins of the SACOC described in section §5.2.1 is installed on the outer fixed structure (OFS) of a turbofan by-pass duct (BPD). As shown schematically in Figure 5.2, the SACOC is placed slightly downstream of the outlet guide vane (OGV).

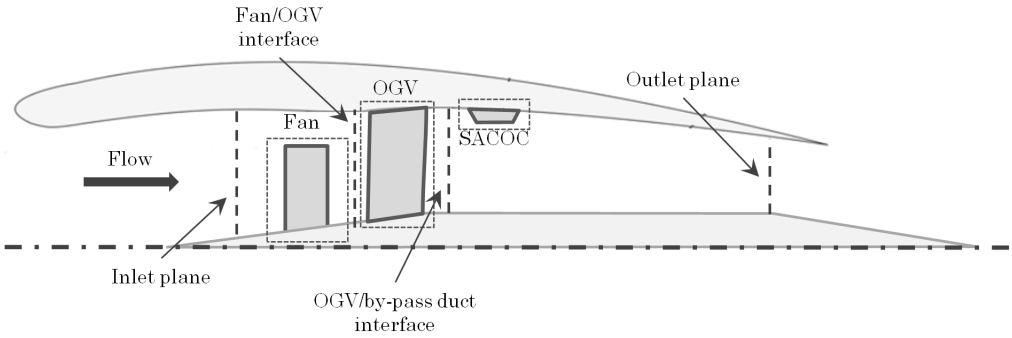

Figure 5.2: Schematic section of a turbofan by-pass duct with SACOC.

The fluid domain, of which a three-dimensional view is given in Fig. 5.3, represents an angular sector of the BPD (with azimuthal periodic conditions imposed at the lateral boundaries), wide enough to include one fan/OGV blade. The coordinate system, as shown in Fig. 5.3, is cylindrical, with X representing the engine's axis, R the radial direction (pointing downward so that $R = 0$ on the OFS) and Θ the azimuth. The domain, discretised with a structured mesh of around 60 million nodes, extends from the inlet, situated downstream of the air-intake (which is consequently not simulated) to the outlet, placed at the throat of the nozzle, and can be conceptually divided into three sub-domains:

— *Fan sub-domain*: in the axial direction it extends from the inlet to the interface with the OGV sub-domain, while the azimuth ranges between $\Theta \in [-10°, 10°]$; at the inlet, uniform stagnation pressure and stagnation temperature are imposed, thus neglecting the thickness of the boundary layer originating at the air-intake; the fan blade is completely immersed in the fluid at the centre of the domain and an adiabatic no-slip boundary condition is applied at its wall; finally, in order to simulate the rotation of the blade, the steady-state Navier-Stokes equations are solved in a non-inertial frame of reference, rotating at the speed of the fan. The fan operates at take-off in standard conditions (*i.e.*, at standard pressure $P_{std} = 101325$ Pa and temperature $T_{std} = 288.15$ K).

— *OGV sub-domain*: in the axial direction it extends from the rotor-stator interface to the entry of the BPD, while $\Theta \in [-4.5°, 4.5°]$; the OGV blade is considered to be an adiabatic no-slip wall; since the blade does not rotate, the frame of reference is Galilean and a simple way of ensuring the communication between the rotor and the stator is that of interposing a mixing-plane (see Dawes, 1990, 1991), which applies a circumferential average of the flow properties. As a consequence, a certain degree of homogenization is introduced

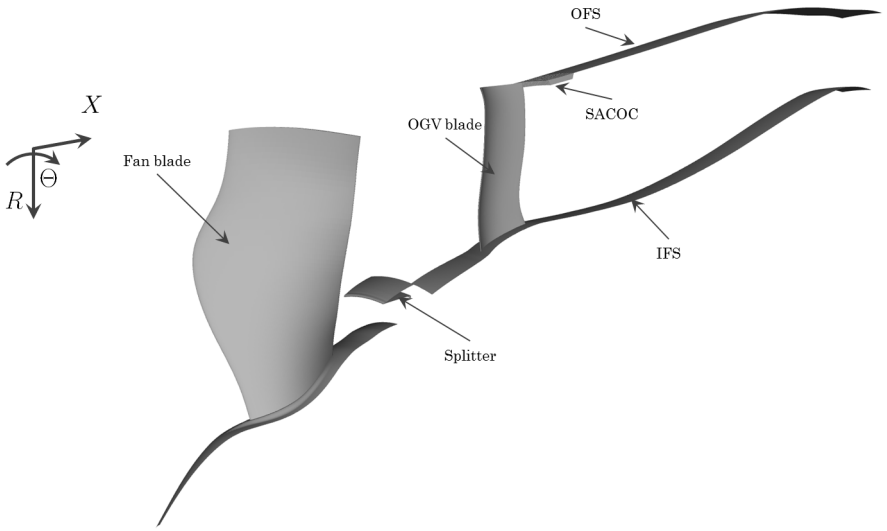

Figure 5.3: Three-dimensional view of the turbofan fluid domain.

into the flow (with, in particular, the elimination of the fan wake), yet radial gradients are nevertheless preserved. Note that the fan and OGV sub-domains have different extensions along the azimuth Θ, implying that they communicate through a non-matching interface; in fact, given the circumferential average applied by the mixing-plane, the interface only has to be consistent on the radial direction R; a view of the two sides of the mixing-plane and of the effect of the average on the Mach number is given in Figure 5.4.

— *BPD sub-domain*: extending from the interface with the OGV sub-domain to the outlet and between $\Theta \in [-4.5°, 4.5°]$, it includes the SACOC, placed on the OFS. Since the mesh requirements of this domain, especially because of the presence of the SACOC fins, are different from those of the OGV domain, the two fluid zones are independently meshed, and a non-matching interface, through which flow properties are adequately interpolated, is inserted in between; the SACOC surface is thermally coupled with the solid domain described in §5.2.1 and a Dirichlet boundary condition on the temperature, according to the numerical setup described in Chapter 2, is prescribed; an adiabatic no-slip condition is applied to the remaining surfaces of the by-pass duct; finally, at the outlet, a pressure imposed boundary condition is prescribed ($P_s = P_{std}$).

Due to the presence of the fan and OGV, several aspects of the functioning of a realistic turbofan can be taken into account, such as: the aerodynamic interaction which may occur between the SACOC and the OGV; the impact of the heat exchange and of the pressure drop generated by the heat exchanger on the engine's thrust; the real conditions of the flow making contact with the SACOC fins, *i.e.*, a non-equilibrium boundary layer with residual swirl coming from the fan. In this work, we will be focusing on the latter.

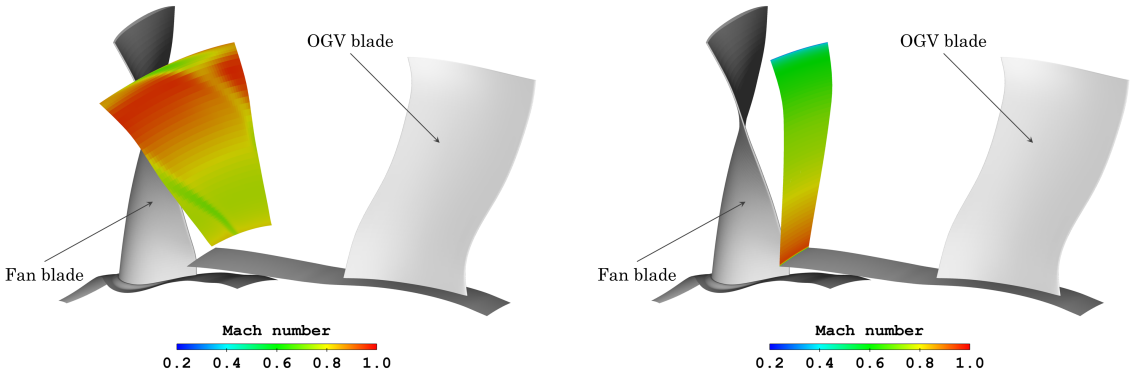

(a) (b)

Figure 5.4: Turbofan configuration. Distribution of Mach number over the fan (a) and OGV (b) side of the mixing plane. Note the non-coincidence of the interface and the disappearance of the fan's wake.

ii. *Test-bench configuration*

As mentioned in §5.1, the performances of a SACOC would, ideally, always be assessed in its operating environment, in this case a turbofan; however, cheaper and less time-consuming smaller-scale tests and simulations are still today a necessity. Therefore, the most common testing configuration still remains the wind tunnel and it is important to understand to which extent such an experimental environment can be representative of the real engine conditions.

The aim of the second configuration studied in this work is, therefore, to analyse the performance of a SACOC in a typical test rig and to compare the results with those obtained with the engine configuration described in the previous paragraph. The geometry of the test bench, shown in Figure 5.5, is that of a square wind tunnel of side H_{WT} so that $H/H_{WT} = 0.15$, where H, recall, is the SACOC fin height (see §5.2.1).

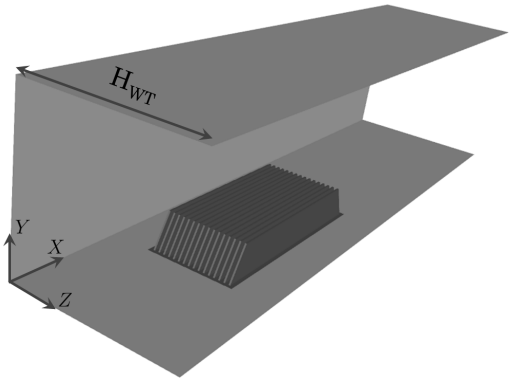

The domain is discretised with a structured mesh of around 30 million nodes and

Figure 5.5: SACOC implemented in square wind tunnel.

includes 16 fins of the SACOC described in §5.2.1, which are placed on the lower wall of the wind tunnel at the same distance from the inlet as the one separating the SACOC and the OGV/BPD interface described in the previous paragraph. At the side walls, as well as at the upper and lower ones, adiabatic no-slip boundary conditions are applied; the SACOC surface is thermally coupled with the solid domain described in §5.2.1 and a Dirichlet boundary condition is prescribed to the temperature; at the inlet, flow properties computed in the engine configuration are extracted from the OGV/BPD interface and applied as boundary conditions. This is done with various levels of complexity, as follows:

— Uniform profiles: at the OGV/BPD interface, the fluid properties (stagnation pressure, stagnation temperature, turbulent kinetic energy and length-scale) are averaged between $R \in [0, H_{WT}]$ and $\Theta \in [-4.5°, 4.5°]$ and imposed at the inlet of the square wind-tunnel. Both radial and azimuthal gradients thus disappear and the flow reaching the SACOC is homogeneous.

— One-dimensional profiles: the fluid properties extracted from the engine configuration are averaged along $\Theta \in [-4.5°, 4.5°]$ for each value of R. While azimuthal gradients vanish, radial gradients are preserved and the SACOC is reached by an average boundary layer. The effect is thus very similar to that of a mixing-plane.

— Two-dimensional profiles: the boundary conditions are extracted from the OGV/BPD interface and simply interpolated on the wind tunnel's grid without any azimuthal or radial average so that all gradients are preserved. These boundary conditions are meant to reproduce the engine conditions at the highest degree of fidelity.

These boundary conditions mimic three different experimental tests, in which the incoming flow is manipulated to yield different degrees of representativeness of the by-pass duct flow. At the outlet, a pressure imposed boundary condition is prescribed and the pressure is calibrated so that the bulk velocity coincides between the two configurations.

5.3 Numerical setup and stability

According to the numerical setup described in §2.3, the full compressible RANS equations are solved to steady state through an implicit cell-centered second-order time-marching scheme on structured meshes. The local time step is calculated in every fluid cell with a Courant-Friedrichs-Lewy number CFL = 10 and the fluid-solid coupling takes place every 50 fluid iterations. The fluid is considered to be a calorically perfect gas with heat capacity ratio $\gamma = 1.4$ and specific gas constant $R = 287\ \mathrm{J/(kg\,K)}$; its dynamic viscosity depends on temperature through the Sutherland law and thermal conductivity is computed with the Prandtl number $\mathrm{Pr} = 0.72$. The contribution of turbulence to the mean flow, in this chapter, is taken into account with the two-equation $k - \ell$ model of Smith Smith (1994) with a constant turbulent Prandtl number $\mathrm{Pr}_t = 0.9$. The choice is motivated by the high Mach number in the fan sub-domain, and the same model is used in the wind-tunnel for consistency.

	Bi_ν	$\alpha_f^{opt}/\alpha_f^{min}$	K_f/α_f^{min}
$\Lambda_s = H$	0.85	-	-
$\Lambda_s = L_{base}$	5.68	1.2	8.6

Table 5.2: Estimation of the main stability parameters for the present case. Since $\alpha_f^{min} < 0$ for $\Lambda_s = H$, the ratios $\alpha_f^{opt}/\alpha_f^{min}$ and K_f/α_f^{min} are not given.

Concerning the stability of the coupling process, Table 5.2 summarises the fundamental parameters discussed in Section 2.5. Values are given for two solid characteristic lengths Λ_s, *i.e.*, the fin height H and length L_{base}. For every parameter requiring fluid physical properties (such as K_f, for example), an *a posteriori* surface average is performed on the SACOC surface. During the simulation, of course, every parameter is computed using the local, instantaneous values, included the fluid pseudo-time-step. As can be seen, radically different results are obtained for the two values of Λ_s, illustrating the difficulty of estimating the numerical Biot number Bi_ν in a practical three-dimensional case. With $\Lambda_s = H$, the coupling interaction is weak, $\mathrm{Bi}_\nu < 1$ and the use of the classic Dirichlet-Neumann boundary conditions is justified. Yet, with $\Lambda_s = L_{base}$, we have $\mathrm{Bi}_\nu \gg 1$, the coupling interaction is rather strong and Dirichlet-Robin conditions are necessary. Most probably, the real Bi_ν is situated between the two and, since the temperature gradients are for the most part (even if not exclusively) oriented along the wall-normal direction, $\Lambda_s = H$ could be the most representative characteristic length. In any case, in order to avoid numerical instabilities and perform robust simulations, we have opted for α_f^{opt} for all the cases described in this chapter.

5.4 Results: engine configuration

In this section the results obtained with the engine configuration described in §5.2.2 are presented. In the following, the cylindrical coordinate system of Fig. 5.3 is used. Therefore, the radial direction points towards the axis of the engine and $R = 0$ on the OFS; besides, the azimuth Θ ranges between $[-4.5°, 4.5°]$; the subscript $(\cdot)_{ref}$ indicates a fluid property averaged over the surface of the OGV/BPD interface between $R \in [0, H_{WT}]$ and $\Theta \in [-4.5°, 4.5°]$; finally, $\overline{(\cdot)}$ denotes Reynolds average.

5.4.1 Nusselt number and pressure drop

Figure 5.6 shows the distribution of some flow properties at the OGV/BPD interface. As can be seen, the flow is highly heterogeneous downstream of the OGV, with the distribution of the Mach number (5.6a) revealing the presence of a strong wake originating at the trailing edge of the OGV blade. Figure 5.6b, instead, shows the pitch angle α of the velocity vector; it can be seen that two counter-rotating vortices are generated at the hub and at the tip of the OGV, the latter being particularly significant as a consequence of the ongoing effect of the fan blade slack. Finally, Fig. 5.6c shows the distribution of the yaw angle β of the velocity vector which,

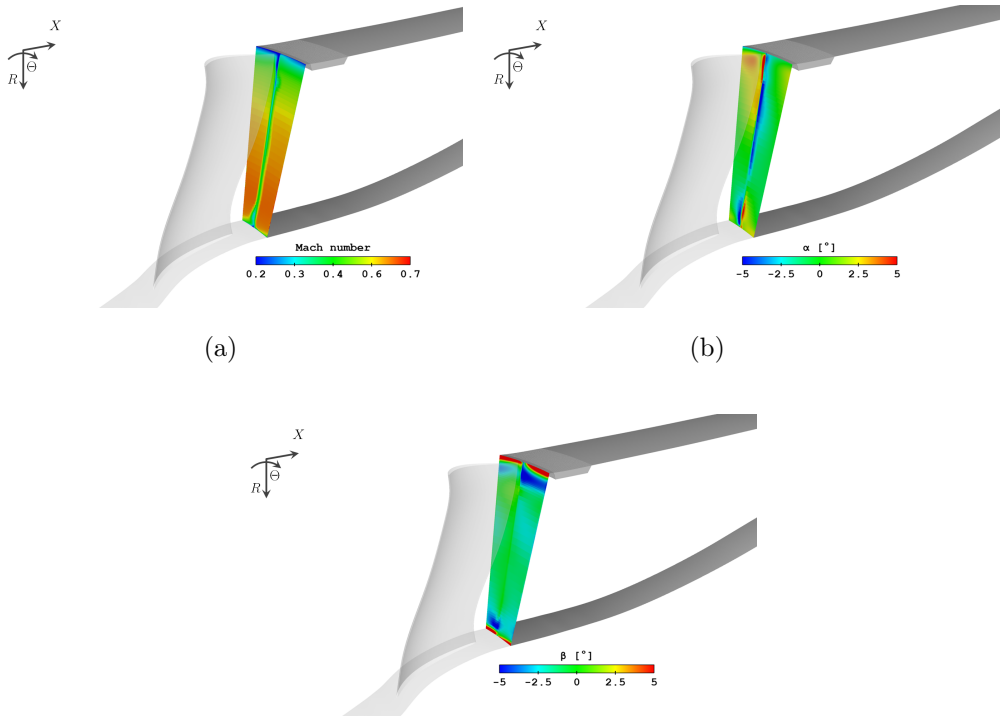

(a) (b)

(c)

Figure 5.6: Characteristics of the flow at the OGV/BPD interface: Mach number (a), pitch (b) and yaw (c) angles of the velocity vector.

except in proximity of the OGV hub and tip, is essentially negative, showing the presence of residual swirl coming from the fan.

The SACOC fins are therefore reached by a complex, three-dimensional, non-equilibrium flow. The temperature field resulting from the forced convection with this flow, is shown in Fig. 5.7, with

$$\theta = \left(\overline{T} - T_{ref}\right) / \left(T_p - T_{ref}\right) \ ,$$

where T_p denotes the temperature at the base of the SACOC fins (see §5.2.1). The temperature distribution is remarkably heterogeneous, with the fins situated on the pressure side of the OGV being significantly colder than those located on the suction side and, especially, in the wake, indicating that certain fins exchange more heat than others.

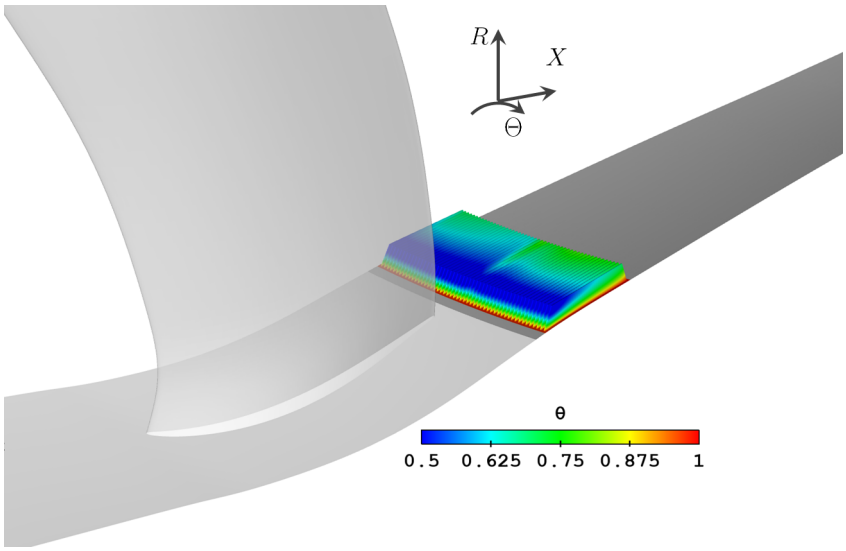

Figure 5.7: Non-dimensional temperature field θ on the SACOC fins.

Figure 5.8a shows the average Nusselt number, computed as

$$\langle \mathrm{Nu} \rangle = \frac{\Phi_w H}{(\lambda_{ref}\,(T_p - T_{ref}))} \ ,$$

fin per fin from the pressure side to the suction side; Φ_w is the wall heat flux averaged over the surface of the fin and H is the fin height. As can be seen, the two central fins, placed behind the trailing edge of the OGV blade, exchange approximately 30% less heat than the best performing fins. It is interesting to compare the distribution of the Nusselt number with that of the drag coefficient

$$\mathrm{C}_D = \frac{\mathcal{T}_w}{\frac{1}{2}\rho_{ref} u_{ref}^2} \ ,$$

where $\mathcal{T}_w$ is the wall shear stress averaged over the surface of the fin, which is shown in Fig. 5.8b. The more heat is exchanged by a fin, the more important is the total viscous drag contributing to the pressure drop. This analogy can be explained by analysing the distribution of the mass flow rate passing through every channel separating two consecutive fins. In Figure 5.8c both the entering (by the leading edge) and leaving (by the trailing edge) mass flow rates of every fin are shown, non-dimensionalized with respect to P^t_{ref} and T^t_{ref}, with P^t and T^t the stagnation pressure and temperature, respectively. The distribution of the entering mass flow rate qualitatively resembles those of the Nusselt number and of the drag coefficient, which is rather intuitive: the more mass flows between two fins, the higher the average speed of the flow is, and both the heat exchange and the head losses increase.

It is also interesting to investigate the distribution of the leaving mass flow rate, which actually resembles that of $\langle \mathrm{Nu} \rangle$ and C_D even more than the entering one. For every fin, it can be observed that there is a loss of mass flow between the leading and trailing edges. This can be explained by the fact that the SACOC, because of both

its shape and the heat it provides, constitutes an aerodynamic obstacle that the flow prefers to avoid. Therefore, a significant portion of the mass flow escapes from the upper part of the SACOC without crossing its whole length, thereby reducing the thermal efficiency of the fins. On the pressure side of the OGV (left-hand side of Fig. 5.8c), around 50% of the mass flow rate is lost through the upper side of the fins, yet this phenomenon is exacerbated on the suction side, where, for some fins, less than 30% of the entering mass flow rate attains the trailing edge. Not surprisingly, these fins have amongst the lowest average Nusselt number and drag coefficient.

A possible explanation for the stronger loss of mass flow on the suction side might be the interaction between the heat exchanger and the vortex generated at the trailing edge of the OGV blade, the sense of rotation of which might help drive the flow away from the SACOC fins. Visualizations of the flow are given in Figure 5.9. Figure 5.9a shows the temperature iso-surface $\theta = 0.4$ colored by the Mach number; Figure 5.9b depicts the velocity streamlines on two azimuthal planes $\Theta = 2.25°$ (*i.e.*, on the pressure side of the OGV) and $\Theta = -2.25°$ (*i.e.*, on the suction side of the OGV). As can be seen, on the pressure side the flow remains well attached to the OFS downstream of the SACOC and, while the velocity streamlines do deviate from the fins causing the aforementioned loss of mass flow, the temperature iso-surface adheres to the wall; on the other hand, the suction side is characterized by a stronger deviation of the velocity streamlines with an important flow separation (approximately as high as the SACOC fins and at least twice as long) taking place downstream of the heat exchanger.

Table 5.3 summarises the global performance parameters of the SACOC on both the pressure and suction side. The global Nusselt number and drag coefficient are simply computed by averaging the values of the fins located on each side; the head losses, instead, are calculated between the OGV/BPD interface and a plane located two fin lengths downstream of the SACOC by computing the average stagnation pressure between $\Theta \in [0°, 4.5°]$ for the pressure side and $\Theta \in [-4.5°, 0°]$ for the suction side. As can be seen, despite the drag coefficient being higher for the pressure side fins, the global pressure drop is more important on the suction side. Indeed, the dissipation caused by the skin friction between the fins is only one of the contributions to the head losses and, in this case, the separation bubble shown in Fig. 5.9 seems to play a much more important role. Therefore, it is possible to conclude that the pressure side of the SACOC is significantly better performing than the suction side, since not only is the global heat exchange approximately 15% higher, yet the global pressure drop is around 70% lower.

	Pressure side	Suction side	Comparison
$\langle \mathrm{Nu} \rangle$	140.1	123.12	+13.7%
C_D	0.0022	0.0016	+37.5%
Head losses	0.7%	2.2%	− 68%

Table 5.3: SACOC's performances in terms of average Nusselt number, drag coefficient and global head losses on the pressure and the suction side of the OGV.

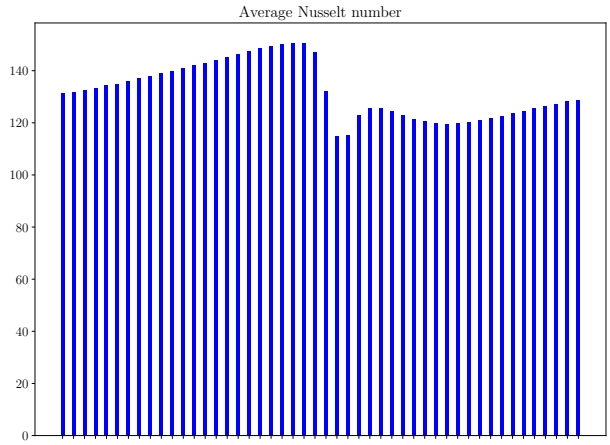

(a)

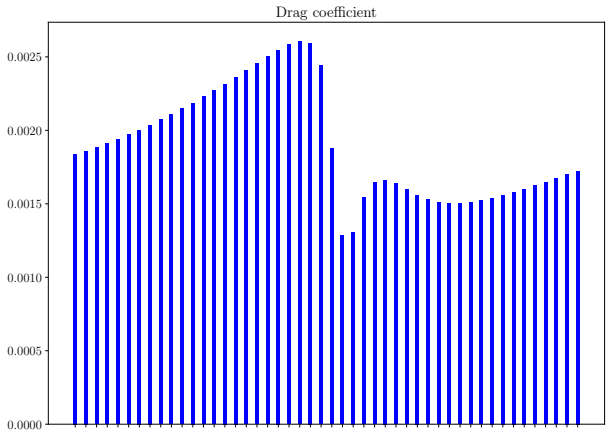

(b)

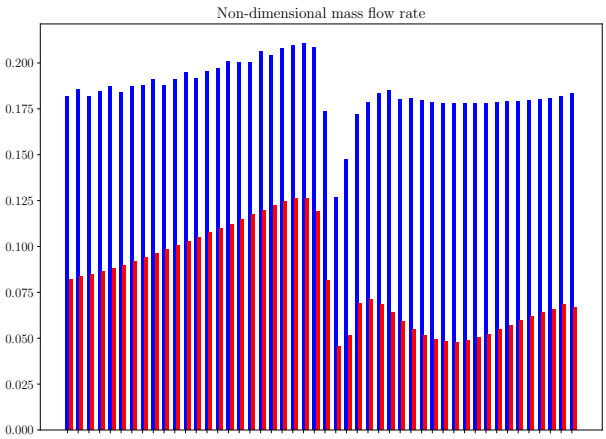

(c)

Figure 5.8: Engine configuration. Distribution of average Nusselt number (a), drag coefficient (b) and mass flow rate (c) on the 50 SACOC fins, from the pressure side to the suction side of the OGV. For Fig. (c) the blue and red bars represent the entering and leaving mass flow rates, respectively.

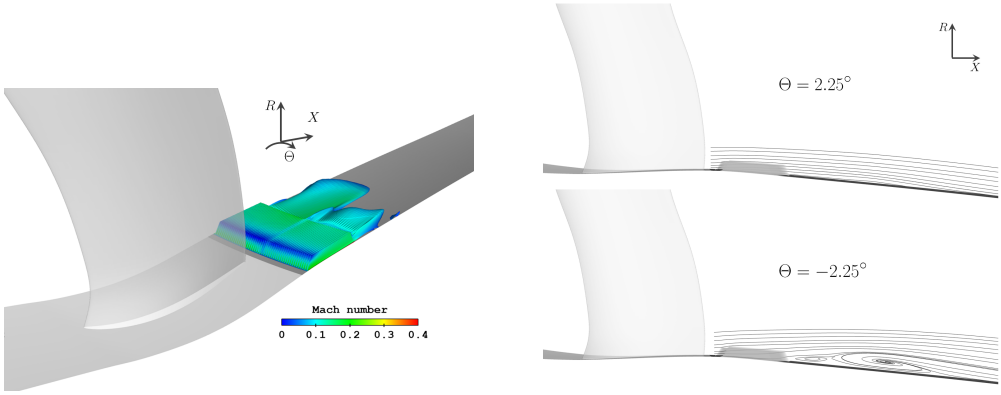

(a) (b)

Figure 5.9: Temperature iso-surface $\theta = 0.4$ colored by the Mach number (a) and velocity streamlines on two azimuthal planes at $\Theta \pm 2.25°$ (b).

5.4.2 Thermal boundary layer development

In this section, we aim at finely characterising the forced convection taking place within the SACOC. Our purpose, in particular, is to gain insight into the conditions of the flow between two consecutive fins, even though the RANS modelling of the flow constrains us to a rather qualitative analysis.

As explained in the Introduction, one important phenomenological aspect of the SACOC is that an essentially temperature-homogeneous flow makes contact with a heated surface, and, as a consequence, turbulent heat transfer takes place in non-equilibrium conditions. This aspect has been the object of Part II and, above all, of Chapter 3, where this phenomenon has been studied by direct numerical simulation in a simplified configuration. We have seen that the sudden step-change in surface temperature generates a thermal boundary layer, and that an equilibrium sub-layer can be identified at any stage of its development. As illustrated in Chapter 4, the existence, the extension and the evolution of the equilibrium region are fundamental to determine whether a simplified modelling of the inner layer may be justified or not. In this section, we intend to investigate the behaviour of the flow traversing the heat exchanger, and to understand whether any equilibrium assumption might stand in the present case.

For this purpose, we propose to examine the thermal boundary layer at twelve different locations of a SACOC fin's side wall, as illustrated in Figure 5.10. With respect to the engine axis, the fin is at $\Theta \approx -2.5°$, *i.e.*, on the suction side of the OGV which, as explained in §5.4.1, is the most perturbed one and is characterised by flow separation downstream of the SACOC. As shown in Figure 5.10, the twelve wall-points are located at three different distances from the base of the fin (*i.e.*, $R/H = 1/4, 1/2$ and $3/4$) and at four different distances from the leading edge (*i.e.*, $x/L_{base} = 0.01, 0.2, 0.5$ and 0.9). In the following, the temperature profiles are plotted along the local wall-normal direction y for a total distance of $\delta = S_{fin}/2$, where S_{fin}, recall, is the distance between two consecutive fins (see Fig. 5.1).

Figure 5.11 shows the profiles of non-dimensional temperature θ obtained at $R/H = 1/4$ (Fig. 5.11a), $R/H = 1/2$ (Fig. 5.11b) and $R/H = 3/4$ (Fig. 5.11c)

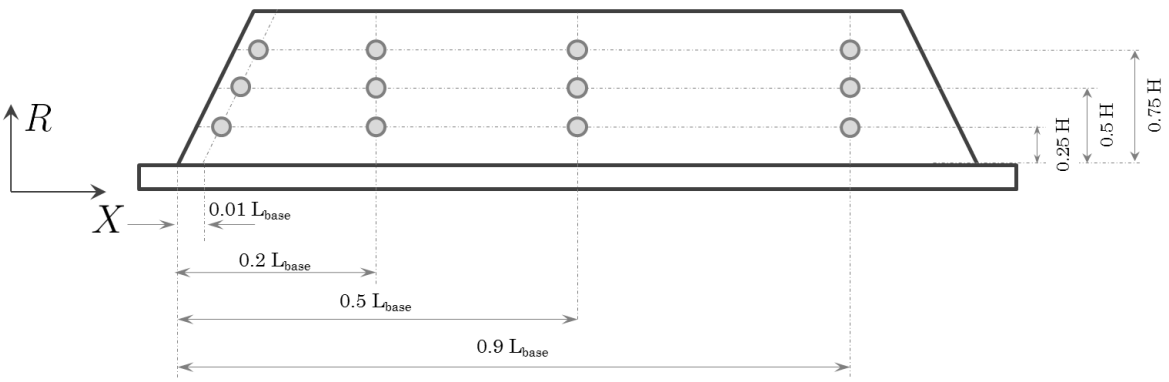

Figure 5.10: Location on the fin's side wall of the twelve thermal boundary layers.

for the different streamwise coordinates x/L_{base}. The behaviour of the temperature profile is rather intuitive. As can be seen, θ decreases along the wall-normal direction until attaining a minimum at y/δ, *i.e.*, half the distance between two consecutive fins; only the profiles at $x/L_{base} = 0.01$ exhibit a different behaviour, which is due to the proximity to the leading edge of the SACOC and the heterogeneity of the static temperature downstream of the OGV. The plateau seen at $y/\delta \approx 1$ for the profiles at $x/L_{base} = 0.01$ is typical of external flow boundary layers. On the other hand, the other profiles are more rounded, which, associated with an increase in the central temperature at $y/\delta = 1$, indicate an internal flow regime. Hence, the channel entry zone from the fins' leading edges extends up to a location between $x/L_{base} = 0.01$ and 0.2, where the initially separated boundary layers developing on the two adjacent fins are joining at the centre. The increase in the central temperature seems to be particularly accentuated for $R/H = 1/4$, suggesting that the thermal boundary layer is also interacting with the one developing along the radial direction R on the bottom wall of the SACOC, *i.e.*, at $R = 0$. This aspect is particularly evident in Figure 5.12, where the two-dimensional cartography of θ is displayed for the three crosswise sections $x/L_{base} = 0.2, 0.5$ and 0.9. As can be seen, at $x/L_{base} = 0.9$ the heated pockets developing from the base of the heat exchanger have reached $R/H = 1/4$, where the thermal boundary layer appears to be considerably thicker with respect to $R/H = 1/2$ or $3/4$.

The temperature profiles, expressed in semi-local scaling, are plotted in Figure 5.13, where the equilibrium profile of a bi-periodic channel flow (see Appendix A for the details) is also displayed for comparison. As can be seen, there are several similarities with the evolution of the thermal boundary layer described in Chapter 3. First of all, notice the qualitative resemblance of the evolution of the temperature profile illustrated in Figures 5.13 and 3.15; in both cases the initial temperature plateau at $y/\delta \approx 1$ quickly disappears along the streamwise direction, while a logarithmic region develops as the thermal boundary layer thickens.

Also observe how, for every temperature profile, we can identify a region in reasonable agreement with the canonic temperature evolution. In some cases (*e.g.*, the

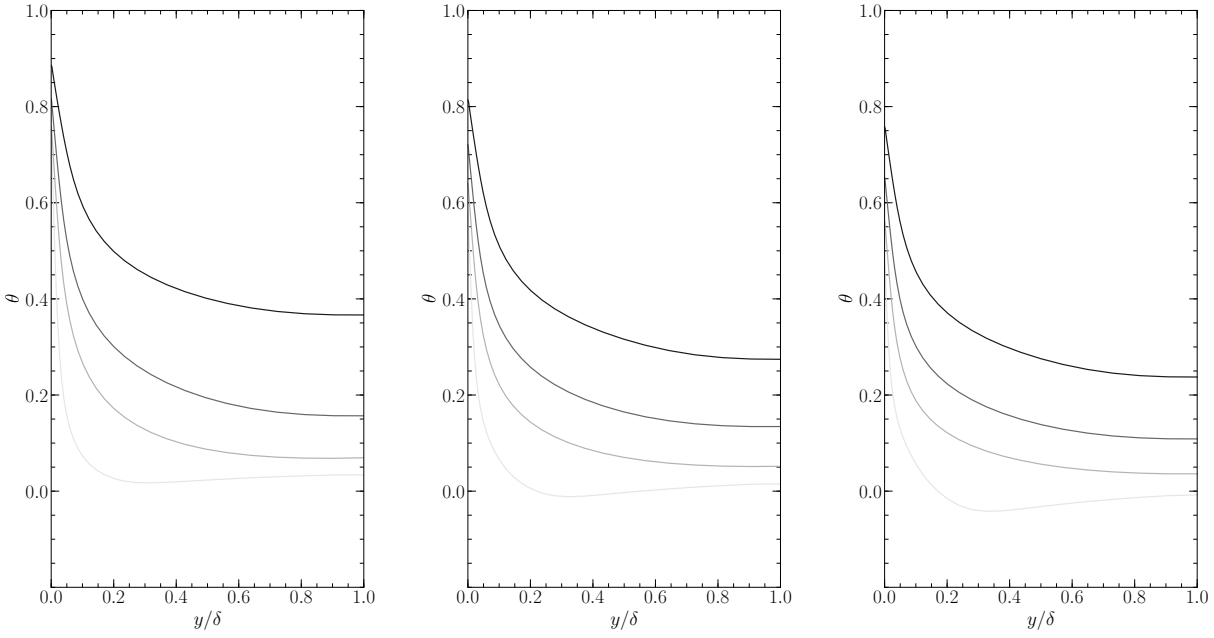

Figure 5.11: Profiles of non-dimensional temperature θ at $R/H = 1/4$ (a), $R/H = 1/2$ (b) and $R/H = 3/4$ (c) and at $x/L_{base} = 0.01, 0.2, 0.5$ and 0.9 (from light to dark gray).

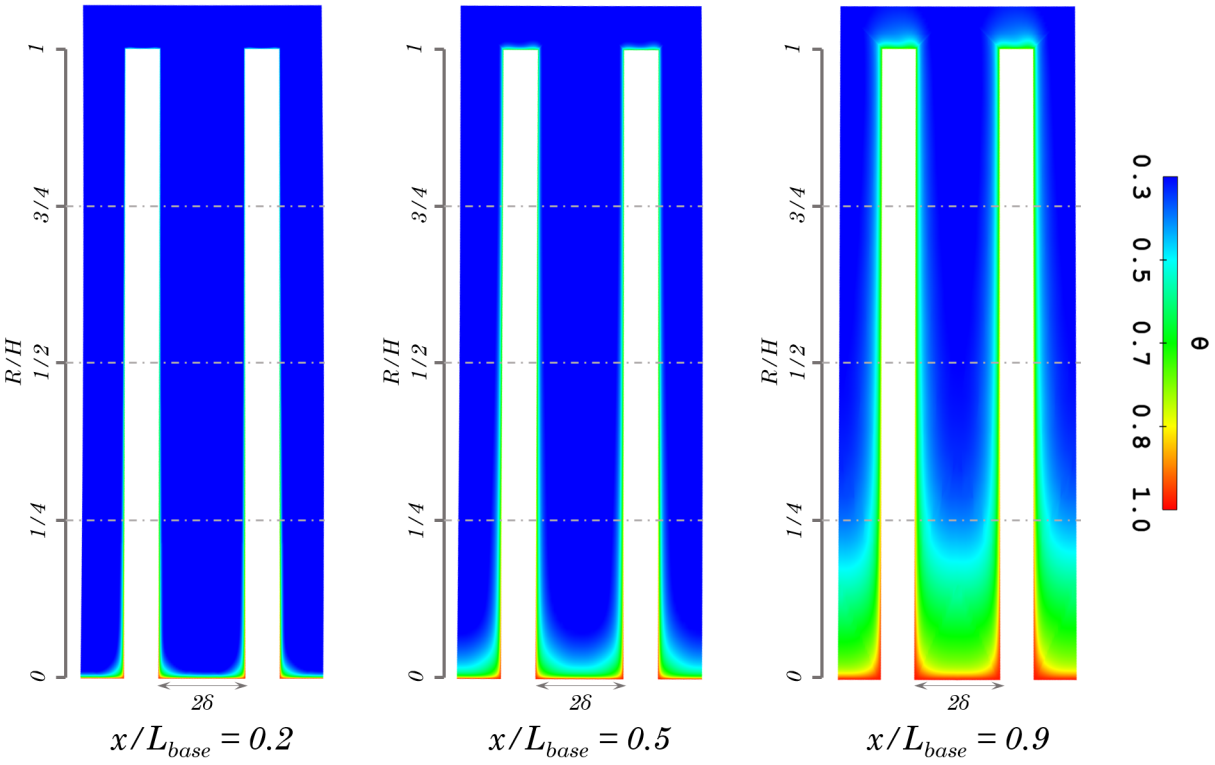

Figure 5.12: Field of non-dimensional temperature at the three crosswise sections $x/L_{base} = 0.2, 0.5$ and 0.9.

profile at $R/H = 1/4$ and $x/L_{base} = 0.01$ of Fig. 5.13a), this region does not extend far beyond the conductive sub-layer, but in other cases (*e.g.*, the profile at $R/H = 1/4$ and $x/L_{base} = 0.5$ of Fig. 5.13a) it reaches and covers the entire logarithmic layer. These results seem to confirm the existence of a clearly identifiable equilibrium sub-layer even in the present case, which, recall, is characterised by extremely complex inflow conditions and by a realistic industrial operating environment. As x/L_{base} increases, the thermal boundary layer grows, and a logarithmic evolution of the temperature is discernible for every R/H, even though some disparities with the canonic profile are sometimes observed (see, for instance, Figure 5.13c). This suggests that other non-equilibrium effects than the ones identified in Chapter 3 in the channel flow configuration, are very much present within the SACOC.

The temperature profiles at $x/L_{base} = 0.9$, *i.e.*, in proximity to the trailing edge of the fin, have a more counter-intuitive behaviour. At $R/H = 1/2$ and $R/H = 3/4$ (see Figures 5.13b and 5.13c), both T^* and y^* at $y/\delta = 1$ decrease between $x/L_{base} = 0.5$ and $x/L_{base} = 0.9$. Since, as shown for θ in Figure 5.11, the temperature increases with x/L_{base} and, intuitively, the wall heat flux diminishes, this effect is due to an important drop of the wall shear-stress, which, between $x/L_{base} = 0.5$ and $x/L_{base} = 0.9$, decreases by over 80% (not shown here). Consequently, the friction velocity u_τ drops, and so do the semi-local scaled temperature and wall-distance. The reduction of the wall-shear stress might be explained by the loss of mass flow through the upper side of the SACOC illustrated in §5.4.1, which causes a drop of the local Reynolds number. However, notice that the slope of the logarithmic region remains approximately the same. Hence, the thermal boundary layer seems to well adapt to the strongly modified wall-shear stress, conserving a semi-equilibrium behaviour.

Observe, now, the temperature evolution at $R/H = 1/4$ of Figure 5.13a. At $x/L_{base} = 0.5$, the thermal boundary layer appears to be fully developed, with a well-defined logarithmic region (also, in excellent agreement with the canonic law) that reaches $y/\delta \approx 1$. However, at $x/L_{base} = 0.9$, not only do T^* and $\mathrm{Re}_\tau = \delta u_\tau/\nu$ decrease as described above, yet the slope of the logarithmic profile also lowers and drifts from the equilibrium law. Given the proximity to the lower wall $R = 0$, this is possibly an effect of the interaction with the thermal boundary layer developing on the base of the heat exchanger.

The configuration that we have introduced and analysed by DNS in Chapter 3 is, undoubtedly, rather simplistic, and extremely far from the complexity of the engine's BPD. However, as the results presented in this section suggest, the flow traversing two consecutive fins seems, in fact, to be predominantly driven by the same phenomenological aspect of the SACOC that we have isolated and reproduced in the channel flow. Despite the undeniable presence of non-equilibrium effects, which lead to the deviation of some temperature profiles from the canonic equilibrium one, the results obtained in this section suggest that equilibrium assumptions in the inner-layer might not be hasty in the present case.

5.5 Results: test-bench configuration

The objective of this section is to investigate to which extent the performances of a SACOC installed in a turbofan by-pass duct are reproducible in a common test rig configuration like the one introduced in §5.2.2. In the following, the frame of reference is the one of Fig. 5.5; therefore, X represents the axial direction, Y the wall-normal direction (with the SACOC installed on the $Y = 0$ wall) and Z the spanwise direction;

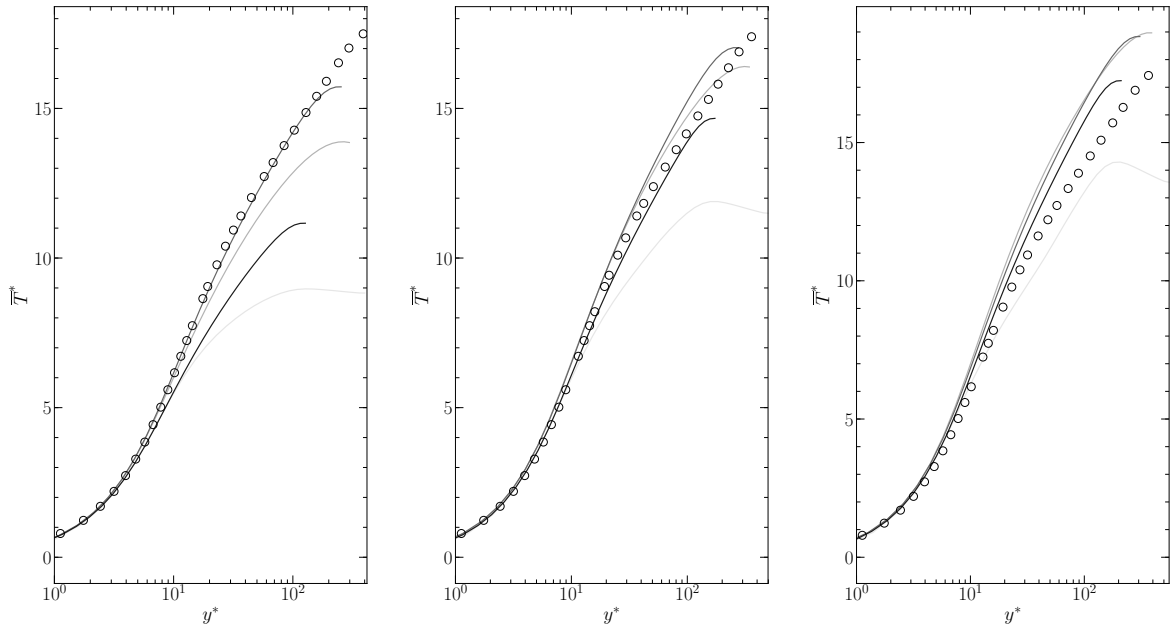

Figure 5.13: Profiles of temperature in semi-local scaling $\overline{T}^*$ at $R/H = 1/4$ (a), $R/H = 1/2$ (b) and $R/H = 3/4$ (c) and at $x/L_{base} = 0.01, 0.2, 0.5$ and 0.9 (from light to dark gray); ○ equilibrium profile from DNS of bi-periodic channel flow (see Appendix A).

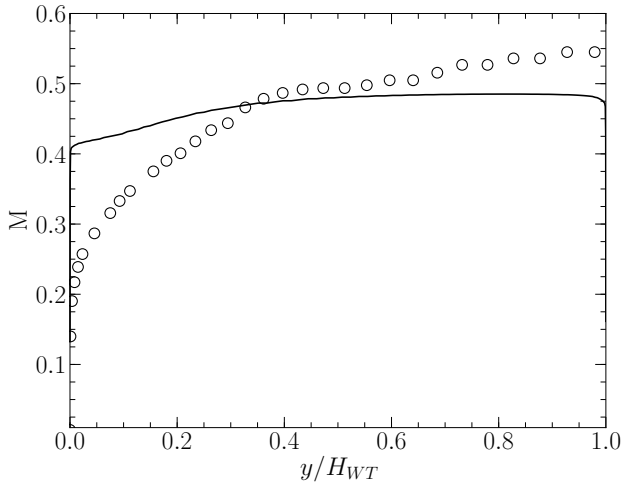

Figure 5.14: Uniform boundary conditions. Comparison of Mach number profiles: —— wind-tunnel's inlet with uniform boundary conditions; ○ OGV/BPD interface of the engine configuration.

as shown in §5.2.2, 16 fins are installed in the wind tunnel; furthermore, as already mentioned, the boundary conditions imposed at the inlet of the test channel are extracted from the OGV/BPD interface of the engine configuration with different levels of complexity. In the next paragraphs, the results obtained with uniform (§5.5.1), one-dimensional (§5.5.2) and two-dimensional (§5.5.3) boundary conditions are presented.

5.5.1 Uniform boundary conditions

At the inlet, constant values for the stagnation pressure, stagnation temperature and turbulence are imposed; furthermore, the flow is supposed to be completely axial (*i.e.*, oriented along the X direction, see Fig. 5.5). Such homogeneous inlet flow conditions are typical of test rigs where the flow reaches the test section after crossing a settling chamber without any further manipulation (see, for instance, Lau and Mahajan (1989)). In order for this flow to be somewhat representative, the inlet conditions are extracted from the OGV/BPD interface and averaged between $R \in [0, H_{WT}]$ and $\Theta \in [-4.5°, 4.5°]$.

Figure 5.14 shows the comparison between the Mach number profiles at the wind tunnel's inlet (averaged along the spanwise direction Z) and at the OGV/BPD interface (averaged along the azimuth Θ). As can be seen, at the inlet the Mach profile is essentially flat, except for a small inflection near $y/H_{WT} = 0$, which is due to the deceleration of the flow running into the aerodynamic blockage of the SACOC. In other words, no boundary layer is injected at the inlet and, with respect to the engine profile, the Mach number is significantly overestimated for $y < H$, where H, recall, represents the fin height.

Figure 5.15 plots the Nusselt number, drag coefficient and entering as well as leaving mass flow rate for each SACOC fin compared to the results presented in §5.4.1. The same non-dimensionalisation used in §5.4.1 is employed here. As could be expected, all the SACOC fins have a similar behaviour (except for a small border

effect visible on the mass flow rate distribution) as a consequence of the homogeneous injection. As can be seen, the higher Mach number in the lower part of the wind tunnel leads to a strong overestimation of all the performance parameters. The Nusselt number is around 60% higher compared to the average engine SACOC fin, while the drag coefficient is more than 100% more elevated. Concerning the mass flow rate, not only is the entering mass flow over-estimated, yet the ejection event described in §5.4.1 is in this case significantly weaker compared to the engine configuration; indeed, around 30% of the mass flow is lost by the upper part of the SACOC, compared to more than 50% for the engine fins.

Thanks to these results, it is possible to conclude that uniform boundary conditions, despite being representative of the mean flow at the OGV/BPD interface, do not allow us to predict any performance parameter of interest of the SACOC. There certainly exists a homogeneous flow capable of reproducing, at least on average, the behaviour of the complex, anisotropic flow downstream of the OGV, yet the values to be imposed to the stagnation pressure at the inlet cannot be known *a priori*. In practice, in case where the test rig cannot generate but homogeneous flows, it could be preferable to limit the average of the fluid properties at the OGV/BPD interface to a lower radius, in order for the boundary conditions to be representative of the portion of the flow that the SACOC actually encounters. Figure 5.16 depicts the Nusselt number obtained while imposing the stagnation pressure averaged over $R \in [0, 1.5H]$, where H is the fin height, and $\Theta \in [-4.5°, 4.5°]$. Despite the Nusselt number still being not only above the average but also above the best exchanging engine fin, the overestimation is limited to around 20%.

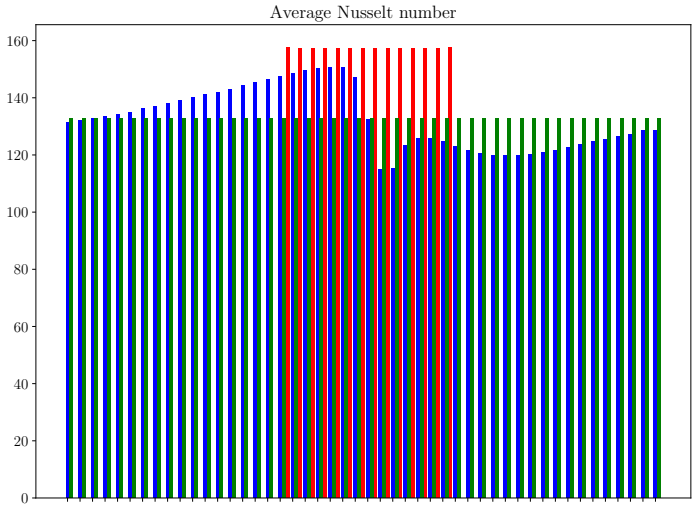

5.5.2 One-dimensional boundary conditions

At the inlet, one-dimensional profiles of stagnation pressure, stagnation temperature and turbulence are imposed; these profiles are obtained through an azimuthal average at the OGV/BPD interface of the engine configuration; in this case, the pitch and yaw angles of the velocity vector are also averaged and imposed as boundary conditions. Therefore, the direction of the velocity vector at the inlet is not fully axial. Similar boundary conditions, in practice, can be obtained through distortion screens of heterogeneous porosity which, thanks to the pressure drop the flow

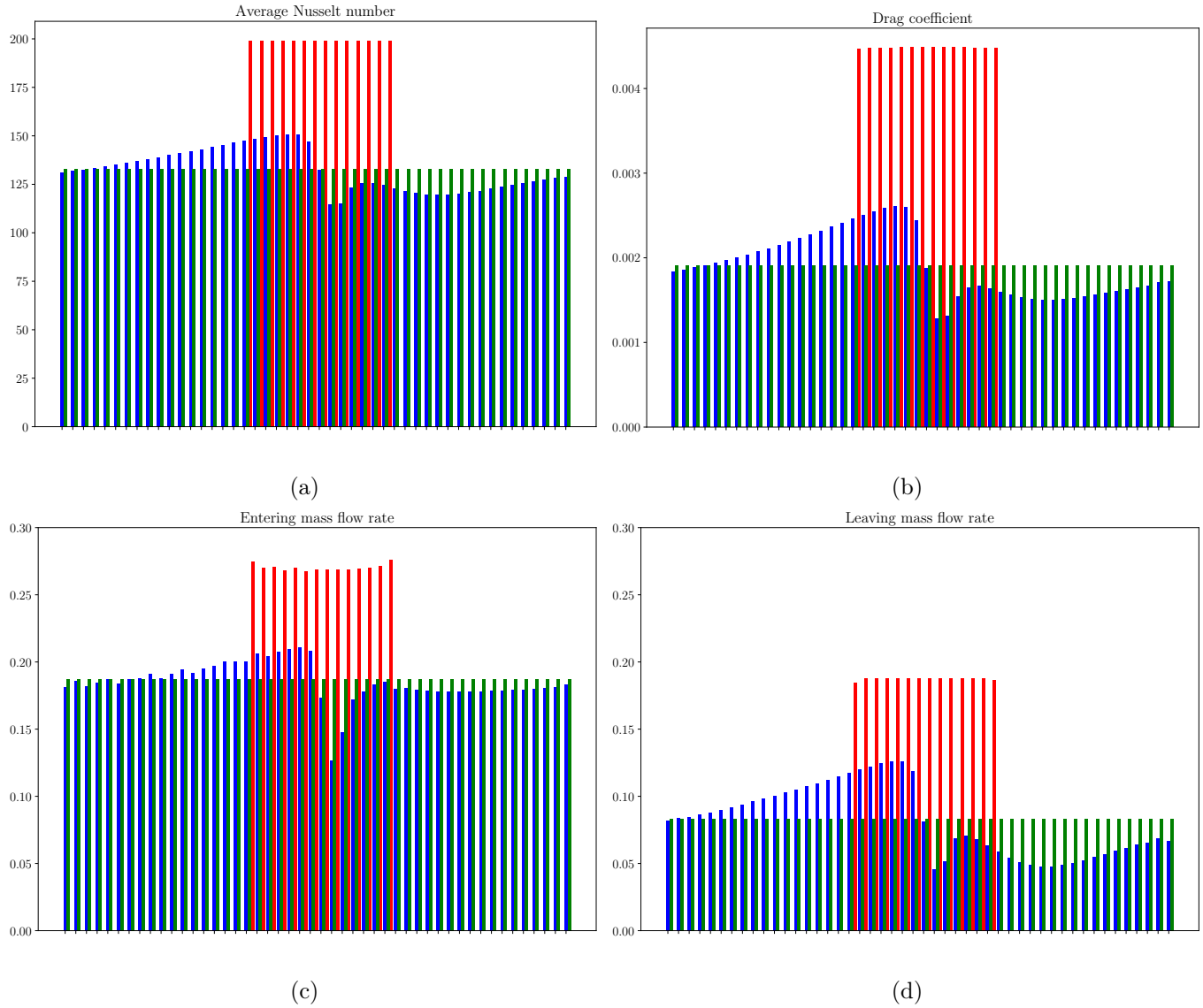

Figure 5.15: Uniform boundary conditions. Distribution of average Nusselt number (a), drag coefficient (b), entering (c) and leaving (d) mass flow rate on the SACOC fins: results from engine configuration of §5.4.1, blue bars; average over SACOC fins of the engine configuration, green bars; results from test bench configuration with uniform boundary conditions, red bars.

Figure 5.16: Uniform boundary conditions, average of boundary conditions limited to $R \in [0, 1.5H]$. Distribution of average Nusselt number. See Fig. 5.15 for a reference to colors.

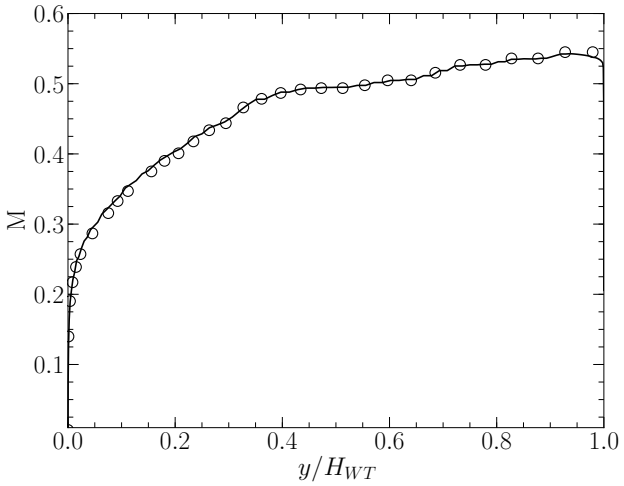

Figure 5.17: One-dimensional boundary conditions. Comparison of Mach number profiles: —— wind-tunnel's inlet with one-dimensional boundary conditions; ○ OGV/BPD interface of the engine configuration.

blockage induces, modify the stagnation pressure profile allowing the reproduction a non-uniform flow (see, for instance, Davis et al. (2002)). As we shall see in Chapter 6, a similar strategy will be used for our experimental investigations.

Figure 5.17 shows the comparison between the Mach number profiles at the inlet and at the OGV/BPD interface (averaged along the azimuth Θ). As illustrated, these boundary conditions allow us to recreate the boundary layer seen by the average engine fin.

Figure 5.18 shows the Nusselt number, drag coefficient and entering as well as leaving mass flow rate for each SACOC fin compared to the results presented in §5.4.1. All the SACOC fins have a similar behavior (except for some slight differences for the leaving mass flow rate, see Fig. 5.18d), which, despite the boundary conditions being uniform along the spanwise direction, is not entirely obvious since the entering flow is not axial. The local distribution of the performance parameters of interest is not captured, yet, as can be seen from Fig. 5.18a, the average Nusselt number is very well predicted with respect to the average engine fin, with an overestimation of around 6%, which is a significant improvement compared to the results obtained with uniform boundary conditions. The drag coefficient (see Fig. 5.18b), on the other hand, is characterised by an over-prediction of around 20%. The overestimation of both the Nusselt number and drag coefficient can be explained by the behaviour of the entering and leaving mass flow rate. If the average entering mass flow rate is extremely well predicted (see Fig. 5.18c), the leaving mass flow is almost 50% higher compared to the average engine fin. Consequently, more flow runs through the length of the SACOC and both the heat exchange and viscous drag are more elevated. These results illustrate the critical role played by the ejection event taking

place within the fins and the importance of accurately reproducing it.

The results shown in Fig. 5.18, as explained at the beginning of the paragraph, are obtained by imposing a one-dimensional profile for all the inlet fluid properties, *i.e.*, the stagnation pressure, stagnation temperature, turbulence and pitch/yaw velocity angles. So as to understand which profiles are actually fundamental to reproduce in a wind tunnel to obtain accurate results, additional simulations are run, where a mix of one-dimensional and uniform boundary conditions are imposed at the inlet. Figure 5.19 shows the results obtained for the average Nusselt number, where the darkest bars represent the case where all the inlet profiles are one-dimensional (and therefore coincide with the results shown in Fig. 5.18a) and the lightest bars represent the case where all the boundary conditions are uniform (and therefore coincide with the results shown in Fig. 5.15a). As can be seen, as long as a one-dimensional profile is imposed for the stagnation pressure, the prediction of the heat exchanged by the SACOC fins does not significantly change regardless of whether the other inlet variables are uniform or not.

Thanks to these results, it is possible to conclude that the complex, anisotropic flow downstream of the OGV described in §5.4.1, can be rather accurately represented by a one-dimensional flow obtained through a circumferential average. The absence of spanwise gradients does not enable us to capture the local distribution of the heat exchange observed on the engine fins, yet the behaviour of the average SACOC fin is well retrieved. It is also evident how the fluid property that influences the performance parameters the most is the stagnation pressure; indeed, imposing a 1D profile of stagnation pressure at the inlet amounts to injecting a boundary layer. This leads to a good prediction of the mass flow entering the SACOC fins and, therefore, of the global heat exchange. However, the under-prediction of the ejection event taking place within the fins with respect to the engine configuration leads to a slight overestimation. In practice, such boundary conditions are certainly more laborious to recreate compared to a homogeneous flow, yet, as these results show, necessary.

5.5.3 Two-dimensional boundary conditions

The two-dimensional cartography of the stagnation pressure, stagnation temperature, turbulence and direction of the velocity vector is extracted from the OGV/BPD interface of the engine and imposed as boundary conditions at the inlet of the wind-tunnel. These boundary conditions recreate the most faithful representation of the engine flow with the given test bench geometry.

In Figure 5.20 the main performance parameters of the SACOC are compared to the results obtained in §5.4.1. As can be seen from Fig. 5.20c, imposing the exact field of stagnation pressure at the inlet leads to a very good prediction of the entering mass flow rate of every fin. Furthermore, the distribution of the Nusselt number and of the drag coefficient resembles that of the engine configuration, with the fins on the left-hand side (*i.e.*, the pressure side in the engine configuration) exchanging more heat and being characterized by a higher viscous drag than the fins on the right-hand side (*i.e.*, the suction side in the engine configuration); on the other hand, a certain level of overestimation can be observed, particularly accentuated for the drag coefficient on the right-hand side fins. This can be explained once again by the distribution of the leaving mass flow rate, which is significantly higher for every SACOC fin compared to the engine configuration; this indicates that despite the representativeness of the boundary conditions, it is extremely arduous to finely reproduce the ejection event observed in the SACOC of the engine configuration.

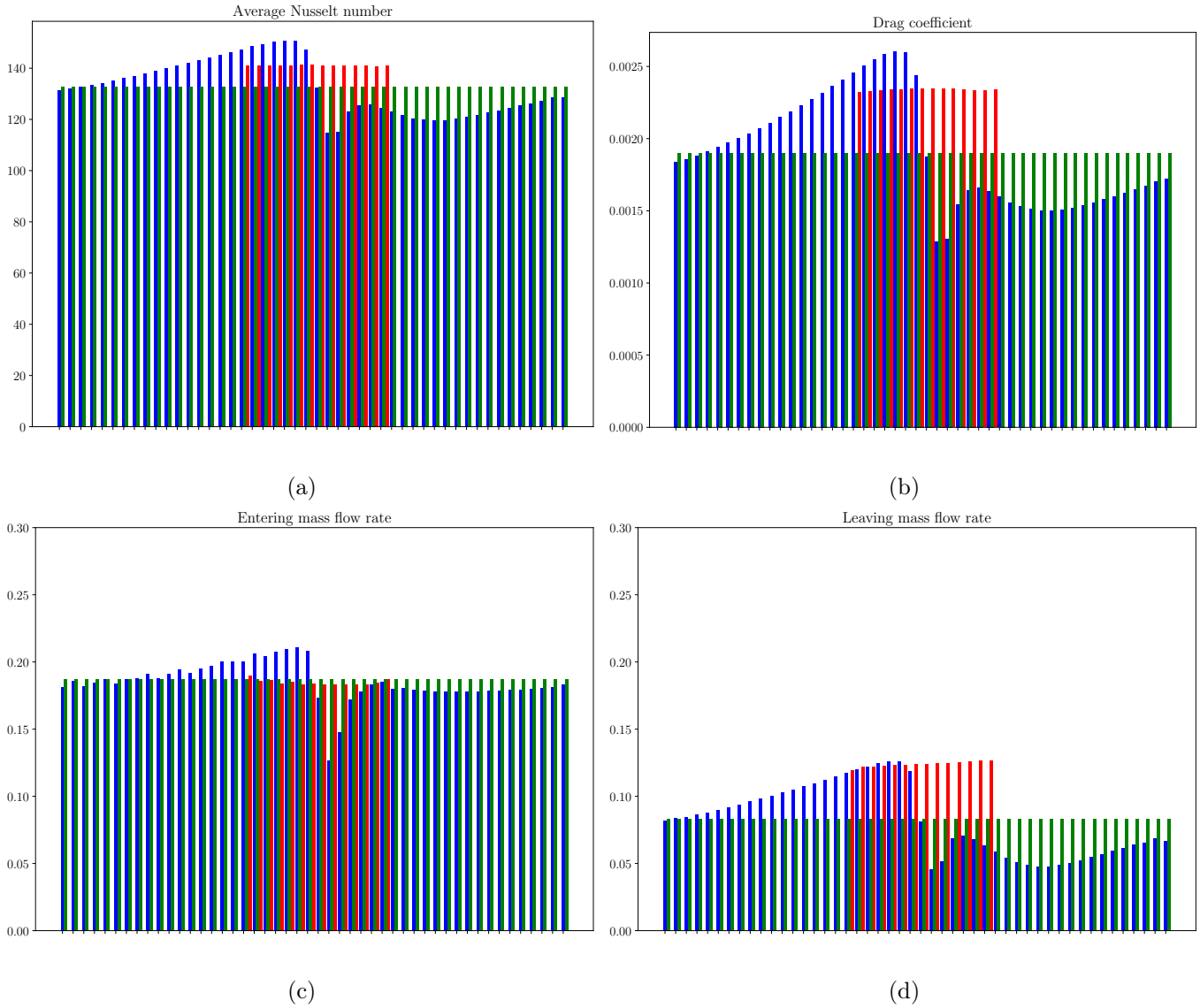

Figure 5.18: One-dimensional boundary conditions. Distribution of average Nusselt number (a), drag coefficient (b), entering (c) and leaving (d) mass flow rate on the SACOC fins: blue bars, results from engine configuration of §5.4.1; green bars, average over SACOC fins of the engine configuration; red bars, results from test bench configuration with one-dimensional boundary conditions.

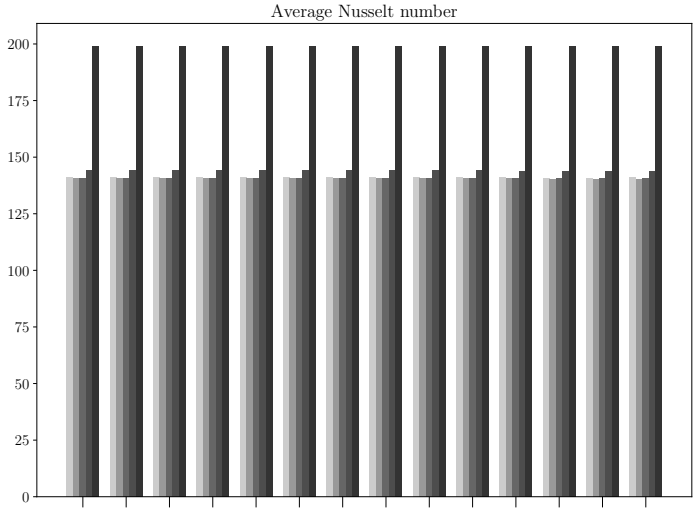

Figure 5.19: Mix of uniform and one-dimensional boundary conditions. Distribution of average Nusselt number. From light to dark gray: 1D profiles for all boundary conditions and non-axial flow; same as previous bars but turbulence 0D; same as previous bars but axial flow; same as previous bars but stagnation temperature 0D; 0D profiles for all boundary conditions and axial flow.

So as to further investigate the behaviour of the flow in the wind tunnel, visualizations of the $\theta = 0.4$ iso-surface and velocity streamlines on the left- and right-hand side of the wind tunnel are given in Fig. 5.21. The analogous flow visualizations given in Fig. 5.9 showed how the suction side in the engine configuration is affected by a strong flow separation, which explains the higher overall pressure drop and higher mass flow loss of the suction-side fins. As can be seen, the wind tunnel flow has a completely different behaviour, since no flow separation is observed on the right-hand side of the channel, and the only difference between the two sides is the stronger deflection of the velocity streamlines on the right-hand side (Fig. 5.21b, bottom). Given the precision with which the inflow conditions are prescribed, the difficulties encountered in reproducing the engine flow reveal the limited representativeness of the wind tunnel configuration. Its small size in both the wall-normal and spanwise directions might, for instance, confine the inlet vortex in a much narrower space, and thus lead to a weaker interaction with the SACOC. Or, its limited length in the streamwise direction, at the end of which a uniform static pressure is imposed, might force a premature homogenization of the flow.

Table 5.4 summarises the global performance parameters of the SACOC on the left- and right-hand side of the wind tunnel, computed as was done in §5.4.1 for building Table 5.3. The values of the Nusselt number and drag coefficient for both the left- and right-hand side are higher compared to the engine configuration; this is partly due to the aforementioned over-prediction of these quantities and partly due to the fact that fewer fins are installed in the wind tunnel with respect to the engine. On the other hand, the relative difference between the two sides is close to the one observed between the pressure and suction sides (see Table 5.3). The same cannot be said about the head losses which, due to the absence of flow separation on the

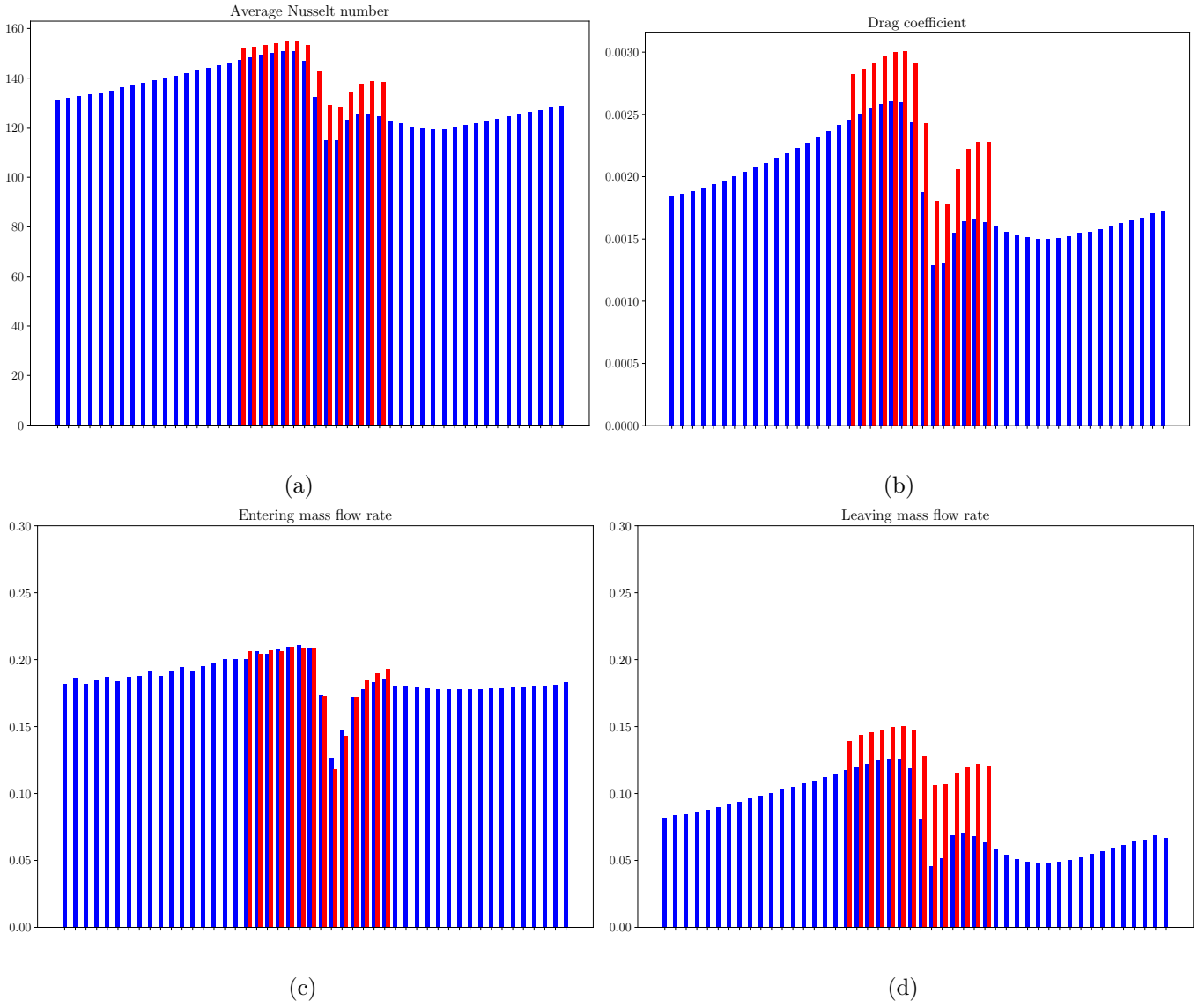

Figure 5.20: Two-dimensional boundary conditions. Distribution of average Nusselt number (a), drag coefficient (b), entering (c) and leaving (d) mass flow rate on the SACOC fins: blue bars, results from engine configuration of §5.4.1; red bars, results from test bench configuration with two-dimensional boundary conditions.

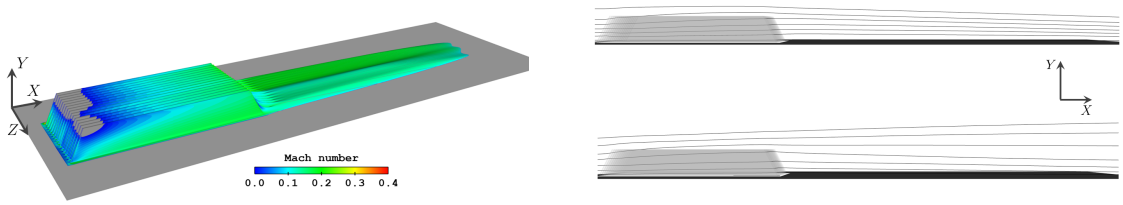

(a) (b)

Figure 5.21: Two-dimensional boundary conditions. Temperature iso-surface $\theta = 0.4$ colored by the Mach number (a) and velocity streamlines (b) on the left-hand side (top) and right-hand side (bottom).

right-hand side, present a significantly lower difference between the two sides with respect to the engine configuration.

	Left-hand side	Right-hand side	Comparison
$\langle \mathrm{Nu} \rangle$	152.32	134.43	+13.3%
C_D	0.0028	0.0021	+38.4%
Head losses	1.05%	1.2%	− 12%

Table 5.4: SACOC's performances in terms of average Nusselt number, drag coefficient and global head losses on the left- and right-hand side of the wind tunnel.

Finally, an additional simulation is performed where the flow is considered to be fully oriented along the streamwise direction X, while all the other boundary conditions remain identical. The purpose of the simulation is to assess the impact of the wall-normal and spanwise velocity components on the heat exchange. Figure 5.22 plots the distribution of the Nusselt number distribution compared to the previous results. As can be seen, the differences with respect to the non-axial flow are very small. These results might corroborate the hypothesis that it is the inflow stagnation pressure which plays the most important role, as seen with the one-dimensional boundary conditions in §(5.5.2). On the other hand, given the poor resemblance of the flow downstream of the SACOC with respect to the engine flow even in the case where the exact direction of the velocity vector is imposed at the inlet (see Figs. 5.9 and 5.21), the effect of the inflow gyration on the performance of the heat exchanger remains in fact unclear.

In conclusion, imposing the exact same flow conditions of the OGV/BPD interface at the inlet leads to a marked improvement in the prediction of all the quantities of interest, and allows us to capture certain local effects, such as the asymmetrical distribution of the heat exchange among the different SACOC fins. Other phenomena, however, such as the strong recirculation zone observed in the engine config-

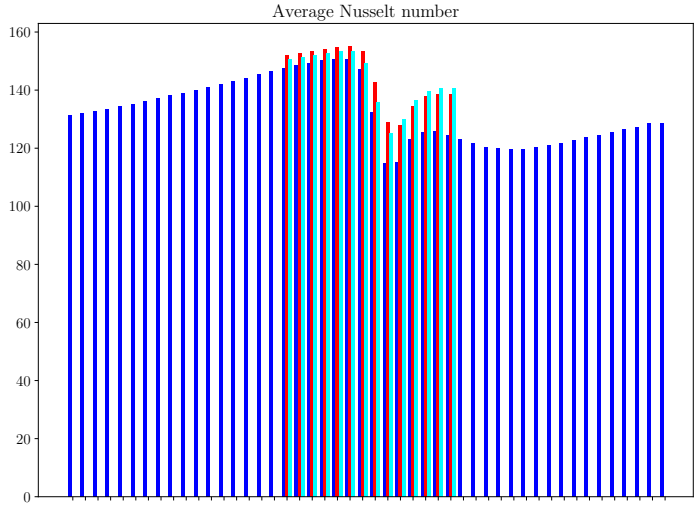

Figure 5.22: Two-dimensional boundary conditions. Distribution of average Nusselt number. Blue bars, results from engine configuration of §5.4.1; red bars, results from test bench configuration with two-dimensional boundary conditions; light blue bars, same as red bars but axial flow.

uration, have been impossible to reproduce. In practice, these results confirm, on the one hand, the importance of recreating inlet conditions that are representative of the studied flow; on the other hand, they show how the representativeness of a certain configuration is far from being guaranteed by the mere inlet flow conditions, and how other limits of the test bench, such as its geometry, have to be taken into consideration.

5.6 Conclusion

The conjugate heat transfer analysis of a state-of-the-art surface air-cooled oil cooler (SACOC) of a turbofan aircraft engine has been performed in two distinct configurations. The objective has been to both identify the main integration effects influencing the performance of the heat exchanger, and understand how these effects should be appropriately reproduced in smaller-scale wind tunnel experiments and simulations.

The first configuration, set up to meet the first objective, is the by-pass duct of a turbofan engine, where a series of SACOC fins are installed on the OFS just downstream of the OGV. Results show that the flow reaching the heat exchanger is strongly heterogeneous, and characterized by residual swirl coming from the fan, two counter-rotating vortexes at the hub and tip of the OGV and an important wake. As a result, the SACOC fins behave differently depending on their position along the OFS, with the pressure-side (resp. suction-side) fins characterized by a higher (resp. lower) heat exchange and viscous drag on their surface. An important flow separation taking place downstream of the SACOC is observed on the suction side which significantly increases the overall pressure drop generated by the heat exchanger. Furthermore, the fins are affected by an ejection event, more accentuated on the suction side, which leads to an important mass flow loss through the upper part

of the SACOC, which reduces the thermal efficiency of the heat exchanger. Finally, the analysis of the developing thermal boundary layer between two consecutive fins, reveals that an equilibrium sub-layer can be qualitatively identified.

The second configuration, relevant to the second objective, is a typical square wind tunnel test rig, where a reduced number of SACOC fins are installed on the lower wall. At the inlet, three different inflow conditions are considered. First, an axial, homogeneous flow representing the surface average of that reaching the SACOC in the engine configuration; very poor predictions are obtained for all quantities of interest, since the lack of a representative boundary layer at the inlet leads to the overestimation of both the heat exchange and viscous drag. Second, a one-dimensional flow obtained through a circumferential average of the engine flow; better results are achieved for all quantities, even though only the behaviour of the average engine SACOC fin is captured due to the lack of spanwise gradients; besides, further investigations show that as long as a one-dimensional profile of stagnation profile is prescribed at the inlet, the prediction of the heat exchange and of the viscous drag remains satisfactory, regardless of whether the other inflow conditions are homogeneous or not, confirming the criticality of injecting a representative boundary layer. Third, a two-dimensional flow where every fluid property is directly taken from the engine flow; these boundary conditions lead to a considerable improvement of the predictions of all the quantities of interest and some local effects, such as the distribution of the heat exchange among the fins, are captured; on the other hand, certain features of the engine flow, such as the aforementioned mass loss by the upper part of the heat exchanger and the large flow separation taking place downstream of the SACOC on the suction side, are not observed in the wind tunnel, thus revealing the limited representativeness of this configuration.

The study allows us to draw several conclusions. First of all, the interest in analysing the performances of the SACOC in its operating environment, *i.e.*, the turbofan by-pass duct, has proven to be unquestionably concrete. This work has thus allowed us to clarify in which sense the operating conditions of SACOC have to be considered challenging. Our RANS simulations have thrown light on a considerable asymmetry between the pressure and suction sides of the OGV, as well as on an important flow separation which, presumably, would have not occurred without the presence of the heat exchanger. At the time of writing, we do not know if these effects actually take place in the by-pass duct, and experimental investigations are necessary to clarify the behaviour of the flow. In perspective, it is also essential to perform engine simulations at different fan regimes, since it cannot be excluded that the effects we have observed are nothing but due to the take-off regime, during which the fan turns at almost its maximal speed, and the flow is affected by higher distortion.

We also want to stress that in this work, only the effect of the OGV on the SACOC has been studied, although it cannot be excluded that investigating the reciprocal, *i.e.*, the effect of the presence of the SACOC on the performance of the OGV, is equally important. In fact, the static pressure rise caused by the aerodynamic blockage of the heat exchanger, which is located in close proximity to the trailing edge of the blade, might considerably modify the profiles of stagnation temperature and pressure downstream of the OGV.

Concerning the thermal performance of the heat exchanger, it appears from the study that it is essentially driven, on the one hand, by the mass flow entering at the leading edge and, on the other hand, by the mass flow leaving the SACOC from the upper part without reaching the trailing edge. The study demonstrates that the

former is relatively easy to reproduce, since it only depends on the inlet stagnation pressure; the latter, on the contrary, seems to depend on features of the flow, such as the flow separation taking place downstream of the SACOC, which are more challenging to recreate. The reader should also keep in mind that the investigation of these phenomena has been done with steady RANS simulations, with the results of the engine configuration treated as reference. Since the ejection event that we have been mentioning seems to have such a decisive impact on the performance of the heat exchanger, higher-fidelity analyses might be required, in the future, to characterise its causes and its real extent.

We hint, in particular, at wall-modelled LES, which might offer, at a reasonable cost, greater insight into the aerodynamic interactions between the SACOC and the upcoming flow. For this purpose, as we have already mentioned in Chapter 4, the most complete three-dimensional wall-models might be required to take into account the interactions between the different boundary layers and the presence of strong non-equilibrium effects. However, as the analysis of the development of the thermal boundary layer within the heat exchanger has illustrated, equilibrium assumptions in the inner-layer might not, after all, be inconsiderate even in such a challenging configuration.

The importance in the present case of the inlet flow conditions in wind tunnel experiments has been assessed; as the study shows, satisfactory average results can *a priori* be obtained by injecting a representative one-dimensional boundary layer. This, in practice, can be done with distortion screens. However, the study illustrates that the accuracy of smaller-scale experiments does not entirely rest on the inflow conditions, and that the representativeness of the test rig itself needs to be questioned. In other words, increasing the complexity and the fidelity of the inlet flow without increasing those of the test rig, does not necessarily guarantee that considerably better results will be obtained. In perspective, it would certainly be of great interest to investigate the effects of the geometry of the wind tunnel, and to test different configurations which, as we have done in this chapter for the inflow conditions, mimic the shape of the by-pass duct with different degrees of representativeness.

Chapter 6

Numerical and experimental study of a surface air-oil exchanger installed in a square wind tunnel

6.1 Introduction

At this stage of the work, several aspects of the physical complexity of the SACOC's aerothermal interactions have been addressed.

In Part II, we have focused on the impact of an abrupt temperature gradient on a temperature-homogeneous flow. The configuration we have investigated is an extremely simplified system, characterised by a trivial heat exchanger (*i.e.*, an isothermal wall) and a canonical flow (*i.e.*, a fully developed channel flow at low Reynolds number). Nevertheless, our high-fidelity simulations have thrown light on several non-equilibrium phenomena, such as the leading edge effects, the non-equilibrium development of the thermal boundary layer and the progressive increase and settlement of turbulent heat transfer; these phenomena, which in the complex SACOC functioning environment can only be expected to be amplified, challenge our conventional turbulence modelling strategies.

In Chapter 5, instead, we have focused on the effects of the peculiar operating conditions of a SACOC; the use of conjugate heat transfer (CHT), although with a less faithful flow modelling with respect to Part II, has allowed us to quantify the impact of inflow conditions on SACOC's macroscopic performance parameters, such as the heat exchange and the pressure drop; furthermore, the analysis has helped us understand how simpler small scale tests should be performed.

The last step which remains to be done, is to evaluate to which extent the CHT numerical methodologies we have introduced in Chapter 2, can enable us to investigate the aerothermal interactions of a SACOC. This brings a complete novelty into this, so far, purely numeric work, *i.e.*, experimental aerodynamics. During the years of work which have led to this writing, experimental tests have been performed over different SACOC configurations implemented in a wind tunnel, which, as we shall see, strongly resembles the one introduced in Chapter 5; these tests, which have

been carried out in the context of a very particular project we will introduce later on, have been specified and designed in collaboration with Safran Aircraft Engines (Safran AE) and, in particular, with the author of this writing, allowing us to perform meticulous numerical-experimental comparisons. As seen in the literature review of Chapter 5, open literature regarding finned heat exchangers in aircraft engines applications is extremely limited. Open works involving an engine manufacturer of the stature of Safran Aircraft Engines, are even more of a rarity.

In this last chapter we will thus operate in two distinct environments. The former is the experimental test bench, where sixteen SACOC fins are mounted in a square wind tunnel; inflow conditions have been specified by Safran AE and represent an average by-pass duct flow; the heat exchanger is heated by a hot-oil circuit located beneath the fins, mimicking the functioning of the real engine SACOC. The latter environment, is the numerical one; on the one hand, the domain geometrically coincides with the test bench, and the experimental data is directly used as boundary conditions, allowing for a significant representativeness of our simulations; on the other hand, a certain number of necessary simplifications, as we shall see, are introduced. The objective of this chapter, is to verify the prediction capability of our CHT strategy and to assess the sensitivity of numerical results to the aforementioned simplifications and uncertain experimental parameters.

The chapter is organised as follows. In §6.2, we will introduce the context in which the experimental tests have been performed, present the partners of the project and detail the objectives of our investigations. In §6.3, the test requirements that, as Safran Aircraft Engines, we have specified to the partners are detailed. In §6.4, the experimental setup is described, validated, and the results obtained on the test-bench are discussed. In §6.5, after a brief presentation of the numerical setup, the results are compared with the experiments, and the predicting capabilities of our methodologies is assessed. This is followed by the conclusions in §6.6.

6.2 Working context: a *Clean Sky 2* project

6.2.1 The project and its partners

Clean Sky 2 (CS2) is a research program managed by the Clean Sky Joint Undertaking (CSJU) as a part of the European Commission's Horizon 2020 Research and Innovation Program. CS2 aims at realising the Advisory Council for Aeronautics Research in Europe (ACARE) Flightpath 2050 environmental objectives for the aeronautical industry, which are:

— A 75% reduction in carbon dioxide (CO_2) emissions;

— A 90% reduction in mono-nitrogen oxides (NO_X);

— A noise reduction of flying aircraft of 65%;

— Mitigate the environmental impact of the lifecycle of aircraft and related products by designing and manufacturing aircraft to be recyclable.

Improving the efficiency of aircraft engines is of primary importance to meet these goals, and a specific program has been introduced in CS2, *i.e.*, the Engines Integrated Technology Demonstrator (ITD) Program, which aims at *developing full engine and major engine system solutions that can deliver a step change reduction in emissions*

(see CleanSky2, 2021). The program consists of different demonstrators, divided into several work packages (WP), which, in turn, are constituted of several topics (*i.e.*, the specific projects).

Our project is the Aerodynamic upgrade of Surface Air Cooled Oil Coolers[1] (SACOC) which, in this intricate bureaucratic web, is located in the WP2 of the Engine ITD Ultra High Propulsive Efficiency (UHPE) demonstrator, addressing short/medium range aircraft market 2014-2021. The work package aims at designing, developing and validating the low pressure modules and nacelle technology bricks necessary to enable Ultra High By-pass Ratio (UHBR) engines. The objectives of the project are the following:

— To develop a predictive numerical methodology to assess the performance of any new air heat exchanger concept. The methodology should be validated against an experimental database to be acquired in this project.

— To evaluate numerically but also experimentally new SACOC concepts to improve the current technology.

In 2018, a consortium of academic partners has been created to realise the project, and its members are:

— *Universitat Politècnica de València*, UPV: topic leader of the project and interface between the consortium and the European Commission; beyond their coordinating activities, UPV is in charge of the experimental investigations of the project.

— *Universidad Politécnica de Madrid*, UPM: in charge of the numerical investigations and, in particular, of the optimisation of the SACOC design.

— *Trustees of Purdue University*: member of the consortium without budget, Purdue provides further expertise and testing facilities, and is in charge of additional experimental tests.

Safran AE, as topic manager, is instead in charge of specifications, validation and approval of the project's deliverables.

The project has officially started on the 24$^{\text{th}}$ of April, 2019, and had an initial duration of exactly two years, later extended to the overall duration of 29 months due to the impact of the coronavirus disease (COVID-19) global pandemic.

6.2.2 Objectives of our numerical investigations

The project is organised in four work packages (schematically shown in Fig. 6.1), and the experimental characterisation of surface heat exchangers has been performed over four distinct geometries and test campaigns:

– Version 1: flat plate configuration;

– Version 2: baseline SACOC design, provided by Safran AE;

– Version 3: improved SACOC design, provided by UPM;

– Version 4: further improvement of SACOC design.

[1]Reference to the project: JTI-CS2-2018-CfP08-ENG-01-37, https://cordis.europa.eu/project/id/831977.

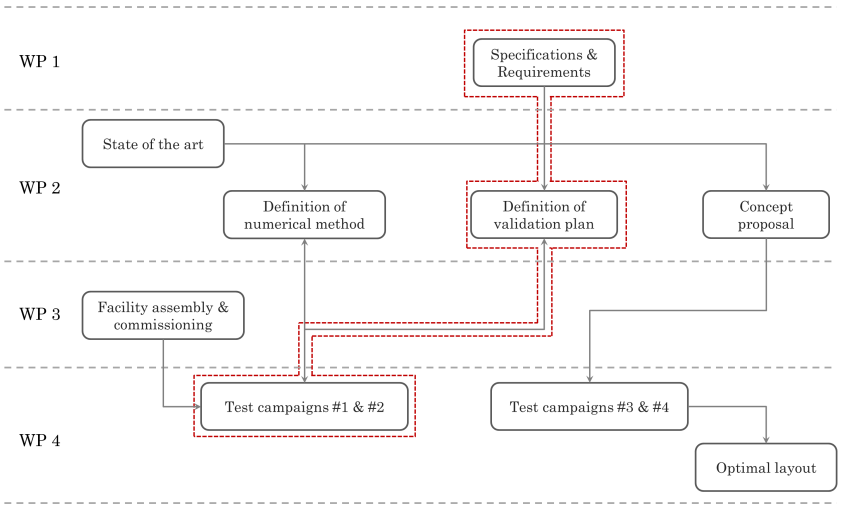

Figure 6.1: Scheme of the project's work plan with, in red, the parts of the project discussed in this chapter.

Certain activities, which are highlighted in red in Fig. 6.1, have been deemed critical by Safran Aircraft Engines, that has thus decided to actively participate to their realisation.

These activities include, first of all, the specifications and requirements of the experimental tests (WP1); the objective has been that of guaranteeing, within the limits of the experimental facilities, that the tests be as representative as possible of realistic engine's by-pass duct conditions, such as the ones described in Chapter 5. Only in these conditions the characterisation and optimisation of the SACOC can be meaningful; therefore, Safran AE has provided a baseline SACOC design, used as reference, as well as offered its expertise, gained with past experiences in wind tunnel tests of SACOC, in generating non-uniform inflow conditions in order to inject a representative boundary layer at the inlet.

The second lot of essential activities, is that concerning the validation of the numerical methodologies on, at least, the reference SACOC geometry tested during the second experimental campaign (see WP4 in Fig. 6.1); the objective has been that of validating our in-house numerical setup (described, recall, in Chapter 2) *during* the test campaigns; indeed, this has allowed us to monitor and adjust the experimental setup according to the most sensible parameters detected by preliminary and concomitant simulations; furthermore, it has allowed us to compare our numerical results with those obtained by UPM with a completely different numerical setup, thus verifying the robustness of our respective simulations.

It is only on these aspects that we focus in this chapter. The reader may find further details concerning the rest of the activities following the reference we have given in §6.2.1, where all the results will be openly published once the project has come to its end.

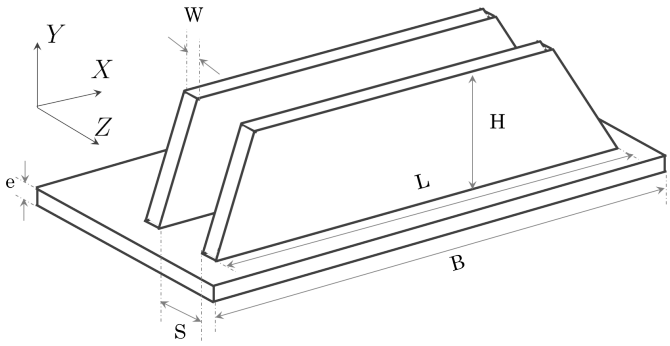

Figure 6.2: Schematic representation of two fins of SACOC with dimensions.

6.3 Test requirements and specifications

From now on, we only focus on the 2nd experimental campaign of the project, which aims at verifying the predicting capabilities of our CHT simulations. For this purpose, we have proposed to implement a reference SACOC geometry in a rectangular wind tunnel, and to reproduce inflow conditions resembling the engine's by-pass duct flow, so that the characterisation of the heat exchanger is effectuated in a representative configuration. In the following sections, we detail the requirements and specifications of the experimental campaign, from the design of the SACOC (§6.3.1), to the testing conditions (§6.3.2) and desired measurements (§6.3.3).

6.3.1 SACOC design

Figure 6.2 schematically shows the SACOC design we have specified for the tests. Sizes (see Table 6.1) are non-dimensionalised with respect to the SACOC's base length (*i.e.*, $(\cdot)^L$) or height (*i.e.*, $(\cdot)^H$). As can be seen, the SACOC is topologically identical to the one used in Chapter 5, yet the sizes are different.

L^H	B^L	H^H	W^H	S^H	e^H
6.25	1.064	1	0.05	0.11	0.075

Table 6.1: SACOC's dimensions (normalised with respect to the fin height H or length L.

The SACOC has been mounted in a rectangular wind-tunnel and we have required:

— To install the maximum number of fins, provided that a distance of at least one fin-height H separates both sides of the tunnel from the SACOC block to avoid interaction with the lateral walls; the more fins are present, the more the effect of the two external fins of the SACOC block is reduced; however, the lateral size of the wind-tunnel (along the Z direction in Fig. 6.2) is limited by the maximum mass flow rate delivered by the test rig.

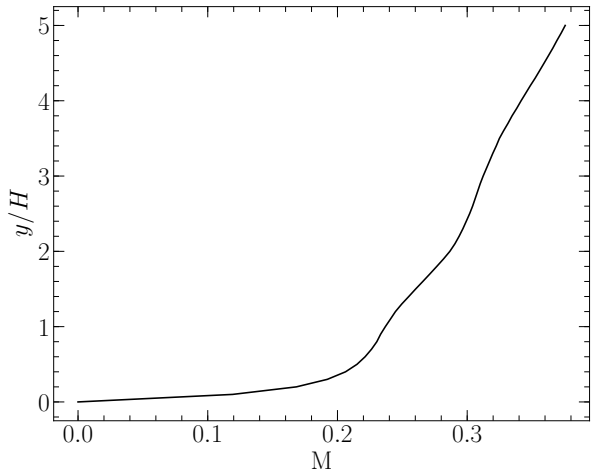

Figure 6.3: Specified Mach number profile for the test bench inflow conditions.

— To guarantee that the height of the wind-tunnel (along the Y direction in Fig. 6.2) is sufficiently large to avoid interaction between the SACOC and the upper wall; a height of $H_{WT}/H \sim 5$, according to past experiences at Safran AE, has proven to be enough, provided that the SACOC is not placed too far from the inlet of the tunnel and, therefore, that the thickness of the boundary layer on the upper wall is negligible; the height H_{WT}, as above, is limited by the maximum mass flow rate.

— To fabricate the SACOC with an aluminium alloy, which is the most common material used for heat exchangers.

6.3.2 Inflow conditions and thermal management

As explained in Chapter 5, inflow conditions are of utmost importance in wind-tunnel tests to accurately reproduce the by-pass duct flow. We have seen that good results, at least in an averaged sense, can be obtained with one-dimensional inflow conditions representing the azimuthal average of the engine flow. Such inflow conditions, in practice, can be obtained through distortion screens of heterogeneous porosity which, thanks to the pressure drop the flow blockage induces, modify the stagnation pressure profile allowing the reproduction a non-uniform flow (see, for instance, Davis et al. (2002)). We have thus required to reproduce the Mach profile shown in Figure 6.3 as a function of the non-dimensional wall-distance y/H, which allows us to inject a representative average boundary layer.

So as to evaluate the aerothermal performance of the SACOC, we have requested to implement a hot source beneath the heat exchanger. We have not specified how the fins should be heated, leaving all options open (*e.g.*, electric resistances, hot oil circuit). However, we have required to guarantee a temperature difference of $\Delta T \sim 100$ K between the hot source and the air flow as well as to ensure that the heat provided by the hot source is dissipated as much as possible by the heat exchanger, avoiding heat losses that cannot be predicted numerically.

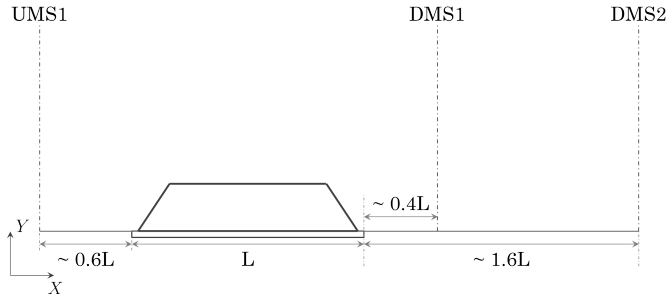

Figure 6.4: View of the specified measurement planes in the wind tunnel with their distance with respect to the SACOC.

6.3.3 Measurements

For the aerodynamic characterisation of the SACOC, we have requested the measurement of the velocity, of the stagnation pressure and of the stagnation temperature at three sections of the wind tunnel, which are schematically shown in Figure 6.4. For every section, measures should be taken all over the spanwise $Y - Z$ plane, in order to have a two-dimensional characterisation allowing us to perform surface averages of the results. Furthermore, only steady-state values are sought and, therefore, time-averaging of sufficient duration is required.

The first plane (Upstream Measurement Station 1, UMS1) is located upstream of the SACOC, at a distance of approximately $0.6L$ from the leading edge of the heat exchanger; it is located, instead, slightly downstream of the distortion screen, so that at UMS1 the Mach profile should resemble that of Fig. 6.3. The measurements taken at this plane serve to characterise the actual inflow conditions of the wind tunnel, allowing us to prescribe precise numerical boundary conditions at the inlet. The distance of $\sim 0.6L$ from the SACOC should also allow us to avoid interference between the heat exchanger and the distortion screen.

The two remaining planes, *i.e.*, Downstream Measurement Stations 1 and 2 (DMS1, DMS2), are located downstream of the SACOC at a distance from the trailing edge of $0.4L$ and $1.6L$, respectively. DMS1 allows us to capture the flow at its most perturbed state after the passage through the fins, where the comparison with our RANS simulations is the most challenging. At DMS2, instead, the flow is expected to show some level of homogenisation and to be much closer to equilibrium.

Concerning the thermal characterisation of the SACOC, it is fundamental to assure that the total heat dissipated by the fins is accurately calculated; for this purpose, we thus prefer the more reliable measurements taken directly from the hot source (*e.g.*, power dissipated by the thermal resistances or the oil), even though they inevitably include the heat losses, rather than a measurement based on the difference of stagnation temperature between the inlet and outlet of the wind tunnel. Furthermore, it is important to precisely measure the temperature distribution at the base of the heat exchanger since, as we shall see, it is at that location that the numerical thermal boundary conditions are prescribed.

6.4 Experimental setup & results

In this section, the experimental setup and results are presented in §6.4.1 and §6.4.2, respectively.

Although we have not directly participated to the assembly of the test rig, we include Section 6.4.1 for the sake of completeness. Section 6.4.1, as well as all the figures, are a courtesy of UPV, where all the experimental results we will analyse in this chapter have been obtained.

In Section 6.4.2, the test-rig is validated with respect to the specifications of §6.3, the global performance parameters of the SACOC are given and several stagnation pressure, temperature and velocity profiles at the measuring planes are shown. Results, unless differently specified, have been obtained by averaging the outcome of several runs performed in January and February 2021 and thus represent consolidated results.

6.4.1 Experimental setup

The experimental tests have been performed in the High Mass-flow and High Temperature (HMHT) flow bench, installed in the 8P laboratory of UPV. It is a multipurpose experimental facility for aerodynamic studies in both automotive and aeronautical engineering (see Serrano et al., 2019a,b; Torregrosa et al., 2020), as it provides a fairly large flow rate, more than 2 kg/s cold flow and hot flows at temperatures that can reach 1000°C with 1 kg/s flow rates. This facility is powered by a 500 kW two-stage centrifugal compressor in series with a 1 MW Diesel combustor. This setup allows performing tests in which both the Mach and Reynolds numbers of the flow can be controlled.

In this facility, a continuous mass flow rate of 2.15 kg/s at 3 bar(A) and 30°C is available at the measurement room. To regulate the total mass flow delivered to the test room, a series of venting valves are placed in the main pipe between two settling tanks. These reservoirs of 3 m^2 are capable of dampening sudden changes in the operating conditions, which helps to protect different parts of the facility and deliver a more uniform and controlled mass flow to the test room. A schematic of the facility is shown in Figure 6.5, while a CAD view of the test section is given in Figure 6.6.

i. *Wind tunnel*

In the test room of the HMHT stand, a bespoke modular rig is installed. It is principally formed by a settling chamber, a transition device, a distortion panel holder, and the test section where the SACOC has been fixed. The wind tunnel, depicted in Figure 6.7, discharges with a large silencer that is then routed upward outside of the building to avoid noise pollution.

The flow is delivered from the HMHT stand through an S-shaped pipe. At the top of this pipe, a tap has been set to characterise the incoming air temperature. This pipe drives the flow into the settling chamber via a pierced ending that enhances a smooth transition to the test chamber. The settling chamber is a reservoir contemplated to stagnate the fluid, diminish the turbulence level of the flow, and to straighten the streamlines upstream of the test section. Several CFD studies were performed to determine the best configuration of the settling chamber and the best performance was found with a configuration based on Purdue's PETAL settling

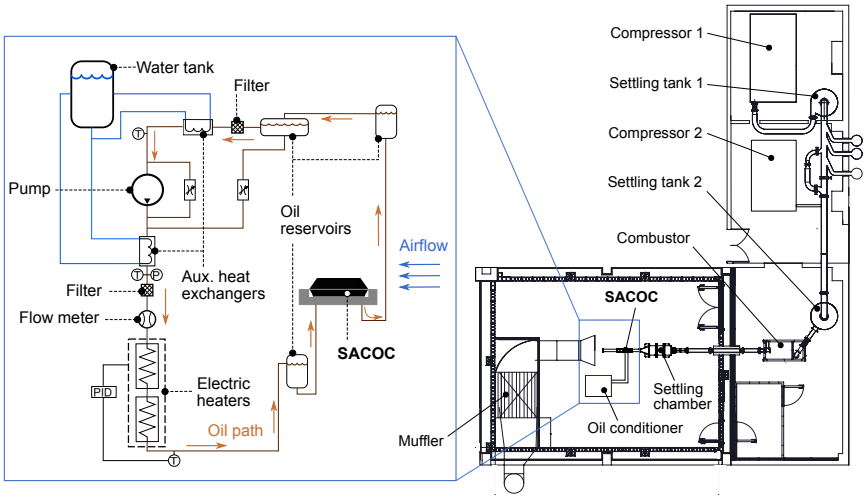

Figure 6.5: Detail of the oil conditioning system (left) and schematic of the facility and wind tunnel (right). By courtesy of UPV.

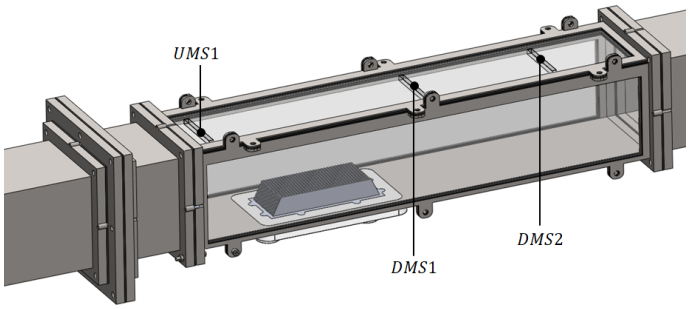

Figure 6.6: CAD of the experimental test section. By courtesy of UPV.

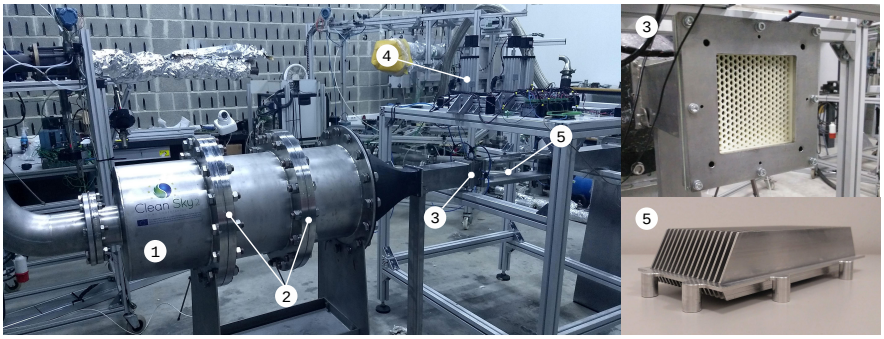

Figure 6.7: Experimental test rig with distortion screen and SACOC details. (1) Settling chamber; (2) Honeycombs; (3) Distortion screen; (4) Traverse system; (5) SACOC. By courtesy of UPV.

chamber (see Paniagua et al., 2019). In order to achieve better flow conditions in the test section, two honeycomb straighteners are placed inside the settling chamber.

Afterwards, to gently drive the flow into the test section which, recall, is rectangular, a 3D-printed transition which connects the circular settling chamber with a squared-pipe has been placed. The interior surface of the transition has been treated to be as smooth as possible and the geometry presents no abrupt changes to avoid flow detachment. Then, the flow develops in the straight section and reaches a distortion screen capable of transforming a uniform flow into the required velocity profile described in §6.3 and shown in Fig. 6.3. The distortion screen is a 3D-printed honeycomb panel with variable porosity which induces a determined pressure drop depending on that porosity (see detail of Fig. 6.7). The pores have a hexagonal shape as it is structurally sound and produces less pressure drop across the panel. Between the distortion screen and the test section, a straight pipe has been placed, so the first measurement plane, UMS1, is at a distance of around $1.84L$ from the panel.

The test section is a square duct of size $5H \times 5H$, where 16 fins of the SACOC specified in §6.3 and shown in the detail of Fig. 6.7 have been mounted; with this number of fins, a distance of $1.25H$ between the SACOC and the lateral walls is guaranteed on both sides. The lateral and top walls are made of borosilicate, specially treated for laser wavelength transparency. The bottom wall, instead, is a thick steel plate. There are three apertures on the top wall of the test section to allow intrusive measurements. In case non intrusive techniques are required, the top wall can be replaced by a continuous borosilicate glass. To allow thermal measurements with infrared cameras, additional walls with specially treated windows in the SACOC region for infrared transparency in the spectrum from 0.3 to 13 µm can be installed. This attachment is a rectangular 3D-printed part with the window off-centre to allow a wider filed of view when rotating the attachment.

The SACOC is a heat exchanger made of aluminium AW7075-T651[2]. Its heating is performed by a hot-oil circuit, located beneath the fins. On the oil side, 18 fins with a height of $0.3H$ and with the same thickness W of the air fins, are symmetrically distributed. To enhance the heat transfer, the oil circuit is in counterflow, *i.e.*, the oil flows below the SACOC in the opposite direction to the air above. Since the bottom wall where the SACOC has been mounted is made of steel, and to maintain the heat exchanger as adiabatic as possible (extracting heat through the SACOC solely), a 3D-printed oil pan separating the SACOC from the wall has been added. The material utilised for the oil pan is ULTEM 1010[3], a thermoplastic ideal for long-term heat resistance.

Finally, a straight section discharges the flow to the ambient. This pipe is facing the ventilation system so the air leaves the test room smoothly.

ii. *Oil conditioner*

Oil that responds to SAE 5w-30 rheological and thermal specifications (see Gyimah et al., 2016; Wrenick et al., 2005) has been used, although almost any type of lubricant can be used in this circuit. The oil is driven throughout the circuit by means of a pump. Upstream of the pump, a water-cooled heat exchanger reduces the temperature below 110°C, with a typical drop of 40°C. The pump works at a constant speed of 1450 rpm with a power of 370 W, so to regulate the mass flow in

[2]For its characteristics, see: https://www.spacematdb.com/spacemat/manudatasheets/alcoa_alloy_7075.pdf

[3]For its characteristics, see: https://www.stratasys.com/es/materials/search/ultem1010

the circuit a bypass with a manually controlled valve has been used. Then, the oil passes through another heat exchanger devoted to keep the flow meter temperature at the nominal value of operation, with a temperature typically under 60°C. In between the heat exchanger and the flow meter, the filter eliminates possible impurities that could be created along the circuit, using a series of paper walls with micrometric porosity. Once filtered, the fluid passes through a high precision Coriolis mass flow meter.

Afterwards, the oil temperature is increased by means of an electric heater. This element is composed of two electrical resistors mounted in series, with 2.6 and 2.5 kW, respectively. A thermocouple has been set after the electric heater to feed a PID control system that regulates the power needed in the resistors to reach the desired fluid temperature. Finally, the oil goes to the SACOC oil pan. To ensure the pan is filled up with oil and no air bubbles are retained below the aluminium, two oil reservoirs are placed before and after the exchanger, at higher altitude.

Once the lubricant leaves the SACOC and the outlet reservoir, it returns to the oil storage tank. The pump suctions oil from this tank, passing it through a filter that avoids the entrance of dirtiness into the circuit. Additionally, one branch connects the tank to the main circuit downstream of the pump, so if the pressure exceeds a certain value, the valve opens and returns fluid to the tank. A scheme showing the oil conditioner operation is displayed in Fig. 6.5.

iii. *Measurements*

For the aerodynamic measurements, a set of Kiel probes of 3.2 mm diameter has been utilised. The Kiel probes have a surrounding shield around the pressure port, so they are not influenced by swirling, being also less sensitive to the flow direction. In this way, Kiel probes are the best option to determine the total pressure in the section. To perform the measurements in an automatised way, traverse systems have been designed and constructed. In total, three biaxial traverses, one for each measurement plane, are used. For non-intrusive measurements, high-frequency Particle Image Velocimetry (PIV) and three-axis Laser Doppler Anemometry (LDA) systems are available.

For thermal measurements, the Kiel probes have also incorporated T-type thermocouples, so both total pressure and temperature can be acquired at the same time. However, due to a gap between the location of the thermocouple and the top of the head, the bottom-most region cannot be reached by this thermocouple. To perform a more precise analysis of the temperature variation, 4 K-type thermocouples are centred downstream of the SACOC fins on the lower wall to see the evolution of the thermal wake and boundary layer at four additional planes DMP1, DMP2, DMP3 and DMP4. These planes are located at a distance from the trailing edge of the heat exchanger of $2H$, $4H$, $6H$ and $8H$, respectively. These thermocouples can be moved to analyse the temperature distribution along their verticals.

To measure the heat exchanged during the process, both inlet and outlet oil temperatures of the oil pan are measured at different radii and at the center of the pipe: three RTDs are used to characterise the Radial Temperature Distribution and one is inserted co-axially to the pipe line. Averaging the temperature measurements at each section and computing the difference, the heat dissipated by the SACOC can be calculated taking into account the mass flow rate of oil circulating across the pan,

assuming a constant heat capacity:

$$\dot{Q} = \dot{m}\Delta h = \dot{m}c_p\Delta T = \frac{\dot{m}c_p}{4}\left(\sum_{i=1}^{4} T_{in_i} - \sum_{i=1}^{4} T_{out_i}\right) , \tag{6.4.1}$$

where $\dot{Q}$ is the thermal power, $\dot{m}$ the oil mass-flow-rate, h the enthalpy, c_p the thermal capacity of the oil and T_{in} and T_{out} are the inlet and outlet temperatures measured by the RTDs, respectively.

A FLIR A400 thermographic camera is used for measuring the wall temperature distribution of the specimen, from which the heat transfer efficiency of the prototype can be estimated. To validate the results obtained with the IR camera, surface K-type thermocouples can be introduced through the bottom screws to measure the aluminium temperature at different points. For a better determination of the temperature distribution, the SACOC and its surroundings are painted in black with a special graphite-based paint with high conductivity, which does not modify the temperature on the surface.

6.4.2 Experimental results

In the following, all physical properties have to be considered in a Reynolds-averaged sense. The origin of the axes is placed at UMS1 for the streamwise direction X, at the lower wall for the wall-normal direction Y and at the center of the channel for the spanwise direction Z. Note that the SACOC, as shown in §6.3, is located on the lower wall of the channel. The subscript $(\cdot)_{ref}$ refers to a fluid property averaged over the surface of UMS1, which, by construction, coincides between the simulations and the experiments. Superscripts $(\cdot)^H$ and $(\cdot)^L$, instead, denote a variable of length non-dimensionalised with respect to the fin height H and length L, respectively. Finally, all experimental results are presented with their relative uncertainty, *i.e.*, with their standard deviation.

i. *Validation of the test-rig*

Figure 6.8 shows the comparison between the Mach profile specified in Section 6.3 and some experimental profiles at UMS1; in particular we have plotted three *local* profiles at $z^H = -1$, $z^H = 0$ and $z^H = 1$ as well a spanwise average computed along $z^H \in [-1, 1]$. The effect of the distortion screen described in §6.4.1 is evident, as the flat profile exiting the settling chamber is deformed and mimics the desired boundary layer. In general, satisfying agreement is obtained with the specified profile. The largest discrepancy is observed near the upper wall (*i.e.*, for $y^H \approx 5$), where the no-slip condition yields an inevitable thin boundary layer that deviates the velocity from the desired profile. A smaller inaccuracy is also observed towards $y^H \approx 1$ which, nevertheless, remains below 10% for the average profile. Finally, note the overall homogeneity of the Mach profile along the spanwise direction, with only some slightly different behaviour at $z^H = \pm 1$. We can thus conclude that the distortion screen allows us to reproduce a representative Mach profile at the inlet of the wind tunnel.

Figure 6.9a illustrates the temperature distribution as it has been captured (from above) by the IR camera. The temperature is non-dimensionalised as

$$\theta = \frac{T - T_{ref}}{T_{oil} - T_{ref}} ,$$

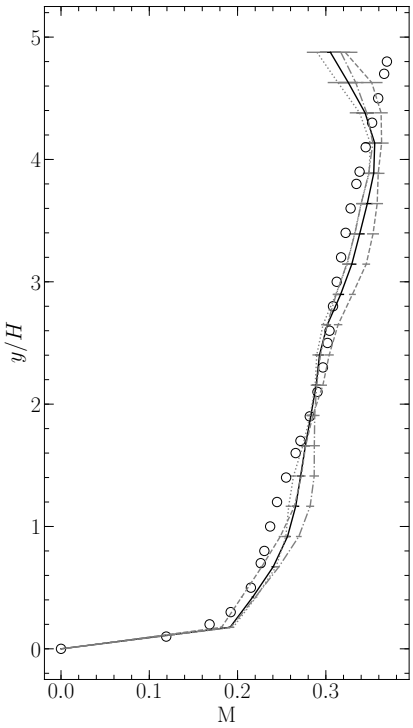

Figure 6.8: Validation of the test-rig. Comparison of specified Mach profile with values obtained in the experiments at UMS1. ○, specified profile of Section 6.3; —— experimental profile averaged along $z^H \in [-1, 1]$; ····· exp. profile at $z^H = 0$; – · – · – exp. profile at $z^H = 1$; - - - - exp. profile at $z^H = -1$.

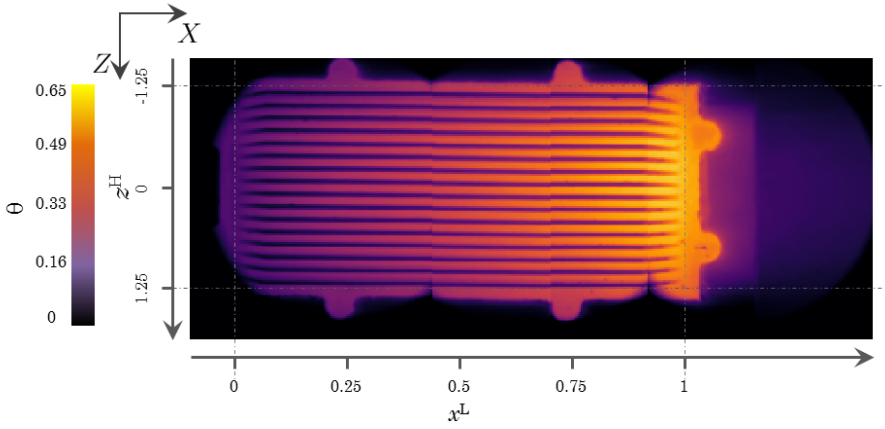

(a)

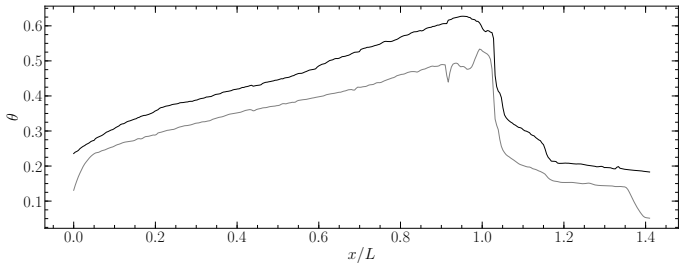

(b)

Figure 6.9: Validation of the test-rig. Image composition from the IR camera (a) and distribution of temperature (b) at $z^H = 0$ (black) and $z^H = 1.25$ (gray).

where T_{oil} is the oil temperature at the inlet of the circuit and $(T_{oil} - T_{ref}) \approx 100$ K. For this case, the origin of the axes is temporarily placed at the leading edge of the fins, for the sake of clarity. As can be seen, the oil circuit allows us to perform an appreciable level of heat exchange, with a peak of around $\theta \approx 0.6$ at the trailing edge of the SACOC. Figure 6.9b, instead, plots the temperature distribution along the centreline (*i.e.*, at $z^H = 0$) and at the side (*i.e.*, at $z^H = 1.25$) of the SACOC block; as can be seen, the temperature is not uniform along the spanwise direction and the SACOC is considerably hotter at the centre. It can also be noticed that the temperature level abruptly decreases after the trailing edge (*i.e.*, $x^L = 1$), showing the good (even if not perfect) insulation of the heat exchanger provided by the thermoplastic oil pan. As a whole, these results allow us to validate the thermal setup of the experiments. Also note that in our simulations the two-dimensional temperature cartography extracted from the IR camera is prescribed at the bottom of the heat exchanger as boundary condition. Further details will be give in §6.5.2.

ii. *Aerodynamic results*

In Figure 6.10a, the Mach profile in the wall-normal direction at the different measuring stations is plotted; the same is done in Figure 6.10b for the stagnation pressure,

non-dimensionalised with respect to the standard pressure $P_{std} = 101325$ Pa. This data has been extracted with the Kiel probes described in §6.4.1, and the SACOC fins are heated. In both cases, the profiles result from the spanwise average $z^H \in [-1, 1]$. This average is performed to illustrate the overall tendency of these profiles, evening out the local effects.

The behaviour of the Mach number is in qualitative agreement with what is expected to happen to a confined flow encountering an aerodynamic obstacle. Observe, for instance, its distribution at DMS1, *i.e.*, slightly downstream of the SACOC; the Mach profile exhibits a strong perturbation for $y^H \in [0, 1]$, that is the height of the fins; this behaviour signals a considerable perturbation taking place near the lower wall, as a consequence of the passage through the fins. Also note the slight thickening of the upper-wall's boundary layer and the acceleration of the flow at the centre of the channel, which is necessary to conserve the mass flow rate. At DMS2, *i.e.*, about two fin-lengths downstream of the heat exchanger, the perturbation in the lower region is less important, marking a certain degree of homogenisation of the flow. The upper-wall's boundary layer has further grown and, consistently, the flow exhibits a stronger acceleration toward the centre.

The stagnation pressure, instead, exhibits a more puzzling behaviour. On the one hand, certain intuitive aspects are retrieved; along the channel, the stagnation pressure diminishes on both the lower and upper walls and, understandably, the effect is more visible on the lower one due to the presence of the SACOC fins; furthermore, the upper-wall's boundary layer is thicker at DMS2 than at DMS1, while for $y^H \in [0, 1]$ the flow has slightly homogenised between the two measuring planes, in agreement with the behaviour of the Mach number. On the other hand, the decrease of stagnation pressure at the centre of the channel has no apparent physical explanation; indeed, the global perturbation of the SACOC and of the upper-wall should be limited to approximately $y^H \lessapprox 1.5$ and $y^H \gtrapprox 4$, and the stagnation pressure should remain untouched in the remaining part of the channel. This spurious pressure drop might reveal some measuring errors, or an important level of mass flow loss through the upper-wall's apertures mentioned in §6.4.1. However, the behaviour of the stagnation pressure is most probably a post-processing error. Indeed, the consolidated data have been cumulated over several testing days; now, if the Mach number profile at UMS1 can be assumed to be the same every day, since the wind-tunnel operates at the same regime with the same distortion screen, the stagnation pressure, instead, depends on the ambient pressure of that particular day. Unfortunately, the data at UMS1 have been measured and assessed during the very first testing days of the campaign, while DMS1 and DMS2 have been treated several weeks and months later. This aspect has to be taken into account in the analysis of our numerical results. Therefore, we will limit the detailed comparison of our simulations with the experiments to the Mach number profiles, while using the stagnation pressure measures of one particular testing day to characterise the pressure drop.

Figure 6.11 illustrates the mean (6.11a) and r.m.s. (6.11b) wall-normal velocity at the three measuring planes at the centre of the channel z^H, non-dimensionalised with respect to the mean streamwise velocity. This data has been extracted via the non-intrusive LDA technique mentioned in §6.4.1, and the fins, in this case, are not heated. First of all, notice that the vertical velocity represents a small fraction of the streamwise component at every plane of the channel and, especially, at UMS1, thus justifying the assumption of axial flow in our simulations. At UMS1 one can also observe that the mean vertical velocity, despite a variance of the same order of magnitude, is negative everywhere, indicating the tendency of the flow to

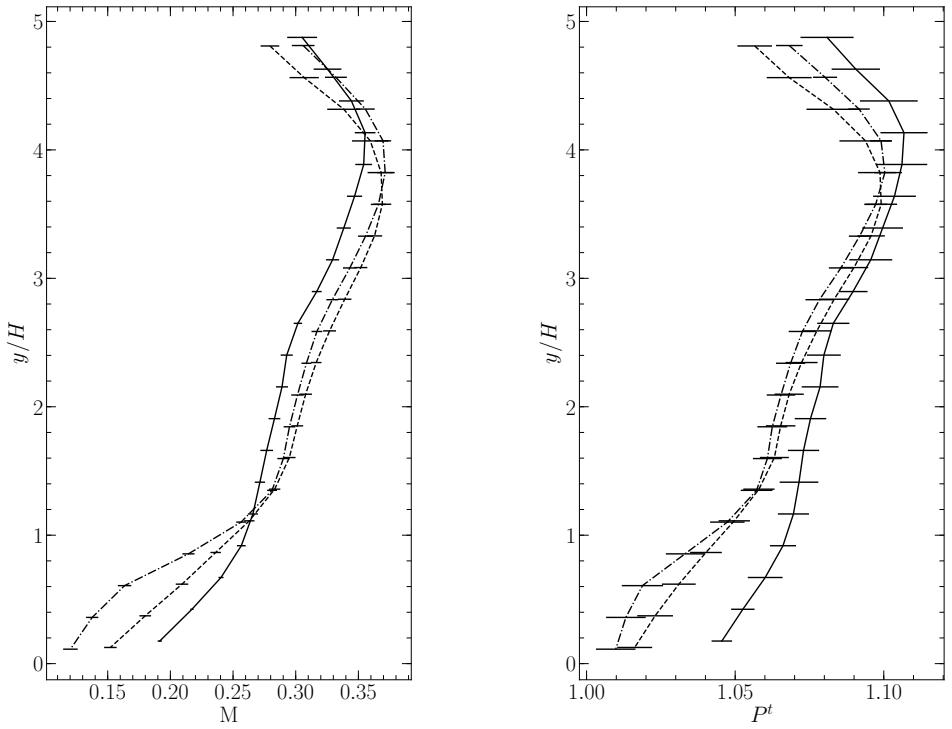

Figure 6.10: Aerodynamic results. Mach (a) and stagnation pressure (b) profiles, averaged along $z^H \in [-1, 1]$, at the different measuring stations: —— UMS1; – · – · – DMS1; - - - - DMS2.

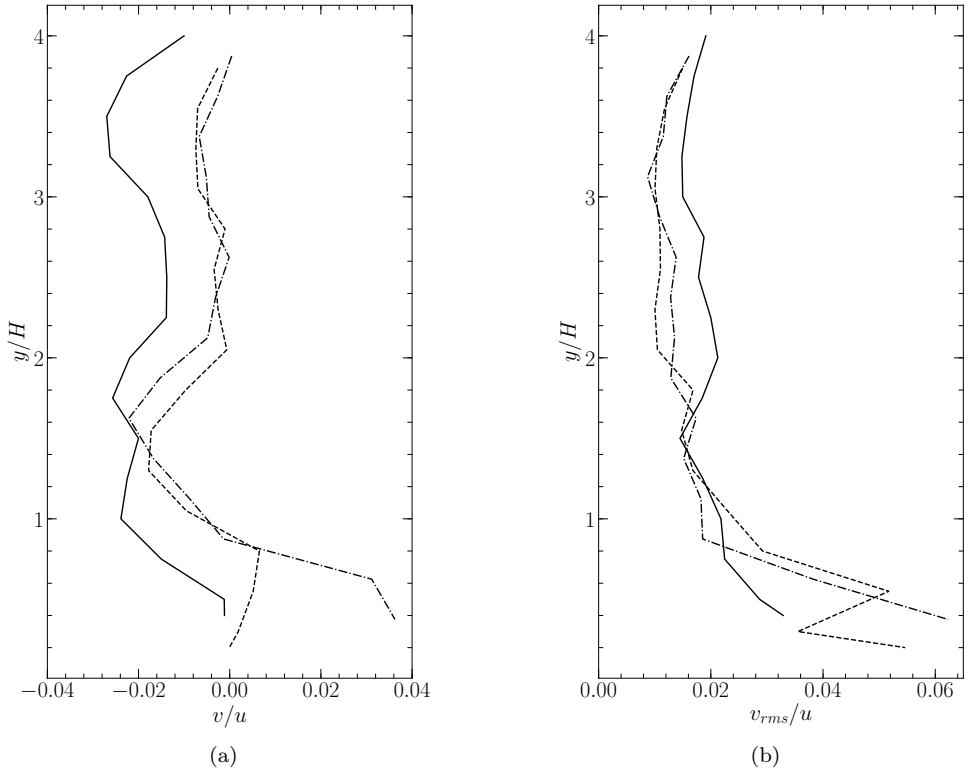

Figure 6.11: Aerodynamic results. Mean (a) and r.m.s. (b) profiles of vertical velocity v normalised by the mean streamwise velocity u at $z^H = 0$ and at the different measuring stations. See Figure 6.10 for a reference to the lines.

slightly slope downwards. This behaviour is most probably an effect of the distortion screen, which induces a stronger head loss in proximity to the lower wall (see the Mach profile of Fig. 6.8), thus inviting the flow towards it. At the two downstream measuring stations, and especially at DMS1, the profiles exhibit a perturbation at $y^H \in [0, 1]$, *i.e.*, the region occupied by the SACOC, where the mean vertical velocity is positive. This could be an effect of the ejection event induced by the aerodynamic blockage of the fins, as discussed in Chapter 5. Intuitively, at DMS2 some level of homogenisation is already visible.

Finally, Figure 6.12 shows the evolution of the turbulent kinetic intensity (TKI) at the three measuring stations. Also in this case the data has been extracted via the LDA system. At UMS1, it is evident how the level of turbulence is more elevated near the lower wall, where the apertures of the distortion screen are narrower and turbulence is enhanced. In the remaining part of the channel, the turbulence intensity is instead of the order of magnitude of 2%. This profile has been prescribed at the inlet of our RANS simulation as boundary condition. At the two downstream stations, the TKI is understandably higher with respect to UMS1, as an effect of the perturbation of the SACOC. As with what we have observed in Figure 6.11 for the vertical velocity, the disturbance is located in the near-wall region. Interestingly, the turbulence intensity is higher at DMS2 than DMS1. It is not clear whether this is

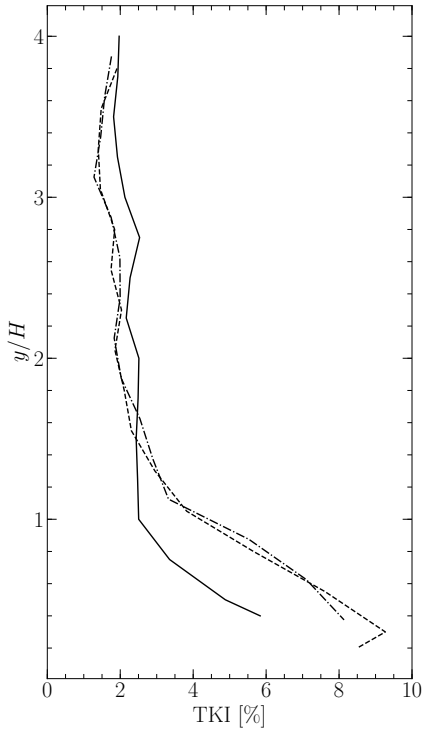

Figure 6.12: Aerodynamic results. Turbulent kinetic intensity at $z^H = 0$ at the three measuring stations. See Figure 6.10 for a reference to the lines.

due to the increase of turbulence of a thickening boundary layer, or if it is simply a local effect of the centreline $z^H = 0$, since no spanwise average has been performed.

iii. *Thermal results*

So as to capture the thermal wake and boundary layer, recall, four additional measurement planes have been implemented, *i.e.*, DMP1, DMP2, DMP3 and DMP4, which are located at the distance of $2H$, $4H$, $6H$ and $8H$, respectively, from the trailing edge of the SACOC. The thermocouples are placed on the centreline $z^H = 0$ and, therefore, only one-dimensional profiles are available. Figure 6.13 shows the evolution of the total temperature along the wall-normal direction at these locations. As can be seen, the passage through the fins generates a thermal wake and boundary layer, the thickness of which is, intuitively, of the order of magnitude of the fin height. Indeed, at $y^H \approx 1.2$, all the different profiles join at $\theta = 0$. It can also be observed that due to the homogenisation of the flow, the thermal layer quickly tends to disappear with the distance, as the peak temperature at DMP4 is almost 50% lower compared to DMP1. Yet, the most striking aspect of these profiles is their behaviour in the very near wall region, where below $y^H \approx 0.1$ the temperature gradient is negative, indicating a negative heat flux and, therefore, a heat loss through the lower wall which, recall, is made of steel. The imperfect insulation of the SACOC thus has a non-negligible impact on the temperature profiles, and this aspect needs to be taken into account numerically.

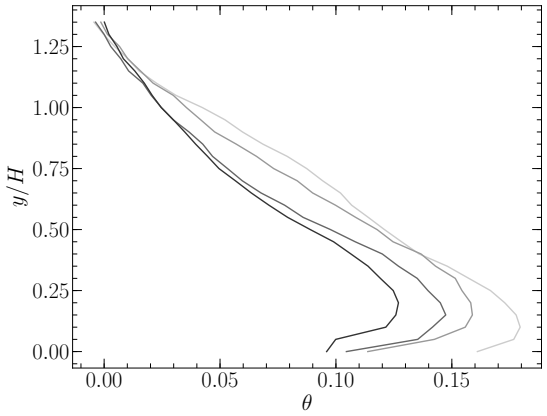

Figure 6.13: Thermal results. Profiles of total temperature at $z^H = 0$ and DMP1, DMP2, DMP3 and DMP4, from light to dark gray.

Finally, the total heat dissipated by the heat exchanger, non-dimensionalised to yield a global Nusselt number, gives:

$$\mathrm{Nu} = \frac{H}{S_{SACOC}} \frac{\dot{Q}}{\lambda_{ref}(T_{base} - T_{ref})} = 148.2 \ , \tag{6.4.2}$$

where S_{SACOC} is the total surface of the SACOC, $\dot{Q}$ is the total heat computed as in Eq. (6.4.1), λ is the thermal conductivity of the air and T_{base} is the average temperature at the base of the heat exchanger extracted through the IR camera. In Eq. (6.4.2) we employ T_{base} instead of T_{oil} as it is the temperature we prescribe as numerical boundary condition and, therefore, should be more physically representative in our simulations. The scrupulous reader will notice that the numerical value of the Nusselt number is very similar to the ones obtained in Chapter 5. However, the SACOC geometry, the inflow Mach number and even the conductivity of the material considerably differ between these two cases of study. Although it is always pleasing to obtain the same orders of magnitude, comparing the performance parameters of the two configurations should not be of great interest.

6.5 Numerical setup, boundary conditions & results

6.5.1 Numerical setup

The geometry of the fluid and solid domains is shown in Figures 6.14a & 6.14b, respectively. The fluid domain coincides with the test section described in §6.4.1, thus extending from UMS1, which is the inlet, to DMS2, which is the outlet. It is discretised with a structured mesh of around 30M nodes.

The solid medium consists of 16 SACOC fins, geometrically coincident to the ones depicted in Fig. 6.2. The material is considered to be isotropic and has a uniform conductivity which ranges between $\lambda = 115 - 140$ W/(m K), according to the supplier's specifications. The impact of this uncertainty will be evaluated in §6.5.3. The domain is discretised with a structured mesh (although interpreted as unstructured by *Zset*) of around 10M nodes.

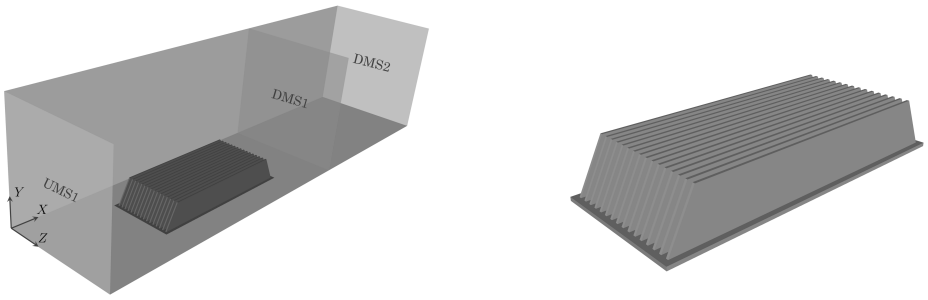

(a) (b)

Figure 6.14: Fluid (a) and solid (b) domains of the CHT simulations.

	Bi_ν	$\alpha_f^{opt}/\alpha_f^{min}$	K_f/α_f^{min}
$\Lambda_s = H$	1.12	8.9	62.4
$\Lambda_s = L$	7.04	1.2	8.2

Table 6.2: Estimation of the main stability parameters for the present case.

We employ the exact same numerical setup of Chapter 5, described in §2.3. Yet, differently from Chapter 5, we use the $k-\omega$ model of Menter (1993) with SST correction. We have tested other turbulence models and we report that we have not observed any significant difference in the results. Finally, concerning the stability of the coupling process, Table 6.2 summarises the estimated milestone parameters discussed in Section 2.5. Values are given for two solid characteristic lengths Λ_s, *i.e.*, the fin height H and length L. As can be seen, despite the apparently innocuous air-aluminium coupling process, $\mathrm{Bi}_\nu > 1$ in both cases, and Dirichlet-Neumann boundary conditions are thus expected to yield numerical instability. The case $\Lambda_s = L$, according to the theory of Section 2.2 is clearly the most problematic one, yet, as can be seen from Table 6.2, α_f^{opt} provides a sufficient margin over the stability limit. Also note that in both cases K_f is much larger than α_f^{min}. As a whole, our simulations clearly fall into the second of the scenarios listed in §2.5, and the use of α_f^{opt} is thus completely justified.

6.5.2 Boundary conditions

Concerning the fluid domain, the two-dimensional experimental cartography of stagnation pressure, stagnation temperature and turbulent intensity are directly prescribed as boundary conditions at UMS1; the flow is supposed to be completely axial, as we have justified in §6.4.2; finally, a default value of $\mu_t/\mu = 10$ is prescribed to the turbulent to laminar viscosity ratio, since it has not been measured experimentally; we report that no significant sensitivity has been observed for $\mu_t/\mu \in [10, 1000]$.

At DMS2, uniform static pressure is prescribed. The value is calibrated in order to yield the same distribution of Mach number at UMS1 between our simulations

and the experiments. Therefore, reasonably assuming that the head losses are not perfectly captured numerically, a certain disparity between the static pressure at the numerical and experimental DMS2 is to be expected.

The side and upper walls are adiabatic, and a no-slip condition is prescribed to the velocity. The choice is justified by the low conductivity of the borosilicate used for those walls, *i.e.*, $\lambda \sim 1$ W/(m K). The lower wall, instead, requires a different thermal condition. Since it is made of steel ($\lambda \sim 15$) and its thickness is of the order of a few millimetres, its thermal conductance is *a priori* not negligible. In fact, as the temperature profiles of Figure 6.13 have proved, an appreciable heat loss is observed through the lower wall. Ideally, its thickness would be discretised, and CHT would be performed with the flow. However, given the high conductance of the medium, we assume that the heat exchange can be reasonably mimicked by a temperature imposed surface, more precisely at $\theta = 0$. Finally, the surface of the SACOC is in thermal contact with the solid domain and, as described in §2.3.3, a Dirichlet boundary condition on the temperature is prescribed.

Concerning the solid medium, the upper surface of the SACOC is in thermal contact with the fluid domain, and, as justified in §6.5.1, a Robin boundary condition with the coupling coefficient α_f^{opt} is prescribed. The side walls of the lower platform are adiabatic (implying, once again, that the SACOC is assumed to be perfectly insulated), while at the bottom wall the experimental temperature cartography is prescribed. This undoubtedly represents the most significant difference between the numerical and experimental environments, since we do not simulate the oil circuit and, therefore, make use of *a posteriori* data which result from the accomplished aerothermal coupling observed experimentally. In other words, we only focus on the air-side of the aerothermal problem which, despite being extremely challenging *per se*, should not mislead us into disregarding the complexity of the oil-side. We will further discuss this aspect in §6.6.

Another observation has to be made concerning the experimental characterisation of the bottom temperature. Ideally, several thermocouples would be placed at the bottom of the SACOC, giving access to a two dimensional cartography as it is done for the inlet plane UMS1. Since such intrusive measurements are not possible in this case, our best option is to rely on the IR imagery described in §6.4.1 and shown in §6.4.2. However, the IR image shown in Figure 6.9a is taken from above and, therefore, does not actually represent the temperature at the bottom of the SACOC. The major issue, in particular, is represented by the tip of the fins, which are considerably colder ($\theta \sim 0.1$) than the base of the heat exchanger. Therefore, we test two different bottom boundary conditions, which are depicted in Figure 6.15. The former is simply represented by the temperature extracted from the IR image of Figure 6.9a, without any manipulation. The latter, is a temperature cartography in which the spanwise coordinates corresponding to the tip of the fins have been filtered out (see Figure 6.15, left). The filtering yields a difference of temperature gap $\Delta T = T_{base} - T_{ref}$ of around 10% between the two distributions, and the impact will be evaluated in §6.5.3.

6.5.3 Numerical results

In this section, the numerical results are presented and compared to the experiments. In the following, the same notation of §6.4.2 is used. For the aerodynamic part (§i.), only one numerical setup has been used, *i.e.*, with the conductivity of the solid domain $\lambda_s = 140$ W K/m and the unfiltered bottom temperature. In fact, we report that we have not observed any appreciable sensitivity of the pressure drop or velocity

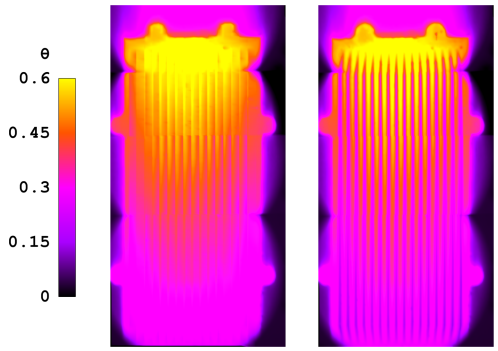

Figure 6.15: Temperature boundary conditions at the bottom of the SACOC. Filtered (left) and unfiltered (right) IR measures.

profiles on the thermal setup of the solid medium. For the thermal part (§ii.), instead, we will test both $\lambda_s = 115$ W K/m and $\lambda_s = 140$ W K/m, as well as the filtered and unfiltered bottom boundary conditions.

i. *Aerodynamic results*

Figure 6.16 displays the Mach number profiles obtained at UMS1. In particular, in Fig. 6.16a the profiles are averaged along $z^H \in [-1, 1]$, while in Fig. 6.16b the values are taken at three spanwise coordinates. Although the numerical boundary conditions at UMS1 have been extracted from the experiments, some small discrepancies can be observed, especially near the upper wall. In fact, remember, only the stagnation pressure was prescribed, and the Mach number thus results from the static pressure imposed at the outlet; despite the calibration mentioned in the previous section, some differences inevitably remain. In any case, these discrepancies are negligible, and the Mach regime of our simulations is in good agreement with the experiments.

Similar curves are given in Figure 6.17 for the first downstream station DMS1. Furthermore, the two-dimensional cartography of our simulation and of the wind tunnel, allowing for a qualitative comparison, is given in Figure 6.18. All profiles exhibit excellent agreement with the experiments for $y^H \gtrapprox 1$, both on average and locally with respect to z^H; notice, for instance, how the level of acceleration at the centre of the channel is practically identical, and how the development of the upper-wall's boundary layer is well predicted. These results suggest that a good prediction of the free stream region of the flow has actually been obtained during the experiments, thus corroborating the hypothesis that the incorrect behaviour of the stagnation pressure shown in §6.4.2, is indeed due to the ambient-pressure dependence of the measurements. Regarding the lower region $y^H \lessapprox 1.5$ where the SACOC is located, good agreement is obtained only when widening the spanwise average to the whole channel width (see Figure 6.17b), thereby reducing the relative influence of the heat exchanger. For the other curves, it is evident how our numerical simulations tend to overestimate the impact of the SACOC, as can also be qualitatively seen in Fig. 6.18. In any case, the discrepancy does not exceed 20% for the worst predicted point. These results are not totally unexpected, since DMS1 is located close to the trailing edge

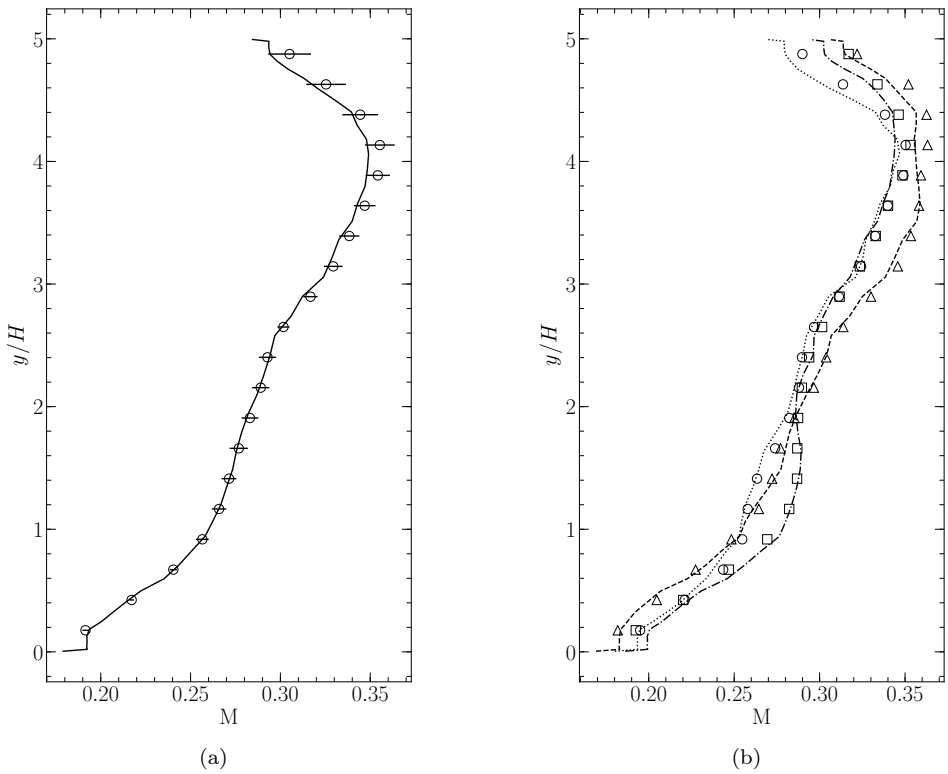

Figure 6.16: Aerodynamic results. Mach number profiles at UMS1. Average along $z^H \in [-1, 1]$ (a): —— present numerical results; ○ experimental results. Profiles at $z^H = 0$, $z^H = 1$ and $z^H = -1$, respectively (b): $\cdots\cdots$, $- \cdot - \cdot -$ and - - - - present numerical results; ○, □ and △ experimental results.

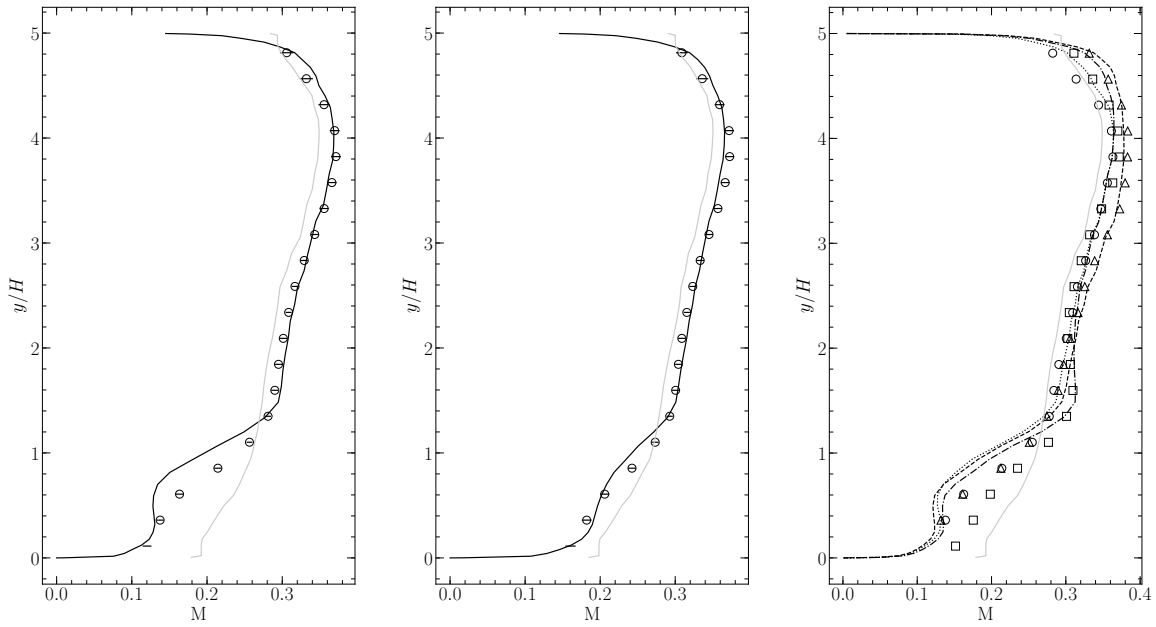

Figure 6.17: Aerodynamic results. Mach number profiles at DMS1. Average along $z^H \in [-1, 1]$ (a), average along $z^H \in [-2.5, 2.5]$ (b) and profiles at $z^H = 0$, $z^H = 1$ and $z^H = -1$ (c). The gray solid line represents the average profile at UMS1, as reference. Other lines and symbols, see Fig. 6.16.

of the heat-exchanger, where the flow is highly perturbed. It is not surprising that our steady RANS simulations fail to finely capture these effects. Results, however, do not significantly change at DMS2 (see Fig. 6.19), where the flow already exhibits some degree of homogenisation, as seen in §6.4.2. Although the acceleration of the flow at the centre of the channel is still well predicted, the thickness of the upper-wall's boundary layer seems to be slightly underestimated. Concerning the lower-wall region, good agreement with the experiments is, once again, only obtained when a complete spanwise average is applied to the profiles. In all the other cases, the maximal discrepancy remains of the order of 20%. We can therefore conclude that our RANS simulations are only able to capture the qualitative evolution of the velocity along the channel, with the major deviations being localised in the region y^H where the SACOC is situated. However, it should also be noted that the Mach number, in fact, is not directly acquired by the Kiel probes, but computed in post-processing using the static pressure measured at the wall by an independent pressure tap.

Let us now analyse the evolution of the stagnation pressure. As mentioned in §6.4.2, the profiles are affected by a spurious pressure drop, which we have ascribed to the fact that the consolidated data have been obtained by averaging the measurements of different testing days for the planes UMS1, DMS1 and DMS2. Therefore, we propose to use the results of one particular day, *i.e.*, the 15$^{\text{th}}$ of January 2021 (JAN15), to investigate the behaviour of the stagnation pressure, and characterise the pressure drop generated by the heat exchanger. The consolidated (*i.e.*, the data

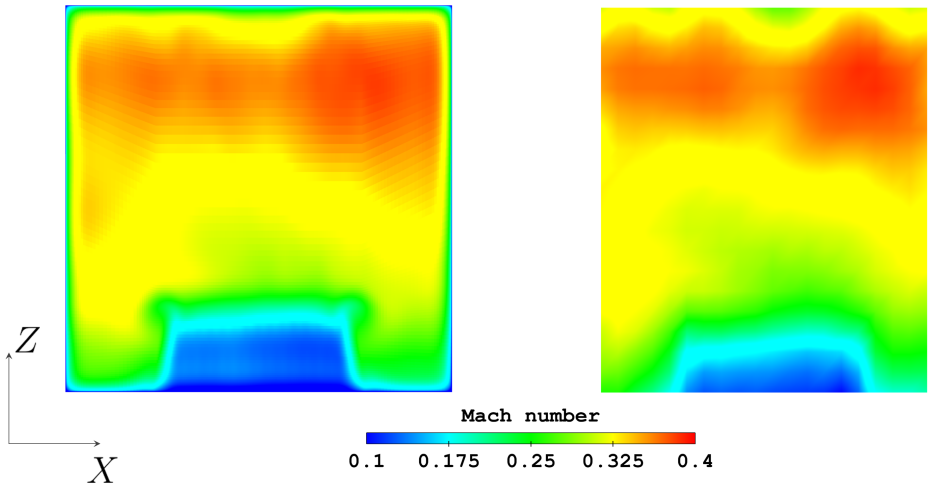

Figure 6.18: Two dimensional cartography of the Mach number at DMS1 in our simulation (left) and in the test-rig (right).

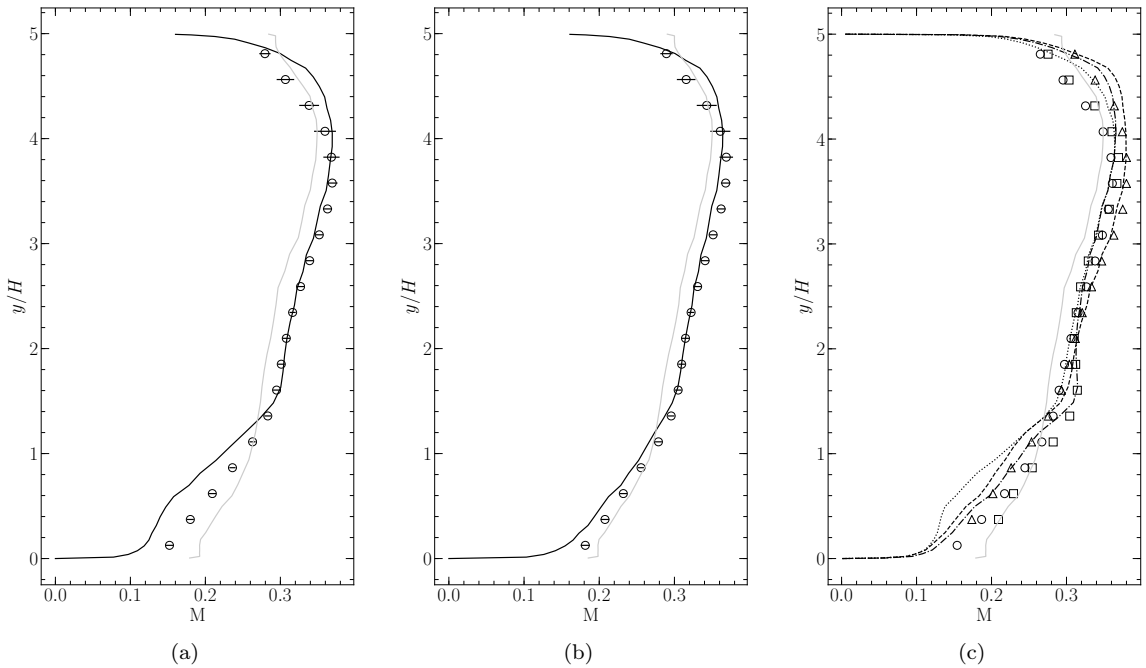

Figure 6.19: Aerodynamic results. Mach number profiles at DMS2. Average along $z^H \in [-1, 1]$ (a), average along $z^H \in [-2.5, 2.5]$ (b) and profiles at $z^H = 0$, $z^H = 1$ and $z^H = -1$ (c). See Figs. 6.16 & 6.17 for a reference to lines, colours and symbols.

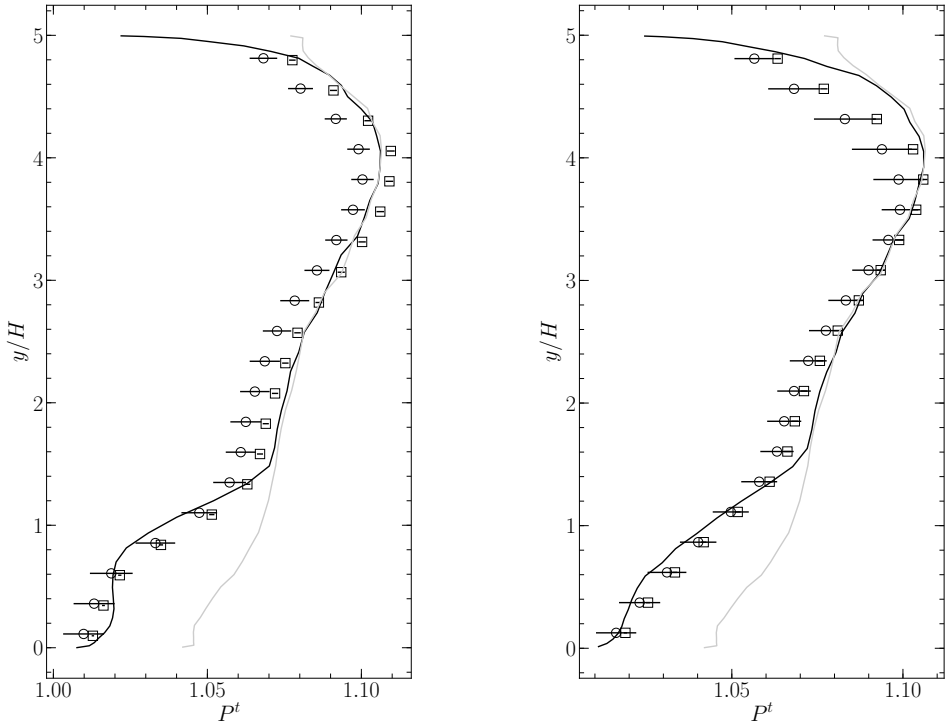

Figure 6.20: Aerodynamic results. Stagnation pressure profiles at DMS1 (a) and DMS2 (b), averaged along $z^H \in [-1, 1]$: ○ consolidated experimental data; □ JAN15 experimental data; —— present numerical results at the downstream stations (black) and at UMS1 (gray).

discussed in §6.4.2) and JAN15 profiles are displayed in Figure 6.20 for both DMS1 and DMS2. The profile at UMS1 (gray solid line) is also added as a reference. As expected, a significant deficit of stagnation pressure is observed at the centre of the channel for the consolidated data, which is (correctly) not present in our simulations. Comparing the JAN15 results with our numerical profiles, instead, one can observe that good agreement is obtained in the free stream part of the channel, suggesting that these data were collected in similar ambient pressure conditions of the measurement days of UMS1. Concerning the portion of the channel occupied by the SACOC, where the major perturbation is localised (*i.e.*, $y^H \lessapprox 1.5$), one can observe that at DMS1 and DMS2 good agreement is obtained with, in fact, both the consolidated and JAN15 results. In particular, we obtain better agreement compared to the Mach number profiles discussed above.

Finally, we proceed with the estimation of the pressure drop generated between UMS1 and DMS2. To do this, we compute the average stagnation pressure of these two stations as follows:

$$\langle P^t \rangle = \frac{1}{3 \times 5} \int_{y^H=0}^{y^H=5} \int_{z^H=-1.5}^{z^H=1.5} P^t \mathrm{d}y^{H'} \mathrm{d}z^{H'} \tag{6.5.1}$$

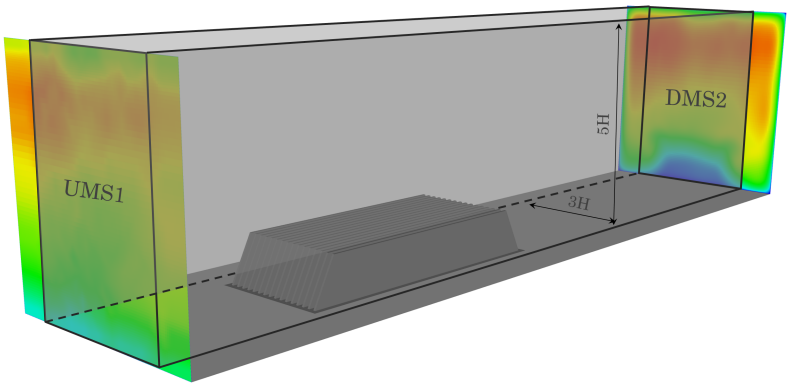

Figure 6.21: Schematic view of the surfaces used to compute the average stagnation pressure.

	Simulation	Consolidated data	JAN15
Pressure drop	1.12%	1.48%	1.05%
Difference	[-]	32%	6%

Table 6.3: Pressure drop in percentage. Comparison between our simulations and the experiments.

As can be seen from Figure 6.21, the spanwise average includes the whole SACOC block (*i.e.*, $z^H \in [-1.25, 1.25]$) as well as a part of the two lateral corridors, so that the border effects are taken into account in $\langle P^t \rangle$. The pressure drop can thus be computed as:

$$\Delta P_{\%} = \frac{\langle P^t \rangle_{UMS1} - \langle P^t \rangle_{DMS2}}{\langle P^t \rangle_{UMS1}} \, . \tag{6.5.2}$$

Table 6.3 summarises the values obtained from our simulation as well as from the consolidated and JAN15 experimental data. As can be seen, the spurious pressure drop of the consolidated data yields a much higher value of ΔP. Once the free stream region of the flow is properly accounted for, as in JAN15, a difference of no more than 6% is obtained with our simulation.

ii. *Thermal results*

As mentioned in §6.5.1 and §6.5.2, the thermal characterisation of the SACOC is plagued by two important uncertainties. The former concerns the conductivity of the aluminium alloy, which, according to the supplier's specifications, ranges between $\lambda_s \in [115, 140]$ W/(m K). The latter, regards the temperature distribution at the base of the heat exchanger, which has been experimentally characterised by an IR image taken from above; as explained in §6.5.2, we have introduced a filtered temperature field to obviate the disturbance of the tip of the fins. Therefore, we have

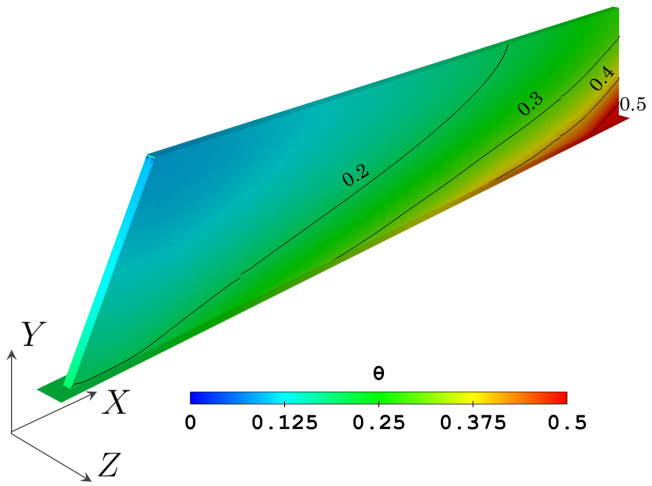

Figure 6.22: Contours of non-dimensional temperature θ over the surface of a SACOC fin.

performed four different simulations, using the highest and lowest thermal conductivity and the two temperature distributions at the bottom of the SACOC. Figure 6.22 displays some contours of temperature over the surface of a fin. Figure 6.23, instead, shows the total temperature profiles at DMP1, DMP2, DMP3 and DMP4 obtained with our four simulations and compared to the experiments. The gray and black lines refer to the filtered and non-filtered boundary conditions, respectively, while the style of line distinguishes between the two thermal conductivities.

Let us commence the discussion of these results with an overall assessment. First of all, it should be noted that the measurement stations DMP1 to DMP4 are not planes but lines located at the centre of the channel, *i.e.*, $z^H = 0$ (see §6.4.1). Consequently, differently from the previous paragraph (§i.), we cannot make use of spanwise averages to even out some local effects. This inevitably affects the quality of the comparisons, at least at the first measuring stations, where the flow still has not homogenised. Second, notice how the different temperature profiles we have obtained numerically are logically arranged, with the hottest bottom boundary conditions (*i.e.*, the filtered ones) and the highest solid conductivity yielding the most pronounced thermal boundary layers. This allows us to distinguish, in the uncertainty range, between the scenario realising the highest heat exchange (*i.e.*, filtered boundary conditions with highest conductivity) and the scenario realising the lowest heat exchange (*i.e.*, non-filtered boundary conditions and lowest conductivity), with the hope that the experimental results are situated between the two. Furthermore, it can be seen that the thickness of the thermal wake amounts to approximately $1.4H$, and that all our simulations predict it well. Finally, observe how the use of the isothermal condition $\theta = 0$ for the lower wall of the wind tunnel, has allowed us to qualitatively reproduce the heat loss through the channel.

Now we proceed to a more detailed analysis. Figure 6.23a is relative to the first measuring station DMS1. As can be seen, the experimental thermal wake is more pronounced than any of the numerical profiles, with temperatures underestimated

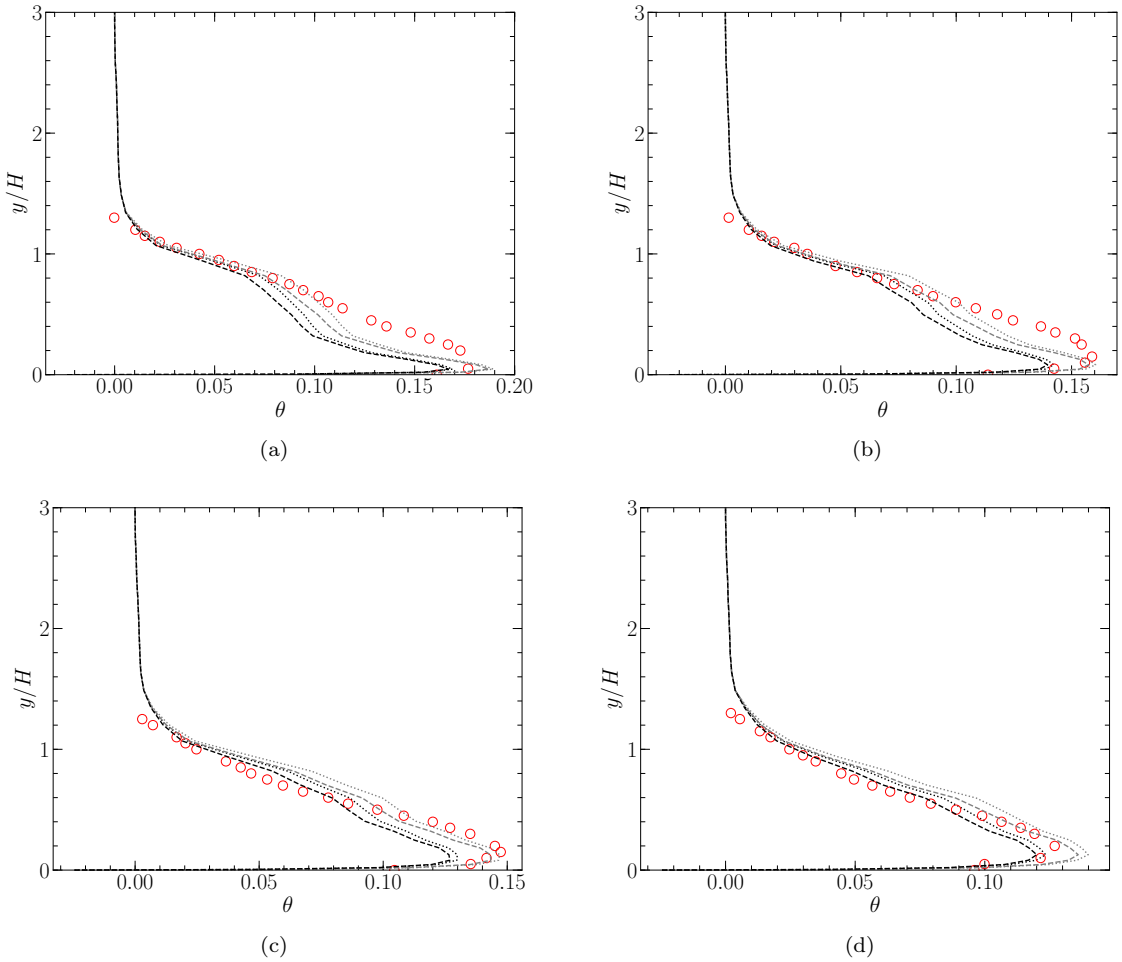

Figure 6.23: Thermal results. Non-dimensional total temperature θ at DMP1 (a), DMP2 (b), DMP3 (c) and DMP4 (b). Colours: filtered (gray) and non-filtered (black) boundary conditions; lines: - - - - $\lambda_s = 115$ W/(m K); ····· $\lambda_s = 140$ W/(m K); ○ experimental data.

by around 15% in the region $y^H \in [0.2, 0.8]$. These discrepancies do not necessarily imply that the global heat exchange has been underestimated, since, as mentioned above, these results only refer to a single central line. On the other hand, these results confirm how RANS modelling is unable to capture the evolution of extremely localised profiles.

Similar observations can be made about Fig. 6.23b, which is relative to the second measurement station DMP2. However, the discrepancy zone has reduced to approximately to $y^H \in [0.2, 0.6]$, with the profiles obtained with the non-filtered boundary conditions yielding the best agreement.

The homogenisation of the flow starts becoming visible at DMP3 (see Figure 6.23c). In reality, it is the numerical profiles which have qualitatively evolved the most between DMP2 and DMP3, with an extremely less pronounced inward bump at $y^H \approx 0.4$. We can therefore conclude that our RANS simulations are characterised, in fact, by a delayed flow homogenisation. Concerning the comparison with the experiments, the temperature profile is, as a whole, included within the uncertainty range, with only some slight over- and under-predictions for $y^H \approx 0.7$ and $y^H \approx 0.3$.

Finally, Figure 6.23d is relative to DMP4. As can be seen, both the experiments and our numerical simulations exhibit the same level of flow homogenisation, with a temperature profile satisfyingly situated within the lowest and highest heat-exchanging configurations. Only some small discrepancies of the order of $2-5\%$ can be noticed for $y^H \approx 0.7$.

As a whole, the comparison of the temperature profiles has yielded good results, except for the delayed flow homogenisation at the trailing edge of the SACOC. So as to assess whether this has any impact on the overall performance of the heat exchanger, we proceed to the comparison of the global heat dissipated by the heat exchanger. Since we perform steady state simulations, we can simply compute the total heat exchange through the base of the SACOC:

$$\Phi = \int_{S_{base}} \boldsymbol{\phi} \cdot \hat{\boldsymbol{n}} \mathrm{d}S = -\lambda_s \int_{S_{base}} \frac{\partial T}{\partial y} \mathrm{d}S \ , \tag{6.5.3}$$

which yields the following global Nusselt number:

$$\mathrm{Nu} = \frac{H}{S_{SACOC}} \frac{\Phi}{\lambda_{ref} \left(T_{base} - T_{ref}\right)} \ , \tag{6.5.4}$$

where the same reference properties of Eq. (6.4.2) are used. Table 6.4 summarises the results obtained with the four simulations with their error with respect to the experimental value. As can be seen, the experimental value is well centred in the uncertainty range. The over- and under-predictions are limited to around 10% for the most and least heat-exchanging simulations, which is a satisfying precision, since these two cases represent the most extreme scenarios.

6.6 Conclusion

In this last chapter, we have performed the experimental and numerical study of a surface heat exchanger installed in a wind tunnel.

In the first sections, we have described the context in which the experimental tests have been realised. We have mentioned the *Clean Sky 2* project, its objectives, as well as the goals of our own investigations, *i.e.*, to rigorously validate our conjugate heat

	Exp.	Filtered, $\lambda_s = 140$	Filtered , $\lambda_s = 115$	Non-filt., $\lambda_s = 140$	Non-filt., $\lambda_s = 115$
Nu	148.2	163.2	153.05	143.23	134.33
Error	[-]	10.1%	3.3%	−3.4%	−9.4%

Table 6.4: Global Nusselt number. Comparison between our simulations and the experiments. The solid conductivity is expressed in W/(m K).

transfer methodologies on the targeted industrial application. Furthermore, we have detailed the test requirements that, as Safran Aircraft Engines, we have specified to the partners of the project. In particular, we have asked to assess the aerothermal performances of a realistic SACOC in a wind-tunnel, with specific inflow conditions.

In §6.4, we have focused on the experimental tests which have been carried out by UPV. First of all, the results have shown that the experimental setup allows us to meet the scope of the study. In particular, a satisfying level of heat is exchanged between the SACOC and the oil circuit, and the inflow conditions, thanks to the distortion screen designed and implemented by UPV, reproduce the targeted Mach number profile. As a whole, the experimental results are in agreement with the expected behaviour of the flow. However, the stagnation pressure profiles exhibit a spurious deficit at the centre of the channel between the inlet and the downstream measuring planes. Since the Mach number, on the other hand, seems to evolve correctly, we have ascribed the issue to the ambient-pressure dependence of the stagnation pressure, which was measured and averaged over different days for the different measurement stations. Furthermore, we have seen that the imperfect insulation of the wind tunnel's lower wall has an appreciable impact on the thermal boundary layer, which presents a negative heat flux at the wall.

In §6.5, we have focused on the numerical environment. We have described the numerical setup and put into evidence several fundamental aspects of our simulations. First, that we have not simulated the oil circuit and we have replaced the hot source of the heat exchanger with a temperature-imposed surface. Second, that the conductivity of the SACOC's material is uncertain and, according to the supplier's specifications, ranges between two particular values. Third, that the characterisation of the temperature distribution at the base of the SACOC is necessarily erroneous, since it was measured from an IR image taken from above; to obviate this issue, we have introduced a filtered temperature distribution which excludes the coldest portions of the cartography. As a whole, we have obtained satisfying results with respect to the experiments, with a 6% discrepancy on the pressure drop and a 10% dispersion on the global heat exchange (taking into account all the aforementioned uncertainties). On the other hand, our RANS simulations have failed to capture certain local effects and, in particular, have shown the tendency to underestimate and delay the homogenisation of the flow. This has been particularly evident when analysing the Mach number evolution near the lower wall, and the thermal wake immediately downstream of the SACOC. Better agreement with the experiments has generally been obtained when introducing spanwise averages, which, nevertheless, reduce the relevance of the results.

Several conclusions can be drawn from this study. First of all, we can conclude

that the conjugate heat transfer methodologies we have implemented and tested, allow us to obtain satisfying predictions of the global performances of the SACOC, *i.e.*, in terms of pressure drop and heat exchange. However, one major limit of our study has to be highlighted, *i.e.*, the fact that the oil side of the heat exchanger has not been simulated, and the hot source has been replaced by a temperature distribution. In other words, we have only focused on the air side of the heat exchanger, yet an accurate assessment of our CHT methodologies should be done by considering the whole aerothermal problem. In fact, the temperature cartography we have used as a boundary condition, represents strong *a posteriori* data, which has driven our simulations on the good path. Certainly, this aspect does not diminish the importance of our results. In perspective, however, the design and sizing of a SACOC cannot be realised by assuming a temperature distribution at its base, as it is a result of the SACOC configuration itself. Performing CHT simulations including the presence of the oil side, and comparing their outcome with the same experimental results presented here, is thus of fundamental importance and represents the most natural continuation of our work.

Concerning the turbulence modelling, the RANS approach has shown its well known limits. Nevertheless, if the objective of Safran Aircraft Engines is that of assessing the overall behaviour of the heat exchanger at steady state, without the pretence of capturing the finest features of the flow, RANS certainly represents the optimal compromise. The simulations we have performed have generally required $\approx$ 6000 CPU hours each, which is absolutely reasonable for the standards of our engineering offices. We also report that the resolution of the heat diffusion in the solid domain at every coupling instance, has required approximately 30% of the total computing power, keeping in mind that we have not optimised the performance of our implementation. Major improvements could have simply been obtained by using less refined meshes for the solid domains, or by using progressively higher coupling periods as the simulation advances and converges. In any case, the cost of CHT, although not negligible, seems to be worth the considerable amount of additional physical phenomena it gives us access to.

Conclusion

In this work, we have taken an interest in aircraft engine's surface air-oil cooled oil coolers (SACOC). The most standard SACOC is formed by a series of staggered fins, oriented along the direction of the flow. Implemented in the by-pass duct of modern turbofans, the cold source of the heat exchanger is thus the by-pass duct airflow, while its hot source is the engine oil, which flows into a system of channels placed beneath the fins. These heat exchangers are growing in popularity for their potential to dissipate the required heat load with weaker flow disturbances, compared to their box-shaped predecessors. Since, on the one hand, the heat exchange is a stringent operability constraint, and, on the other hand, the pressure drop generated by the fins has a direct impact on the engine's thrust, the correct characterisation of the aerothermal performance of SACOC is of utmost importance.

The review of the state of the art realised at Safran Aircraft Engines at the beginning of this Ph.D., has thrown light on two major issues that our work should have addressed:

— The general incomprehension of the aerothermal behaviour of the SACOC.

— The lack of predictive aerothermal numerical methodologies.

These challenges have led to the formulation of two macro-objectives of this work, *i.e.*:

— Improving our physical understanding of aircraft engine's heat exchangers.

— Providing predictive numerical methodologies for better investigating complex aerothermal interactions.

The main achievements of this thesis are described in the following.

Convective and conjugate heat transfer: methodology and validation

Main achievements

— An equilibrium wall-model for WMLES based on ordinary differential equations for the momentum and energy has successfully been implemented in AVBP, and validated with respect to canonic bi-periodic fully developed channel flows. The implementation also involves the off-wall location of the so-called matching-point proposed by Kawai and Larsson (2012). This strategy has proven to be effective against the logarithmic-layer mismatch, which completely vanishes

once the matching-point is located at the third or fourth off-wall grid-point. In our case, only cartesian meshes have been employed. However, the method has been implemented to function with all types of meshes. All these features were not available in the standard version of AVBP, and their implementation and validation is a major achievement of the first months of this Ph.D. work.

— In partitioned conjugate-heat-transfer (CHT) approaches, numerical instabilities can be provoked by the exchange of boundary conditions between the two media. In this work, we have validated the stability analysis by Errera and Chemin (2013), who investigated Dirichlet-Robin boundary conditions and found a lower stability bound for the relaxation coefficient. For this purpose, we have employed a new specifically designed code which respects all the assumptions of the theoretical study. The exactness of the lower stability bound by Errera and Chemin (2013) has been confirmed.

— The theoretical stability analysis by Errera and Chemin (2013) has been extended to more general cases. In particular, we have taken into account the heterogeneity of the solid medium and the presence of radiation. Furthermore, a systematic study of the influence of the coupling period (intended as the number of fluid iterations between two consecutive coupling instances) on stability has been performed. We have found that increasing the coupling period has a stabilising effect. The systematic study has revealed that the lower stability bound can probably be expressed as a function of the coupling period and of the mesh Fourier number. However, no analytical expression has been found.

— A partitioned conjugate-heat-transfer approach has successfully been implemented in *elsA* and *Zset*. The approach is based on steady RANS modelling on the fluid side. The implementation has been tested on complex industrial configurations, and can thus be considered ready to be integrated in the engineering offices of Safran Aircraft Engines.

Perspectives

— Our implementation of an equilibrium wall-model in AVBP is far from being optimal. Several improvements could be made in the future. First, the research of the off-wall matching-points is effectuated at the beginning of every simulation, even if the mesh and its MPI distribution have not changed; this step, therefore, could be performed by a specific tool in pre-processing, and all the connectivity information could be stored in a file which is read by AVBP at the beginning of the computation; this could also allow the user to verify the connectivity table before the computation, or to modify it by hand according to the specific requirements of the studied configuration. Second, the load balancing does not take into account the presence of the wall-model; however, solving the aforementioned ODE has a non-negligible cost that makes the wall grid-points considerably more burdensome with respect to the other nodes; a correct load balancing should take this additional cost into account. Third, it is probably not necessary to couple the LES and the wall-model at every time step; hence, it could be envisaged to let the user specify a coupling period.

— More complex wall-models are necessary for non-equilibrium flows. We refer, in particular, to full three-dimensional RANS models which have already been assessed in the literature (see, for instance, Park and Moin, 2014). Such an

implementation demands an important effort, which would probably be out of reach of a single Ph.D. student. A solid LES framework providing complex wall-modelling features, would be a decisive step towards the maturity of WMLES and its application to industrial configurations.

— The evolution of the lower stability bound as a function of the coupling period, suggests the existence of an analytical expression. Further mathematical investigations could bring it to light.

— The stability analyses we have performed, are not only motivated by the need of stabilising our coupling processes (which can be achieved by any sufficiently elevated coupling coefficient), but also by the desire not to penalise its convergence rate more than necessary. However, in practice, the convergence rate has proven not to considerably evolve for a large range of coupling coefficients. This has been observed in the past (see Errera et al., 2019), and also in this work. We believe that the parameter that affects the convergence rate of a coupled simulation the most, is the coupling frequency. When optimised, both the number of total fluid iterations and the number of coupling instances are minimised. It is well known that it is necessary to couple the fluid and solid media very frequently at the beginning of simulation, and much less often once close to convergence. We do not know if an optimal coupling frequency can be found, but simpler one-dimensional investigations might help gaining some insight. For the time being, a sort of coupling CFL, proportional to the one of the fluid and increasing during the simulation, could be envisaged.

High-fidelity study of a non-equilibrium turbulent heat transfer case

Main achievements

— The direct numerical simulation of a non-equilibrium turbulent thermal boundary layer has been performed in a channel flow, where a wall temperature step change perturbs an adiabatic flow initially at equilibrium. Although DNS has extensively been used to investigate turbulent heat transfer, very few works have been realised in non-equilibrium configurations, and our study represents a considerable progress of the state of the art, which has allowed for a deepened knowledge of the behaviour of such flows. Although the simulation has been performed at one single flow regime, several physical aspects that we have studied are expected to be encountered in phenomenologically similar flows. The leading edge of the isothermal wall is expected to be the most perturbed region of the flow; the abrupt change of wall thermal conditions acts on the wall shear stress and, consequently, on the pressure gradient, which leads to modified velocity profiles; in our case, the effect is corrected by the introduction of a different wall-scaling, which takes both the mean fluid property variation and the pressure gradient into account. The study has also allowed for the identification of an equilibrium sub-layer, defined as the region of the flow where the equilibrium contributions to the energy balance are preponderant; in the equilibrium sub-layer, several quantities appear to be fully developed, like the mean temperature, wall-normal turbulent heat flux and, by construction, the mean energy fluxes. However, other quantities do not have the expected behaviour

in this near-wall region; we refer to the temperature fluctuations and to the turbulent Prandtl number, which need a longer distance from the leading edge to stabilise.

— The study has allowed us to clarify the aerothermal interactions which are expected to be observed in flows characterised by similar temperature gradients and heat flux parameter. We have observed that the thermal field has a small influence on the behaviour of the flow, with the only exception of the leading edge, where the perturbation, in any case, is not expected to play a major role on the overall performance parameters.

— The same non-equilibrium configuration has been investigated by WMLES. The first model that we have tested is the aforementioned equilibrium wall-model. Very poor results have been obtained near the leading edge, where the heat flux is severely underestimated, and, as the flow visualisations have illustrated, the heated wall is not perceived by the model until further downstream, where good agreement with the DNS is eventually retrieved. These results have shown the overall inadequacy of equilibrium wall-models in non-equilibrium configurations.

— A new wall-model has been constructed using the DNS data, which have clearly indicated that a mean streamwise convective term, at the very least, has to be included in the energy equation. Our *a priori* tests have suggested that the remaining terms, as well as the modified behaviour of the turbulent Prandtl number, are instead negligible. Very good agreement with the DNS has been obtained all along the channel, with a particular good prediction of the Nusselt overshoot near the leading edge. The results have shown how more complex wall-models can bring considerable benefits to WMLES, the main drawback of which appears to be its lack of maturity.

Perspectives

— Despite its Reynolds number limitation, DNS is a fundamental tool for investigating complex flows, and other non-equilibrium simulations could be envisaged in the future. The most straightforward continuation to our DNS work, would be that of studying other flow regimes and/or temperature ratios in order to generalise our findings concerning, in particular, the behaviour of the leading edge and the evolution of the equilibrium sub-layer. It is, of course, also possible to use the same flow regime but take an interest in a slightly different flow configuration, presenting, for instance, a fin aligned along the direction of the flow. These are only a few examples of fundamental studies which could considerably deepen our understanding of thermal non-equilibrium flows, and constitute a solid database of validation for future WMLES studies.

— The non-equilibrium wall-model which we have introduced has led to better predictions, yet has been constructed on the basis of very detailed information regarding the flow, which, in the most general case, are not at our disposal. Only complete three-dimensional wall-models can provide all the (mean) physical phenomena taking place in the inner-layer, stopping the tendency to slightly modify existing equilibrium wall-models according to the requirements of a particular configuration.

— With the tools available to us, more applied studies are anyway a possibility. We can suggest, for instance, a simplified heat exchanger presenting a few fins. In fact, the analysis of the thermal boundary layer performed on the SACOC, has revealed that equilibrium assumptions in the inner-layer might not be inconsiderate at all. Completely different configurations can, of course, also be considered. In turbofan by-pass ducts, for instance, WMLES could be interesting to analyse the behaviour of mixers, where the attention is drawn towards the core of the flow, where the primary and secondary flows mix, and not to the near-wall region, for which equilibrium assumptions might be acceptable. We wish to stress, in any case, the importance for Safran Aircraft Engines to continue high-fidelity studies. The work we have realised during this Ph.D. with WMLES represents an interesting opportunity which needs to be nourished and deepened, if we want to attain concrete results for our engine's applications.

Conjugate heat transfer investigation of a surface air-oil heat exchanger

Main achievements

— The conjugate heat transfer RANS simulation of a SACOC mounted on a turbofan by-pass duct has been performed. The computational domain includes the fan and OGV modules, and extends until the nozzle. No similar coupled simulations, to the best of our knowledge, can be found in the literature. The study has allowed us to clarify in which way the operating environment of the SACOC has to be considered challenging. The airflow delivered by the OGV is indeed characterised by strong mean three-dimensionality and, in particular, two strong vortices appear at the tip and hub of the blade. The forced convection with this flow generates a heterogeneous temperature field on the SACOC, with the fins located on the pressure side of the OGV being clearly better performing than those located on the suction side. The interaction between the SACOC and the OGV tip's vortex also leads to the generation of a significant flow separation taking place downstream of the heat exchanger on the suction side. The separation bubble appears to have a strong impact on the global pressure drop created by the SACOC. The study has also suggested that the thermal performance of the SACOC is, on the one hand, enhanced by the mass flow which penetrates the fins from the leading edge, and, on the other hand, penalised by the mass flow that leaves the SACOC from the upper side. Both, therefore, need to be accurately retrieved in smaller-scale experiments or simulations. The analysis of the development of the thermal boundary layer between two consecutive fins, has instead illustrated that an equilibrium sub-layer can be qualitatively identified, although the interactions with the boundary layers growing on other surfaces, as well as the presence of non-equilibrium effects, can alter its structure.

— Several wind-tunnel simulations have been performed using as boundary conditions the flow fields extracted from the engine. These fields have been manipulated with different surface or azimuthal averages, so as to determine which inflow conditions are the most representative in smaller-scale simulations and/or

experiments. The results have clearly shown that, in order to yield tolerably accurate thermal predictions, it is fundamental to recreate a representative boundary layer at the inlet of the channel, thanks to which the SACOC fins are traversed by the correct mass flow. On the other hand, we have found that even prescribing the exact inflow conditions with a two-dimensional cartography does not lead to a perfect recreation of the engine environment. In particular, the portion of mass flow that leaves the SACOC by the upper side is underestimated, and no flow separation is observed downstream of the heat exchanger. This clearly indicates that inflow conditions, although fundamental, are not the only factor playing an important role on the SACOC, and that the limited representativeness of square wind-tunnel configurations should also be addressed.

— Throughout the duration of the Ph.D., wind-tunnel experimental tests of a realistic SACOC have been carried out. Safran Aircraft Engines and, in particular, the author of this writing, have actively participated in the specification and in the monitoring of these tests, which have consequently allowed for rigorous experimental-numerical comparisons. As a whole, good agreement has been obtained for both the global pressure drop and heat exchange, with discrepancies that do not exceed 10%. On the other hand, our RANS simulations have failed to capture certain local effects, and only through partial spanwise averages a better agreement with the experiments has been retrieved. In particular, we have observed that our numerical simulations tend to underestimate and delay the flow homogenisation taking place immediately downstream of the SACOC. Despite these minor aspects, the experimental and numerical campaigns can be considered successful, and our CHT methodology can be implemented in the engineering offices of Safran Aircraft Engines for future aerothermal investigations of SACOC and other engine components.

Perspectives

— Our engine simulation has been performed at a single fan regime, *i.e.*, take-off. However, it is important to evaluate the SACOC in all phases of flight, from ground-idle to top of climb and cruise. Since the rotation speed of the fan and the mass flow rate are considerably different from a phase to another, different aerothermal behaviours of the SACOC are expected to be observed. Moreover, unsteady simulations investigating the transition between one flight phase to the other could also be extremely interesting. In particular, it would give access to the time needed by the SACOC to find itself back to steady state.

— From our study it has evidently appeared that the square wind-tunnel has a limited representativeness. Hence, our study could be continued to evaluate the most important geometrical sensitivities and try to reproduce the effects observed in the engine. This would allow to determine better wind-tunnel configurations. However, in practical tests, the recreation of the exact engine flow conditions would remain an insurmountable obstacle.

— The major limit of our numerical-experimental comparisons is represented by the fact that the oil-side of the heat exchanger has not been simulated, and the hot source has been replaced by the experimentally measured temperature distribution. This implies that we have only focused on half of the whole

aerothermal problem, *i.e.*, the air-side. However, the temperature distribution of the SACOC is a result of the aerothermal problem itself, and a proper validation of our methodologies should be effectuated by considering the oil circuit too. This is particularly important for the future design and sizing of our heat exchangers, which cannot be realised by assuming *a priori* that the oil has been cooled down to the desired temperature.

— The experimental validation of our CHT simulations provides Safran Aircraft Engines with a predictive numerical methodology which allows us to simultaneously investigate the aerodynamic and thermal fields of the SACOC. The most natural following step, is that of using these methodologies in our engineering offices. The SACOC can now be designed, optimised and characterised in all phases of flight and configurations. Of course, CHT can also be applied to other engine components featuring significant aerothermal interactions like, for instance, turbine blades.

Appendix A

Direct numerical simulation of equilibrium channel flows

The study of Chapter 3 is characterised by two distinct equilibrium states between which the flow evolves along the streamwise direction. The former is an adiabatic, fully developed turbulent flow in the upstream part of the domain; the latter is a fully developed turbulent thermal boundary layer at the outlet. Two distinct simulations are performed in the same regime conditions specified in Tables 3.1 and 3.3 in a bi-periodic channel flow, of which size and mesh information is summarised in Table A.1. The mesh distribution is the same as in Tables 3.1 and 3.2 in the wall-normal and spanwise direction, while in the X direction the point distribution is in this case uniform, since there are no streamwise singularities. Figure A.1 displays a schematic view of the computational domain.

As explained in §3.3, these computations are performed to both validate the numerical set-up introduced, and as reference solutions for the aforementioned equilibrium states of the spatially evolving channel flow of Chapter 3. The results presented in this Appendix are also repeatedly used in Chapter 1 to validate the equilibrium wall-model LES implementation. Furthermore, as mentioned in §3.2.3, the adiabatic bi-periodic channel flow is also used for initialisation.

In the following sections, details about these simulations are given, as well as the main results compared to the literature. In the following, $\overline{(\cdot)}$ and $\widetilde{(\cdot)}$ denote Reynolds and Favre averages while $(\cdot)'$ and $(\cdot)''$ denote their respective fluctuating parts.

Size	$n_X \times n_Y \times n_z$	ΔX^+	ΔY^+	ΔZ^+
$[2\pi\delta, 2\delta, \pi\delta]$	$200 \times 179 \times 200$	12.4 (8.88)	$[0.75 - 7.0]$ ($[0.54 - 5]$)	6.2 (4.44)

Table A.1: Size, mesh and spatial resolution (in parentheses for the case with isothermal walls) of the channel flow used for validation.

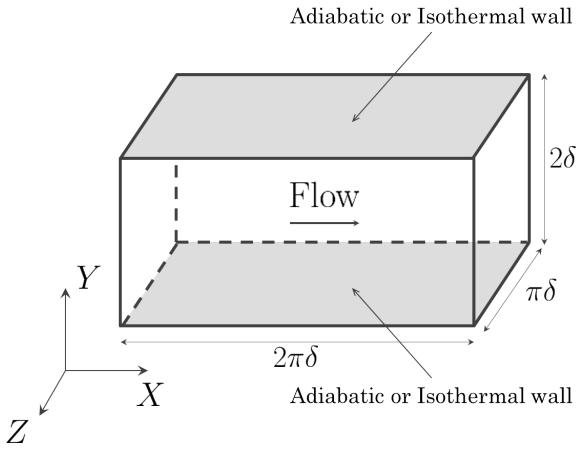

Figure A.1: Computational domain: the bi-periodic channel flow.

Re_τ	M	T_b (K)
395	0.16	304.5

Table A.2: Regime conditions of the adiabatic equilibrium channel flow: Re_τ is the friction Reynolds number, M the average Mach number and T_b the bulk temperature.

A.1 Adiabatic bi-periodic channel flow

The regime conditions of the flow are those specified in Table 3.1, which are also reported in Table A.2. Since the channel flow is periodic in the streamwise direction, a source term S_{QdM} is needed in the momentum equation in the streamwise direction in order to attain (and maintain) the specified friction Reynolds number. An energy source term S_{ener} is also applied to the energy equation, in order to prevent the flow from progressively heating up because of viscous effects and of the influence of S_{QdM}. The two source terms dynamically control the bulk Reynolds number Re_b and the bulk enthalpy h_b of the channel flow acting like a PI controller as described in Zhang and Vicquelin (2016) (also see Appendix B). The new set of equations is then the following:

$$\frac{\partial \rho}{\partial t} + \frac{\partial \rho u_i}{\partial x_i} = 0 \ , \tag{A.1.1}$$

$$\frac{\partial \rho u_i}{\partial t} + \frac{\partial \rho u_i u_j}{\partial x_j} = -\frac{\partial p}{\partial x_i} + \frac{\partial \boldsymbol{\tau}_{ij}}{\partial x_j} + S_{QdM}\delta_{1i} \ , \tag{A.1.2}$$

$$\frac{\partial \rho h}{\partial t} + \frac{\partial \rho u_j h}{\partial x_j} = \frac{\mathrm{D}p}{\mathrm{D}t} - \frac{\partial q_j^{cd}}{\partial x_j} + \boldsymbol{\tau}_{ij}\frac{\partial u_i}{\partial x_j} + u_i S_{QdM}\delta_{1i} + S_{ener} \ . \tag{A.1.3}$$

For the two source terms one only has to specify the target value for the bulk Reynolds number and bulk enthalpy as well as the temporal constant of the PI controller, after

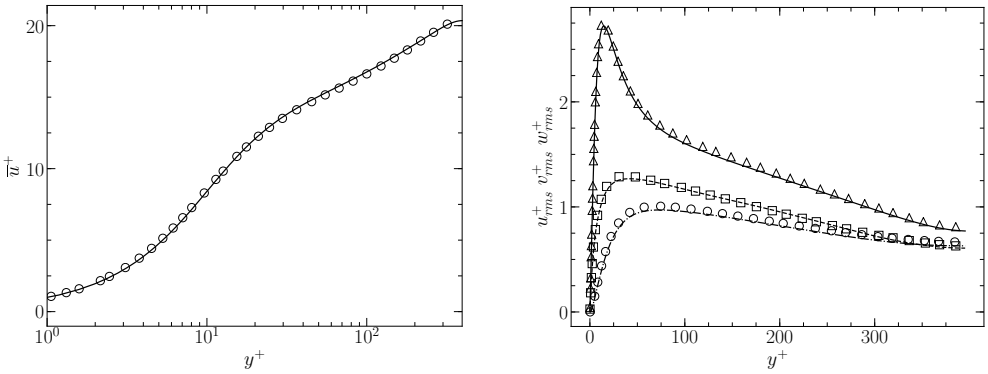

Figure A.2: Mean profile of streamwise velocity (a): —— present results; ○ results from Kawamura et al. (1999). Profiles of r.m.s. streamwise, wall-normal and spanwise velocity respectively (b): ——, – · – · – and - - - - present results; △, ○ and □ results from Kawamura et al. (1999).

T_w (K)	B_q^{eq}	Nu^{eq}	Re_τ^{eq}	$\left(\frac{T_w}{T_c}\right)^{eq}$
400	0.018	26.6	292	1.38

Table A.3: Regime conditions of isothermal equilibrium channel flow.

which the two time-dependent source terms adapt automatically until the targets are reached.

Figure A.2 shows the mean streamwise velocity profile $\overline{u}^+$ and the three root-mean-square (r.m.s.) velocity profiles non-dimensionalised with respect to the friction velocity u_τ as a function of the wall distance expressed in wall units $y^+ = yu_\tau/\nu_w$, where ν_w is the kinematic viscosity at the wall. Results are compared to those by Kawamura et al. (1999) and a very good agreement is obtained for all the profiles.

A.2 Isothermal bi-periodic channel flow

The regime conditions are those specified in Table 3.3, which are also reported in Table A.3. Also in this case, two source terms are added to the Navier-Stokes equations in order to attain the regime specified.

Figure A.3 shows the mean streamwise velocity and the three r.m.s. velocity profiles compared to those by Kawamura et al. (1999) obtained for an incompressible flow and the temperature treated as a passive scalar. In this case, two different wall scalings are used. The first, denoted as $(\cdot)^+$, is the classic wall scaling adopted in §A.1; the second, denoted as $(\cdot)^*$ is the semi-local scaling. Figures A.3a and A.3b show how semi-local scaling allows us to take into account fluid property variations in the wall-normal direction, and make velocity profiles collapse to those with constant

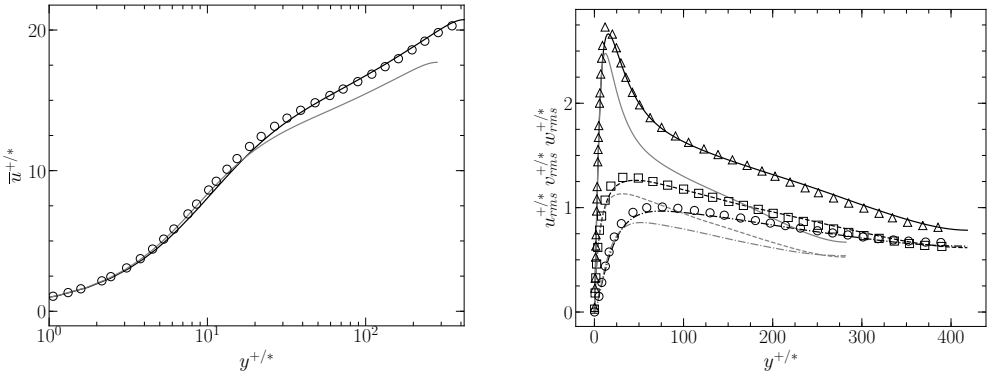

(a) (b)

Figure A.3: Mean profile of streamwise velocity (a): —— present results in classic (gray) and semi-local (black) scaling; ○ results from Kawamura et al. (1999). Profiles of r.m.s. streamwise, wall-normal and spanwise velocity respectively (b): — —, – · – · – and - - - - present results in classic (gray) and semi-local (black) scaling; △, ○ and □ results from Kawamura et al. (1999).

properties of Kawamura et al. (1999). Similar results are shown for mean and r.m.s. temperature profiles in Figure A.4. Fluid mean property variations seem to be the only remarkable impact of the heated wall on the flow, as suggested by Morkovin (1962) and seen in several studies concerning compressible flows (*e.g.*, Huang and Coleman, 1994; Huang et al., 1995; Nicoud, 1999). This is supported by results shown in Figure A.5, where the mean wall-normal velocity, normalised with respect to the mean streamwise velocity and the friction velocity is plotted. Indeed, if the continuity equation and the absence of streamwise gradients guarantee that the Favre-averaged normal velocity $\widetilde{v}$ is zero, mean density variations do generate ejection events in the boundary layer. Nevertheless, the mean normal velocity is at most of the order of 1% and 1‰ with respect to the friction velocity and the mean streamwise velocity, respectively.

Figure A.6 shows the total shear stress as well as the total heat flux

$$q^{tot} = -\overline{\lambda \frac{\partial T}{\partial y}} + \overline{\rho} \widetilde{v'' h''} - \int_0^y \overline{\boldsymbol{\tau} : \nabla \mathbf{v}} dy \ .$$

In both cases the linear profile demonstrates that the computing time is long enough to obtain time steady statistics. Notice that the viscous heating contribution is not strictly zero even if small due to the low Mach number of the simulated flow.

Finally, Figure A.7 shows turbulent budgets for $\widetilde{h''^2}$ and wall-normal heat flux $-\overline{\rho} \widetilde{v'' h''}$ (normalised with respect to $\overline{q_w}^2/\mu_w$ and $\overline{q_w}.\overline{\tau_w}/\mu_w$ respectively) compared to those of Kawamura et al. (1999). A good agreement is obtained although not as precise as in previous figures. The slight differences can be attributed to small compressibility effects in the present case and variable properties effects that the semi-local scaling most likely does not correct in these budgets. Finally, remaining numerical errors in both computations is another possible source of disagreement.

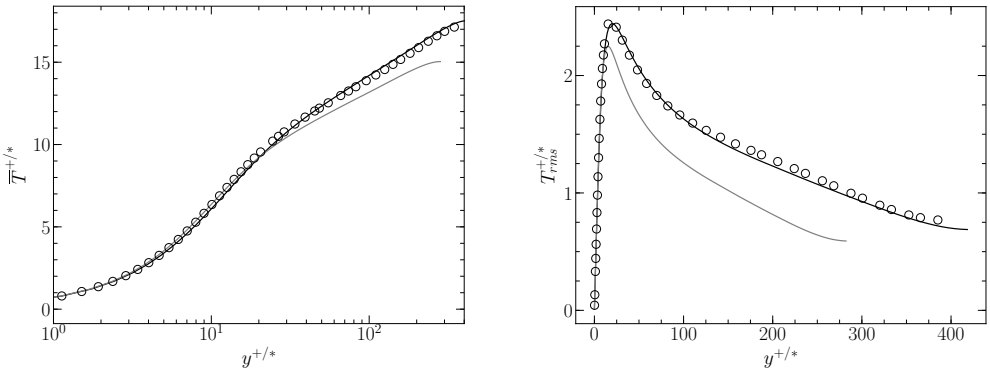

Figure A.4: Profiles of mean (a) and r.m.s. (b) temperature: —— present results in classic (gray) and semi-local (black) scaling; ○ results from Kawamura et al. (1999).

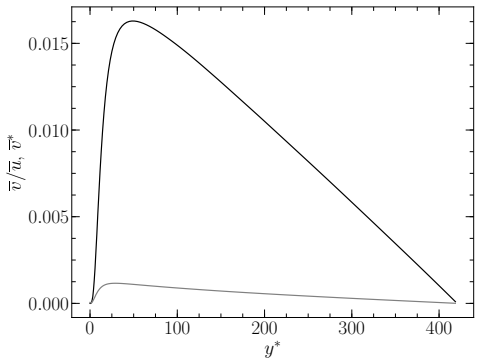

Figure A.5: Wall-normal velocity normalised with respect to the friction velocity $\overline{v}^*$ (black line) and mean streamwise velocity $\overline{v}/\overline{u}$ (gray line).

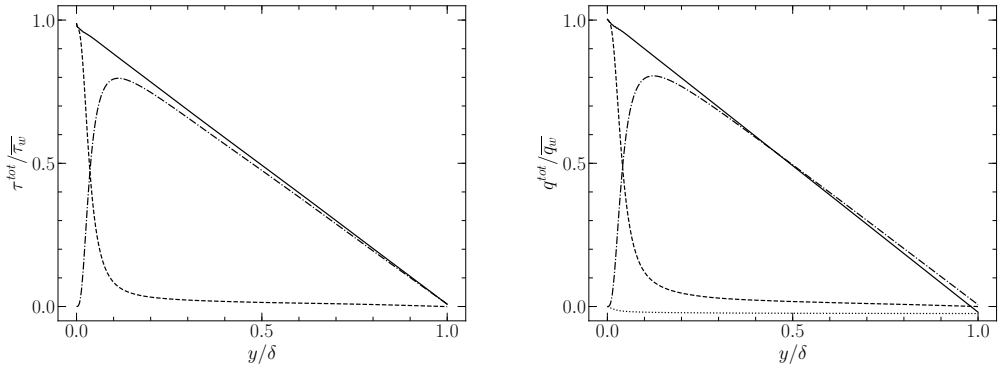

Figure A.6: Profiles of shear stress scaled by the wall shear stress (a): —— total shear stress τ^{tot} ; - - - - viscous term $\overline{\tau_{12}} = \overline{\mu \frac{\partial u}{\partial y}}$; – · – · – turbulent term $-\overline{\rho}\widetilde{u''v''}$. Heat fluxes scaled by the wall heat flux (b): —— total heat flux q^{tot}; - - - - conductive term $\overline{q}_y^{cd} = -\overline{\lambda \frac{\partial T}{\partial y}}$; – · – · – turbulent term $\overline{\rho}\widetilde{v''h''}$; ····· viscous heating term $-\int_0^y \overline{\boldsymbol{\tau} : \nabla \mathbf{v}} dy$.

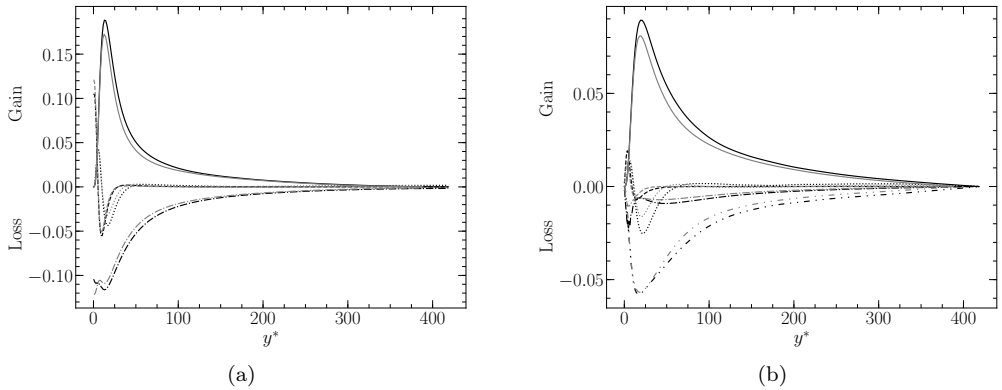

Figure A.7: Budgets of enthalpy variance (a) and wall-normal turbulent heat flux (b), present results (black) and Kawamura et al. (1999) (gray) : —— production ; – · – · – molecular dissipation; - - - - molecular diffusion; ····· turbulent diffusion; – · · – enthalpy-pressure-gradient correlation.

Appendix B

Controlling bulk pressure in channel flow simulations

In bi-periodic channel flow simulations, the user might need to control certain key quantities with extreme accuracy. We refer, in particular, to the bulk Reynolds number, according to which the grid is designed, and to the bulk enthalpy. As discussed in Chapter 1 (see, in particular, §1.1.3), these quantities are usually controlled with two source terms. The former, added to the momentum equation, prevents the flow from progressively slowing down under the effect of the wall friction; the latter, if both channel walls are at the same temperature (like in the configuration studied in Part II), allows for a specific temperature gradient to be preserved in the wall-normal direction.

The value that these source terms should take for a specific regime, in the most classic channel flow configurations, are usually easy to determine. Let us consider, for instance, an adiabatic channel flow at a given Re_τ. Knowing the temperature of the flow and the size of the channel δ, on can easily deduce the mean wall-shear stress τ_w, which gives access to the momentum source term to be added:

$$S_{QdM} = \frac{\tau_w}{\delta} \ . \tag{B.0.1}$$

However, even in slightly more complicated flows, characterised, for instance, by a temperature gradient, S_{QdM} and S_{ener} are more arduous to compute and, in some cases, actually not known *a priori*. This has motivated the work by Zhang and Vicquelin (2016), who introduced dynamic momentum and energy source terms which control the bulk Reynolds number and enthalpy in the channel flow. In this work, we have used these source terms in all our DNS or WMLES bi-periodic channel flow simulations.

Yet, there is one additional source term that we have employed, and that has not been introduced in Zhang and Vicquelin (2016). It is an analogous dynamic mass source term, which allows us to control the bulk pressure of the flow which, in the most general case, is perturbed by S_{QdM} and S_{ener} during the transient regime. The objective of this appendix, is to illustrate how the dynamic mass source term is computed during the simulation, and to show how its influence should be included in the momentum and energy equations. For the other two source terms, the reader is referred to Zhang and Vicquelin (2016). In §B.1, the mathematical details are given.

In §B.2, a test case is performed, allowing us to validate the implementation in the AVBP code.

B.1 Mathematical details

In the following, we consider a bi-periodic channel flow like the one introduced in §1.4. The equation expressing mass conservation writes:

$$\frac{\partial \rho}{\partial t} + \frac{\partial \rho u_i}{\partial x_i} = S_\rho(t) \ , \tag{B.1.1}$$

where S_ρ is the aforementioned mass source term, which, being dynamic, depends on time. On the other hand, S_ρ is supposed to be constant in space. Integrating Eq. (B.1.1) over the whole volume of the channel yields:

$$\int_{\mathcal{V}} \frac{\partial \rho}{\partial t} \mathrm{d}V + \int_{\mathcal{V}} \frac{\partial \rho u_i}{\partial x_i} \mathrm{d}V = \int_{\mathcal{V}} S_\rho(t) \mathrm{d}V \ . \tag{B.1.2}$$

Now, since S_ρ is uniform in space, and since the divergence of $\rho \mathbf{v}$ is zero due to the periodic boundary conditions, Eq. (B.1.2) becomes:

$$\int_{\mathcal{V}} \frac{\partial \rho}{\partial t} \mathrm{d}V = S_\rho(t) V \ , \tag{B.1.3}$$

or, as well,

$$\frac{\mathrm{d}}{\mathrm{d}t} \int_{\mathcal{V}} \rho \mathrm{d}V = S_\rho(t) V \ . \tag{B.1.4}$$

Defining the bulk density ρ_b as the volumetric average of the mass density of the flow, Eq. (B.1.4) can be rewritten as:

$$\frac{\mathrm{d}\rho_b}{\mathrm{d}t} = S_\rho(t) \ . \tag{B.1.5}$$

Equation (B.1.5) expresses the fact that the only effect of the mass source term is that of controlling the bulk mass density of the flow. If $S_{ener} = 0$, then the bulk density (and, therefore, the mass) is constant in time. Thus, under the effect of the energy source term S_{ener}, which controls the bulk enthalpy and makes the temperature of the flow evolve, the bulk pressure would also vary to respect the ideal gas law. We can also deduce that, once the flow has attained the desired bulk enthalpy, the dynamically controlled mass source term must be zero. In other words, regardless of the controlling strategy implemented, we must retrieve:

$$\lim_{t \to \infty} S_\rho(t) = 0 \ . \tag{B.1.6}$$

The bulk density is linked to the bulk pressure and temperature through the ideal gas relation:

$$\rho_b = \frac{p_b}{r T_b} \ , \tag{B.1.7}$$

where p_b is the bulk pressure, T_b is the bulk temperature and r is the mass-specific gas constant. Therefore, Equation (B.1.5) can be written as:

$$\frac{\mathrm{d}}{\mathrm{d}t} \left(\frac{p_b}{r T_b} \right) = S_\rho(t) \ , \tag{B.1.8}$$

which becomes:

$$\frac{1}{T_b}\frac{\mathrm{d}p_b}{\mathrm{d}t} + p_b\frac{\mathrm{d}}{\mathrm{d}t}\frac{1}{T_b} = rS_\rho(t) \ . \tag{B.1.9}$$

So as to make the time derivative of S_ρ appear, we derive Eq. (B.1.9) with respect to time, which yields:

$$\frac{\mathrm{d}}{\mathrm{d}t}\left[\frac{1}{T_b}\frac{\mathrm{d}p_b}{\mathrm{d}t} + p_b\frac{\mathrm{d}}{\mathrm{d}t}\frac{1}{T_b}\right] = r\frac{\mathrm{d}S_\rho}{\mathrm{d}t} \ . \tag{B.1.10}$$

Developing Eq. (B.1.10), one has:

$$\frac{\mathrm{d}^2p_b}{\mathrm{d}t^2} + 2T_b\frac{\mathrm{d}}{\mathrm{d}t}\left(\frac{1}{T_b}\right)\frac{\mathrm{d}p_b}{\mathrm{d}t} + p_bT_b\frac{\mathrm{d}^2}{\mathrm{d}t^2}\left(\frac{1}{T_b}\right) = rT_b\frac{dS_\rho}{dt} \ . \tag{B.1.11}$$

Now, for a proportional-integral (PI) type of controller, we can impose that the evolution of the time derivative of S_ρ be:

$$\frac{\mathrm{d}S_\rho}{\mathrm{d}t} = a_1(t)\frac{\mathrm{d}p_b}{\mathrm{d}t} + a_2(t) \ , \tag{B.1.12}$$

where the coefficients $a_1(t)$ and $a_2(t)$ are, at this stage, unknown. Inserting Eq. (B.1.11) into Eq. (B.1.12) yields:

$$\frac{\mathrm{d}^2p_b}{\mathrm{d}t^2} + 2T_b\frac{\mathrm{d}}{\mathrm{d}t}\left(\frac{1}{T_b}\right)\frac{\mathrm{d}p_b}{\mathrm{d}t} + p_bT_b\frac{\mathrm{d}^2}{\mathrm{d}t^2}\left(\frac{1}{T_b}\right) = rT_b\left(a_1(t)\frac{\mathrm{d}p_b}{\mathrm{d}t} + a_2(t)\right) \ , \tag{B.1.13}$$

or, as well,

$$\frac{\mathrm{d}^2p_b}{\mathrm{d}t^2} + \left[2T_b\frac{\mathrm{d}}{\mathrm{d}t}\left(\frac{1}{T_b}\right) - rT_ba_1(t)\right]\frac{\mathrm{d}p_b}{\mathrm{d}t} + p_bT_b\frac{\mathrm{d}^2}{\mathrm{d}t^2}\left(\frac{1}{T_b}\right) - rT_ba_2(t) = 0 \ . \tag{B.1.14}$$

As we have said, $a_1(t)$ and $a_2(t)$ are unknown. Therefore, they can be defined to yield a second-order differential equation with constant coefficients for Equation (B.1.14), as follows:

$$\frac{\mathrm{d}^2}{\mathrm{d}t^2}\left(p_b(t) - p_b^t\right) + \alpha\frac{\mathrm{d}}{\mathrm{d}t}\left(p_b(t) - p_b^t\right) + \beta\left(p_b(t) - p_b^t\right) = 0 \ , \tag{B.1.15}$$

where p_b^t is the target bulk pressure prescribed by the user. The coefficients $a_1(t)$ and $a_2(t)$ are thus:

$$\begin{aligned} a_1(t) &= \frac{2}{r}\frac{\mathrm{d}}{\mathrm{d}t}\left(\frac{1}{T_b}\right) - \frac{\alpha}{rT_b} \\ a_2(t) &= \frac{p_b}{r}\frac{\mathrm{d}^2}{\mathrm{d}t^2}\left(\frac{1}{T_b}\right) - \frac{\beta}{rT_b}\left(p_b(t) - p_b^t\right) \ . \end{aligned} \tag{B.1.16}$$

There are still two degrees of freedom, *i.e.*, α and β. Depending on their values, the target will be attained with different regimes. In fact, the dynamic of the controller is determined by only one parameter, *i.e.*, the discriminant $\Delta = \alpha^2 - 4\beta$, which gives the maximal convergence rate towards the specified target when $\Delta = 0$, *i.e.*, when $\alpha = 2\beta^{1/2}$. Therefore, we now have only one degree of freedom, which is the time constant $\tau = 2/\alpha$, that we can freely choose.

Inserting τ into Eq. (B.1.16) and, successively, $a_1(t)$ and $a_2(t)$ into Eq. (B.1.12), yields the final form for the time derivative of the mass source term:

$$\frac{\mathrm{d}S_\rho}{\mathrm{d}t} = \left[\frac{2}{r}\frac{\mathrm{d}}{\mathrm{d}t}\left(\frac{1}{T_b}\right) - \frac{2}{r\tau T_b}\right]\frac{\mathrm{d}p_b}{\mathrm{d}t} + \frac{p_b}{r}\frac{\mathrm{d}^2}{\mathrm{d}t^2}\left(\frac{1}{T_b}\right) - \frac{(p_b(t) - p_b^t)}{rT_b\tau^2} \ , \tag{B.1.17}$$

which allows us to compute, from iteration to iteration, the value of S_ρ at the time instant $k+1$:

$$S_\rho^{k+1} = S_\rho^k + \left(\frac{\mathrm{d}S_\rho^k}{\mathrm{d}t}\right)\left(t^{k+1} - t^k\right) \ . \tag{B.1.18}$$

The presence of S_ρ, of course, also needs to be taken into account by the source terms controlling the bulk Reynolds number Re_b and enthalpy h_b. Since Zhang and Vicquelin (2016) did not consider the control of the bulk pressure, their expressions of S_{QdM} and S_{ener} need to be adapted. Following the same approach described by Zhang and Vicquelin (2016), one obtains for S_{QdM}:

$$\begin{aligned}\frac{\mathrm{d}}{\mathrm{d}t}S_{QdM} \quad = \quad & -\frac{\delta}{\mu_b}\left\{\frac{2}{\tau}\frac{\mathrm{d}\mathrm{Re}_b}{\mathrm{d}t} + \frac{\mathrm{Re}_b(t) - \mathrm{Re}_b^t}{\tau^2} - \frac{\mathrm{d}}{\mathrm{d}t}\left(\frac{\tau_{tot}}{2\mu_b}\right) + S_{QdM}\delta\frac{\mathrm{d}}{\mathrm{d}t}\left(\frac{1}{\mu_b}\right) + \right. \\ & \left. + \frac{\mathrm{d}}{\mathrm{d}t}\left[\frac{S_\rho\overline{u}\delta}{\mu_b}\right] - \frac{\mathrm{d}}{\mathrm{d}t}\left[\frac{\mathrm{Re}_b}{\mu_b}\frac{\mathrm{d}\mu_b}{\mathrm{d}t}\right]\right\} \ ,\end{aligned} \tag{B.1.19}$$

where μ_b is the bulk dynamic viscosity, $\tau_{tot} = 2\tau_w$ is the total stress, and τ is the time constant (which can differ from the one used for S_ρ in Eq. (B.1.17)). For the energy source term S_{ener}, instead, one has:

$$\begin{aligned}\frac{\mathrm{d}}{\mathrm{d}t}S_{ener} \quad = \quad & -\frac{2\rho_b}{\tau}\frac{\mathrm{d}h_b}{\mathrm{d}t} + \rho_b\left\{\frac{h_b^t - h_b(t)}{\tau^2} + \frac{1}{2\delta}\frac{dq_w^{tot}}{\rho_b} - \frac{\mathrm{d}}{\mathrm{d}t}\left(\frac{\overline{\dot{Q}_{tot}}}{\rho_b}\right) - S_{ener}\frac{\mathrm{d}}{\mathrm{d}t}\left(\frac{1}{\rho_b}\right) + \right. \\ & \left. - \frac{\mathrm{d}}{\mathrm{d}t}\left(\frac{S_{QdM}\overline{u}}{\rho_b}\right) - \frac{\mathrm{d}}{\mathrm{d}t}\left[\frac{S_\rho}{\rho_b}\left(\overline{e + \frac{1}{2}v^2}\right)\right] + \frac{\mathrm{d}}{\mathrm{d}t}\left[\frac{h_b}{\rho_b}\left(\frac{\mathrm{d}\rho_b}{\mathrm{d}t}\right)\right]\right\} \ ,\end{aligned} \tag{B.1.20}$$

where $q_w^{tot} = 2q_w$ is the total heat flux, $\dot{Q}$ is an additional energy source term which might be present in the simulation (*e.g.*, radiation), e is the internal energy of the gas, and the operator $\overline{(\cdot)}$ represents a volumetric average.

Finally, the Navier-Stokes equations, once all the three source terms are present, become:

$$\frac{\partial\rho}{\partial t} + \frac{\partial\rho u_i}{\partial x_i} = S_\rho \ , \tag{B.1.21}$$

$$\frac{\partial\rho u_i}{\partial t} + \frac{\partial\rho u_i u_j}{\partial x_j} = -\frac{\partial p}{\partial x_i} + \frac{\partial\boldsymbol{\tau}_{ij}}{\partial x_j} + S_{QdM}\delta_{1i} + S_\rho u_i\delta_{1i} \ , \tag{B.1.22}$$

$$\frac{\partial\rho h}{\partial t} + \frac{\partial\rho u_j h}{\partial x_j} = \frac{\mathrm{D}p}{\mathrm{D}t} - \frac{\partial q_j^{cd}}{\partial x_j} + \boldsymbol{\tau}_{ij}\frac{\partial u_i}{\partial x_j} + S_{QdM}u_1 + S_\rho\left(e + \frac{1}{2}v^2\right) + S_{ener} \ . \tag{B.1.23}$$

B.2 Test case

The three source terms (B.1.17), (B.1.19) and (B.1.20) have been implemented in the AVBP code and used throughout this Ph.D. work for controlling bulk quantities in bi-periodic channel flows. In this section, we present a validation test case.

The computational domain is a bi-periodic channel flow with isothermal walls, *i.e.*, identical to the one described in §A.2. At the beginning of the simulation, *i.e.*, at $t = 0$, the flow is at a generic regime Re_b, h_b and p_b, while the three target values Re_b^t, h_b^t and p_b^t are prescribed to the controller.

The objective is to compare the time evolution of the three bulk quantities in the channel flow with the theoretical response of a PI controller. It can be shown that if $\Delta = 0$, where, recall, Δ is the discriminant, then the evolution of a variable x towards the target x^t is the following:

$$x(t) = x^t + \left[\left(x|_{t=0} - x^t \right) \left(1 + \frac{t}{\tau} \right) + \left(\frac{\mathrm{d}x(t)}{\mathrm{d}t}|_{t=0} \right) t \right] e^{-\frac{t}{\tau}} \tag{B.2.1}$$

Figure B.1 shows the evolution of p_b, Re_b and h_b towards the target values, compared to the theoretical response given by Eq. (B.2.1). As can be seen, all the bulk quantities converge towards the target after $t/\tau \approx 10$. Concerning the bulk pressure, $p_b(t) = p_b^t$ at $t = 0$. However, the presence of the other source terms and, in particular, the temperature variation the flow is subjected to, perturb the bulk pressure, and active control through S_ρ is needed to retrieve the target value. Good agreement is obtained with the theoretical response. Concerning the bulk Reynolds number, excellent agreement is obtained, while the transient phase of the bulk enthalpy has a more puzzling behaviour, with a slight overshoot at $t \approx \tau$. However, the target h_b^t is extremely close to the initial solution $h_b(t)$, and any small inaccuracy on the time derivatives of Eq. B.1.20 at $t = 0$ becomes visible. The target h_b^t is in any case reached, allowing us to validate our implementation in the AVBP code.

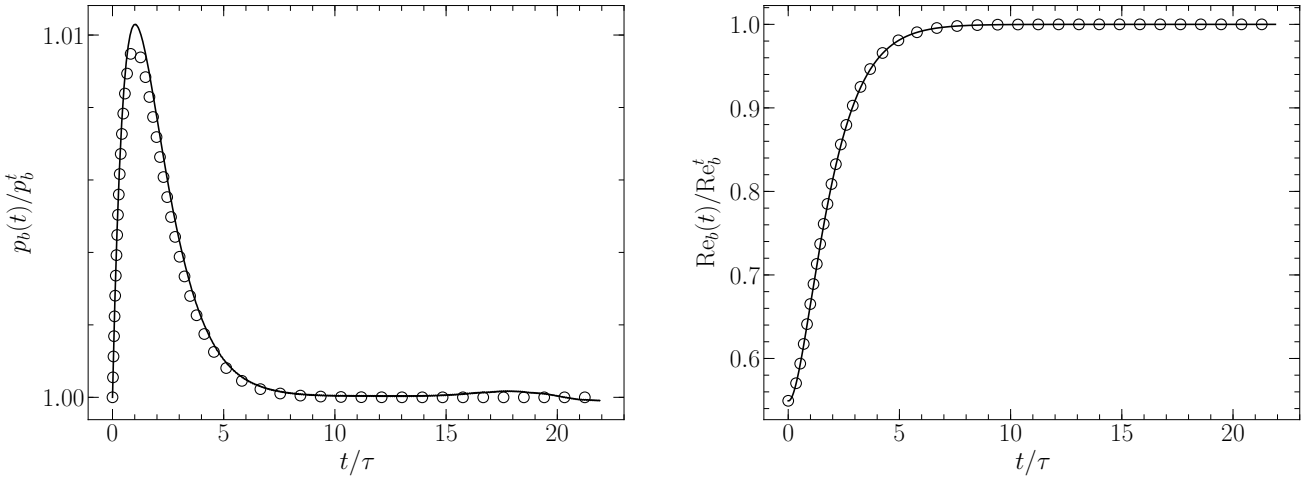

(a)

(b)

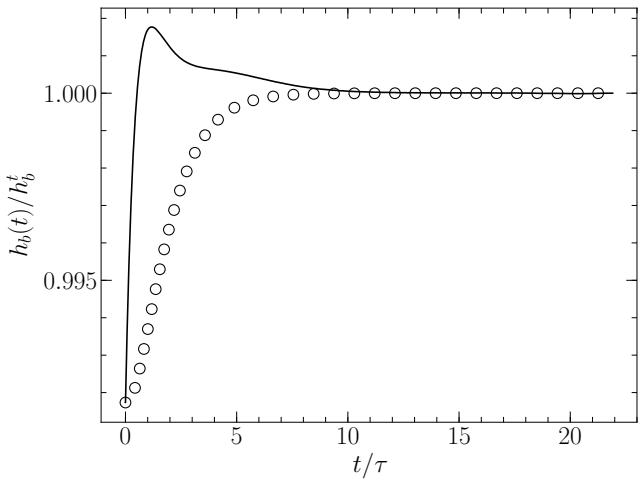

(c)

Figure B.1: Evolution of p_b (a), Re_b (b) and h_b (c) towards the target values (solid lines), compared to the theoretical response (circles).

Appendix C

Derivation of averaged momentum and energy balances

C.1 Averaged momentum equation

The momentum equation (3.2.2), projected along the streamwise direction, is the following:

$$\frac{\partial \rho u}{\partial t} + \frac{\partial \rho u u_j}{\partial x_j} = -\frac{\partial p}{\partial x} + \frac{\partial \boldsymbol{\tau}_{xj}}{\partial x_j} \ . \tag{C.1.1}$$

After averaging in time and along the spanwise direction, which is homogeneous for the study configuration of Chapter 3, one has:

$$\frac{\partial}{\partial x}\left(\overline{\rho}\widetilde{u}\widetilde{u}\right) + \frac{\partial}{\partial y}\left(\overline{\rho}\widetilde{u}\widetilde{v}\right) = -\frac{\partial \overline{p}}{\partial x} + \frac{\partial \overline{\boldsymbol{\tau}_{xx}}}{\partial x} + \frac{\partial \overline{\boldsymbol{\tau}_{xy}}}{\partial y} - \frac{\partial}{\partial x}\left(\widetilde{\overline{\rho}u''u''}\right) - \frac{\partial}{\partial y}\left(\widetilde{\overline{\rho}u''v''}\right) \ , \tag{C.1.2}$$

where the non-steady term as well as all the derivatives along the Z axis are zero. In a similar manner, the time-averaged continuity equation (3.2.1) gives :

$$\frac{\partial \overline{\rho}\widetilde{u}}{\partial x} + \frac{\partial \overline{\rho}\widetilde{v}}{\partial y} = 0 \ , \tag{C.1.3}$$

allowing us to rewrite Equation (C.1.2) in the following manner:

$$\overline{\rho}\widetilde{u}\frac{\partial \widetilde{u}}{\partial x} + \overline{\rho}\widetilde{v}\frac{\partial \widetilde{u}}{\partial y} = -\frac{\partial \overline{p}}{\partial x} + \frac{\partial \overline{\boldsymbol{\tau}_{xx}}}{\partial x} + \frac{\partial \overline{\boldsymbol{\tau}_{xy}}}{\partial y} - \frac{\partial}{\partial x}\left(\widetilde{\overline{\rho}u''u''}\right) - \frac{\partial}{\partial y}\left(\widetilde{\overline{\rho}u''v''}\right) \ . \tag{C.1.4}$$

Equation (C.1.4) can now be integrated over the wall-normal direction in order to obtain the momentum fluxes, which yields:

$$C = \int_0^y \left[-\overline{\rho}\widetilde{u}\frac{\partial \widetilde{u}}{\partial x} - \overline{\rho}\widetilde{v}\frac{\partial \widetilde{u}}{\partial y} - \frac{\partial \overline{p}}{\partial x} + \frac{\partial \overline{\boldsymbol{\tau}_{xx}}}{\partial x} + \frac{\partial \overline{\boldsymbol{\tau}_{xy}}}{\partial y} - \frac{\partial}{\partial x}\left(\widetilde{\overline{\rho}u''u''}\right) - \frac{\partial}{\partial y}\left(\widetilde{\overline{\rho}u''v''}\right) \right] dy \ , \tag{C.1.5}$$

where the constant C is simply the right-hand side of Eq. (C.1.5) evaluated at $y = 0$, i.e. $C = \overline{\tau_{xy}}|_{y=0} = \overline{\tau_w}$. Finally, one has:

$$\begin{aligned}\overline{\tau}_w(x) &= -\underbrace{\int_0^y \left(\overline{\rho}\widetilde{u}\frac{\partial \widetilde{u}}{\partial x}\right) dy}_{I_x} - \underbrace{\int_0^y \left(\overline{\rho}\widetilde{v}\frac{\partial \widetilde{u}}{\partial y}\right) dy}_{I_y} - \underbrace{\int_0^y \left(\frac{\partial \overline{p}}{\partial x}\right) dy}_{II} + \\ &+ \underbrace{\int_0^y \left(\frac{\partial \overline{\boldsymbol{\tau}_{xx}}}{\partial x}\right) dy}_{III_x} + \underbrace{\overline{\boldsymbol{\tau}_{xy}}(y)}_{III_y} + \\ &- \underbrace{\int_0^y \left(\frac{\partial}{\partial x}\left(\overline{\rho}\widetilde{u''u''}\right)\right) dy}_{IV_x} - \underbrace{\overline{\rho}\widetilde{u''v''}(y)}_{IV_y} ,\end{aligned} \tag{C.1.6}$$

where on the right-hand side of the equation there are two mean convective terms (I_x and I_y), the pressure gradient (II), two viscous terms (III_x and III_y) and two terms associated with turbulent transport (IV_x and IV_y).

C.2 Averaged energy equation

The energy equation, as seen in §3.2.1, is the following:

$$\frac{\partial \rho h}{\partial t} + \frac{\partial \rho u_j h}{\partial x_j} = \frac{\mathrm{D}p}{\mathrm{D}t} - \frac{\partial q_j^{cd}}{\partial x_j} + \boldsymbol{\tau}_{ij}\frac{\partial u_i}{\partial x_j} + S_{ener} \ . \tag{C.2.1}$$

After averaging in time and along the spanwise direction, one has:

$$\begin{aligned}\frac{\partial \overline{\rho}\widetilde{u}\widetilde{h}}{\partial x} + \frac{\partial \overline{\rho}\widetilde{v}\widetilde{h}}{\partial y} &= \frac{\mathrm{D}\overline{p}}{\mathrm{D}t} - \frac{\partial \overline{q_x^{cd}}}{\partial x} - \frac{\partial \overline{q_y^{cd}}}{\partial y} + \overline{\boldsymbol{\tau} : \nabla \mathbf{v}} + \\ &- \frac{\partial}{\partial x}\left(\overline{\rho}\widetilde{u''h''}\right) - \frac{\partial}{\partial y}\left(\overline{\rho}\widetilde{v''h''}\right) + S_{ener} \ ,\end{aligned} \tag{C.2.2}$$

where the non-steady term as well as all the derivatives along the Z axis are zero, $\mathbf{v}$ is the velocity vector and no averaging operator is applied to S_{ener} since it is constant in time and space (see §3.2.2). Considering Eq. (C.1.3), one can rewrite Equation (C.2.2) as follows:

$$\begin{aligned}\overline{\rho}\widetilde{u}\frac{\partial \widetilde{h}}{\partial x} + \overline{\rho}\widetilde{v}\frac{\partial \widetilde{h}}{\partial y} &= \frac{\mathrm{D}\overline{p}}{\mathrm{D}t} - \frac{\partial \overline{q_x^{cd}}}{\partial x} - \frac{\partial \overline{q_y^{cd}}}{\partial y} + \overline{\boldsymbol{\tau} : \nabla \mathbf{v}} + \\ &- \frac{\partial}{\partial x}\left(\overline{\rho}\widetilde{u''h''}\right) - \frac{\partial}{\partial y}\left(\overline{\rho}\widetilde{v''h''}\right) + S_{ener} \ .\end{aligned} \tag{C.2.3}$$

Integrating over the wall-normal direction in order to obtain the heat fluxes, one has:

$$\begin{aligned}\overline{q_w}(x) &= \underbrace{\int_0^y \left(\overline{\rho}\widetilde{u}\frac{\partial \widetilde{h}}{\partial x}\right) dy}_{I_x} + \underbrace{\int_0^y \left(\overline{\rho}\widetilde{v}\frac{\partial \widetilde{h}}{\partial y}\right) dy}_{I_y} + \underbrace{\int_0^y \left(\frac{\partial \overline{q_x^{cd}}}{\partial x}\right) dy}_{II_x} + \\ &+ \underbrace{q_y^{cd}}_{II_y} + \underbrace{\int_0^y \left(\frac{\partial}{\partial x}\left(\overline{\rho}\widetilde{u''h''}\right)\right) dy}_{III_x} + \underbrace{\overline{\rho}\widetilde{v''h''}}_{III_y} + \\ &- \underbrace{\int_0^y \left(\frac{\mathrm{D}\overline{p}}{\mathrm{D}t} + \overline{\boldsymbol{\tau} : \nabla \mathbf{v}}\right) dy}_{IV} - \underbrace{yS_{ener}}_{V} \end{aligned} \tag{C.2.4}$$

where the integration constant is simply the mean wall heat flux $\overline{q_w}$, while on the right-hand side of the equation there are two mean convective terms (I_x and I_y), two conductive terms (II_x and II_y), two terms associated with turbulent transport (III_x and III_y), one flux combining the compressibility effects, *i.e.*, the pressure gradient and the viscous heat (IV) and the source term contribution (V).

C.3 Averaged transport equation for the enthalpy variance

The energy balance reads (see Eq. (3.2.3)):

$$\frac{\partial \rho h}{\partial t} + \frac{\partial \rho u_j h}{\partial x_j} = \frac{\mathrm{D}p}{\mathrm{D}t} - \frac{\partial q_j^{cd}}{\partial x_j} + \boldsymbol{\tau}_{ij}\frac{\partial u_i}{\partial x_j} + S_{ener} \ , \tag{C.3.1}$$

which can also be rewritten as:

$$\frac{\partial \rho h}{\partial t} + \frac{\partial \rho u_j h}{\partial x_j} = -\frac{\partial q_j^{cd}}{\partial x_j} + N \ , \tag{C.3.2}$$

where N regroups all those terms (pressure gradient, viscous heat and source term) which play a marginal role in the development of the transport equation. Applying the Reynolds average to Equation (C.3.2), one has:

$$\frac{\partial}{\partial t}\overline{\rho}\widetilde{h} + \frac{\partial}{\partial x_j}\overline{\rho}\widetilde{u}_j\widetilde{h} = -\frac{\partial \overline{q_j^{cd}}}{\partial x_j} - \frac{\partial}{\partial x_j}\overline{\rho}\widetilde{u_j''h''} + \overline{N} \ , \tag{C.3.3}$$

which, multiplied by $\widetilde{h}$, yields:

$$\frac{\partial}{\partial t}\overline{\rho}\frac{\widetilde{h}^2}{2} + \frac{\partial}{\partial x_j}\overline{\rho}\widetilde{u}_j\frac{\widetilde{h}^2}{2} = -\widetilde{h}\frac{\partial \overline{q_j^{cd}}}{\partial x_j} - \widetilde{h}\frac{\partial}{\partial x_j}\overline{\rho}\widetilde{u_j''h''} + \widetilde{h}\overline{N} \ . \tag{C.3.4}$$

On the other hand, multiplying Equation (C.3.2) by h and applying the Reynolds average, one has:

$$\frac{\partial}{\partial t}\overline{\rho}\widetilde{\frac{h^2}{2}} + \frac{\partial}{\partial x_j}\overline{\rho}\widetilde{\frac{u_j h^2}{2}} = -\overline{h\frac{\partial q_j^{cd}}{\partial x_j}} + \overline{hN} \ , \tag{C.3.5}$$

allowing us to obtain the transport equation for $\widetilde{h''^2} = \widetilde{h^2} - \widetilde{h}^2$ by simply subtracting Eq. (C.3.4) from Eq. (C.3.5):

$$\begin{aligned}\frac{\partial}{\partial t}\overline{\rho}\frac{\widetilde{h''^2}}{2} + \frac{\partial}{\partial x_j}\left[\overline{\rho}\frac{\widetilde{u_j h^2}}{2} - \overline{\rho}\widetilde{u_j}\frac{\widetilde{h}^2}{2}\right] &= -\overline{h\frac{\partial q_j^{cd}}{\partial x_j}} + \widetilde{h}\frac{\partial \overline{q_j^{cd}}}{\partial x_j} + \widetilde{h}\frac{\partial}{\partial x_j}\overline{\rho}\widetilde{u_j'' h''} + \\ &\quad + \overline{hN} - \widetilde{h}\overline{N} \ . \end{aligned} \tag{C.3.6}$$

The convective term can be expressed as

$$\frac{\partial}{\partial x_j}\left[\overline{\rho}\frac{\widetilde{u_j h^2}}{2} - \overline{\rho}\widetilde{u_j}\frac{\widetilde{h}^2}{2}\right] = \frac{\partial}{\partial x_j}\overline{\rho}\left[\frac{\widetilde{u_j}\widetilde{h''^2}}{2} + \widetilde{h}\widetilde{u_j'' h''} + \frac{1}{2}\widetilde{u_j'' h'' h''}\right] \ ,$$

allowing us to write:

$$\begin{aligned}\frac{\partial}{\partial t}\overline{\rho}\frac{\widetilde{h''^2}}{2} + \frac{\partial}{\partial x_j}\overline{\rho}\frac{\widetilde{u_j}\widetilde{h''^2}}{2} &= \underbrace{-\overline{h\frac{\partial q_j^{cd}}{\partial x_j}} + \widetilde{h}\frac{\partial \overline{q_j^{cd}}}{\partial x_j}}_{I} + \underbrace{\overline{hN} - \widetilde{h}\overline{N}}_{II} + \\ &\quad + \underbrace{\widetilde{h}\frac{\partial}{\partial x_j}\overline{\rho}\widetilde{u_j'' h''} - \frac{\partial}{\partial x_j}\overline{\rho}\widetilde{h u_j'' h''}}_{III} + \\ &\quad - \frac{1}{2}\frac{\partial}{\partial x_j}\overline{\rho}\widetilde{u_j'' h'' h''} \ , \end{aligned} \tag{C.3.7}$$

where the term I can be simplified as:

$$\begin{aligned}-\overline{h\frac{\partial q_j^{cd}}{\partial x_j}} + \widetilde{h}\frac{\partial \overline{q_j^{cd}}}{\partial x_j} &= -\overline{\left(\widetilde{h} + h''\right)\frac{\partial q_j^{cd}}{\partial x_j}} + \widetilde{h}\frac{\partial \overline{q_j^{cd}}}{\partial x_j} \\ &= -\overline{h''\frac{\partial q_j^{cd}}{\partial x_j}} \\ &= -\overline{h''}\frac{\partial \overline{q_j^{cd}}}{\partial x_j} - \overline{h''\frac{\partial q_j^{cd'}}{\partial x_j}} \ , \end{aligned} \tag{C.3.8}$$

or, considering that for any physical quantities ϕ and ψ one has $\overline{\phi'\psi''} = \overline{\phi'\psi'}$ as well as $\widetilde{\phi'\psi''} = \widetilde{\phi''\psi''}$:

$$\begin{aligned}&-\overline{h''}\frac{\partial \overline{q_j^{cd}}}{\partial x_j} - \overline{h''\frac{\partial q_j^{cd'}}{\partial x_j}} \\ &\qquad = -\overline{h''}\frac{\partial \overline{q_j^{cd}}}{\partial x_j} - \overline{h'\frac{\partial q_j^{cd'}}{\partial x_j}} \\ &\qquad = -\overline{h''}\frac{\partial \overline{q_j^{cd}}}{\partial x_j} - \frac{\partial}{\partial x_j}\overline{q_j^{cd'}h'} + \overline{q_j^{cd'}\frac{\partial h'}{\partial x_j}} \ . \end{aligned} \tag{C.3.9}$$

Term II of Eq. (C.3.7) can be simplified, in a similar manner, as:

$$\overline{hN} - \widetilde{h}\overline{N} = \overline{h''}.\overline{N} + \overline{h'N'} \ , \tag{C.3.10}$$

and term III as:

$$\widetilde{h}\frac{\partial}{\partial x_j}\overline{\rho}\widetilde{u_j''h''} - \frac{\partial}{\partial x_j}\overline{\rho}\widetilde{h}\widetilde{u_j''h''} = -\overline{\rho}\widetilde{u_j''h''}\frac{\partial\widetilde{h}}{\partial x_j} \ . \tag{C.3.11}$$

Replacing expressions (C.3.9), (C.3.10) and (C.3.11) into Equation (C.3.7), one obtains:

$$\begin{aligned}\frac{\partial}{\partial t}\overline{\rho}\frac{\widetilde{h''^2}}{2} + \frac{\partial}{\partial x_j}\overline{\rho}\frac{\widetilde{u}_j\widetilde{h''^2}}{2} \quad = \quad & -\frac{\partial}{\partial x_j}\overline{q_j^{cd'}h'} + \overline{q_j^{cd'}\frac{\partial h'}{\partial x_j}} + \overline{h'N'} - \overline{\rho}\widetilde{u_j''h''}\frac{\partial\widetilde{h}}{\partial x_j} + \\ & -\frac{1}{2}\frac{\partial}{\partial x_j}\overline{\rho}\widetilde{u_j''h''h''} + \overline{h''}\left(-\frac{\partial\overline{q_j^{cd}}}{\partial x_j} + \overline{N}\right) \ , \end{aligned} \tag{C.3.12}$$

where $\overline{h''}$ can also be written as $-\overline{\rho'h'}/\overline{\rho}$. The unsteady term as well as all derivatives of mean quantities in the spanwise direction are zero, which leads to the final expression of the mean transport equation for the enthalpy variance:

$$\begin{aligned} 0 \quad = \quad & \underbrace{-\frac{\partial}{\partial x}\left(\overline{\rho}\widetilde{u}\frac{\widetilde{h''^2}}{2}\right)}_{I_x}\underbrace{-\frac{\partial}{\partial y}\left(\overline{\rho}\widetilde{v}\frac{\widetilde{h''^2}}{2}\right)}_{I_y}\underbrace{-\frac{\partial}{\partial x}\left(\overline{q_x^{cd'}h'}\right)}_{II_x}\underbrace{-\frac{\partial}{\partial y}\left(\overline{q_y^{cd'}h'}\right)}_{II_y} + \\ & \underbrace{+\overline{q_x^{cd'}\frac{\partial h'}{\partial x}} + \overline{q_y^{cd'}\frac{\partial h'}{\partial y}} + \overline{q_z^{cd'}\frac{\partial h'}{\partial z}}}_{III} + \underbrace{\overline{h'N'}}_{IV}\underbrace{-\overline{\rho}\widetilde{u''h''}\frac{\partial\widetilde{h}}{\partial x}}_{V_x} + \\ & \underbrace{-\overline{\rho}\widetilde{v''h''}\frac{\partial\widetilde{h}}{\partial y}}_{V_y}\underbrace{-\frac{1}{2}\frac{\partial}{\partial x}\left(\overline{\rho}\widetilde{u''h''h''}\right)}_{VI_x}\underbrace{-\frac{1}{2}\frac{\partial}{\partial y}\left(\overline{\rho}\widetilde{v''h''h''}\right)}_{VI_y} + \\ & \underbrace{+\overline{h''}\left(-\frac{\partial\overline{q_x^{cd}}}{\partial x} - \frac{\partial\overline{q_y^{cd}}}{\partial y} + \overline{N}\right)}_{VII} \ , \end{aligned} \tag{C.3.13}$$

composed of the streamwise and wall-normal mean convective terms (I_x and I_y) and molecular diffusion (II_x and II_y), molecular dissipation (III), a term of correlation between the enthalpy and N (IV), where, recall, $N = \frac{\mathrm{D}p}{\mathrm{D}t} + \boldsymbol{\tau}_{ij}\frac{\partial u_i}{\partial x_j} + S_{ener}$ regroups the compressibility effects and the source term, the streamwise and wall-normal production (V_x and V_y) and turbulent diffusion terms (VI_x and VI_y), and, finally, a term related to the enthalpy-density correlation (VII).

C.4 Averaged transport equation for the wall-normal turbulent heat flux

In order to obtain the transport equation for $\widetilde{v''h''}$, both the energy equation (3.2.1) and the momentum equation (3.2.2) projected along the wall-normal direction are needed. The latter reads:

$$\frac{\partial\rho v}{\partial t} + \frac{\partial\rho v u_j}{\partial x_j} = -\frac{\partial p}{\partial y} + \frac{\partial\boldsymbol{\tau}_{2j}}{\partial x_j} \ , \tag{C.4.1}$$

which, once the Reynolds average is applied, gives:

$$\frac{\partial}{\partial t}\overline{\rho}\widetilde{v} + \frac{\partial}{\partial x_j}\overline{\rho}\widetilde{v}\widetilde{u_j} = -\frac{\partial \overline{p}}{\partial y} + \frac{\partial \overline{\boldsymbol{\tau}_{2j}}}{\partial x_j} - \frac{\partial}{\partial x_j}\overline{\rho}\widetilde{u_j''v''} \ . \tag{C.4.2}$$

Now, by multiplying (C.4.2) by $\widetilde{h}$, and the averaged energy equation (C.3.3) by $\widetilde{v}$ and summing them, one has:

$$\begin{aligned}\frac{\partial}{\partial t}\overline{\rho}\widetilde{v}\widetilde{h} + \frac{\partial}{\partial x_j}\overline{\rho}\widetilde{u_j}\widetilde{v}\widetilde{h} \ &= \ -\widetilde{h}\frac{\partial \overline{p}}{\partial y} + \widetilde{h}\frac{\partial \overline{\boldsymbol{\tau}_{2j}}}{\partial x_j} - \widetilde{v}\frac{\partial \overline{q_j^{cd}}}{\partial x_j} + \widetilde{v}\overline{N} + \\ &\quad -\widetilde{h}\frac{\partial}{\partial x_j}\overline{\rho}\widetilde{u_j''v''} - \widetilde{v}\frac{\partial}{\partial x_j}\overline{\rho}\widetilde{u_j''h''} \ ,\end{aligned} \tag{C.4.3}$$

which is a transport equation for $\widetilde{v}\widetilde{h}$. A similar equation for $\widetilde{vh}$ can be obtained by multiplying Eq. (C.4.1) by h, Eq. (C.3.2) by v, and averaging the sum:

$$\frac{\partial}{\partial t}\overline{\rho}\widetilde{vh} + \frac{\partial}{\partial x_j}\overline{\rho}\widetilde{u_j vh} = -\overline{h\frac{\partial p}{\partial y}} + \overline{h\frac{\partial \boldsymbol{\tau}_{2j}}{\partial x_j}} - \overline{v\frac{\partial q_j^{cd}}{\partial x_j}} + \overline{vN} \ , \tag{C.4.4}$$

where the convective term can be rewritten as

$$\frac{\partial}{\partial x_j}\overline{\rho}\widetilde{u_j vh} = \frac{\partial}{\partial x_j}\overline{\rho}\left[\widetilde{u_j}\widetilde{vh} + \widetilde{h}\widetilde{u_j''v''} + \widetilde{v}\widetilde{u_j''h} + \widetilde{u_j''v''h''}\right] \ ,$$

yielding:

$$\begin{aligned}\frac{\partial}{\partial t}\overline{\rho}\widetilde{vh} + \frac{\partial}{\partial x_j}\overline{\rho}u_j\widetilde{vh} \ &= \ -\overline{h\frac{\partial p}{\partial y}} + \overline{h\frac{\partial \boldsymbol{\tau}_{2j}}{\partial x_j}} - \overline{v\frac{\partial q_j^{cd}}{\partial x_j}} + \overline{vN} + \\ &\quad - \ \frac{\partial}{\partial x_j}\overline{\rho}\widetilde{u_j''v''h''} - \frac{\partial}{\partial x_j}\overline{\rho}\widetilde{h}\widetilde{u_j''v''} - \frac{\partial}{\partial x_j}\overline{\rho}\widetilde{v}\widetilde{u_j''h''} \ ,\end{aligned} \tag{C.4.5}$$

Subtracting equation (C.4.3) to equation (C.4.5), one has:

$$\begin{aligned}\frac{\partial}{\partial t}\overline{\rho}\widetilde{v''h''} + \frac{\partial}{\partial x_j}\overline{\rho}\widetilde{u_j}\widetilde{v''h''} \ &= \ -\overline{h\frac{\partial p}{\partial y}} + \widetilde{h}\frac{\partial \overline{p}}{\partial y} + \overline{h\frac{\partial \boldsymbol{\tau}_{2j}}{\partial x_j}} - \widetilde{h}\frac{\partial \overline{\boldsymbol{\tau}_{2j}}}{\partial x_j} - \overline{v\frac{\partial q_j^{cd}}{\partial x_j}} + \widetilde{v}\frac{\partial \overline{q_j^{cd}}}{\partial x_j} + \\ &\quad - \ \frac{\partial}{\partial x_j}\overline{\rho}\widetilde{h}\widetilde{u_j''v''} + \widetilde{h}\frac{\partial}{\partial x_j}\overline{\rho}\widetilde{u_j''v''} - \frac{\partial}{\partial x_j}\overline{\rho}\widetilde{v}\widetilde{u_j''h''} + \widetilde{v}\frac{\partial}{\partial x_j}\overline{\rho}\widetilde{u_j''h''} + \\ &\quad - \ \frac{\partial}{\partial x_j}\overline{\rho}\widetilde{u_j''v''h''} + \overline{vN} - \widetilde{h}\overline{N} \ .\end{aligned} \tag{C.4.6}$$

Now, for every fluid property ϕ and ψ one has:

$$\overline{\phi\frac{\partial \psi}{\partial x_j}} - \widetilde{\phi}\frac{\partial \overline{\psi}}{\partial x_j} = \overline{\phi''}\frac{\partial \overline{\psi}}{\partial x_j} + \overline{\phi'\frac{\partial \psi'}{\partial x_j}} \ , \tag{C.4.7}$$

as well as,

$$\overline{\phi'\frac{\partial \psi'}{\partial x_j}} = \frac{\partial}{\partial x_j}\overline{\phi'\psi'} - \overline{\psi'\frac{\partial \phi'}{\partial x_j}} \tag{C.4.8}$$

and finally:

$$\frac{\partial}{\partial x_j}\overline{\rho}\widetilde{\phi}\widetilde{u_j''\psi''} - \widetilde{\phi}\frac{\partial}{\partial x_j}\overline{\rho}\widetilde{u_j''\psi''} = \overline{\rho}\widetilde{u_j''\psi''}\frac{\partial \widetilde{\phi}}{\partial x_j} \ . \tag{C.4.9}$$

Using expressions (C.4.7), (C.4.8) and (C.4.9), Equation (C.4.6) becomes:

$$\begin{aligned}\frac{\partial}{\partial t}\overline{\rho}\widetilde{v''h''} + \frac{\partial}{\partial x_j}\overline{\rho}\widetilde{u_j}\widetilde{v''h''} &= \frac{\partial}{\partial x_j}\overline{\boldsymbol{\tau}'_{2j}h'} - \frac{\partial}{\partial x_j}\overline{q_j^{cd'}v'} - \overline{\boldsymbol{\tau}'_{2j}\frac{\partial h'}{\partial x_j}} + \overline{q_j^{cd'}\frac{\partial v'}{\partial x_j}} + \\ &\quad -\overline{h'\frac{\partial p'}{\partial y}} + \overline{v'N'} - \overline{\rho}\widetilde{u''_j v''}\frac{\partial \widetilde{h}}{\partial x_j} - \overline{\rho}\widetilde{u''_j h''}\frac{\partial \widetilde{v}}{\partial x_j} + \\ &\quad -\frac{\partial}{\partial x_j}\overline{\rho}\widetilde{u''_j v'' h''} + \overline{h''}\left(-\frac{\partial \overline{p}}{\partial y} + \frac{\partial \overline{\boldsymbol{\tau}_{2j}}}{\partial x_j}\right) + \\ &\quad +\overline{v''}\left(\overline{N} - \frac{\partial \overline{q_j^{cd}}}{\partial x_j}\right), \end{aligned} \tag{C.4.10}$$

where $\overline{v''} = -\overline{\rho' v'}/\overline{\rho}$ and $\overline{h''} = -\overline{\rho' h'}/\overline{\rho}$.

Finally, the unsteady term as well as all derivatives of mean quantities along the spanwise direction are zero, giving the final expression of the averaged transport equation of the wall-normal turbulent heat flux:

$$\begin{aligned} 0 &= \underbrace{-\frac{\partial}{\partial x}\left(\overline{\rho}\widetilde{u}\widetilde{v''h''}\right)}_{I_x} \underbrace{-\frac{\partial}{\partial y}\left(\overline{\rho}\widetilde{v}\widetilde{v''h''}\right)}_{I_y} + \underbrace{\frac{\partial}{\partial x}\left(\overline{\tau'_{2,1}h'} - \overline{q_x^{cd'}u'}\right)}_{II_x} + \underbrace{\frac{\partial}{\partial y}\left(\overline{\tau'_{2,2}h'} - \overline{q_y^{cd'}v'}\right)}_{II_y} + \\ &\quad \underbrace{-\left(\overline{\tau'_{2,1}\frac{\partial h'}{\partial x}} + \overline{\tau'_{2,2}\frac{\partial h'}{\partial y}} + \overline{\tau'_{2,3}\frac{\partial h'}{\partial z}}\right) + \left(\overline{q_x^{cd'}\frac{\partial v'}{\partial x}} + \overline{q_y^{cd'}\frac{\partial v'}{\partial y}} + \overline{q_z^{cd'}\frac{\partial v'}{\partial z}}\right)}_{III} + \\ &\quad \underbrace{-\overline{h'\frac{\partial p'}{\partial y}}}_{IV} + \underbrace{\overline{v'N'}}_{V} \underbrace{-\overline{\rho}\widetilde{u''h''}\frac{\partial \widetilde{v}}{\partial x} - \overline{\rho}\widetilde{u''v''}\frac{\partial \widetilde{h}}{\partial x}}_{VI_x} \underbrace{-\overline{\rho}\widetilde{v''h''}\frac{\partial \widetilde{v}}{\partial y} - \overline{\rho}\widetilde{v''v''}\frac{\partial \widetilde{h}}{\partial y}}_{VI_y} \underbrace{-\frac{\partial}{\partial x}\left(\overline{\rho}\widetilde{u''v''h''}\right)}_{VII_x} + \\ &\quad \underbrace{-\frac{\partial}{\partial y}\left(\overline{\rho}\widetilde{v''v''h''}\right)}_{VII_y} \underbrace{+\overline{h''}\left(-\frac{\partial \overline{p}}{\partial y} + \frac{\partial \overline{\tau_{2,1}}}{\partial x} + \frac{\partial \overline{\tau_{2,2}}}{\partial y}\right) + \overline{v''}\left(\overline{N} - \frac{\partial \overline{q_x^{cd'}}}{\partial x} - \frac{\partial \overline{q_y^{cd'}}}{\partial y}\right)}_{VIII}, \end{aligned} \tag{C.4.11}$$

composed of the mean streamwise and wall-normal convective terms (I_x and I_y) and molecular diffusion (II_x and II_y), the molecular dissipation (III), the enthalpy-pressure-gradient correlation (IV), the correlation between the wall-normal velocity and N (V), the streamwise and wall-normal production (VI_x and VI_y) and turbulent diffusion (VII_x and VII_y), and, finally, two terms related to the enthalpy-density and wall-normal-velocity-density correlations ($VIII$).

References

A hybrid rans-les approach with delayed-des and wall-modelled les capabilities. *International Journal of Heat and Fluid Flow*, 29(6):1638–1649, 2008.

Abe, H., Kawamura, H., and Matsuo, Y. Direct numerical simulation of a fully developed turbulent channel flow with respect to the reynolds number dependence. *Journal of Fluids Engineering*, 123(2):382–393, 2001.

Antel, W. J., Diaz, C. E., Benignos, J. C., et al. Plate-like air-cooled engine surface cooler with fluid channel and varying fin geometry, March 21 2017. US Patent 9,599,410.

Antonia, R., Danh, H., and Prabhu, A. Response of a turbulent boundary layer to a step change in surface heat flux. *Journal of Fluid Mechanics*, 80(1):153–177, 1977.

Bae, H., Lozano-Durán, A., and Moin, P. Investigation of the slip boundary condition in wall-modeled les. *Annual research briefs. Center for Turbulence Research (US)*, 2016:75, 2016.

Baggett, J. S. Some modeling requirements for wall models in large eddy simulation. *Annual Research Briefs*, 1997:265–275, 1997.

Baggett, J. S. On the feasibility of merging les with rans for the near-wall region of attached turbulent flows. *Annual Research Briefs*, pages 267–277, 1998.

Bagwell, T. G., Adrian, R. J., Moser, R. D., and Kim, J. Inproved approximation of wall shear stress boundary conditions for large eddy simulation. *Near-wall turbulent flows*, pages 265–275, 1993.

Bajusz, D., Cornet, A., Friedel, J., and Raimarckers, N. Air-oil heat exchanger placed at the location of the air separator nose of a turbojet, and a turbojet including such an air-oil heat exchanger, July 2 2009. US Patent App. 12/342,206.

Balaras, E., Benocci, C., and Piomelli, U. Two-layer approximate boundary conditions for large-eddy simulations. *AIAA Journal*, 34(6):1111–1119, 1996.

Bellec, M., Toutant, A., and Olalde, G. Large eddy simulations of thermal boundary layer developments in a turbulent channel flow under asymmetrical heating. *Computers & Fluids*, 151:159–176, 2017.

Benarafa, Y., Cioni, O., Ducros, F., and Sagaut, P. Temperature wall modelling for large-eddy simulation in a heated turbulent plane channel flow. *International journal of heat and mass transfer*, 50(21-22):4360–4370, 2007.

Biles, D., Ebadi, A., Allard, M. P., and White, C. M. The design and validation of a thermal boundary layer wall plate. *Journal of Fluids Engineering*, 141(12), 2019.

Blom, J. Experimental determination of the turbulent prandtl number in a developing temperature boundary layer. 4th int. In *Heat Transfer Conf., Paris—Versailles*, volume 2, 1970.

Bocquet, S., Sagaut, P., and Jouhaud, J. A compressible wall model for large-eddy simulation with application to prediction of aerothermal quantities. *Physics of Fluids*, 24(6):065103, 2012.

Bose, S. T. and Moin, P. A dynamic slip boundary condition for wall-modeled large-eddy simulation. *Physics of Fluids*, 26(1):015104, 2014.

Bose, S. T. and Park, G. I. Wall-modeled large-eddy simulation for complex turbulent flows. *Annual review of fluid mechanics*, 50:535–561, 2018.

Bou-Zeid, E., Meneveau, C., and Parlange, M. B. Large-eddy simulation of neutral atmospheric boundary layer flow over heterogeneous surfaces: Blending height and effective surface roughness. *Water Resources Research*, 40(2), 2004.

Boussinesq, J. Théorie de l'écoulement tourbillant. *Mem. Acad. Sci.*, 23:46–50, 1877.

Brasseur, J. G. and Wei, T. Designing large-eddy simulation of the turbulent boundary layer to capture law-of-the-wall scaling. *Physics of Fluids*, 22(2):021303, 2010.

Cabot, W. Large-eddy simulations with wall models. *Stanford Center for Turbulence Research Annual Research Briefs*, 20, 1995.

Cabot, W. Near-wall models in large eddy simulations of flow behind a backward-facing step. *Annual Research Briefs*, 1996:199–210, 1996.

Cabot, W. and Moin, P. Approximate wall boundary conditions in the large-eddy simulation of high reynolds number flow. *Flow, Turbulence and Combustion*, 63 (1):269–291, 2000.

Cabrit, O. and Nicoud, F. Direct simulations for wall modeling of multicomponent reacting compressible turbulent flows. *Physics of Fluids*, 21(5):055108, 2009.

Cambier, L. and Gazaix, M. elsa-an efficient object-oriented solution to cfd complexity. In *40th AIAA Aerospace Sciences Meeting & Exhibit*, page 108, 2002.

Cartan, H. *Elementary theory of analytic functions of one or several complex variables*. Courier Corporation, 1995.

Cebeci, T. and Bradshaw, P. *Physical and computational aspects of convective heat transfer*. Springer Science & Business Media, 2012.

Chapman, D. R. Computational aerodynamics development and outlook. *AIAA journal*, 17(12):1293–1313, 1979.

Cheng, W., Pullin, D., and Samtaney, R. Large-eddy simulation of separation and reattachment of a flat plate turbulent boundary layer. *Journal of Fluid Mechanics*, 785:78–108, 2015.

Cho, M., Park, G. I., Lozano-Durán, A., and Moin, P. Wall-modeled large-eddy simulation of non-equilibrium turbulent boundary layers. *arXiv preprint arXiv:2001.01020*, 2020.

Cho, M., Lozano-Durán, A., Moin, P., and Ilhwan Park, G. Wall-modeled large-eddy simulation of turbulent boundary layers with mean-flow three-dimensionality. *AIAA Journal*, pages 1–11, 2021.

Choi, H. and Moin, P. Grid-point requirements for large eddy simulation: Chapman's estimates revisited. *Physics of fluids*, 24(1):011702, 2012.

Chung, D. and Pullin, D. Large-eddy simulation and wall modelling of turbulent channel flow. *Journal of fluid mechanics*, 631:281–309, 2009.

CleanSky2. Clean sky 2. https://www.cleansky.eu/engines, 2021. Accessed: 2021-06-22.

Coleman, G. N., Kim, J., and Moser, R. D. A numerical study of turbulent supersonic isothermal-wall channel flow. *Journal of Fluid Mechanics*, 305:159–183, 1995.

Colin, O. and Rudgyard, M. Development of high-order taylor–galerkin schemes for les. *Journal of Computational Physics*, 162(2):338–371, 2000.

Cummings, R. L. and Lance, G. M. Engine lubricating oil cooling systems for turbojets or the like, March 12 1963. US Patent 3,080,716.

CWIPI. Cwipi: coupling with interpolation parallel interface. http://sites.onera.fr/cwipi, 2020.

Davis, M., Hale, A., and Beale, D. An argument for enhancement of the current inlet distortion ground test practice for aircraft gas turbine engines. *J. Turbomach.*, 124 (2):235–241, 2002.

Dawes, W. Towards improved throughflow capability: The use of 3d viscous flow solvers in a multistage environment. In *Turbo Expo: Power for Land, Sea, and Air*, volume 79047, page V001T01A008. American Society of Mechanical Engineers, 1990.

Dawes, W. Multi-blade row navier-stokes simulations of fan-bypass configurations. In *Turbo Expo: Power for Land, Sea, and Air*, volume 78989, page V001T01A060. American Society of Mechanical Engineers, 1991.

Deardorff, J. W. et al. A numerical study of three-dimensional turbulent channel flow at large reynolds numbers. *J. Fluid Mech*, 41(2):453–480, 1970.

Deck, S. Zonal-detached-eddy simulation of the flow around a high-lift configuration. *AIAA journal*, 43(11):2372–2384, 2005.

Deck, S. and Renard, N. Towards an enhanced protection of attached boundary layers in hybrid rans/les methods. *Journal of Computational Physics*, 400:108970, 2020.

Ding, F., Arya, S. P., and Lin, Y.-L. Large-eddy simulations of the atmospheric boundary layer using a new subgrid-scale model–i. slightly unstable and neutral cases. *Environmental Fluid Mechanics*, 1(1):29–47, 2001.

Dorfman, A. and Renner, Z. Conjugate problems in convective heat transfer. *Mathematical Problems in Engineering*, 2009, 2010.

Duchaine, F., Mendez, S., Nicoud, F., Corpron, A., Moureau, V., and Poinsot, T. Conjugate heat transfer with large eddy simulation for gas turbine components. *Comptes Rendus Mecanique*, 337(6-7):550–561, 2009.

Ducros, F., Nicoud, F., and Poinsot, T. Wall-adapting local eddy-viscosity models for simulations in complex geometries. *Numerical Methods for Fluid Dynamics VI*, pages 293–299, 1998.

Duprat, C., Balarac, G., Métais, O., Congedo, P. M., and Brugière, O. A wall-layer model for large-eddy simulations of turbulent flows with/out pressure gradient. *Physics of Fluids*, 23(1):015101, 2011.

El Khoury, R. R., Errera, M., El Khoury, K., and Nemer, M. Efficiency of coupling schemes for the treatment of steady state fluid-structure thermal interactions. *International Journal of Thermal Sciences*, 115:225–235, 2017.

Elder, J. S. Gas turbine engine heat exchanger with tapered fins, July 22 2014. US Patent 8,784,047.

Errera, M.-P. and Duchaine, F. Comparative study of coupling coefficients in dirichlet–robin procedure for fluid–structure aerothermal simulations. *Journal of Computational Physics*, 312:218–234, 2016.

Errera, M.-P., Lazareff, M., Garaud, J.-D., Soubrié, T., Douta, C., and Federici, T. A coupling approach to modeling heat transfer during a full transient flight cycle. *International Journal of Heat and Mass Transfer*, 110:587–605, 2017.

Errera, M.-P. and Chemin, S. Optimal solutions of numerical interface conditions in fluid–structure thermal analysis. *Journal of Computational Physics*, 245:431–455, 2013.

Errera, M.-P., Moretti, R., Salem, R., Bachelier, Y., Arrivé, T., and Nguyen, M. A single stable scheme for steady conjugate heat transfer problems. *Journal of Computational Physics*, 394:491–502, 2019.

Errera, M.-P., Moretti, R., Mayeur, J., Gelain, M., Tessé, L., Lamet, J.-M., and Laroche, E. A numerical predictive model for conjugate heat transfer with radiation. *International Journal of Heat and Mass Transfer*, 160:120155, 2020.

Filburn, T., Kloter, A., and Cloud, D. Design of a carbon-carbon finned surface heat exchanger for a high-bypass ratio, high speed gas turbine engine. In *Turbo Expo: Power for Land, Sea, and Air*, volume 4238, pages 483–490, 2006.

Fulachier, L. *Contribution à l'étude des analogies des champs dynamique et thermique dans une couche limite turbulente: effet de l'aspiration.* PhD thesis, Université de Provence, 1972.

Garaud, J., Rannou, J., Bovet, C., Feld-Payet, S., Chiaruttini, V., Marchand, B., Lacourt, L., Yastrebov, V., Osipov, N., and Quilici, S. Z-set-suite logicielle pour la simulation des matériaux et structures. In *14ème Colloque National en Calcul des Structures*, 2019.

Germano, M., Piomelli, U., Moin, P., and Cabot, W. H. A dynamic subgrid-scale eddy viscosity model. *Physics of Fluids A: Fluid Dynamics*, 3(7):1760–1765, 1991.

Ghosal, S. and Moin, P. The basic equations for the large eddy simulation of turbulent flows in complex geometry. *Journal of Computational Physics*, 118(1):24–37, 1995.

Giles, M. Stability analysis of numerical interface conditions in fluid–structure thermal analysis. *International journal for numerical methods in fluids*, 25(4):421–436, 1997.

Giometto, B., Lozano-Durán, A., Park, G., and Moin, P. Three-dimensional transient channel flow at moderate reynolds numbers: analysis and wall modeling. *Center for Turbulence Research Annual Research Briefs*, pages 193–205, 2017.

Godunov, S. K. and Ryabenki, V. S. Theory of difference schemes-an introduction. *Amsterdam: North Holland*, 1964.

Griffin, J. G., Singer, I. D., and Summers, R. L. Lubrication cooling system for aircraft engine accessory, May 1 1979. US Patent 4,151,710.

Grötzbach, G. Direct numerical and large eddy simulation of turbulent channel flows. *Encyclopedia of fluid mechanics*, 6:1337–1391, 1987.

Gustafsson, B. The godunov-ryabenkii condition: The beginning of a new stability theory. In *Godunov Methods*, pages 425–443. Springer, 2001.

Gustafsson, B., Kreiss, H.-O., and Sundström, A. Stability theory of difference approximations for mixed initial boundary value problems. ii. *Mathematics of Computation*, pages 649–686, 1972.

Gyimah, G. K., Guo, Z.-n., Huang, P., Jiang, S.-z., Barber, G. C., Liu, G.-x., and Liu, J. Improvers of pressure-viscosity coefficients of two-phase liquid-solid lubricants. *DEStech Transactions on Engineering and Technology Research*, (amita), 2016.

Hattori, H., Houra, T., and Nagano, Y. Direct numerical simulation of stable and unstable turbulent thermal boundary layers. *International Journal of Heat and Fluid Flow*, 28(6):1262–1271, 2007.

Hattori, H., Yamada, S., and Houra, T. Dns study of effects of suddenly-vanishing wall heating in turbulent boundary layer. *Journal of Thermal Science and Technology*, 7(1):313–321, 2012.

Hattori, H., Yamada, S., Tanaka, M., Houra, T., and Nagano, Y. Dns, les and rans of turbulent heat transfer in boundary layer with suddenly changing wall thermal conditions. *International journal of heat and fluid flow*, 41:34–44, 2013.

Henshaw, W. D. and Chand, K. K. A composite grid solver for conjugate heat transfer in fluid–structure systems. *Journal of Computational Physics*, 228(10): 3708–3741, 2009.

Hoffmann, P. and Perry, A. The development of turbulent thermal layers on flat plates. *International Journal of Heat and Mass Transfer*, 22(1):39–46, 1979.

Huang, P. and Coleman, G. N. Van driest transformation and compressible wall-bounded flows. *AIAA journal*, 32(10):2110–2113, 1994.

Huang, P., Coleman, G., and Bradshaw, P. Compressible turbulent channel flows: Dns results and modelling. *Journal of Fluid Mechanics*, 305:185–218, 1995.

Inoue, M. and Pullin, D. Large-eddy simulation of the zero-pressure-gradient turbulent boundary layer up to re_θ= o (10ˆ(12)). *Journal of Fluid Mechanics*, 686: 507–533, 2011.

Jafari, S. and Nikolaidis, T. Thermal management systems for civil aircraft engines: Review, challenges and exploring the future. *Applied Sciences*, 8(11):2044, 2018.

Jaure, S., Duchaine, F., Staffelbach, G., and Gicquel, L. Massively parallel conjugate heat transfer methods relying on large eddy simulation applied to an aeronautical combustor. *Computational Science & Discovery*, 6(1):015008, 2013.

Jayakumar, J., Mahajani, S., Mandal, J., Vijayan, P., and Bhoi, R. Experimental and cfd estimation of heat transfer in helically coiled heat exchangers. *Chemical engineering research and design*, 86(3):221–232, 2008.

Jiménez, J. and Vasco, C. Approximate lateral boundary conditions for turbulent simulations. In *Proceedings of the Summer Program*, pages 399–412, 1998.

Johnson, D. et al. Velocity and temperature fluctuation measurements in a turbulent boundary layer downstream of a stepwise discontinuity in wall temperature. *J. Appl. Mech.*, 26:325–336, 1959.

Johnson, D. and Whippany, N. Velocity, temperature and heat transfer measurements in a turbulent boundary layer downstream of a stepwise discontinuity in wall temperature. *ASME Trans. J. Appl. Mech*, 24:2–8, 1957.

Jonsson, H. and Moshfegh, B. Influence of fin spacing, fin thickness and inlet velocity on the performance of plate fin heat sinks under varying bypass conditions using cfd. *International journal of heat exchangers*, 1(2):177–196, 2000.

Joshi, O. and Leyland, P. Stability analysis of a partitioned fluid–structure thermal coupling algorithm. *Journal of Thermophysics and Heat Transfer*, 28(1):59–67, 2014.

Kader, B. Temperature and concentration profiles in fully turbulent boundary layers. *International journal of heat and mass transfer*, 24(9):1541–1544, 1981.

Kadle, D. and Sparrow, E. M. Numerical and experimental study of turbulent heat transfer and fluid flow in longitudinal fin arrays. *ASME Journal of Heat Transfer*, 108:16–23, 1986.

Kasagi, N., Tomita, Y., and Kuroda, A. Direct numerical simulation of passive scalar field in a turbulent channel flow. *ASME Journal of Heat Transfer*, 114:598–606, 1992.

Kawai, S. and Larsson, J. Wall-modeling in large eddy simulation: Length scales, grid resolution, and accuracy. *Physics of Fluids*, 24(1):015105, 2012.

Kawamura, H., Abe, H., and Shingai, K. Dns of turbulence and heat transport in a channel flow with different reynolds and prandtl numbers and boundary conditions. *Turbulence, Heat and Mass Transfer*, 3:15–32, 2000.

Kawamura, H., Abe, H., and Matsuo, Y. Dns of turbulent heat transfer in channel flow with respect to reynolds and prandtl number effects. *International Journal of Heat and Fluid Flow*, 20(3):196–207, 1999.

Kays, W. M. Turbulent prandtl number. where are we? *ASME Transactions Journal of Heat Transfer*, 116:284–295, 1994.

Kazemi-Kamyab, V., van Zuijlen, A., and Bijl, H. Accuracy and stability analysis of a second-order time-accurate loosely coupled partitioned algorithm for transient conjugate heat transfer problems. *International Journal for Numerical Methods in Fluids*, 74(2):113–133, 2014.

Kim, J. and Moin, P. Transport of passive scalars in a turbulent channel flow. In *Turbulent Shear Flows 6*, pages 85–96. Springer, 1989.

Kim, J., Moin, P., and Moser, R. Turbulence statistics in fully developed channel flow at low reynolds number. *Journal of fluid mechanics*, 177:133–166, 1987.

Kim, M., Ha, M. Y., and Min, J. K. A numerical study on various pin–fin shaped surface air–oil heat exchangers for an aero gas-turbine engine. *International Journal of Heat and Mass Transfer*, 93:637–652, 2016.

Kim, S., Min, J. K., Ha, M. Y., and Son, C. Investigation of high-speed bypass effect on the performance of the surface air–oil heat exchanger for an aero engine. *International Journal of Heat and Mass Transfer*, 77:321–334, 2014.

Koren, C., Vicquelin, R., and Gicquel, O. Multiphysics simulation combining large-eddy simulation, wall heat conduction and radiative energy transfer to predict wall temperature induced by a confined premixed swirling flame. *Flow, Turbulence and Combustion*, 101(1):77–102, 2018.

Kumar, I. Conjugate problem of heat transfer in a laminar boundary layer with injection. *Journal of engineering physics*, 14(5):411–416, 1968.

Kumar, I. and Bartman, A. Conjugate heat transfer in a laminar boundary layer of compressible fluid with radiation. *Heat and Mass Transfer*, 9:481–489, 1968.

Larsson, J., Lien, F., and Yee, E. Feedback-controlled forcing in hybrid les/rans. *International Journal of Computational Fluid Dynamics*, 20(10):687–699, 2006.

Larsson, J., Laurence, S., Bermejo-Moreno, I., Bodart, J., Karl, S., and Vicquelin, R. Incipient thermal choking and stable shock-train formation in the heat-release region of a scramjet combustor. part ii: Large eddy simulations. *Combustion and Flame*, 162(4):907–920, 2015.

Larsson, J., Kawai, S., Bodart, J., and Bermejo-Moreno, I. Large eddy simulation with modeled wall-stress: recent progress and future directions. *Mechanical Engineering Reviews*, 3(1):15–00418, 2016.

Lau, K. S. and Mahajan, R. L. Effects of tip clearance and fin density on the performance of heat sinks for vlsi packages. *IEEE transactions on components, hybrids, and manufacturing technology*, 12(4):757–765, 1989.

Launder, B. E. and Sharma, B. I. Application of the energy-dissipation model of turbulence to the calculation of flow near a spinning disc. *Letters in heat and mass transfer*, 1(2):131–137, 1974.

Lee, J., Cho, M., and Choi, H. Large eddy simulations of turbulent channel and boundary layer flows at high reynolds number with mean wall shear stress boundary condition. *Physics of Fluids*, 25(11):110808, 2013.

Li, Y. and Kong, S.-C. Coupling conjugate heat transfer with in-cylinder combustion modeling for engine simulation. *International Journal of Heat and Mass Transfer*, 54(11-12):2467–2478, 2011.

Lilly, D. K. A proposed modification of the germano subgrid-scale closure method. *Physics of Fluids A: Fluid Dynamics*, 4(3):633–635, 1992.

Lindström, J. and Nordström, J. A stable and high-order accurate conjugate heat transfer problem. *Journal of Computational Physics*, 229(14):5440–5456, 2010.

Lodato, G., Castonguay, P., and Jameson, A. Structural wall-modeled les using a high-order spectral difference scheme for unstructured meshes. *Flow, turbulence and combustion*, 92(1-2):579–606, 2014.

Lozano-Durán, A., Bae, H., Bose, S., and Moin, P. Dynamic wall models for the slip boundary condition. *Annual research briefs. Center for Turbulence Research (US)*, 2017:229, 2017.

Manglik, R. M. and Bergles, A. E. Heat transfer and pressure drop correlations for the rectangular offset strip fin compact heat exchanger. *Experimental Thermal and Fluid Science*, 10(2):171–180, 1995.

Manhart, M., Peller, N., and Brun, C. Near-wall scaling for turbulent boundary layers with adverse pressure gradient. *Theoretical and Computational Fluid Dynamics*, 22(3-4):243–260, 2008.

Marshall, E. V. Oil cooling and drag reducing system, December 23 1958. US Patent 2,865,580.

Mason, P. J. and Thomson, D. J. Stochastic backscatter in large-eddy simulations of boundary layers. *Journal of Fluid Mechanics*, 242:51–78, 1992.

Menter, F. Zonal two equation kw turbulence models for aerodynamic flows. In *23rd fluid dynamics, plasmadynamics, and lasers conference*, page 2906, 1993.

Menter, F., Kuntz, M., and Bender, R. A scale-adaptive simulation model for turbulent flow predictions. In *41st aerospace sciences meeting and exhibit*, page 767, 2003.

Menter, F. and Kuntz, M. Adaptation of eddy-viscosity turbulence models to unsteady separated flow behind vehicles. In *The aerodynamics of heavy vehicles: trucks, buses, and trains*, pages 339–352. Springer, 2004.

Moin, P., Bodart, J., Bose, S., and Park, G. I. Wall-modeling in complex turbulent flows. In *Advances in Fluid-Structure Interaction*, pages 207–219. Springer, 2016.

Moretti, R., Errera, M.-P., Couaillier, V., and Feyel, F. Stability, convergence and optimization of interface treatments in weak and strong thermal fluid-structure interaction. *International Journal of Thermal Sciences*, 126:23–37, 2018.

Morinishi, Y., Tamano, S., and Nakabayashi, K. Direct numerical simulation of compressible turbulent channel flow between adiabatic and isothermal walls. *Journal of Fluid Mechanics*, 502:273–308, 2004.

Morkovin, M. V. Effects of compressibility on turbulent flows. *Mécanique de la Turbulence*, 367:380, 1962.

Moureau, V., Lartigue, G., Sommerer, Y., Angelberger, C., Colin, O., and Poinsot, T. Numerical methods for unsteady compressible multi-component reacting flows on fixed and moving grids. *Journal of Computational Physics*, 202(2):710–736, 2005.

Moureau, V., Barton, I., Angelberger, C., and Poinsot, T. Towards large eddy simulation in internal-combustion engines: simulation of a compressed tumble flow. *SAE transactions*, pages 1315–1324, 2004.

Ng, T., Talbot, L., and Robben, F. The turbulent boundary layer over a flat plate with strong stepwise heating. In *International Symposium on Applications of Laser-Doppler Anemometry to Fluid Mechanics*, 1982.

Nicoud, E., Colin, O., Angelberger, C., Krüger, C., and Nicollet, F. A no-slip wall law formulation for cell-vertex codes, validated for les of internal aerodynamics. In *LES4ICE Conference*, 2016.

Nicoud, F. Numerical study of a channel flow with variable properties. *Annual Research Briefs*, 1999.

Nicoud, F. and Ducros, F. Subgrid-scale stress modelling based on the square of the velocity gradient tensor. *Flow, turbulence and Combustion*, 62(3):183–200, 1999.

Nicoud, F., Winckelmans, G., Carati, D., Baggett, J., and Cabot, W. Boundary conditions for les away from the wall. In *Proceedings of the Summer Program*, page 413. Citeseer, 1998.

Nicoud, F., Baggett, J., Moin, P., and Cabot, W. Large eddy simulation wall-modeling based on suboptimal control theory and linear stochastic estimation. *Physics of Fluids*, 13(10):2968–2984, 2001.

Nicoud, F., Toda, H. B., Cabrit, O., Bose, S., and Lee, J. Using singular values to build a subgrid-scale model for large eddy simulations. *Physics of fluids*, 23(8): 085106, 2011.

Nikitin, N., Nicoud, F., Wasistho, B., Squires, K., and Spalart, P. R. An approach to wall modeling in large-eddy simulations. *Physics of fluids*, 12(7):1629–1632, 2000.

Ockendon, H., Ockendon, J., and Falle, S. The fanno model for turbulent compressible flow. *Journal of Fluid Mechanics*, 445:187–206, 2001.

Paniagua, G., Cuadrado, D., Saavedra, J., Andreoli, V., Meyer, T., Solano, J., Herrero, R., Meyer, S., and Lawrence, D. Design of the purdue experimental turbine aerothermal laboratory for optical and surface aerothermal measurements. *Journal of Engineering for Gas Turbines and Power*, 141(1), 2019.

Pantano, C., Pullin, D. I., Dimotakis, P. E., and Matheou, G. Les approach for high reynolds number wall-bounded flows with application to turbulent channel flow. *Journal of Computational Physics*, 227(21):9271–9291, 2008.

Papavassiliou, D. V. and Hanratty, T. J. Transport of a passive scalar in a turbulent channel flow. *International journal of heat and mass transfer*, 40(6):1303–1311, 1997.

Park, G. I. and Moin, P. An improved dynamic non-equilibrium wall-model for large eddy simulation. *Physics of Fluids*, 26(1):37–48, 2014.

Patankar, S. V. *Numerical heat transfer and fluid flow*. CRC press, 2018.

Patel, A., Peeters, J. W., Boersma, B. J., and Pecnik, R. Semi-local scaling and turbulence modulation in variable property turbulent channel flows. *Physics of Fluids*, 27(9):095101, 2015.

Perelman, T. On conjugated problems of heat transfer. *International Journal of Heat and Mass Transfer*, 3(4):293–303, 1961.

Piomelli, U. Wall-layer models for large-eddy simulations. *Progress in aerospace sciences*, 44(6):437–446, 2008.

Piomelli, U. and Balaras, E. Wall-layer models for large-eddy simulations. *Annual review of fluid mechanics*, 34(1):349–374, 2002.

Piomelli, U., Ferziger, J., Moin, P., and Kim, J. New approximate boundary conditions for large eddy simulations of wall-bounded flows. *Physics of Fluids A: Fluid Dynamics*, 1(6):1061–1068, 1989.

Piomelli, U., Balaras, E., Pasinato, H., Squires, K. D., and Spalart, P. R. The inner–outer layer interface in large-eddy simulations with wall-layer models. *International Journal of heat and fluid flow*, 24(4):538–550, 2003.

Piperno, S., Farhat, C., and Larrouturou, B. Partitioned procedures for the transient solution of coupled aroelastic problems part i: Model problem, theory and two-dimensional application. *Computer methods in applied mechanics and engineering*, 124(1-2):79–112, 1995.

Poinsot, T. and Veynante, D. *Theoretical and numerical combustion*. RT Edwards, Inc., 2005.

Pope, S. B. Turbulent flows, 2001.

Porté-Agel, F., Meneveau, C., and Parlange, M. B. A scale-dependent dynamic model for large-eddy simulation: application to a neutral atmospheric boundary layer. *Journal of Fluid Mechanics*, 415:261–284, 2000.

Reynolds, O. On the extent and action of the heating surface of steam boilers. *Papers on Mechanical and Physical subjects*, page 81, 1901.

Roe, B., Jaiman, R., Haselbacher, A., and Geubelle, P. H. Combined interface boundary condition method for coupled thermal simulations. *International journal for numerical methods in fluids*, 57(3):329–354, 2008.

Roux, F.-X. and Garaud, J.-D. Domain decomposition methodology with robin interface matching conditions for solving strongly coupled fluid-structure problems. *International Journal for Multiscale Computational Engineering*, 7(1), 2009.

Salem, R. *Algorithmes de couplage aérothermique pour des applications turbomachines*. PhD thesis, Université Paris-Saclay, 2020.

Sanchez, M., Aulery, F., Toutant, A., and Bataille, F. Large eddy simulations of thermal boundary layer spatial development in a turbulent channel flow. *Journal of Fluids Engineering*, 136(6), 2014.

Schlichting, H. and Gersten, K. *Boundary-layer theory*. Springer, 2016.

Schmitt, P., Schuermans, B., Geigle, K., and Poinsot, T. Effects of radiation, wall heat loss and effusion cooling on flame stabilisation and pollutant prediction in les of gas turbine combustion. In *ECCOMAS thematic conference on computational combustion*, 2005.

Schonfeld, T. and Rudgyard, M. Steady and unsteady flow simulations using the hybrid flow solver avbp. *AIAA journal*, 37(11):1378–1385, 1999.

Schumann, U. Subgrid scale model for finite difference simulations of turbulent flows in plane channels and annuli. *Journal of computational physics*, 18(4):376–404, 1975.

Schutte, D. J., Rahman, M., and Faghri, A. Transient conjugate heat transfer in a thick-walled pipe with developing laminar flow. *Numerical Heat Transfer*, 21(2): 163–186, 1992.

Schwarz, F. M. and Elsaesser, F. L. Air-oil heat exchanger, March 6 2012. US Patent 8,127,828.

Seki, Y. and Kawamura, H. Dns of turbulent heat transfer in a channel flow with streamwisely varying thermal boundary condition. In *TSFP DIGITAL LIBRARY ONLINE*. Begel House Inc., 2005.

Selle, L., Lartigue, G., Poinsot, T., Koch, R., Schildmacher, K.-U., Krebs, W., Prade, B., Kaufmann, P., and Veynante, D. Compressible large eddy simulation of turbulent combustion in complex geometry on unstructured meshes. *Combustion and Flame*, 137(4):489–505, 2004.

Serrano, J. R., Arnau, F. J., Gracía-Cuevas, L. M., Samala, V., and Smith, L. Experimental approach for the characterization and performance analysis of twin entry radial-inflow turbines in a gas stand and with different flow admission conditions. *Applied Thermal Engineering*, 159:113737, 2019a.

Serrano, J. R., Arnau, F. J., García-Cuevas, L. M., Soler, P., and Cheung, R. Experimental validation of a one-dimensional twin-entry radial turbine model under non-linear pulse conditions. *International Journal of Engine Research*, page 1468087419869157, 2019b.

Shahi, M., Kok, J. B., Roman Casado, J., and Pozarlik, A. K. Study of unsteady heat transfer as a key parameter to characterize limit cycle of high amplitude pressure oscillations. In *Turbo Expo: Power for Land, Sea, and Air*, volume 45738, page V05CT18A011. American Society of Mechanical Engineers, 2014.

Simpson, R. L. A model for the backflow mean velocity profile. *AIAA journal*, 21 (1):142–143, 1983.

Smagorinsky, J. General circulation experiments with the primitive equations: I. the basic experiment. *Monthly weather review*, 91(3):99–164, 1963.

Smith, B. The k-kl turbulence model and wall layer model for compressible flows. In *21st Fluid dynamics, plasma dynamics and lasers conference*, page 1483, 1990.

Smith, B. A near wall model for the k-l two equation turbulence model. In *Fluid Dynamics Conference*, page 2386, 1994.

Smith, B. Prediction of hypersonic shock wave turbulent boundary layer interactions with the kl two equation turbulence model. In *33rd Aerospace Sciences Meeting and Exhibit*, page 232, 1995.

Soliman, M. and Johnson, H. Transient heat transfer for turbulent flow over a flat plate of appreciable thermal capacity and containing time-dependent heat source. *ASME Journal of Heat Transfer*, 89:362–370, 1967.

Sousa, J., Villafañe, L., and Paniagua, G. Thermal analysis and modeling of surface heat exchangers operating in the transonic regime. *Energy*, 64:961–969, 2014.

Spalart, P. Reflections on rans modelling. In *Progress in hybrid RANS-LES modelling*, pages 7–24. Springer, 2010.

Spalart, P. and Allmaras, S. A one-equation turbulence model for aerodynamic flows. In *30th aerospace sciences meeting and exhibit*, page 439, 1992.

Spalart, P. R. Comments on the feasibility of les for wings, and on a hybrid rans/les approach. In *Proceedings of first AFOSR international conference on DNS/LES*. Greyden Press, 1997.

Spalart, P. R. Detached-eddy simulation. *Annual review of fluid mechanics*, 41: 181–202, 2009.

Spalart, P. R., Deck, S., Shur, M. L., Squires, K. D., Strelets, M. K., and Travin, A. A new version of detached-eddy simulation, resistant to ambiguous grid densities. *Theoretical and computational fluid dynamics*, 20(3):181–195, 2006.

Spalding, D. Heat transfer to a turbulent stream from a surface with a step-wise discontinuity in wall temperature. *International Developments in Heat Transfer*, pages 439–446, 1961.

Sparrow, E., Baliga, B., and Patankar, S. Forced convection heat transfer from a shrouded fin array with and without tip clearance. *ASME Journal of Heat Transfer*, 100:572–579, 1978.

Streifinger, H. Fuel/oil system thermal management in aircraft turbine engines. In *RTO Meeting proceedings*, pages 12–1, 1999.

Sullivan, P. P., McWilliams, J. C., and Moeng, C.-H. A subgrid-scale model for large-eddy simulation of planetary boundary-layer flows. *Boundary-Layer Meteorology*, 71(3):247–276, 1994.

Tamano, S. and Morinishi, Y. Effect of different thermal wall boundary conditions on compressible turbulent channel flow at m= 1.5. *Journal of Fluid Mechanics*, 548:361–373, 2006.

Taylor, R., Love, P., Coleman, H., and Hosni, M. Heat transfer measurements in incompressible turbulent flat plate boundary layers with step wall temperature boundary conditions. *ASME Transactions Journal of Heat Transfer*, 112:245–247, 1990.

Teitel, M. and Antonia, R. A step change in wall heat flux in a turbulent channel flow. *International journal of heat and mass transfer*, 36(6):1707–1709, 1993.

Templeton, J. A., Medic, G., and Kalitzin, G. An eddy-viscosity based near-wall treatment for coarse grid large-eddy simulation. *Physics of fluids*, 17(10):105101, 2005.

Tiselj, I., Oder, J., and Cizelj, L. Double-sided cooling of heated slab: Conjugate heat transfer dns. *International Journal of Heat and Mass Transfer*, 66:781–790, 2013.

Torregrosa, A., Broatch, A., García-Tíscar, J., and Roig, F. Experimental verification of hydrodynamic similarity in hot flows. *Experimental Thermal and Fluid Science*, 119:110220, 2020.

Toutant, A. and Bataille, F. Turbulence statistics in a fully developed channel flow submitted to a high temperature gradient. *International Journal of Thermal Sciences*, 74:104–118, 2013.

Townsend, A. *The structure of turbulent shear flow*. Cambridge University Press, 1980.

Travin, A., Shur, M., Strelets, M., and Spalart, P. Detached-eddy simulations past a circular cylinder. *Flow, Turbulence and Combustion*, 63(1):293–313, 2000.

Versaevel, P. *Combustion laminaire diphasique: Etude théorique et expérimentale*. PhD thesis, Châtenay-Malabry, Ecole centrale de Paris, 1996.

Verstraete, T. and Scholl, S. Stability analysis of partitioned methods for predicting conjugate heat transfer. *International Journal of Heat and Mass Transfer*, 101: 852–869, 2016.

Villafañe, L. and Paniagua, G. Aerodynamic impact of finned heat exchangers on transonic flows. *Experimental Thermal and Fluid Science*, 97:223–236, 2018.

Vynnycky, M., Kimura, S., Kanev, K., and Pop, I. Forced convection heat transfer from a flat plate: the conjugate problem. *International Journal of Heat and Mass Transfer*, 41(1):45–59, 1998.

Weigand, B., Ferguson, J., and Crawford, M. An extended kays and crawford turbulent prandtl number model. *International journal of heat and mass transfer*, 40 (17):4191–4196, 1997.

Wilcox, D. C. Reassessment of the scale-determining equation for advanced turbulence models. *AIAA journal*, 26(11):1299–1310, 1988.

Wilcox, D. C. et al. *Turbulence modeling for CFD*, volume 2. DCW industries La Canada, CA, 1998.

Wirtz, R. A., Chen, W., and Zhou, R. Effect of flow bypass on the performance of longitudinal fin heat sinks. *ASME Journal of Electronic Packaging*, 116:206–211, 1994.

Worth, W. Lubrication and cooling problems of aircraft engines. *SAE Transactions*, pages 315–324, 1937.

Wrenick, S., Sutor, P., Pangilinan, H., and Schwarz, E. E. Heat transfer properties of engine oils. In *World Tribology Congress*, volume 42010, pages 595–596, 2005.

Wu, A., Keum, S., and Sick, V. Large eddy simulations with conjugate heat transfer (cht) modeling of internal combustion engines (ices). *Oil & Gas Science and Technology–Revue d'IFP Energies nouvelles*, 74:51, 2019.

Wu, P. and Meyers, J. A constraint for the subgrid-scale stresses in the logarithmic region of high reynolds number turbulent boundary layers: A solution to the log-layer mismatch problem. *Physics of Fluids*, 25(1):015104, 2013.

Yang, X., Bose, S., and Moin, P. A physics-based interpretation of the slip-wall les model. *Annual Research Briefs*, pages 65–74, 2017a.

Yang, X., Sadique, J., Mittal, R., and Meneveau, C. Integral wall model for large eddy simulations of wall-bounded turbulent flows. *Physics of Fluids*, 27(2):025112, 2015.

Yang, X. I., Park, G. I., and Moin, P. Log-layer mismatch and modeling of the fluctuating wall stress in wall-modeled large-eddy simulations. *Physical review fluids*, 2(10):104601, 2017b.

York, W. D. and Leylek, J. H. Three-dimensional conjugate heat transfer simulation of an internally-cooled gas turbine vane. In *Turbo Expo: Power for Land, Sea, and Air*, volume 36886, pages 351–360, 2003.

Zhang, Y. and Vicquelin, R. Controlling bulk reynolds number and bulk temperature in channel flow simulations. *Journal of Computational Physics*, 305:208–216, 2016.

Zhang, Y., Vicquelin, R., Gicquel, O., and Taine, J. A wall model for les accounting for radiation effects. *International Journal of Heat and Mass Transfer*, 67:712–723, 2013.